TKK Dissertations 220
Espoo 2010

# EFFECT OF WELDING PARAMETERS OF PLASMA TRANSFERRED ARC WELDING METHOD ON ABRASIVE WEAR RESISTANCE OF 12V TOOL STEEL DEPOSIT

Doctoral Dissertation

**Marko Keränen**

**Aalto University**
**School of Science and Technology**
**Faculty of Engineering and Architecture**
**Department of Engineering Design and Production**

TKK Dissertations 220
Espoo 2010

# EFFECT OF WELDING PARAMETERS OF PLASMA TRANSFERRED ARC WELDING METHOD ON ABRASIVE WEAR RESISTANCE OF 12V TOOL STEEL DEPOSIT

Doctoral Dissertation

**Marko Keränen**

Doctoral dissertation for the degree of Doctor of Science in Technology to be presented with due permission of the Faculty of Engineering and Architecture for public examination and debate in Auditorium K215 at the Aalto University School of Science and Technology (Espoo, Finland) on the 28th of April 2010 at 12 noon.

**Aalto University**
**School of Science and Technology**
**Faculty of Engineering and Architecture**
**Department of Engineering Design and Production**

**Aalto-yliopisto**
**Teknillinen korkeakoulu**
**Insinööritieteiden ja arkkitehtuurin tiedekunta**
**Koneenrakennustekniikan laitos**

Distribution:
Aalto University
School of Science and Technology
Faculty of Engineering and Architecture
Department of Engineering Design and Production
Engineering Materials
P.O. Box 14200 (Puumiehenkuja 3)
FI - 00076 Aalto
FINLAND
URL: http://edp.tkk.fi/en/
Tel. +358-9-470 23538
Fax +358-9-470 23537
E-mail: marko.keranen@tkk.fi



ISBN 978-952-60-3109-5
ISBN 978-952-60-3110-1 (PDF)
ISSN 1795-2239
ISSN 1795-4584 (PDF)
URL: http://lib.tkk.fi/Diss/2010/isbn9789526031101/

TKK-DISS-2743

Picaset Oy
Helsinki 2010

Aalto University

| ABSTRACT OF DOCTORAL DISSERTATION | AALTO UNIVERSITY<br>SCHOOL OF SCIENCE AND TECHNOLOGY<br>P.O. BOX 11000, FI-00076 AALTO<br>http://www.aalto.fi |
|---|---|

Author Marko Keränen

Name of the dissertation
Effect of welding parameters of plasma transferred arc welding method on abrasive wear resistance of 12V tool steel deposit


| Manuscript submitted 29.10.2009 | Manuscript revised 15.03.2010 |
|---|---|
| Date of the defence 28.04.2010 | |
| ☒ Monograph | ☐ Article dissertation (summary + original articles) |

Faculty Faculty of Engineering and Architecture
Department Department of Engineering Design and Production
Field of research Engineering Materials
Opponent(s) Prof. Leijun Li and Prof. Jyrki Vuorinen
Supervisor Prof. Hannu Hänninen
Instructor Prof. Hannu Hänninen



Abstract

In the plasma transferred arc, PTA, welding method the powder consumable makes it possible to weld wide variety of alloys. The dilution of the deposit is typically 3-10 % and, thus, the properties of the deposit can be achieved with one-layer deposit. The studied alloy was an iron-based 12V tool steel reinforced with primarily precipitating vanadium carbides.

Wide deposits are welded by oscillating the plasma arc and overlapping the weld beads. The mobility of the molten pool of 12V tool steel is good. The location of the plasma arc in relation with the molten pool during perpendicular movement and the shape of the plasma arc had strong effects on both the dilution control and the microstructure of the 12V tool steel deposit. The location of the plasma arc can be in the edge or on top of the molten pool.

Depending on the parameter window the mean sizes and the volume fractions of vanadium carbides were 0,5-1,8 micrometers and 12,2-17,5 vol.-%, respectively. When the plasma arc was precisely in the edge of the molten pool, the size, the distance between vanadium carbides, and the shape of vanadium carbides were optimal. With the studied welding parameters, the 12V tool steel deposit is extremely sensitive to small variations in the welding parameters. If the molten pool is stirred slightly when oscillating the plasma arc, vanadium carbides cannot grow and the shapes of the carbides are mainly more needle-shaped instead of round-shape.

Wear tests were made by the rubber wheel abrasion test according to standard ASTM G 65-94. Round-shaped, 1,2-1,4 micrometer-sized vanadium carbides were the most beneficial according to the wear surface examinations. The optimized PTA welded 12V tool steel deposit had better abrasive wear resistance when compared to the 12V tool steel deposit manufactured by the hot isostatic pressing, HIP.



Keywords PTA, tool steel, powder consumable, dilution, vanadium carbide, abrasive wear resistance

| ISBN (printed) 978-952-60-3109-5 | ISSN (printed) 1795-2239 |
|---|---|
| ISBN (pdf) 978-952-60-3110-1 | ISSN (pdf) 1795-4584 |
| Language English | Number of pages 166 p. |

Publisher Aalto University, Department of Engineering Design and Production

Print distribution Aalto University, Department of Engineering Design and Production, Engineering Materials

☒ The dissertation can be read at http://lib.tkk.fi/Diss/2010/isbn9789526031101/

Aalto-yliopisto

| VÄITÖSKIRJAN TIIVISTELMÄ | AALTO-YLIOPISTO<br>TEKNILLINEN KORKEAKOULU<br>PL 11000, 00076 AALTO<br>http://www.aalto.fi |
|---|---|

Tekijä Marko Keränen

Väitöskirjan nimi

Hitsausparametrien vaikutus jauheplasmamenetelmällä hitsatun 12V työkaluteräspinnoitteen abrasiiviseen kulumiskestävyyteen

| | |
|---|---|
| Käsikirjoituksen päivämäärä 29.10.2009 | Korjatun käsikirjoituksen päivämäärä 15.03.2010 |
| Väitöstilaisuuden ajankohta 28.04.2010 | |
| ☒ Monografia | ☐ Yhdistelmäväitöskirja (yhteenveto + erillisartikkelit) |


| | |
|---|---|
| Tiedekunta | Insinööritieteiden ja arkkitehtuurin tiedekunta |
| Laitos | Koneenrakennustekniikan laitos |
| Tutkimusala | Materiaalitekniikka |
| Vastaväittäjä(t) | Prof. Leijun Li ja Prof. Jyrki Vuorinen |
| Työn valvoja | Prof. Hannu Hänninen |
| Työn ohjaaja | Prof. Hannu Hänninen |



Tiivistelmä

Jauheplasmamenetelmällä, PTA, hitsattaessa jauhemainen lisäaine mahdollistaa laajan lisäainevalikoiman käytön. Menetelmälle tyypillinen sekoittumisaste on 3-10 %, jolloin pinnoitteen halutut ominaisuudet saavutetaan yhdellä palkokerroksella. Koemateriaalina oli rautapohjainen 12V työkaluteräs, jossa on lujitteena primäärisesti erkautuvia vanadiinikarbideja.

Leveä pinnoite hitsataan oskilloimalla plasmakaarta ja limittämällä hitsipalkoja. 12V työkaluteräksen hitsisulan liikkuvuus on hyvä. Plasmakaaren paikalla suhteessa hitsisulaan kaaren poikittaisen liikkeen aikana ja plasmakaaren muodolla oli suuri vaikutus sekä 12V työkaluteräksen sekoittumisasteen kontrollointiin että mikrorakenteeseen. Plasmakaaren paikka voi olla joko sulan reunassa tai sen päällä.

Parametri-ikkunasta riippuen vanadiinikarbidien keskimääräinen koko ja tilavuusosuus olivat 0,5-1,8 mikrometriä ja 12,2-17,5 til.-%, vastaavasti. Kun plasmakaari oli tarkasti sulan reunassa, vanadiinikarbidien koko, karbidien välinen etäisyys ja muoto olivat optimaaliset. Tutkituilla hitsausparametreillä 12V työkaluteräspinnoite on erityisen herkkä hitsausparametrien pienille vaihteluille. Jos hitsisulaa sekoitetaan hieman kun plasmakaarta oskilloidaan, vanadiinikarbidit eivät pääse kasvamaan kokoa, ja niiden muoto on pääasiallisesti enemmän neulasmainen pyöreän muodon sijasta.

Kulutuskokeet tehtiin kumipyöräabraasiokulutuskoelaitteistolla ASTM G 65-94 standardin mukaisesti. Pyöreät, 1,2-1,4 mikrometrin kokoiset vanadiinikarbidit olivat kulutuspinnan SEM tarkastelun perusteella kaikkein hyödyllisimpiä. Optimoidulla jauheplasmalla hitsatulla 12V työkaluteräspinnoitteella oli parempi kulumiskestävyys kuin vastaavalla kuumaisostaattisella puristuksella, HIP, valmistetulla materiaalilla.



| | | | |
|---|---|---|---|
| Asiasanat | PTA, työkaluteräs, jauhemainen lisäaine, sekoittumisaste, vanadiinikarbidi, abrasiivinen kulumiskestävyys | | |
| ISBN (painettu) | 978-952-60-3109-5 | ISSN (painettu) | 1795-2239 |
| ISBN (pdf) | 978-952-60-3110-1 | ISSN (pdf) | 1795-4584 |
| Kieli | englanti | Sivumäärä | 166 s. |
| Julkaisija | Aalto-yliopisto, Koneenrakennustekniikan laitos | | |
| Painetun väitöskirjan jakelu | Aalto-yliopisto, Koneenrakennustekniikan laitos, Materiaalitekniikka | | |
| ☒ Luettavissa verkossa osoitteessa http://lib.tkk.fi/Diss/2010/isbn9789526031101/ | | | |

# Preface

The study was started with the project "Surfacing with different methods", which was conducted during the years 1999-2002. The project was funded by TEKES, Metso Powdermet Oy, Metso Works Oy, Metso Paper Oy, Fortum Power and Heat Oy, Fortum Oil and Gas Oy, Sulzer Pumps Finland Oy, Plasma Modules Oy, and Esab Oy. The dissertation was conducted in the Graduate school on Metallurgy and Metals Technology during the years 2002-2006 and it was funded by Academy of Finland and Metso Powdermet Oy.

I would like to thank the supervisor of the thesis Professor Hannu Hänninen for his guidance and advices. Dr. Jari Liimatainen from Metso Powdermet Oy is acknowledged for his support and for additional funding for my studies during the years 2000-2006. Dr. Pekka Siitonen, Dr. Mikko Uusitalo, M.Sc. Mikko Luukas, Mr. Heikki Vestman, Mr. Samuli Laine, and Mr. Jari Hellgren are acknowledged for helping in the PTA welding tests. M.Sc. Tapio Saukkonen is thanked for helping in the SEM studies. M.Sc. Timo Kiesi is thanked for helping with the X-ray diffraction examinations. Laboratory of Machine Design is thanked for helping in the rubber wheel abrasion tests. Personnel and colleagues in the Laboratory of Engineering Materials are thanked for the great working atmosphere.

I am very thankful to my dear wife Sirpa for her patience and support throughout this work.

Espoo, March 2010

Marko Keränen

# Contents

# LIST OF ABBREVIATIONS

| | |
|---|---|
| Ar | Argon |
| $B_4C$ | Boron carbide |
| $CO_2$ | Carbon dioxide |
| EB | Electron beam welding method |
| F.C.C. | Face-centered cubic |
| FZ | Fusion zone |
| GMAW | Gas metal arc welding method |
| GTA, TIG | Gas tungsten arc welding method, tungsten inert gas welding method |
| HAZ | Heat affected zone |
| He | Helium |
| HIP | Hot isostatic pressing |
| HPTA | High power plasma transferred arc welding method |
| $H_2$ | Hydrogen |
| LB | Laser beam welding method |
| MFP | Mean free path |
| MIG/MAG | Metal inert/active gas welding method |
| MMC | Metal matrix composite |
| MPTA | Micro-plasma transferred arc welding method |
| $O_2$ | Oxygen |
| PA | Plasma arc welding method |
| PH | Preheated |
| PMZ | Partially melted zone |
| PTA | Plasma transferred arc welding method |
| RT | Room temperature, 20 °C |
| RWAT | Rubber wheel abrasion test according to standard ASTM G 65-94 |
| SAW | Submerged arc welding method |
| VC | Vanadium carbide |

# NOMENCLATURE

| | |
|---|---|
| $A$ | Experimentally determined constant, maximum melting efficiency |
| $A_g$ | Volume of a scratch groove [$mm^3$] |
| $A_{r1}$, $A_{r2}$ | Ridges formed during deformation by indented particle or asperity [$mm^3$] |
| $A_1$ | Area of the first weld bead layer without the first weld bead layer dilution [$mm^2$] |
| $A_2$ | Area of the first weld bead layer dilution without the first weld bead layer deposit area [$mm^2$] |
| $A_3$ | Area of the second weld bead layer without the dilution from the first weld bead layer [$mm^2$] |
| $A_4$ | Area of the second weld bead layer dilution from the first weld bead layer without the second weld bead layer deposit area [$mm^2$] |
| $a_1$ | Empirical constant, 60 [μm] |
| $a_2$ | Empirical constant, 0,32 |
| $B$ | Experimentally determined constant, slope on a plot of $\ln(\eta_m)$ against $(\eta_a U I \nu / E_m \nu_{kin,mp} \alpha_{300\ K})^{-1}$ |
| $\mathbf{B}_{mf}$ | Magnetic flux vector |
| $\mathbf{b}$ | Unit of slip, Burgers vector [Å] |
| $b_r$ | Width of the rubber wheel [mm] |
| $C$ | Coefficient of arc concentration [$m^{-2}$] |
| $C_{PL}$ | Specific heat rate of a powder particle at liquid state |
| $C_p$ | Specific heat of a powder particle |
| $CR$ | Cooling rate |
| $D_{sas}$ | Secondary arm spacing, 3-8 [μm] |
| $D_c^{\gamma}$ | Diffusivity of C in austenite |
| $D_{1st\ layer}$ | Dilution of the first weld bead layer [%] |
| $D_{2nd\ layer}$ | Dilution of the second weld bead layer [%] |
| $d$ | Average diameter of the reinforcing carbides [μm] |
| $d_a$ | Average diameter of the abrasives [μm] |
| $d_c$ | Circle diameter on the base material surface, $\frac{2}{\sqrt{C}}$ [mm] |
| $d_0$ | Initial diameter of a powder particle [μm] |
| $E$ | Elastic modulus [GPa] |
| $E_{bm}$ | Melting enthalpy of the base material |
| $E_m$ | Melting enthalpy |
| $E_{pc}$ | Melting enthalpy of the powder consumable |
| $E_s$ | Specific volume enthalpy of the deposit material including latent heat of melting |
| $\mathbf{F}_{arc}$ | Impinging force of the arc plasma |
| $\mathbf{F}_b$ | Buoyancy force |
| $\mathbf{F}_{em}$ | Electromagnetic force |
| $\mathbf{F}_{\gamma}$ | Surface tension force |
| $f$ | Resistance opposing motion of a dislocation (a force per unit length) |
| $f_{ab}$ | Abrasive efficiency |
| $\mathbf{g}$ | Gravitational acceleration [$m/s^2$] |
| $H_a$ | Hardness of the abrasive |
| $H_{bm}$ | Hardness of the base material or the wearing material |

| | |
|---|---|
| $H_{def}$ | Hardness measured on the wear debris |
| h | Average penetration depth of the abrasive particles [μm] |
| $h_b$ | Thickness of the weld bead [mm] |
| $h_r$ | Relative penetration depth of the abrasive particles, h/d |
| I | Arc current [A] |
| $\mathbf{J}_{cd}$ | Current density vector |
| K | Wear coefficient |
| K’ | Geometrical constant |
| $K_c$ | Fracture toughness of the wearing material [$MN/m^{3/2}$] |
| $K_1$, $K_2$ | Coefficients in relation with surface and abrasive hardness |
| k | Modification factor in relation with interphase interaction |
| $L_m$ | Melting heat rate of a powder particle |
| l | Sliding distance [m] |
| $l_d$ | Displacement of the plasma arc, overlapping [mm] |
| $M_s$ | Martensite start temperature [ºC] |
| $m_{net}$ | Abrasive net mass flow rate past the specimen [g/min] |
| $m_p$ | Mass of an abrasive particle [g] |
| $m_{pf}$ | Packing fraction |
| $N_p$ | Number of abrasive particles in contact zone [No.] |
| n | Number of deposited beads without preheating [No.] |
| n´ | Number of deposited beads with preheating [No.] |
| P | Applied load [N] |
| $P_p$ | Dimensionless parameter |
| q(0) | Maximum heat input along arc central axis |
| q(r) | Specific heat input at a radial distance of r from arc axis |
| $q_{eff}$ | Effective thermal power |
| $q_{eff, l}$ | Effective power of the plasma arc in local preheating |
| $q_{eff, n}$ | Effective thermal power at $n^{th}$ turn |
| $q_{net}$ | Net power |
| $R_e$ | Reynolds number of plasma particles system, ~1,06 |
| $R_p$ | Tip radius of an abrasive |
| $R_s$ | Radius of the shaft to be deposited [mm] |
| r | Radial distance from the point source [mm] |
| $r_P$ | Powder particle radius [μm] |
| $S_m$ | Heat conducting potential of argon plasma fluid at powder particles melting point |
| $S_P$ | Heat conducting potential of argon plasma fluid at powder particles temperature |
| $S_\infty$ | Heat conducting potential of argon plasma fluid at plasma temperature |
| s | Relative sliding speed between the rubber wheel and the specimen [m/s] |
| $T_M$ | Melting time for a particle [μs] |
| $T_{LH}$ | Liquid heating time for a particle [μs] |
| $T_{SH}$ | Solid heating time for a particle [μs] |
| $T_{amb}$ | Ambient temperature [ºC] |
| $T_{f, bm}$ | Temperature at front of the surfacing point [ºC] |
| $T_{m, bm}$ | Surface temperature ensuring melting of the deposit and the base material [ºC] |
| $T_{mp}$ | Temperature of the molten pool [°C] |

| | |
|---|---|
| $T_{m,\,p}$ | Temperature of a powder particle at melting point [°C] |
| $T_p$ | Temperature of a powder particle [ºC] |
| $T_r$ | Temperature at radius r from the point source [°C] |
| $T_s$ | Surface temperature of the molten pool [°C] |
| $T_{0,\,bm}$ | Initial temperature of the base material [ºC] |
| $T_{0,\,mp}$ | Reference temperature of the molten pool [ºC] |
| $T_{0,\,p}$ | Initial temperature of a powder particle [ºC] |
| $t_{diss}$ | Time to dissolve a particle [µs] |
| $t_0$ | Powder particle transporting time in the plasma arc [ms] |
| U | Arc voltage [V] |
| $U_c^{\gamma}$ | Carbon content in austenite close to the carbide-matrix interface [%] |
| $U_c^{\gamma\infty}$ | Carbon content in austenite [%] |
| $U_c^{cem}$ | Carbon content in cementite [%] |
| V | Wear volume of the deposit [$mm^3$] |
| $V_m$ | Abrasive wear resistance of the matrix phase |
| $V_{pc}$ | Volumetric powder consumable feed rate |
| $V_{pc,\,max}$ | Maximum volumetric powder consumable feed rate |
| $V_r$ | Abrasive wear rate |
| $V_{sp}$ | Abrasive wear resistance of the second phase |
| $V_{vf}$ | Abrasive wear resistance of the composite material |
| vf | Volume fraction of the second phase [vol.-%] |
| $vf_t(t)$ | Volume fraction of carbides as a function of time |
| $vf_{t_0}$ | Initial volume fraction of carbides [vol.-%] |
| W | Wear resistance |
| $w_b$ | Width of the weld bead [mm] |
| $x_{cl}$ | Contact length between the rubber wheel and the specimen [mm] |
| $x_1$, $x_2$ | Distance from the original deposit surface to the worn phase [mm] |
| y | Coordinate parallel to welding direction |
| $\nabla T$ | Temperature gradient at the weld pool surface |
| $\alpha$ | Thermal diffusivity |
| $\alpha_a$ | Mean attack angle [º] |
| $\alpha_{300\,K}$ | Thermal diffusivity at 300 K |
| $\beta$ | Factor describing the decay of deformation with increasing depth below the wearing surface |
| $\beta_e$ | Coefficient of thermal expansion of liquid metal |
| $\gamma$ | Retained austenite content [%] |
| $\gamma_s$ | Surface tension of liquid metal |
| $\varepsilon_i$ | Wear resistance of *i*th phase |
| $\zeta$ | Relative surfacing step, $l_d/R_s$ |
| $\eta_a$ | Arc efficiency |
| $\eta_m$ | Melting efficiency |
| $\eta_{m,2D}$ | Melting efficiency for the welds having 2D dimensional heat flow |
| $\eta_{m,3D}$ | Melting efficiency for the welds having 3D dimensional heat flow |
| $\eta_t$ | Thermal efficiency |
| $2\vartheta$ | Angle of abrasive tip [°] |
| $\overline{\tan\theta}$ | Weighted average of the tan θ values of all the individual abrasives |
| $\lambda_{MFP}$ | Mean free path, spacing, MFP [µm] |
| $\mu$ | Coefficient of friction |

| | |
|---|---|
| $c\rho$ | Specific volume heat capacity of the material of the component |
| $\rho$ | Density [g/mm$^3$] |
| $\rho_{PL}$ | Mass density of a powder particle at liquid state [g/mm$^3$] |
| $\rho_a$ | Density of an abrasive particle [g/mm$^3$] |
| $\rho_{lm}$ | Density of liquid metal [g/mm$^3$] |
| $\rho_p$ | Mass density of a powder particle [g/mm$^3$] |
| $\sigma$ | Stress in contact area [N/mm$^2$] |
| $\Omega$ | Driving force |
| $\tau$ | Shear stress |
| $\tau_n$ | Dimensionless surfacing time of n turns, $\frac{2\,\pi\,\alpha}{\nu\,R_s}$ n |
| $\tau_y$ | Dislocation yield strength |
| $\nu$ | Welding speed [mm/s] |
| $\upsilon_i$ | Volume fraction of *i*th phase [vol.-%] |
| $\nu_{kin,\,mp}$ | Kinematic viscosity at melting point |
| $\varphi$ | Thermal conductivity |
| $\varphi_{lim}$ | Capability of deformation of the wearing material during abrasive wear |
| $\varphi_s$ | Effective deformation on the wearing surface |
| $\Phi_{(R_s,\tau_n)}$ | Function of heat distribution |
| $\Phi_1$ | Constant |
| $\omega_{po}$ | Initial powder injection speed [m/s] |

# Original features

The studied material was an iron-based 12V tool steel alloy (C 2,9 % and V 11,5 %). The plasma transferred arc welding tests and experimental data of this thesis were firstly directed to evaluate the effects of the dilution on the properties of the 12V tool steel deposit. Secondly, they were directed to the evaluation of the effects of the welding parameters on the microstructure and the abrasive wear resistance of the 12V tool steel deposit.

The following features are believed to be original:

1. Optimization of the microstructure and the abrasive wear resistance of the PTA welded 12V tool steel deposit are systematically studied by varying welding parameters.

2. The effects of varying welding parameters on the vanadium carbide size and the MFP distributions of the 12V tool steel deposit were clearly detected by using seven parameter windows.

3. The effects of varying welding parameters on the volume fraction of vanadium carbides and the retained austenite content of the 12V tool steel deposit were measured. The volume fraction of vanadium carbides of the PTA welded 12V tool steel deposit was lower than in the materials manufactured by the HIP process, but the welding parameters for the volume fraction of vanadium carbides close to that of the HIP material 12V were found.

4. The effect of the location of the plasma arc in relation with the edge of the molten pool and the effect of the main welding parameters on the microstructure were detected by measuring the vanadium carbide shape ratios from the 12V tool steel deposits. The effect of the shape ratio on the abrasive wear resistance was confirmed from the wear surfaces in the SEM examination.

5. The microstructures and the abrasive wear resistances of the PTA welded 12V tool steel deposits were compared to those of the tool steel materials manufactured by the HIP process. The microstructural differences were defined and the welding parameters having better abrasive wear resistance for the used abrasive were found.

# 1 Introduction

## 1.1 General

The plasma transferred arc welding method, PTA, was developed in the 1960's from the plasma arc welding method, PA. The method has become common in the 1980's. It is also possible to use the PTA welding method for joint welding. During last decades the focus of the development has been towards the mechanized, the robotized, or the automated PTA welding method. Therefore, it is possible to reduce the welding costs, enhance the process controllability, improve the deposit quality, and increase the deposition rate. High amount of welding parameters, their interactions, and complicated effects of welding parameters on the properties of the various deposits have restricted the optimization of the properties of the deposits welded by the PTA welding method.

The main feature of the PTA welding method is the powder consumable. The properties of the deposit can be tailored for various applications, because different kinds of powders can be tailor-mixed (Saltzman *et al.*, 1985). Low boiling point alloys, e.g., zinc, cannot be welded because of high temperature of the plasma arc (Wahl *et al.*, 1993). The powder consumable is fed with a flow of carrier gas from the powder consumable hopper through the plasma torch straight into the plasma arc, where the powder melts with the base material and forms the deposit. Gas atomized spherically shaped powders are preferred. The powder fraction is usually 50-150 μm. The powder fraction depends on the deposition rate and, thus, the fraction is typically larger for the high power plasma transferred arc welding method, HPTA.

One of the main features of the PTA welding method is the low dilution of the deposit, which is from 3 to 10 %. The low dilution enables the use of one-layer deposit to achieve the intended deposition properties. Other features are strong metallurgical bond between the deposit and the base material, low heat input, low spattering, low distortion, less finishing, small heat affected zone (HAZ), no significant loss of alloying elements, no slag, high quality of the deposit, and excellent properties of the deposit.

The shape of the plasma arc is narrow and sharp, because of the plasma nozzle which intensifies the plasma arc. The plasma arc is stable from low current levels to extremely high current levels. The deposition rate for the PTA welding method with powder consumable is in the range of 0,1-20 kg/h. Thickness of one bead layer is between 1 and 6 mm. It is possible to weld multi-layer deposits. By oscillating the plasma torch, which helps to control the dilution of the deposit, wider passes up to 100 mm can be welded (Dilthey *et al.*, 1994). Bigger surfaces can be welded by overlapping (distance from the bead centerline to the next bead centerline) the weld beads.

Less expensive material like low alloyed steel can be used as a base material in the applications where wear resistance is only needed. In corrosive environments highly alloyed base materials are preferred to withstand the requirements set to the deposit. It is preferable that the base material has coefficient of thermal expansion close to that of the weld metal. Thus, cracks induced in the fusion line by different coefficients of thermal

expansion can be avoided during cooling of the component. Preheating, weld bead sequencing, and post-weld heat treating can be made if necessary (Raghu *et al.*, 1996).

The equipments of the PTA welding method are nowadays relatively cheap and the PTA welding method can be mechanized or automated economically, which helps to control the welding process. Typical applications for the PTA welding method are valves, valve seats, extrusion machine screws and components for cutting, waste recycling, mining, crushing, energy industry, and pulp and paper industry.

## 1.2 Problem description

The PTA welding method is used to weld several millimeter thick wear and corrosion resistant deposits. Traditionally, the dilution of the deposit has been the most studied parameter. It has been thought that it is the most important parameter of the weld bead, because low dilution means that the process is cost-effective and the properties of the deposit are automatically typical to the deposit alloy. During the surfacing process the dilution of the deposit can be controlled and it is usually adjusted by plasma arc current. Welding parameters affecting most the dilution of the deposit are plasma arc current, temperature of the work piece, working distance, powder feed rate, process gas flow rates, and oscillation parameters like amplitude, frequency, and welding speed.

The 12V tool steel deposit is sensitive to the welding process variations. The abrasive wear resistance of the 12V tool steel deposit is based on the primarily precipitated vanadium carbides (VC). The microstructure of the deposit, i.e., the volume fraction of carbides, the mean free path (MFP), the size of carbides, the morphology, the distribution of carbides, and the matrix phases determine the abrasive wear resistance of the 12V tool steel deposit. The dilution of the deposit has to be controlled during the surfacing procedure to maintain basic features of the PTA welding method. A lot of welding parameters and their interactions have effects on both the dilution and the microstructure of the deposit.

The size of the molten pool is large, when welding thick abrasive wear resistant deposit by oscillating the plasma arc. The location of the plasma arc is normally in the edge of the molten pool (Hallen *et al.*, 1992b). The risk of the weld pool stirring, i.e., convection of the molten pool liquid by the changing location of the plasma arc increases with the size of the molten pool. The location of the plasma arc in relation with the molten pool affects the weld pool convection. The PTA welding method is not stable during the surfacing procedure, e.g., work piece temperature changes from room temperature (RT) up to approximately 300 ºC. This leads to a need to adjust welding parameters. To maintain the optimized microstructure, both the dilution and the effects of the plasma arc on the factors determining the abrasive wear resistance of the 12V tool steel deposit have to be controlled and adjusted during the PTA welding method.

Some experimental tests and models are made during the years to determine the factors, which control the dilution and the abrasive wear resistance of the weld beads. The differences between the welding parameters may be small, but they have major effects

on the microstructure and the abrasive wear resistance of the 12V tool steel deposit, because of high temperature and velocity of the plasma arc.

# 2 PTA welding method

One of the most important features of the PTA welding method is its ability to produce low dilution deposits. This is related to the good plasma arc stability and reproducibility. Low dilution saves the powder consumable and production time. The deposits produced by thermal spray technologies are only mechanically bonded. The bond between the PTA welded deposit and the base material is a metallurgical bond and, thus, the deposit is able to resist many kinds of wear modes including impact wear. The possibilities to use the PTA welded wear and corrosion resistant deposits in industry are broad.

During the last decades the dilution of the PTA welded deposits has been between 5 and 10 %. The development of the equipments has enhanced the ability to control it and nowadays the dilution is from 3 to 10 % for the majority of the PTA applications (Chattopadhyay, 1997; Harris *et al.*, 1983). Because of the improved welding equipments and knowledge about the PTA welding method, the dilution of the deposit below 10 % is possible to maintain during the surfacing process. The dilution is one of the major parameters, which has to be controlled and adjusted during the welding process. Low dilution is important, because highly alloyed consumables are expensive and the base material and the deposit are usually dissimilar. Heat input to the base material is lower with low heat input.

The dilution of the first weld bead layer, $D_{1st\ layer}$, Figure 1, can be estimated from the cross-sectional weld bead sample by an image analysis program using equation 1. If the second weld bead layer is welded, equation 2 can be used to estimate the dilution of the second weld bead layer, $D_{2nd\ layer}$. The dilution is mainly concentrated nearby the fusion line, thus, the estimated dilution is not an exact value. The dilutions of the first and the second weld bead layers are:

$$D_{1st\ layer}\ [\%] = \frac{A_2}{A_1 + A_2} \times 100\ \%, \quad (1)$$

$$D_{2nd\ layer}\ [\%] = \frac{A_4}{A_3 + A_4} \times 100\ \% \times D_{1st\ layer}, \quad (2)$$

where $A_1$ is the area of the first weld bead layer without the first weld bead layer dilution, $A_2$ is the area of the first weld bead layer dilution without the first weld bead layer deposit area, $A_3$ is the area of the second weld bead layer without the dilution from the first weld bead layer, and $A_4$ is the area of the second weld bead layer dilution from the first weld bead layer without the second weld bead layer deposit area.

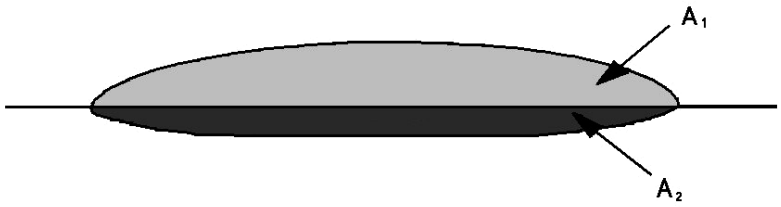


Figure 1 Schematic presentation of the deposit cross-section, where $A_1$ is the deposit area without penetration and $A_2$ is the area of penetration

## 2.1 PTA equipments

The mechanized PTA welding unit consists of the plasma torch, pilot and plasma arc power supplies, mechanized torch oscillation unit or robot, component manipulator or rotating table, consumable feed unit, torch cooling unit, and work piece preheating unit. The powder plasma torches have been manufactured also for manual hand welding (DuMola *et al*., 1988) and mechanized internal cladding for the pipes the inner diameter of which is 70 mm at minimum (Dilthey *et al.*, 1994; Draugelates *et al*., 1993).

### 2.1.1 Plasma torch

A typical powder plasma torch is presented schematically in Figure 2. In the torch the pilot arc (non-transferred arc) is maintained between the non-consumable tungsten electrode (cathode) and the water-cooled plasma nozzle (anode). The pilot arc is needed for initiating and stabilizing the plasma transferred arc. The transferred plasma arc is maintained between the electrode and the work piece. Plasma gas is needed to form the plasma and to shield the electrode during the surfacing process. The transferred plasma arc transmits heat to the base material more efficiently than the non-transferred plasma arc does. Carrier gas is needed to transfer the powder consumable from the hopper through the plasma torch into the plasma arc, where the powder melts. Shielding gas is used to shield the molten pool against air atmosphere. Like in the conventional plasma welding process, also in the PTA welding method the plasma arc is constricted by the plasma nozzle. The shape of the plasma arc can be controlled by the plasma nozzle, which is available in different kinds of diameters.

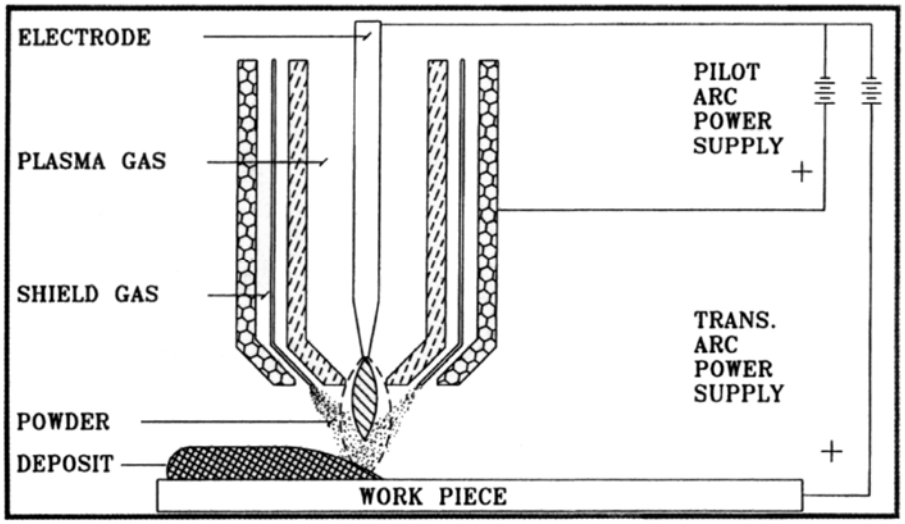


Figure 2 The plasma torch of the PTA welding unit (Raghu *et al.*, 1996)

The basic phenomenon of the plasma arc of the PTA welding method is as follows. Plasma current passes air between the electrode and the work piece, while the gas molecules accelerate and collide with each other. Binding forces between atoms and electrons collapse and electrons are released from the nucleus. The gas, consisting of neutral molecules, positively charged atoms, and negative electrons, is ionized and, thus, the gas is capable to conduct current (Craig, 1988).

The deposition rate of the mechanized PTA welding method with the powder consumable is up to 20 kg/h. The thickness of one bead layer is between 1 and 6 mm. The deposit thickness is usually as much as the tolerance of the wear part. The plasma arc is stable with low to high heat inputs. The plasma torch is designed to weld with a certain deposition rate, i.e., various welding torches have been developed to weld with different deposition rates. For the micro-plasma transferred arc welding method, MPTA, the deposition rate is below 1 kg/h and the bead thickness 0,1-0,5 mm, for instance (Saltzman *et al.*, 1992; Sun *et al.*, 1998).

The pilot and the plasma arcs are maintained with direct current (electrode negative), variable polarity, or alternatively pulsed current, which makes it easier to control heat input, penetration, and the shape of the molten pool (Craig, 1988; Deuis *et al.*, 1997; Fromowicz *et al.*, 1993). The mass flow configuration allows the gas volume to be controlled and allows variations in the gas flow to be made via computer controlled program (Shubert, 1992).

### 2.1.2 Plasma nozzle

Energy density and temperature of the plasma arc are much higher than those in the arc without the plasma nozzle (Elizagàrate *et al.*, 1981). Plasma arc temperatures in the different regions of the plasma arc depend on plasma gas. Argon, Ar, hydrogen, $H_2$, and helium, He, can be used as plasma gas and temperatures of the plasma arc are on

average 15000, 6000, and 20000 °C, respectively. The gas mixtures can be also used as a plasma gas.

In Figure 3 are presented differences between the gas tungsten arc, GTA, and the plasma transferred arc, PTA, arc temperatures, when Ar is used as plasma gas. The highest temperature is nearby the tip of the electrode. Diameter of the plasma nozzle was 4,75 mm. Arc currents were 200 A. Voltages of the GTA and the PTA arcs were 14,5 and 29 V, respectively (Elizagàrate *et al*., 1981).

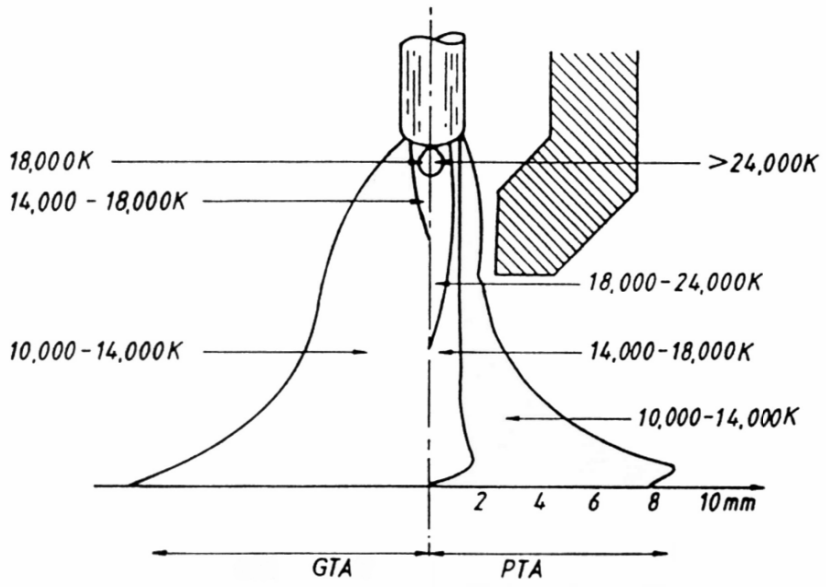


Figure 3 Differences between the GTA and the PTA arc temperatures when argon is plasma gas (Elizagàrate *et al*., 1981)

Temperatures of the top surface and 4 mm below the top surface of the weld pool were estimated to be about 2700 and 1700 ºC (Feng *et al*., 1999). Mean temperature of the weld pool determined by a calorimeter, was around 1650-1700 ºC, indicating that the mean temperature of the weld pool is equal to melting point temperature times 1,01-1,08 (Gladky *et al.*,1990).

Many kinds of powder plasma torches have been designed for the PTA welding method. In Figure 4 is presented a torch, which utilizes a separate external nozzle. Babi (1993) manufactured a torch which utilizes a separate stabilizer gas. This separate “cold gas” flow was introduced to the plasma arc between the electrode and the plasma nozzle. The benefits were reduced turbulence, reduced thermal load to the plasma nozzle, and decreased deposition of the powder particles on the plasma torch. In Figure 4 is presented plasma arc temperature vs. various external plasma arc nozzle diameters and plasma arc currents 100 and 220 A. Plasma gas was Ar. The temperature fields are set based on the experimental data. Temperature of the plasma arc depends mainly on plasma gas, plasma gas flow rate, plasma arc current, and plasma nozzle. The temperature range of the plasma arc column with low plasma stream speed, various plasma nozzle diameters, and plasma arc currents is broad (Dresvin, 1972; Gladky *et al*., 1990).

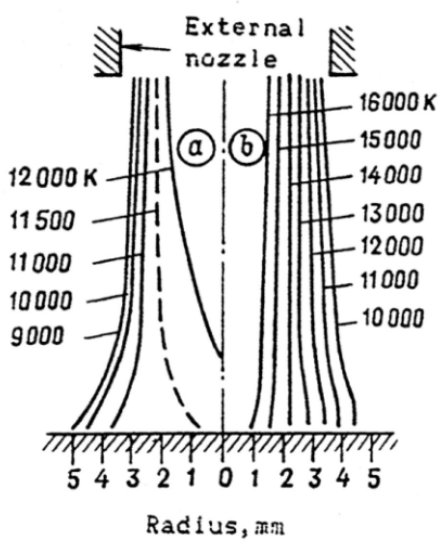


Figure 4 Plasma arc temperatures vs. various external plasma arc nozzle diameters: a) 100 A and b) 220 A plasma arc current (Dresvin, 1972; Gladky *et al.*, 1990)

In Figure 5 is presented radial distribution of plasma gas flow at 1 mm distance from the plasma nozzle. Plasma gas stream velocity has been estimated by a cylindrical probe, being moved across the arc column. Plasma gas stream velocity range in the plasma arc column is 60-200 m/s. Plasma gas stream velocity is higher with high plasma gas flow rate and small plasma nozzle radius. Higher plasma gas velocity increases more columnar and directional plasma flow from the plasma nozzle to the base material (Dresvin, 1972; Gladky *et al.*, 1990; Wilden *et al.*, 2006). Particle velocities of 20 and 7 m/s for powder particle sizes of 63 and 200 μm, respectively, were measured with a high speed camera (Siagam *et al.*, 2008). Plasma gas flow rate was 3,5 l/min.

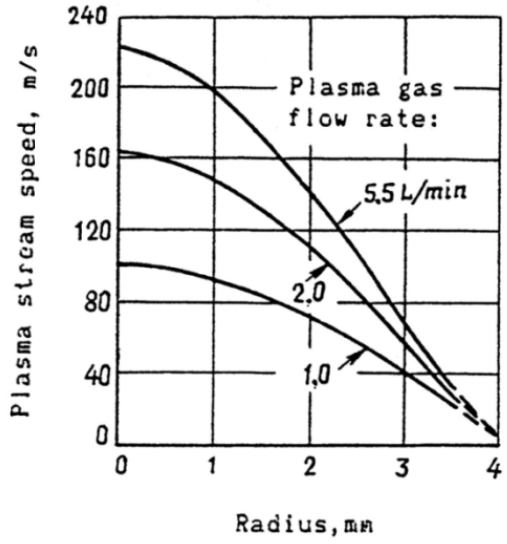


Figure 5 Radial distribution of plasma gas stream speed at 1 mm distance from the plasma nozzle (Dresvin, 1972; Gladky *et al.*, 1990)

In Figure 6 are presented the differences between the GTA and the PTA welding method. In the PTA welding method, the plasma arc is much narrower and more columnar. The electrode locates inside the plasma nozzle. The plasma arc is hotter, the energy density of the plasma arc and the production rate are larger than in the GTA welding method. Heat input concentrates to a small area, thus, producing a narrow weld with low heat input. The intensity of the plasma arc reduces on about ten times longer distance when compared to the GTA welding method. The diameter of the plasma nozzle has also an effect on the intensity of the plasma arc. The bigger plasma nozzle reduces the intensity of the plasma arc. The intensity of the plasma arc decreases on a relatively long distance, which helps to control the dilution, because a small alternation in working distance does not have a significant effect on the plasma arc density (Koivula *et al.*, 1992).

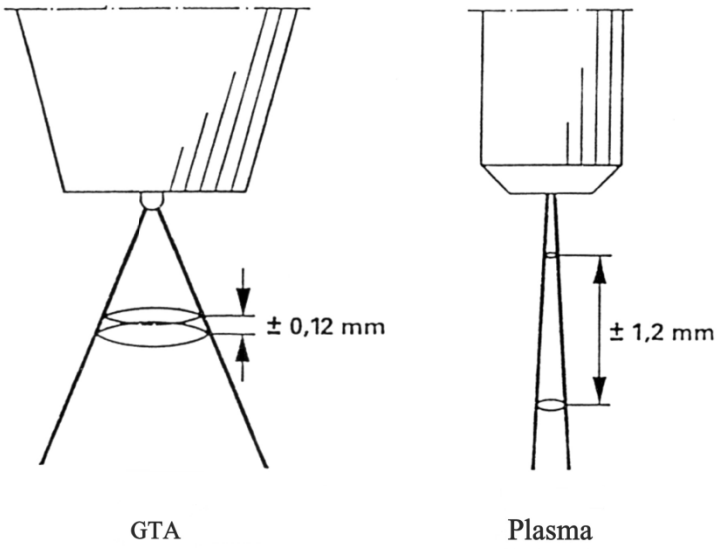


Figure 6 Effect of arc shape on intensity of the arc in the gas tungsten arc, GTA, and the plasma transferred arc, PTA, welding methods (Koivula *et al.*, 1992)

A change in plasma arc voltage may be achieved in two ways, i.e., by changing working distance or by resetting the electrode, while the other parameters are constant. An increase in working distance leads to an increase in plasma arc voltage. The electrode position has an effect on the dilution as well as working distance. By resetting the electrode position ±1 mm changes plasma arc voltage from 0,5 to 1 V. In Figure 7 the effect of working distance on plasma arc voltage is presented (Hunt, 1988; Pfeiffer *et al.*, 1984).

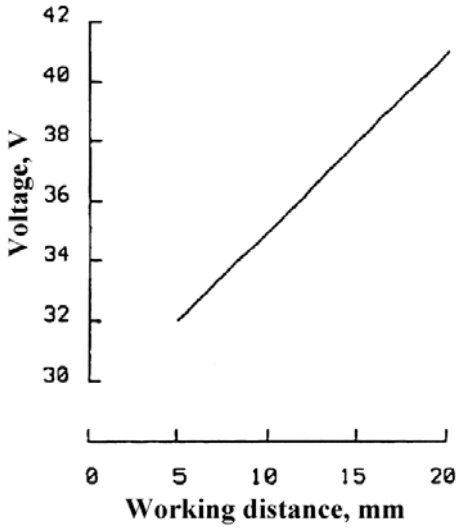


Figure 7 Effect of working distance on plasma arc voltage with plasma arc current 140 A (Pfeiffer *et al.*, 1984)

In the mechanized PTA welding method it is possible to install an automatic control system to control working distance between the plasma torch and the work piece. The control system measures plasma arc voltage and adjusts working distance in relation with plasma arc voltage. Plasma arc voltage changes linearly when working distance varies.

### 2.1.3 Process gas

Three gas lines are needed for the PTA welding process, i.e., plasma, carrier, and shielding gas line. The gas can be the same in all lines, it can be different gas in every line, and it can be changed during the welding process. The process gas affects the mechanical and the metallurgical processes in the molten pool through the loss of the alloying elements and increase of some components from both the process gas and the air atmosphere. Because carrier gas and the powder consumable are fed straight into the plasma arc, carrier gas mixtures partly with plasma gas and its properties, e.g., heat input, concentration, and ionization potential, can change (Craig, 1988; Shubert, 1992).

The process gas in the PTA welding method can be Ar, Ar-$H_2$, Ar-He, or He. The physical properties of the gas have effects on the shape of the plasma arc, the heat input, the shape of the deposit, and the deposit microstructure. The content of $O_2$ or $CO_2$ in shielding gas can lead to burn-out of, e.g., Si and Mn alloying elements (Menzel, 2003).

The properties of the process gas depend mainly on density, ionisation energy, and thermal conductivity. Densities and ionization energies of Ar, He, and $H_2$ gases are 1,78, 0,18, 0,08 kg/m$^3$ and 15,8, 24,6, and 13,6 eV, respectively (Menzel, 2003). Thermal conductivity of the process gas has an effect on temperature of the molten pool, molten pool degassing effect, welding speed, and weld shape. Therefore, thermal conductivity of the process gas is the main feature when high welding speed is needed.

Thermal conductivity of Ar is around 0,015 W/cm°C at 8000 °C. Thermal conductivity of $H_2$ is multiple at 4000 °C temperature when compared to thermal conductivity of Ar. Thermal conductivity of He is higher when compared to thermal conductivity of Ar (Menzel, 2003).

Ar is the most common process gas in the PTA welding method. It is inert and it does not oxidize or react with the weld pool. The properties of Ar as a process gas are good shielding effect due to high gas density, relatively stable narrow plasma arc, good electrical conductivity, low ionization potential, high surface tension of the weld pool, and low burning of alloying elements. While Ar is used as plasma gas it ionizes easily, which determines the ease of the plasma arc ignition and its stability. It has low thermal conductivity and, thus, the plasma arc is narrow and concentrated (Craig, 1988; Yamamoto *et al*., 1997).

Ar-$H_2$ gas mixture has excellent deoxidizing and focusing effects (Lugscheider *et al.*, 1992). Thus, Ar is mainly used as plasma and Ar-$H_2$ gas mixture (5-10 % $H_2$) can be used as shielding gas. Ar-$H_2$ compound can be used also as powder carrier gas. Low amount of $H_2$ in the plasma arc increases thermal intensity, heat input, penetration, and welding speed. Approximately at 3870 °C temperature $H_2$ molecules dissociate, and energy is released when the molecules recombine or contact with the work piece (Craig, 1988). $H_2$ reduces pores, surface tension of the weld pool, and bead surface oxidation. It increases fluidity and wetting of the melted powder, which is useful when the smooth deposit surface is needed (Harris *et al*., 1983; Hunt, 1988; Oechsle *et al.*, 2000).

H can be transported to the deposit with a contaminated powder, for instance. Dissolution of H into the iron melt is low, about 0,00075 % per 100 g of iron at melt temperature at 1 atm. Dissolution of H into iron melt depends on temperature. Solubility decreases at the solidification temperature of iron melt. When the temperature of the molten pool further decreases the solubility of H into the iron melt still decreases. At 1371 ºC temperature the solubility of H increases temporarily. Below this temperature the problems caused by H arise. Diffusivity of H decreases with decreasing temperature. At RT iron is capable to retain only a small part of H soluble at high temperatures. Dislocation interactions can enhance the transportation of H by several orders of magnitude. H diffuses and forms molecular $H_2$ and escapes as a gas. Under rapid cooling H is retained in the austenite and at low temperatures austenite transforms to martensite or bainite. Lattice imperfections may trap H. Inclusions and pores may trap $H_2$. High internal stresses can develop and cracks may initiate at the discontinuities (Stout, 1987).

He has high thermal conductivity and high ionization potential, which offers increased welding speed, penetration, and improved weld quality when compared to Ar gas (Bols *et al*., 1997). Gas densities of He and $H_2$ are lower than air, which causes problems to the shielding efficiency. He content in the process gas can be between 30 and 100 %, thus, flow rates have to be increased to maintain the shielding efficiency. Regular flow rates for He mixtures of 30, 50, 75, and 100 % are 18, 28, 35, and 40 l/min, respectively (Menzel, 2003; Oechsle *et al*., 2000).

Welding tests welded with various gases without preheating gave results as follows. Welding tests with Ar-He-$CO_2$ as a shielding gas resulted in a good bead appearance only for NiCrBSi 80 12 alloy, while Ar, Ar-$H_2$, and Ar-He gas mixtures gave good bead appearances for CoCrWC 64 29 5, NiBSi + 60 % WC, NiCrBSiAl 90 4 1, NiCrBSi 80 12, X 120 WCrMoV 6 5 4 4, and X 3 CrNiMo 18 13 3 alloys. The best weld beads were obtained with Ar and Ar-$H_2$ gas mixture. The deposits welded with Ar had the highest hardnesses. Pores were typically found, when Ar-He gas mixture was used (Oechsle *et al*., 2000).

### 2.1.4 Dilution control

Optical spectroscopy is one of the auxiliary methods for controlling and adjusting the dilution of the weld bead. Spectroscopic analysis is typically used to analyze materials. The significant wave length, 500-1000 nm, has to be set before the welding process and after that the chemical composition of the molten pool is possible to control with the spectrometer. In Figures 8a, b is presented the local maximum and minimum wave length measurements made by the spectrometer in relation with the dilution of the deposit alloys Stellite 12 and Alloy 60. The location of the plasma arc was on the molten pool. The dilution control was more accurate with the bigger dilution ratios (Dilthey *et al*., 1996a; Pavlenko, 1996).

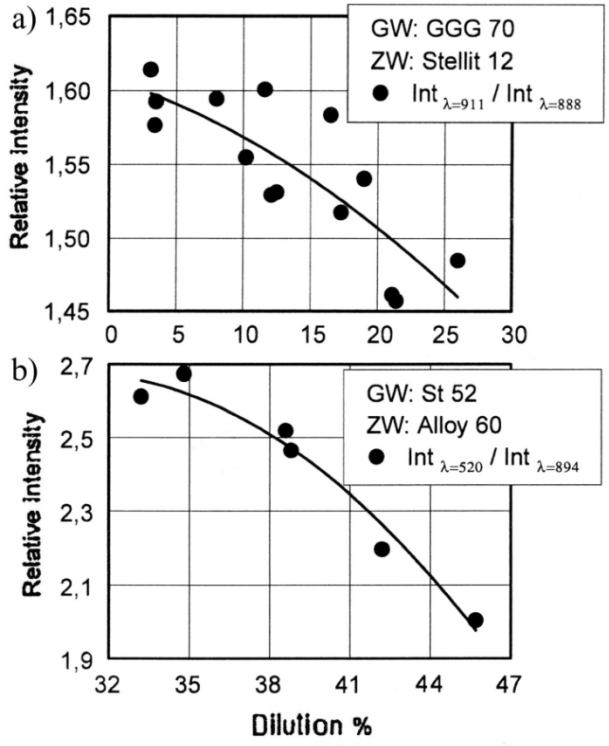


Figure 8 Relative intensities measured by an optical spectrometer as a function of dilution of the deposits deposited onto the base materials GGG 70 and St 52: a) Stellite 12 and b) Alloy 60 (Pavlenko, 1996)

## 2.2 Welding parameters

The effect of an individual welding parameter on the PTA welding method has to be known for optimizing welding parameters and to learn interactions between different welding parameters. In the mass production to obtain equal quality onto the deposited components, the surfacing process has to be consistent enough (Herrström *et al.*, 1993).

The main advantages of the PTA welding method are heat input and cooling rate, which are in the range suitable for depositing a component with a broad range of alloys as well as for surface alloying or surface hardening. Usually brittleness, cracking, and gas porosity can be avoided.

### 2.2.1 Pre-set and adjustable welding parameters

A number of process and material factors affect the dilution of the deposit. 37 variables for the PTA welding method are identified, which have effects on the welding process. 18 variables were identified as pre-set variables and 19 variables as variables, which need to be adjusted. The settings preferred by welding operator and welding engineer may also vary which makes it difficult to find optimized welding parameters (Kapus, 1980).

The main parameters have the biggest effect on the PTA welding method output quality. The selection of the test conditions is vast. Often a large set of welding tests are needed. Stable process conditions during the surfacing process cannot be ensured (Nefedov *et al.*, 1994). Even though straight passes without oscillation can be welded, the PTA welding method is usually maintained by oscillating the plasma torch. The most important factors are (Herrström *et al.*, 1993; Hunt, 1988; Kapus, 1980; Sexton *et al.*, 1994):

- plasma arc current
- current upslope
- plasma gas flow rate
- composition of plasma, carrier, and shielding gas
- powder consumable feed rate
- moisture content of powder and gas pipes
- chemical composition of powder consumable
- overlapping
- preheating temperature
- interpass temperature
- working distance
- arc voltage
- arc polarity
- electrode diameter
- electrode type
- electrode setback
- substrate shape and size

- substrate and consumable materials
- oscillation mode
- oscillation amplitude
- oscillation frequency
- dwell time
- welding speed
- shielding gas flow rate
- transport gas flow rate
- deposit thickness
- cooling water flow rate
- torch angle in relation with base material
- melting temperatures of powder and substrate.

### 2.2.2 Oscillation

The thickness of the deposit is typically between 1 and 6 mm. The wider pass can be obtained by oscillating the plasma torch, Figures 9a-d. The width of a bead is typically from 5 to 50 mm. Pilot arc and plasma arc currents adjustment helps to control the dilution in the reverse points of the oscillation waves (Dilthey *et al.*, 1994). The most common oscillation modes, i.e., zigzag and rectangular wave oscillation modes are presented in Figures 9b, d. Sine wave is almost equal to the zigzag wave mode and many mechanical torch transport units utilize it. In the mechanized or the robotized welding unit the adjustable oscillation parameters are longitudinal welding speed, dwell time, transversal welding speed, and oscillation width amplitude, when rectangular oscillation mode is used. The adjustable oscillation parameters are welding speed, oscillation width amplitude, and frequency, when zigzag or sine wave oscillation mode is used.

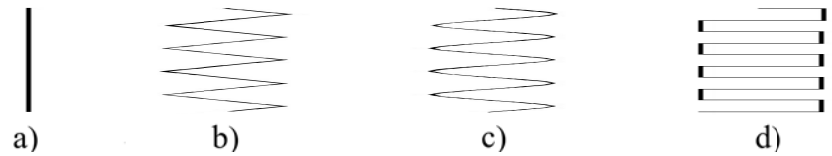


Figure 9 The most common oscillation wave modes used in the PTA welding method: a) straight pass without oscillation, b) triangular or zigzag wave, c) sine wave, and d) rectangular wave mode (Blunt, 2000; Hunt, 1988; Sharples, 1985)

The oscillation wave mode can be modified to face the properties of the deposit and the component. For instance, reverse points may have different kinds of dwell times. Thus, heat input and penetration can be controlled more efficient way, especially, when welding a bead to the surface edge of the component (Rasche, 1973).

When comparing the wear resistance between the surfacing methods, it has to be noticed that the surfacing parameters, e.g., the straight pass or the oscillation mode are

taken into account. In the small components, like the valve heads, the oscillation movement of the plasma torch can cause too high heat input to the component surface and, thus, the valve head can be overheated and distorted (Klimpel *et al.*, 2005).

Magnetic arc oscillation unit can be also used for weld surfacing instead of mechanized oscillation unit. Oscillation and oscillation mode are therefore adjusted by one or two electromagnets, which are located parallel to the welding direction. The time to sweep the plasma arc, the dwell time, and the magnitude of the peak magnetic field can be controlled independently. The quality of the deposit is not as good, when compared to the deposits welded by a mechanized oscillation unit. The defects were found from the bead edges, which were irregularly shaped. Also spattering, arc instability, powder loss, and nozzle damage were seen during the surfacing process. By adjusting the dwell and the sweep time the penetration can be controlled in the edges of the oscillation wave. The consumable efficiency was low, because of excessive deflection of droplets ejecting from the plasma arc. The interaction between the plasma arc and the magnetic field causes a transverse deflection of the arc, because of the Lorentz force, which can be controlled by the field strength and polarity. The deposit width from 8 to 15 mm and the dilution of the deposit between 4 and 16 % can be obtained (Blunt, 2000).

In Figure 10 weld pool shape vs. plasma torch welding speed with oscillating width 15 mm and frequency 50 Hz is presented. The powder particles, which were not melted in the arc, melt in the molten pool. Therefore, the temperature of the molten pool decreases. The result is the decreasing effect on the size, mass, and temperature of the molten pool. The unmelted powder particles melt in the molten pool in $10^{-4}$-$10^{-2}$ s. Welding speed and oscillation parameters also affect the size, mass, and temperature of the molten pool as well as arc location in relation with the edge of the molten pool (Gladky *et al*., 1990).

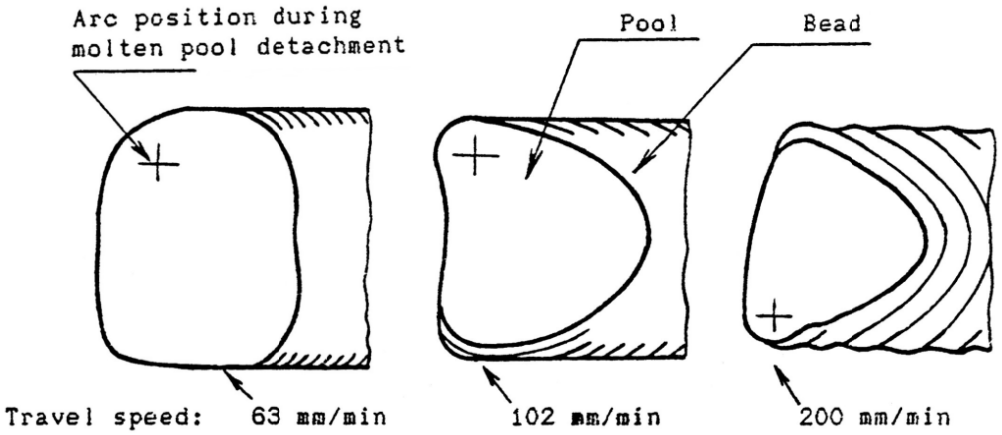


Figure 10 Shape of the weld pool vs. plasma torch welding speed with oscillating width 15 mm and frequency 50 Hz (Gladky *et al*., 1990)

Wider surfaces can be surfaced by overlapping single weld beads. Width of the weld bead and displacement of the plasma arc ratio, $w_b/l_d$, is 1,1-1,2. The difference between heights and valleys on the deposit surface is usually 20 %. When the $w_b/l_d$ ratio

increases, e.g., above $w_b/l_d \geq 2$ the deposit may become more even (Nefedov *et al*., 1994).

## 2.3 Consumables

Term weldability is defined by the American Welding Society as “the capacity of a metal to be welded under the fabrication conditions imposed, into a specific, suitably designed structure, and to perform satisfactorily in the intended service”. The definition of this term is a complex process. The evaluation of the whole successful process from the beginning of the first plan to the use of an application in its real environment is challenging. Term weldability is mainly used to describe and to compare how weldable the consumable is.

Fe-, Co-, and Ni-based alloys are mainly used as powder consumables. All metals can be produced in the powder form. Gas or water atomization powder production methods are the dominant and perhaps the most versatile methods that produce metal powders at high production rates. Various powder production methods allow precise control of the chemical composition and the physical characteristics of the powders. Variation of the chemical composition of the powder and the powder fraction have effects on the properties of the deposit, the viscosity of the molten pool, the consumable efficiency, and the size of the molten pool, even though the chemical composition is in the approved range (Dilthey *et al*., 1996b; Dunkley, 1998; German, 2005).

### 2.3.1 Gas atomized powder

Water, nitrogen, and argon gas are used in the metal powder atomization processes. The nitrogen and argon atomized powders are usually spherical. Nitrogen atomization can lead to a poor powder shape and to a high retained gas content, which may lead to irregular and porous weld deposits (Dunkley, 1998; German, 2005; Hunt, 1988).

The water atomized as well as crushed carbide powders tend to be irregular in shape, while the gas atomized powder is spherically shaped. In Figure 11 is presented the effect of the powder manufacturing method on powder feed rate. The deposit can be thicker or thinner depending on the powder used, if welding parameters are not changed. Therefore, the dilution can also change. Powder feed rate and plasma arc current can be varied so that the thickness and the dilution of the weld bead remain constant during the PTA welding method (Dören *et al*., 1985; German, 2005).

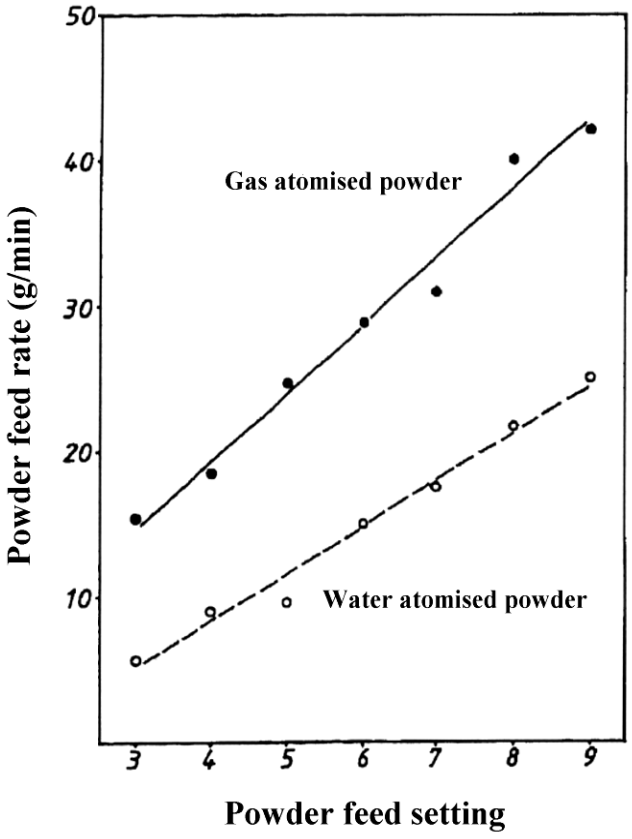


Figure 11 Powder feeding characteristics of the water and the gas atomized powders (Dören *et al*., 1985)

The powder consumables are mainly manufactured by the gas atomization method, Figure 12. The shape of the powder particles can be controlled and usually spherically shaped powder particles are preferred. The range of the powder size is from 10 to 1000 µm. In the PTA welding method the range of the powder consumables used is typically from 50 to 150 µm. Internal porosity exists always regardless of the manufacturing process, and with the bigger fractions the porosity increases (Dunkley, 1998; German, 2005; L'Estrade *et al*., 1988).

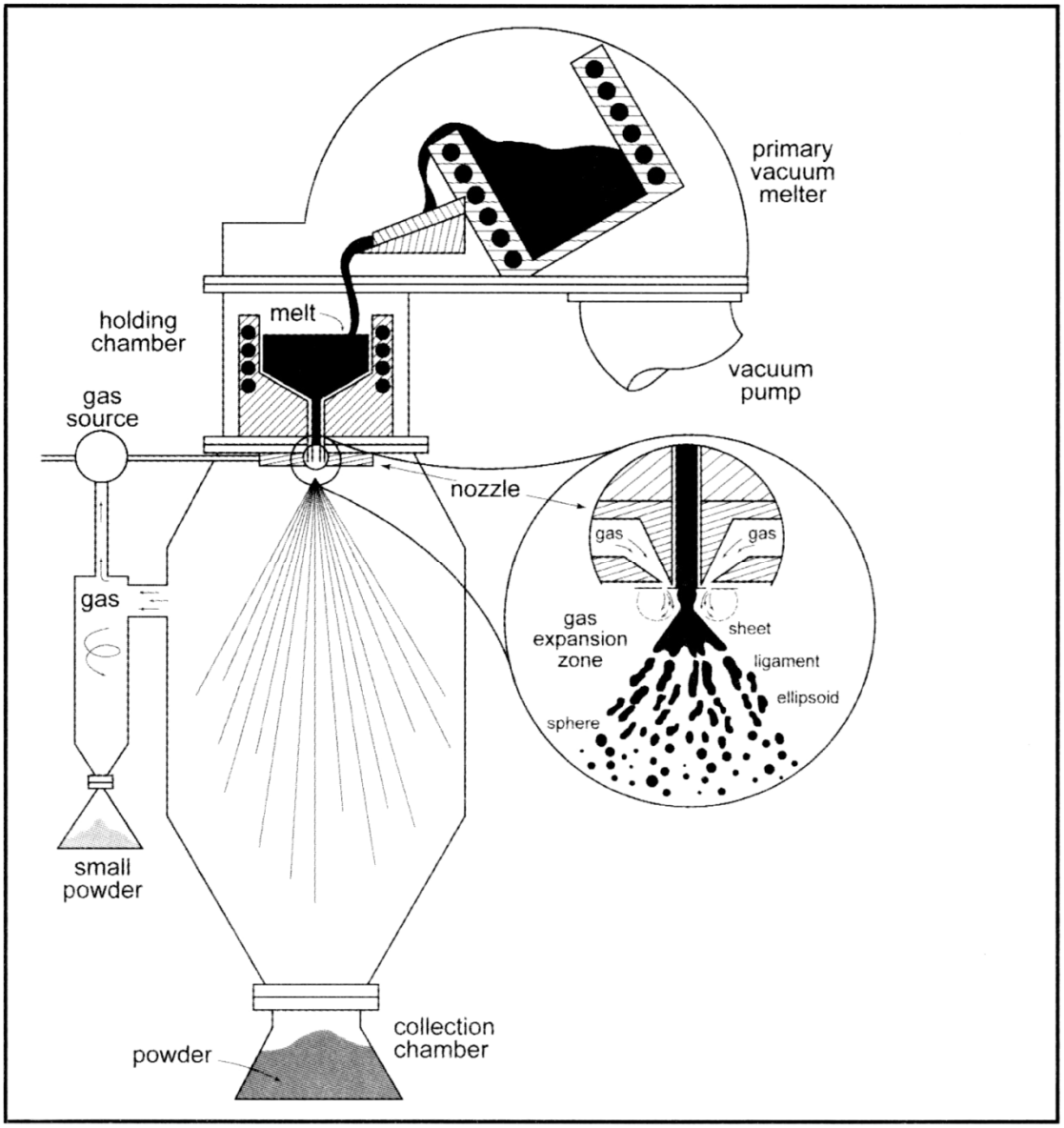


Figure 12 Gas atomized powder production method (German, 2005)

### 2.3.2 Micropellets

The wear resistance can be enhanced by adding ceramic carbides to the matrix alloy. The deposit is then so called metal matrix composite, MMC. MMCs have a combination of mechanical and physical properties, the properties of which can be tailored by selecting a metal matrix alloy and a reinforcing phase or carbide. MMCs have high stiffness, strength, and hardness. The wear and the corrosion resistance can be tailored according to the application. The optimal microstructure of the deposit depends on the application.

Weldability of the powder alloy determines partly the properties of the deposit. The size of ceramic carbides is typically around 100 µm. High volume fraction or large-sized

ceramic carbides decrease the weldability of the alloy. The maximum amount of carbides in the MMC is about 60 vol.-% (Tsubouchi *et al*., 1997). In the wear resistant MMC deposits, large-sized original carbides of the powder consumable have to remain at least partly unmelted during the surfacing procedure. The original carbides can be introduced straight into the weld pool with the external powder feed nozzle, if necessary (Röthig *et al.*, 1997). The melting of the original carbides in the plasma arc is, thus, prevented or minimized (Hunt, 1988; Herrström *et al*., 1993; Kammer *et al*., 1991).

The hard wear resistant carbides are commonly manufactured by crushing and, therefore, the shape of the carbides is irregular. The mixed powders, which are based on the metal powder manufactured by the gas atomization and the crushed carbides, have proneness to separate in the powder consumable hopper and the feeding cable due to differences between the density, the size, and the morphology of the particles. Surfacing layers tend also to exhibit segregation at the time of melting. The particles with a higher density tend to settle to the lower regions of the deposit and the particles with a lower density tend to settle to the upper regions of the deposit (Lugscheider *et al*., 1990; Lugscheider *et al.*, 1995).

The micropelletizing produces agglomerates of spherical form, irrespective of the initial particle form, size, morphology, or density, which is the main reason to use them. Any kinds of mixtures can be adjusted. The density of the agglomerated powder is possible to enhance by sintering. The density of the powder has also an effect on the powder feeding properties (Lugscheider *et al*., 1990; Lugscheider *et al*., 1994).

By micropelletizing, it is possible to manufacture the micropellets from the sub-micrometer-sized particles. As micropellets, the fine particles are agglomerated and, thus, carried together in the powder feeding system. The dust-like fine particles may interfere the feeding of the powder, but when the fine particles are adhered to the larger particles the problems do not appear in the powder feeding system. This increases the ability of flow of the composite powders as compared with the mechanically homogenized ones (Lugscheider *et al*., 1990; Lugscheider *et al*., 1992).

In Figures 13a-d the morphology of differently produced powders are presented. In Figure 14 the basic metal matrix alloys and the reinforcing carbides, which can be included into the micropellets, are schematically presented. The morphology of the micropellets is markedly enhanced when comparing to the morphology of the tailor-mixed powders (Lugscheider *et al*., 1990; Lugscheider *et al*., 1994).

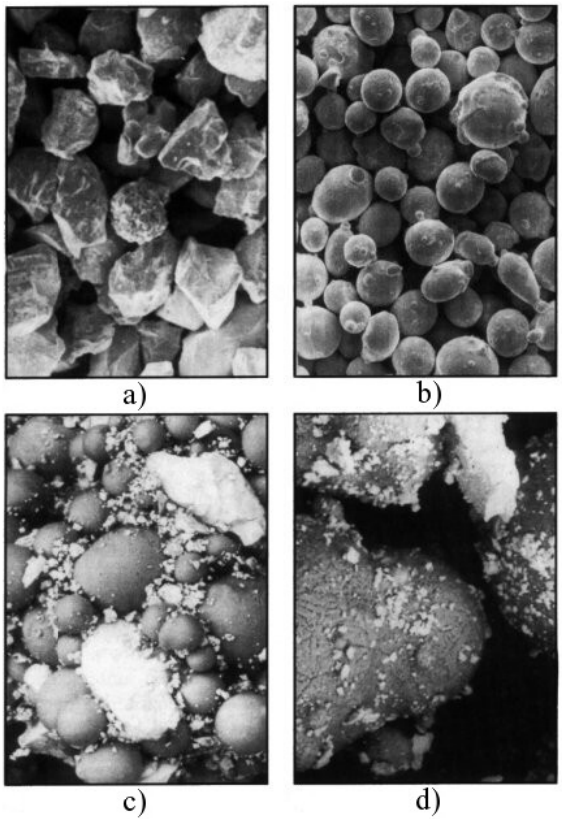


Figure 13 Morphology of differently produced powders (Ait-Mekideche, 1989; Lugscheider *et al.*, 1990):

a) Fused tungsten carbide, crushed powder (magnification 400:1)
b) Cobalt-chromium-tungsten-carbon alloy, gas-atomized powder (magnification 400:1)
c) Composite powder of cobalt-chromium-tungsten-carbon + fused tungsten carbide, agglomerated, grain size of fused tungsten carbide is 5 µm and cobalt-chromium-tungsten-carbon alloy less than 15 µm (magnification 1000:1)
d) Composite powder of cobalt-chromium-tungsten-carbon + fused tungsten carbide, agglomerated and sintered, grain size of fused tungsten carbide is 5 µm and cobalt-chromium-tungsten-carbon alloy less than 45 µm (magnification 1000:1)

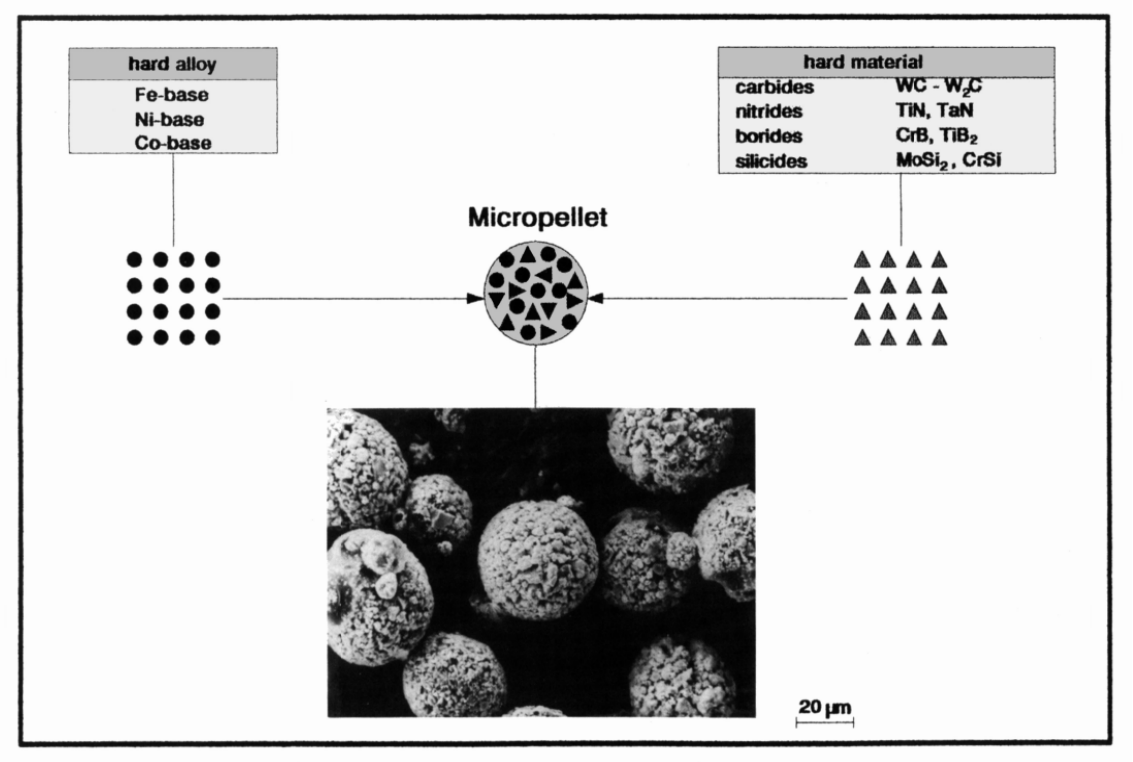


Figure 14 Metal matrix powder, reinforcing particles, and the micropellets (Lugscheider *et al*., 1992)

In Figure 15 is presented a spray dryer, which is used to manufacture the micropellets. The initial components are stirred to form a suspension together with an organic binder (polyvinyl alcohol) and water. The suspension is sprayed through the atomizer into the hot air, where the droplets dry in free atmosphere. The size of the micropellets is dependent on the selected parameters. To increase the strength of adhesion between the initial components, the micropellets can be sintered after agglomeration. When sintered in a reducing atmosphere ($H_2$) at 1050 to 1150 °C with a dwell time of 60 min the agglomerated and sintered micropellets loose their binder content, because the organic binder evaporates. The welding behavior of the micropellets is improved as a result of sintering. Also heating during free-fall evaporates the volatile agent (German, 2005; Lugscheider *et al*., 1990; Lugscheider *et al*., 1994).

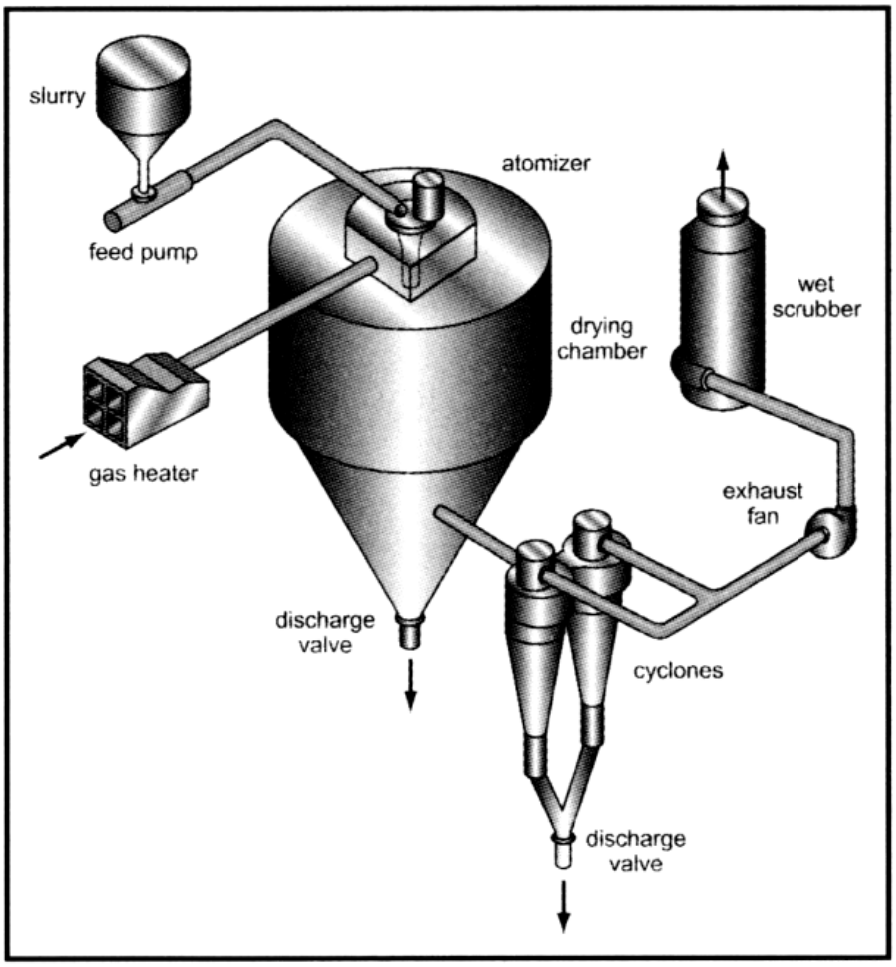


Figure 15 Spray dryer for manufacturing the micropellets (German, 2005)

### 2.3.3 Rods and wires

Rod, external powder feeding torch for carbides, hot wire, or cold wire can be used at the same time with the powder consumable, e.g., for increasing the deposition rate. Coarse carbides can be encased into the steel wire tubes, but optimized mixtures of metals and carbides are seldom achieved for rod and wire welders. Twin hot wire operation increases efficiently the deposition rate, while cold wire may cool the molten pool and limit the deposition rate (Sexton *et al.*, 1994). Temperature of the hot wire can be increased close to the melting point by electrical resistance heating and additional arc heating, which is introduced to the wire.

The bead thickness and the deposition rate for the plasma arc hot wire surfacing are from 4 to 10 mm and from 18 to 31 kg/h, respectively (Meyer, 1976). Deposition rate up to 23 and 33 kg/h with one 3 and 4 mm diameter hot wire can be welded, respectively. The dilution was between 5 and 50 %. The length of the weld pool in the surfacing direction was less than 6 mm. Surfacing speed was approximately 0,8 $m^2$/h. The optimized welding parameters were plasma arc current 300-315 A, arc current

heating the wire 280-300 A, current passing through the wire 180-200 A, voltage 26-28 V, welding speed 8 m/h, frequency 60 Hz, amplitude 50 mm, wire diameter 3 mm, shielding gas Ar + 8-10 % $H_2$ with flow rate 5-6 l/min, and plasma gas Ar with flow rate 2-3 l/min (Steklov *et al*., 1989).

### 2.3.4 Consumable efficiency

Before the surfacing process the powder consumable is usually dried at 120 ºC for several hours or over the night to eliminate the moisture from the powder particles. The powder feeding nozzle is needed for feeding the powder consumable with carrier gas to the plasma arc. The powder range is normally 50-150 µm. The powder particles, the diameters of which are lower than 50 µm, tend to blow away due to high pressure of the plasma arc column. Instability in the plasma arc column and the molten pool can be obtained, when the powder diameter is above 150 µm.

In the PTA welding method the evaporation of the powder particles is not usually obtained (Xibao, 2003). The loss of the powder is due to spattering and the loss of unmelted powder particles. The best reported consumable efficiency in the PTA welding method is between 95-99 % (Dilthey *et al*., 1996b). The powder alloy was Alloy 60 (X40CrSiMo 10 2). Anderson *et al*. (2003) reported the consumable efficiency of +95 %. Oberländer *et al*. (1992) reported the consumable efficiency of 80-90 %.

In Figure 16 the best consumable efficiency is 97 % and the lowest 68 %. Decreasing arc intensity lowers the melting efficiency of the plasma arc. An increase of the grain diameter causes a decrease in the consumable efficiency, if plasma arc current is not changed. Higher plasma arc current causes an increase in the consumable efficiency, because the increased enthalpy of the plasma arc is then sufficient to melt a given volume of the powder consumable. The finer fractions are too dust-like and evaporation of the finer particles in the plasma arc may occur. The reason for lower consumable efficiency with high plasma arc currents presented in Figure 16 is not clear (Babiak *et al*., 1986; Xibao *et al*., 1998).

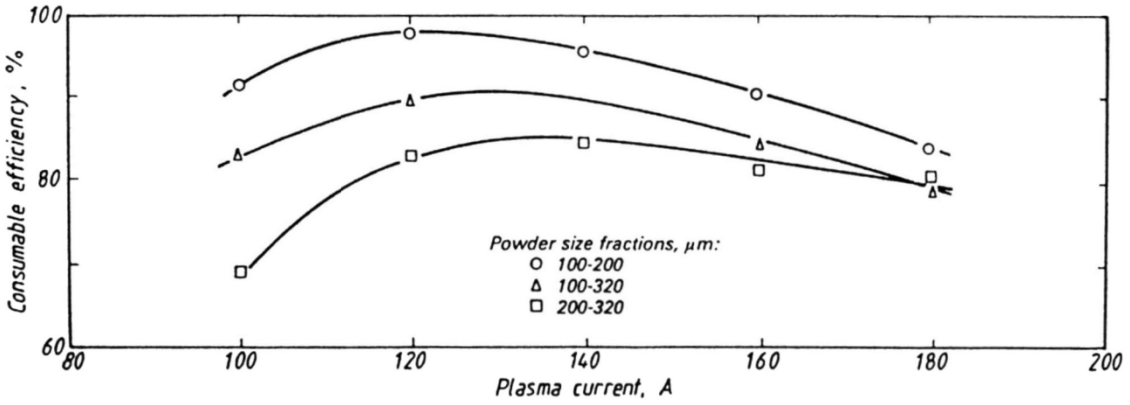


Figure 16 Effect of plasma arc current and powder fraction (NiCrBSiFeC) on consumable efficiency (Babiak *et al*., 1983; Babiak *et al*., 1986)

The consumable efficiency can vary depending on how the powder is fed to the plasma arc. According to Dilthey *et al*. (1998) the consumable efficiency is not optimized, when external coaxial annular powder feed nozzle is utilized. This nozzle allows melting of the powder particles up to 200 μm. Also arc deflections can occur especially if the powder is fed to the arc from several channels instead of an annular nozzle. Internal powder feed system, where the powder is fed with a carrier gas through the hollow electrode straight to the plasma arc, provides longer dwell time for a powder particle. Thus, larger particles up to 300 μm can be melted. It is also possible to feed the powder straight to the molten pool, which is more common in the laser welding method, LB (Klimpel *et al.*, 2005). A simple and useful system is to use gravitational force to assist the powder feed. Anyway, the powder traveling time in the plasma arc is very short, at least, when compared to the time in the molten pool.

With an increase in the consumable feed rate, more plasma arc heat is required to melt the consumable and less heat remains to melt the base material and, thus, the dilution decreases. At the same time the thickness of the deposit increases, if the other parameters are not changed. Larger deposition rate basically requires an increase in plasma arc current. However, it is obvious that finally, when the thickness of the bead increases the plasma arc is no more able to form penetration. The plasma arc location is then on the molten pool (DuPont, 1998; Marantz, 1980).

## 2.4 Modeling

The effect of the plasma arc on the PTA welding method can be modeled. The arc and the melting efficiencies and their effects on heat input as well as physical properties of materials and welding parameters have to be known to get exact estimation about the PTA welding method. The oscillation of the plasma torch is not included to the equations, thus, these equations describe more the conventional PA welding method. However, the physical properties and welding variables, which have an effect on the arc and the melting efficiencies, are determined.

### 2.4.1 Arc and melting efficiency

Term thermal efficiency, $\eta_t$, considers both the arc efficiency, $\eta_a$, and the melting efficiency, $\eta_m$. The arc efficiency describes a fraction of total heat load which has been transferred from the plasma arc to the component to be welded. A fraction of energy which has been used to melt the powder and the base material is considered as melting efficiency. The weld material has no effect on the arc efficiency. The melting efficiency depends strongly on the process parameters (DuPont *et al.*, 1996).

The plasma arc efficiency in the PA welding method is lower and more variable than the arc efficiency in the GTA welding method, because of the plasma nozzle. However, the penetration of the weld bead at the same heat input is higher in the deposits welded by the PA welding method when compared to the deposits welded by the GTA welding method. Increasing welding speed to a certain rate and pulsating plasma arc current effectively increase the plasma arc efficiency. The effect of the pulsed plasma arc on the

arc efficiency is not as stable in the PA welding method as in the GTA welding method. Decreasing pulsed current duty cycle decreases the arc efficiency in the welding process, while decreasing pulsed current duty cycle increases the melting efficiency. One benefit of the pulsed current is high melting efficiency at low welding speeds. The main difference between the GTA and the PA welding methods, i.e., the plasma nozzle, has an effect on both the arc and the melting efficiency. Thus, the plasma nozzle diameter depends on, e.g., powder feed rate, following the inability to get an exact comparison between the methods and the surfacing situations. The plasma nozzle is also water-cooled, and the removed heat energy is not known. As a conclusion melting efficiencies of the PA and the GTA welding methods are close to equal. The melting efficiency was slightly better for the PA welding method (Fuerschbach *et al*., 1991). However, DuPont *et al*. (1996) measured that both calculated and measured melting efficiencies were lower in the PA welding method when compared to the other conventional welding methods.

The difference between measured and predicted results was observed to be within ± 10 % (Giedt *et al.*, 1989). The plasma arc efficiency is assumed to be 0,47±0,03 (DuPont *et al*., 1996), 0,50-0,75 (Fuerschbach *et al*., 1991), and 0,55-0,80 (Gladky *et al.*,1990). The measurements conducted by Seebeck Envelope arc welding calorimeter disclose that the arc efficiency of the plasma arc decreases slowly from 0,50 to 0,44 with increasing plasma arc current from 200 to 400 A (DuPont *et al*., 1996). Seebeck Envelope arc welding calorimeter has been disclosed by Giedt *et al.* (1989). The combination of the thermopile and gradient layer forms a heat-rate meter based on the Seebeck thermoelectric effect, thus, the calorimeter is called as Seebeck Envelope Calorimeter. The arc efficiency measurements are usually based on measurements made with calorimeters. The reproducibility of the measurements is excellent, the errors being about $\pm$2 % (Dilthey *et al.*, 1993; Giedt *et al.*, 1989; Kou *et al.*, 1986). Equation 3 estimates the arc efficiency, $\eta_a$, and it is based on heat conduction and average constant thermal properties, even though fluid flow and convection heat transfer can be very important affecting the weld penetration (Giedt *et al*., 1989):

$$\eta_a = [(T_r - T_{amb}) \frac{2\pi\varphi r}{U I}] \, exp^{[(\frac{\nu}{2\alpha})(y+r)]}, \quad (3)$$

where $T_r$ is temperature at radius r from the point source, $T_{amb}$ is ambient temperature, $\varphi$ is thermal conductivity, r is radial distance from the point source, U is arc voltage, I is arc current, $\nu$ is welding speed, $\alpha$ is thermal diffusivity, and y is coordinate parallel to the welding direction.

A dimensionless parameter, $P_p$, which correlates with the melting efficiency, $\eta_m$, is presented in equation 4 (Fuerschbach *et al*., 1991):

$$P_p = q_{net} \frac{\nu}{E_m \nu_{kin,mp} \alpha_{300\,K}}, \quad (4)$$

where $q_{net}$ is net power, $E_m$ is melting enthalpy, $\nu_{kin,\,mp}$ is kinematic viscosity at melting point, and $\alpha_{300\,K}$ is thermal diffusivity at 300 K.

The melting efficiency depends about two- or three-dimensional heat flow and base material thermal diffusivity. Higher thermal diffusivity as well as thicker work piece cause low melting efficiency, because heat is transported more rapidly away from the welding area. The melting efficiency depends on oscillation width, i.e., wider pass increases the melting efficiency (Rykalin, 1957). It is generally supposed that no spattering occurs. Equations 5 and 6, which are based on experimental data, disclose melting efficiencies for the welds having 2D or 3D dimensional heat flows (Fuerschbach *et al.*, 1991):

$$\eta_{m,2D} = 0{,}407\, e^{\frac{-29{,}6}{Pp}}, \quad (5)$$

$$\eta_{m,3D} = 0{,}346\, e^{\frac{-0{,}90}{Pp}}. \quad (6)$$

The melting efficiency, $\eta_m$, can be also estimated by equation 7 which includes experimentally determined constants A and B (DuPont *et al.*, 1996; Fuerschbach *et al.*, 1991):

$$\eta_m = \mathrm{A}\, exp^{\left(\frac{-B}{\eta_a \mathrm{U\,I\,v\,/\,E_m}\ \nu_{kin,mp}\ \alpha_{300\,K}}\right)}, \quad (7)$$

where A is maximum melting efficiency, e.g. 0,5 and B is slope on a plot of $\ln(\eta_m)$ against $(\eta_a \mathrm{U\,I\,v\,/\,E_m}\ \nu_{\mathrm{kin,mp}}\ \alpha_{300\,\mathrm{K}})^{-1}$, e.g. 175.

### 2.4.2 Heat input

The temperature of the molten pool depends mainly on the physical properties of the material. The main thermal parameters are thermal conductivity, $\varphi$, [J/mmsK], specific heat capacity, cρ, [J/gK], density, ρ, [g/mm$^3$], and thermal diffusivity, α, [mm$^2$/s]. These parameters depend on the temperature. Thus, the constants are average values of the parameters which vary in a wide temperature range (Radaj, 1992).

The transferred plasma arc, i.e., the heat source can be assumed to be a spot or a circular heat source. Thermo-physical properties of the base material are constant and correspond to the mean process temperature. Heat transfer to the air is not considered. Heat conduction from the surface of the deposited area is poor resulting in hot surface in relation with interior parts of the base material if preheating is not used.

General presentation of Gaussian distribution of radial specific heat input to the surface of the base material is presented in equation 8. It is presumably designed for the open arc, but can be used to explain the phenomena of the plasma arc. Arc intensity, i.e., plasma nozzle, plasma gas, plasma gas flow rate, and plasma arc current, have an effect on the coefficient of arc concentration. Gaussian distribution of the specific heat input to the base material is (Pavelic *et al.*, 1969; Rykalin, 1957):

$$\mathrm{q(r)} = \mathrm{q(0)}\, exp^{-c\, r^2}, \quad (8)$$

where q(r) is specific heat input at a radial distance of r from arc axis, q(0) is maximum heat input along arc central axis, and C is coefficient of arc concentration.

If a uniform power density is distributed into a circle, its diameter on the base material is $d_c = \frac{2}{\sqrt{C}}$. The energy input into this area is presented in equation 9 (Goldak *et al*., 1984). More concentrated arc has smaller circle diameter, $d_c$, and larger value of C. Energy input is then (Goldak *et al*., 1984; Kou, 1987):

$$q(0) = \eta_a \, U \, I. \quad (9)$$

Effective thermal power of the arc, which is needed for melting the powder consumable and a thin layer from the surface of the base material, is presented in equation 10. The estimated and the measured data were in good agreement. The actual temperature of the work piece was slightly higher at the start and lower at the end when compared to the estimated work piece temperatures. Effective thermal power of the arc is (Nefedov *et al*., 1995):

$$q_{eff} = \nu \, ( l_d \, h_b \, E_s + 1{,}07 \, c\rho \, w_b^2 \, (T_{m,\,bm} - T_{f,\,bm})), \quad (10)$$

where $l_d$ is displacement of the plasma arc, $h_b$ is thickness of the weld bead, $E_s$ is specific volume enthalpy of the deposit material including latent heat of melting, cρ is specific volume heat capacity of the material of the component, $w_b$ is width of the weld bead, $T_{m,\,bm}$ is surface temperature ensuring melting of the deposit and the base material, and $T_{f,\,bm}$ is temperature at front of the surfacing point.

If the component is welded by oscillating the plasma arc, heat input is difficult to estimate. Modeling of heat input can be made for the straight beads and for the rotating shafts, which are surfaced with rotational movement of the rotating table and the work piece and with linear movement of the plasma torch. Thus, the movement of the weld spot in the surface of the work piece is a spiral.

The effective thermal power of the plasma arc in the second and the subsequent beads when the rotating shaft is surfaced with longitudinal displacement of the plasma arc in relation with the shaft axle is presented in equation 11. The bead width, $w_b$, is constant and it can be estimated from equation 10. The effective thermal power of the first and the subsequent turns is (Nefedov *et al*., 1995):

$$q_{eff,\,n\geq 2} = l_d \, h_b \, E_s \, \nu + 1{,}07 \, c\rho \, w_b^2 \, \nu \times [T_{m,\,bm} - T_{0,\,bm} - \frac{1}{\nu \, R_s{}^2 \, c\rho \sqrt{\pi}} \sum_{n=1}^{n} q_{eff,n} \, \Phi_{(R_s,\tau_n)} \times ( e^{-\frac{\zeta^2 n^2}{4\tau_n}} / \sqrt{\tau_n} )], \quad (11)$$

where $T_{0,\,bm}$ is initial temperature of the base material, $R_s$ is radius of a shaft to be deposited, $\tau_n = \frac{2\,\pi\,\alpha}{\nu \, R_s}$ n is dimensionless surfacing time of n turns, n is number of deposited beads without preheating, $q_{eff,\,n}$ is effective thermal power at $n^{th}$ turn, $\Phi_{(R_s,\tau_n)}$ is function of heat distribution, and ζ is relative surfacing step ($l_d/R_s$).

If the shaft is preheated in the area of the first bead, the effective thermal power of the first and the subsequent beads can be estimated from equations 12 and 13 (Nefedov *et al.*, 1995):

$$q_{eff,\ n=1} = l_d\ h_b\ E_s\ \nu + 1{,}07\ c\rho\ w_b^2\ \nu \times [\ T_{m,\ bm} - T_{0,\ bm} - \frac{q_{eff,n}}{\nu\ R_s^2\ c\rho\ \sqrt{\pi}}\ \sum_{n=1}^{n'} \frac{\Phi_{(R_s,\tau_n)}}{\sqrt{\tau_n}}\ ]\ , \quad (12)$$

$$q_{eff,\ n\geq 2} = l_d\ h_b\ E_s\ \nu + 1{,}07\ c\rho\ w_b^2\ \nu \times \{\ T_{m,\ bm} - T_{0,\ bm} - \frac{1}{\nu\ R_s^2\ c\rho\ \sqrt{\pi}} [\ \sum_{n=1}^{n-1}\ q_{eff,n}\ \Phi_{(R_s,\tau_n)} \times (e^{-\frac{\zeta^2 n^2}{4\tau_n}}\ /\sqrt{\tau_n}\ ) + q_{eff,\,l} \sum_{n\,=\,n\,+\,1}^{n\,+\,n'\,+\,1}\ \Phi_{(R_s,\tau_n)}\ (\ e^{-\frac{\zeta^2 n^2}{4\tau_n}}/\sqrt{\tau_n}\ )\ ]\ \}, \quad (13)$$

where $q_{eff,l}$ is effective power of the plasma arc in local preheating and n´ is number of deposited beads with preheating.

### 2.4.3 Thermal changes of powder particles

Thermal changes of a powder particle are (Xibao, 2003):

1. formation of a powder particle active boundary,
2. elevating of a powder particle temperature at solid state,
3. melting of a powder particle,
4. elevating of a powder particle temperature at liquid state,
5. evaporation of a powder particle.

The parts 3-5 do not initiate if the plasma arc energy is not enough to initiate these steps. The powder particle can be so large or it has high melting or evaporation point and, thus, some of these steps may not always initiate. The 50 µm sized powder particles of Fe and boron carbide, $B_4C$, require about 0,8 and 1,0 µs for formation of powder particle active boundaries, respectively. The solid heating time, $T_{SH}$, melting time, $T_M$, and liquid heating time, $T_{LH}$, for a particle in the plasma arc column can be estimated by using equations 14, 15, and 16 (Xibao *et al.*, 2002):

$$T_{SH} = \frac{2}{3}\ \rho_p r_P^2\ \int_{T_{o,p}}^{T_{m,p}} \frac{C_p dT_p}{(\ S_\infty - S_p)\ (\ 2 + 0{,}514\ R_e^{0,5}\ )}\ , \quad (14)$$

$$T_M = \frac{2\ \rho_p\ L_m\ r_P^2}{3\ (\ 2{+}0{,}514\ R_e^{0,5})\ (S_\infty - S_m)}\ , \quad (15)$$

$$T_{LH} = \frac{2\rho_{PL}\ r_p^2}{3}\ \int_{T_{m,p}}^{T_s} \frac{C_{PL} dT}{(\ S_\infty - S_p)\ (\ 2 + 0{,}514\ R_e^{0,5}\ )}, \quad (16)$$

where $\rho_p$ is mass density of a powder particle, $r_p$ is radius of a powder particle, $T_{0,\ p}$ is initial temperature of a powder particle, $T_{m,\ p}$ is temperature of a powder particle at melting point, $C_p$ is specific heat of a powder particle, $T_p$ is temperature of a powder particle, $S_\infty$ is heat conducting potential of Ar plasma fluid at plasma temperature, $S_P$ is heat conducting potential of Ar plasma fluid at powder particles temperature, $R_e$ is

Reynolds number of plasma particle system, ~1,06, $L_m$ is melting heat rate of a powder particle, $S_m$ is heat conducting potential of Ar plasma fluid at powder particles melting point, $\rho_{PL}$ is mass density of a powder particle at liquid state, $T_s$ is surface temperature of the molten pool, and $C_{PL}$ is specific heat rate of a powder particle at liquid state.

The plasma arc energy, which interacts with the thermal behavior of the particles in the plasma arc, affects strongly especially the ceramic carbide structures and further the microstructure and properties of the whole deposit. The non-transferred arc current can be increased up to 400 A and transferred arc up to 200 A without wear of anode (Dilthey *et al.*, 1993). Theoretically high non-transferred arc current improves the possibility for isothermal heat input. Heat input via non-transferred arc is four to five times less than via transferred arc. Transportation time is one of the parameters affecting the properties of the carbide particles. Density of the powder particles has an effect on the transportation time. In Table 1 is presented the estimated average transportation times in the central plasma arc column from the plasma nozzle to the molten pool for the Fe-base and the $B_4C$ particles.

Table 1 Average transportation times in the central plasma arc column from the plasma nozzle to the molten pool for Fe-base and boron carbide particles (Xibao *et al.*, 2002)

| Particle size $d_0$ ( $\times 10^{-4}$ m) | | | 0.5 | 1.0 | 1.5 | 2.0 |
|---|---|---|---|---|---|---|
| Transporting time $t_0$/ms | $I$ = 200 A | Fe-base particles | 1.10 | 2.03 | 2.88 | 3.75 |
| | | Boron carbides particles | 0.63 | 1.16 | 1.67 | 2.14 |
| | $I$ = 100 A | Fe-base particles | 1.13 | 2.09 | 2.96 | 3.86 |
| | | Boron carbides particle | 0.66 | 1.20 | 1.70 | 2.21 |

In Figures 17a-d are presented powder particle trajectories in relation with powder particle sizes, powder initial injection speeds, and powder particle injection angles. The plasma torch has an external nozzle and an internal nozzle. It was assumed that the powder particle is spherical, under aerodynamic force, and its diameter is above 50 µm. The powder particle has no effect on the plasma stream. The maximum powder particle size, which can be melted in the plasma arc depends a lot about the plasma torch powder feed nozzle and whole powder feed design. 250-300 µm sized particles with axial injection, 150-200 µm sized particles with annular slit, and 80-100 µm sized particles through the aperture of nozzle tip can be melted in the plasma arc. The main parameters affecting it are diameter of the powder particle, arc current, and working distance (Gladky *et al.*, 1990).

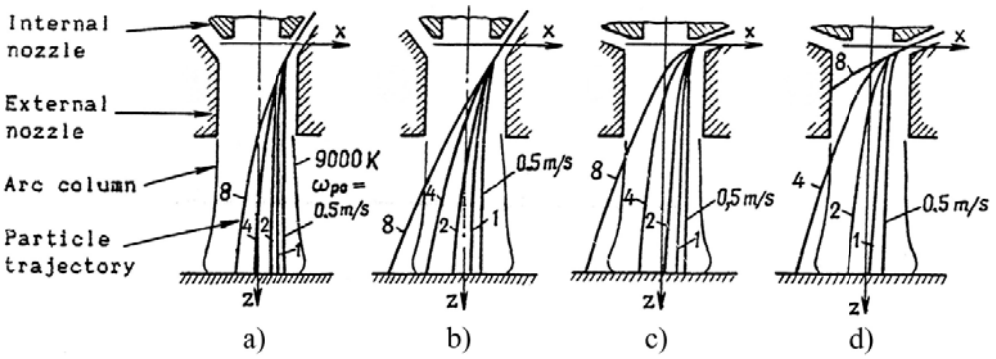


Figure 17 Schematic presentation of powder particle trajectories in relation with a), c) 50 µm and b), d) 150 µm powder particle sizes, various powder initial injection speeds, $\omega_{po}$, 0,5-8,0 m/s, and powder particle injection angles a), b) 35° and c), d) 70° (Gladky *et al*., 1990)

In Figure 18 the effect of the Fe-Cr-C powder grain size on the maximum temperatures of the powder particles is presented. The temperatures of the powder particles are estimated on plasma arc currents 100 and 200 A at the moment the particles are leaving the plasma arc column. The elevation of the temperature of the Fe-based particles at 200 A plasma arc current is about three times higher than at 100 A plasma arc current, even though transportation time in the plasma arc column is not significantly changed. When plasma arc current is 100 A, the plasma arc can melt only the powder particles, the sizes of which are below 80 µm. However, the powder particles below 60 µm evaporate in the plasma arc, when the current is 200 A. Thus, both the lower and the upper limit of the powder fraction have to be changed, when the intensity of the plasma arc and the deposition rate increase (Xibao *et al*., 1998).

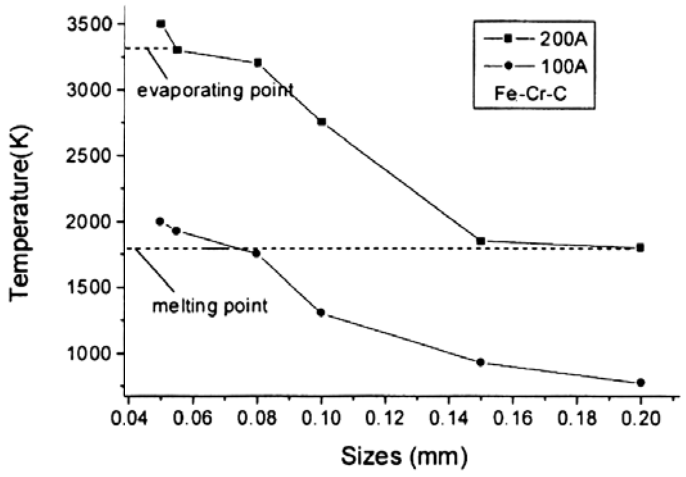


Figure 18 Maximum temperatures of Fe-Cr-C particles of various sizes exiting the central plasma space (Xibao *et al*., 1998)

In Figure 19 are presented the main parameters affecting heating of the powder particles in the plasma arc. The powder consumables were Cu-Al-Fe-Mn-Zn, Ni-Cr-Si-B-C, and AISI 306L stainless steel. Heating is a result of convective exchange with the plasma

arc stream. Temperature gradients of the powder particles were not obtained. Equation for estimating heating of the powder particles is described in studies of Donskoi *et al*. (1979). Increasing plasma arc intensity and working distance and decreasing particle diameter enhance the ability of the plasma arc to melt the powder particles (Gladky *et al.*, 1990).

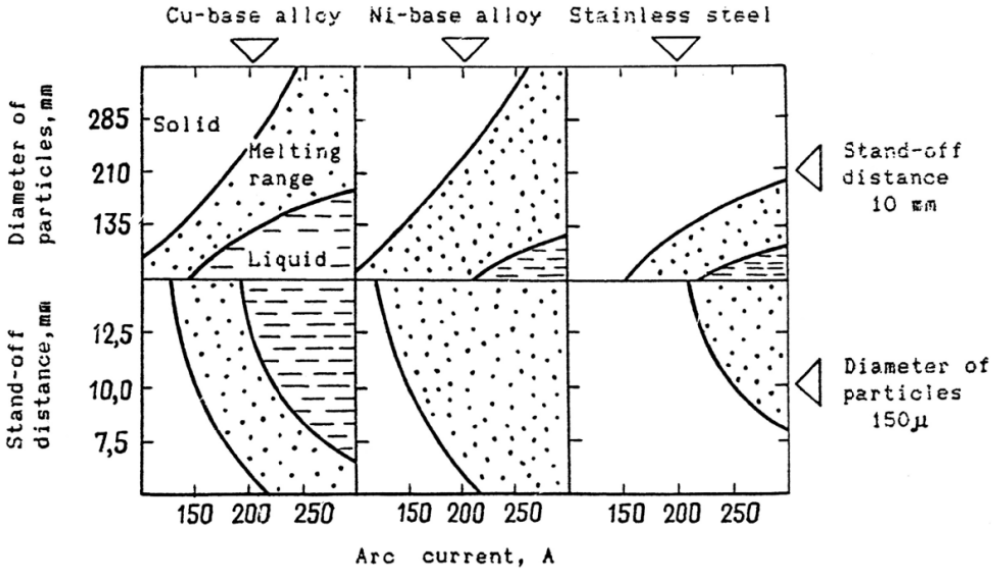


Figure 19 Heating of different kinds of powder particles in plasma arc column (Donskoi *et al.*, 1979; Gladky *et al*., 1990)

Larger particles may cool the molten pool and the formation of the weld bead may be prevented. The thermal reserve of the molten pool has to be enough to melt the powder particles, but the increasing heat input via the plasma arc into the base material can lead to an increase of penetration and detrimental microstructure effects (Nefedov *et al.*, 1995).

It has to be noticed that the presupposition about thermal conductivity of the powder particles often makes a significant error. Ceramic carbide particles have low thermal conductivity and, thus, larger thermal load leads to melting of the surface at lower plasma arc currents than was estimated. Fe-based particles, for instance, have relatively high thermal conductivity and the estimation can be more precise (Xibao, 2003).

### 2.4.4 Dilution

Equation 17 discloses a process condition, where all energy of the plasma arc is used to melt the powder. Therefore, according to equation 17 the plasma arc is not used to melt the base material at all, i.e., the dilution of the deposit is zero. When the maximum volumetric powder consumable feed rate, $V_{pc,\,max}$, ratio to $\eta_a\ \eta_m$ U I, increases, less of the powder is melted in the plasma arc $V_{pc,\,max}$ / $\eta_a\ \eta_m$ U I ratio below 0,08 $mm^3$/J leads to the consumable efficiency above 0,8 according to single-pass welding tests, the tests of which were welded onto A36 steel substrate with AISI 308 austenitic stainless steel

powder consumable (DuPont, 1998). It is obvious that the plasma torch design has an effect on the plasma arc melting efficiency.

Equation 17 estimates the maximum volumetric powder consumable feed rate, $V_{pc,\,max}$, of the metal powder consumable (DuPont *et al.*, 1996):

$$V_{pc,\,max} = \frac{1}{E_{pc}} \eta_a \ \eta_m \, U \, I, \tag{17}$$

where $E_{pc}$ is melting enthalpy of the powder consumable.

Estimation of the dilution is possible in theory if precise arc and melting efficiencies of the plasma arc are known. The dilution of the weld bead can be estimated by equation 18 and the melting efficiency of the arc by equations 5, 6, or 7. The correlation between the measured and the estimated melting efficiency is good for GMAW and SAW methods, moderate for the GTAW method, and poor for the PAW method. Low and varying arc efficiency of the PA welding method limits the accuracy of the melting efficiency. The dilution correlates at least with welding parameters U, I, ν, and volumetric powder consumable feed rate, $V_{pc}$. Equation 18 does not notice welding speed. Studied welds were deposited onto 6,4 mm thick A36 carbon steel. The powder consumable was AISI 308 austenitic stainless steel alloy. The dilution of the first bead layer is (DuPont *et al.*, 1996):

$$D_{1st\ layer}\,[\%] = [1 + \frac{V_{pc}\, E_{bm}}{\eta_a\, \eta_m\, U\, I - E_{pc}\, V_{pc}}]^{-1} \times 100, \tag{18}$$

where $E_{bm}$ is melting enthalpy of the base material.

### 2.4.5 Dissolution of carbides

The dissolution of a carbide particle depends strongly on the initial particle size, $d_0$. The thermal stability can be estimated from bond enthalpy of the particle (Lugscheider *et al.*, 1994). The most important factors controlling the dissolution of the carbide are the temperature of the molten pool, the melting point of the carbide, the size of the carbide, the chemical content of the alloy, and the distribution of the alloying elements in the matrix. Equation 19 is valid only for short intervals, because it is derived by considering one particle in an infinite matrix. Equation is for a cementite particle in a steel matrix, but it can be used also for the other types of carbides. Time to dissolve a particle, $t_{diss}$, is (Ågren, 1990):

$$t_{diss} = \frac{r_p^2}{2\,\Omega D_c^{\gamma}}, \tag{19}$$

where $\Omega$ is driving force and $D_c^{\gamma}$ is diffusivity of carbon in austenite. Driving force, $\Omega$, is a measure of driving force depending on carbon contents at the matrix and the carbide particle. Carbon content is typically higher nearby the carbide-matrix interface when compared to carbon content at a relative distance from the carbide-matrix interface. Thus, carbon tends to dissolve from the carbide. The carbon flux in cementite is

approximated to be negligible. Driving force is obtained from equation 20 (Ågren, 1990):

$$\Omega = \frac{U_c^{\gamma} - U_c^{\gamma\infty}}{U_c^{cem} - U_c^{\gamma}}, \quad (20)$$

where $U_c^{\gamma}$ is carbon content in austenite close to the carbide-matrix interface, $U_c^{\gamma\infty}$ is carbon content in austenite, and $U_c^{cem}$ is carbon content in cementite.

The volume fraction of carbides as a function of time is presented in equation 21 (Ågren, 1990):

$$vf_t(t) = vf_{t_0} \left\{ 1 - \frac{2\,\Omega\,D_c^{\gamma}\,t}{r_p^2} \right\}^{3/2}, \quad (21)$$

where $vf_t(t)$ is the volume fraction of carbides as a function of time, t, and $vf_{t_0}$ is the initial volume fraction of carbides.

### 2.4.6 Weld pool convection

Fluid in gaseous or liquid form is subject to convection, which is fluid motion caused by an external force. Convection has effect on the weld pool shape, mixing, homogeneity, segregation, porosity, evaporation of alloying elements, and weld pool oscillation. Especially, convection promotes mixing and homogeneity of the weld microstructure (Messler, 1999).

The factors affecting the weld pool convection are electromagnetic or Lorentz force (Figure 20c), $\mathbf{F}_{em}$, buoyancy or gravity force (Figure 20a), $\mathbf{F}_b$, surface tension or Marangoni force (Figure 20b), $\mathbf{F}_{\gamma}$, and impinging, friction or aerodynamic drag force of the arc plasma (Figure 20d), $\mathbf{F}_{arc}$, are the driving forces for convection in the weld pool (Messler, 1999; Ushio, 1991). Only surface tension force is not originally based on an external force. Flow in the cross-section of the weld pool is called as poloidal or meridional flow. Flow from the edge to the center of the molten pool is called as convergent flow, Figure 20c and 20d, and flow from the center to the edge is called as divergent flow, Figure 20a and 20b. Convergent flow is unstable and tends to form a spin. The reason is fluid flow caused by depression of the arc in the centerline of the molten pool and the fluid flow from the other parts of the molten pool, i.e., resulting in collision between these two flows. Finally, the result can be toroidal flow, which is flow around the center hole in the molten pool. Divergent flow is more stable (David *et al.*, 1989; Messler, 1999).

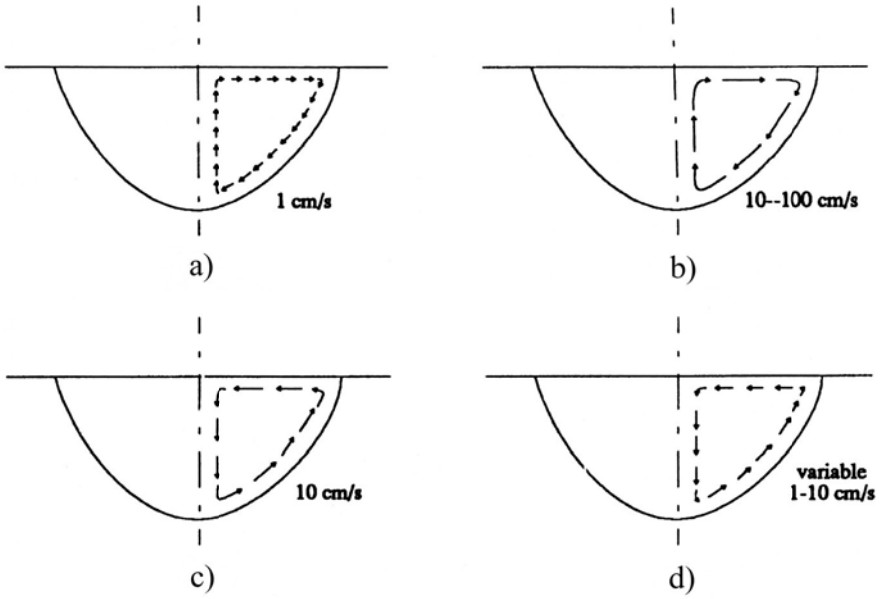


Figure 20 Convection patterns induced by: a) buoyancy force, b) surface tension force, c) electromagnetic force, and d) impinging force (Messler, 1999)

Electromagnetic force is caused by the interaction between the divergent current path in the weld pool and the magnetic field, which is generated by the divergent current path. The degree of stirring is proportional to the magnetic fields, i.e., arc current (Burgardt *et al.*, 1986). An estimation of the electromagnetic force distribution can be made after assumption that current density is uniform on the anode area and on a cylindrical surface area of the base material. Electromagnetic force can be increased by arc oscillation and pulsed current (Ishizaki *et al.*, 1994; Messler, 1999; Ushio, 1991).

Buoyancy force is generated by the temperature gradients in the molten pool, density differences due to differences in local composition, and gravity. Above melting temperature the density of a liquid decreases, thus, superheated regions of the molten pool are in lower density than cooler regions (Kou *et al.*, 1986; Messler, 1999).

Surface tension gradient is caused by the temperature gradients at the free surface and the surface active agents of the molten pool. Marangoni effect describes the moving fluid interface according to local changes of surface tension caused by distribution of temperature and composition (Burgardt *et al.*, 1986; Heiple *et al.*, 1982). In general, surface tension decreases with increasing temperature (Kou *et al.*, 1986; Ushio, 1991).

The impinging force is a result of momentum transfer through friction between impinging particles and metal atoms in the molten weld pool. Since most welding process use arc, the phenomenon can be called as arc plasma force. The momentum of rapidly moving active particles, i.e., electrons or ions in the arc, is kinetic energy. The momentum of rapidly moving electrons is greater than that of photons, because of their greater mass. Thus, kinetic energy of the impinging particles cause circulation in the molten pool and the flow pattern is always from edge-to-center. Most of the arc energy is deposited at the central part of the weld pool. Thus, penetration is deepening at the

bottom of the molten pool. Impinging force tends to promote mixing in the welds welded by the PA welding method (Messler, 1999).

Arc oscillation and current pulsing have also effects on convection of the molten pool by reducing macrosegregation, removing porosity, and refining the microstructure (Messler, 1999). It is concluded that electromagnetic force is the major determinant of the penetration shape and aerodynamic drag force has a secondary role (Yokoya *et al.*, 1994). The weld pool convection is usually the result of combinations of forces caused by the welding method, the welding parameters, the material characteristics, and the environment (Messler, 1999).

Three major factors which have effect on the weld pool convection are (Yokoya *et al.*, 1994):

1. the pattern of heat input from the arc,
2. the current distribution,
3. the interaction between complex convection driving factors.

The first three forces can be presented in the next three equations (Ishizaki *et al.*, 1994; Kou, 1987; Messler, 1999; Yokoya *et al.*, 1994):

$$\mathbf{F}_{em} = \mathbf{J}_{cd} \times \mathbf{B}_{mf}, \tag{22}$$

$$\mathbf{F}_{b} = -\rho_{lm}\,\beta_{e}\,\mathbf{g}\,(T_{mp} - T_{0,mp}), \tag{23}$$

$$\mathbf{F}_{\gamma} = -\frac{\partial \gamma_s}{\partial T}\nabla T, \tag{24}$$

where $\mathbf{J}_{cd}$ is current density vector, $\mathbf{B}_{mf}$ is magnetic flux vector, $\rho_{lm}$ is density of liquid metal, $\beta_e$ is coefficient of thermal expansion of liquid metal, $\mathbf{g}$ is gravitational acceleration, $T_{mp}$ is temperature of the molten pool, $T_{0,\,mp}$ is reference temperature of the molten pool (e.g. melting temperature), $\gamma_s$ is surface tension of liquid metal, and $\nabla T$ is temperature gradient at the weld pool surface.

### 2.4.7 Weld pool solidification

A weld bead consists of four zones, i.e., fusion zone, FZ, partially melted zone, PMZ, unmelted heat affected zone, HAZ, and unaffected base material. Parameters, which are important in determining the microstructure of the molten pool are growth rate, temperature gradient, undercooling, and chemical composition of weld alloy. Thermal gradient is strongly affected by convection in the molten pool. Cooling rate mainly depends on welding speed. Cooling rate in the weld pool varies from 10 to $10^3$ $Ks^{-1}$ for arc welding processes. Cooling rate which is even greater can be achieved (Chen *et al.*, 1993). For the laser, LB, and the electron beam, EB, welding methods cooling rate varies between $10^3$-$10^6$ $Ks^{-1}$ depending on the welding parameters. Solidification behaviour has a strong effect on the size and the shape of grains, segregation, distribution of inclusions, porosity, and hot cracks. Soaking time at high temperatures

and cooling time from 800 to 500 ºC have an effect on the microstructure and the mechanical properties of the weld deposit (David *et al.*, 1989; Oberländer *et al.*, 1992).

Cooling rate 0,4-8,0 x $10^3$ $Ks^{-1}$ can be estimated with equation 25. Cooling rate can be estimated when the secondary arm spacing is measured from the microstructure and placed into equation 25 (David *et al.*, 1989; Jones, 1990; Oberländer *et al*., 1992):

$$CR = \left(\frac{a_1}{D_{sas}}\right)^{1/a_2}, \quad (25)$$

where CR is cooling rate, $a_1$ is an empirical constant, 60 µm, $a_2$ is an empirical constant, 0,32, and $D_{sas}$ is secondary arm spacing, 3-8 µm.

### 2.4.8 Interactions of welding parameters

The comparison between direct and interaction effects of welding parameters can be made by factorial analysis experiments (Box *et al*., 1978; Cochran *et al*., 1950; Harris *et al*., 1983). The costs and time can be reduced, when information is required about the effects of the welding parameters on the bead geometry or the dilution, for instance. Babi (1991) disclosed that the parametric relationship of the PTA welding method has unpredictable nature especially when blended nickel alloys are used. In this method it is possible to decrease the number of experimental runs. Always, successful surfacing procedure requires optimization of welding parameters to have low dilution and crack-free overlay (Murugan *et al*., 1994). The models can be checked for adequacy and significance by using significance tests and confidence intervals (Box *et al*., 1978; Harris *et al*., 1983; Herrström *et al*., 1993; Marimuthu *et al.*, 2003).

The factorial technique for estimating weld quality has so far been utilized only for estimating deposit dimensions like height, width, hardness, and dilution. The effects of welding parameters and the interactions between welding parameters on the microstructure and the properties of the deposits in the wear tests and the real environments have not been studied. The state of the process changes during the surfacing process in a way, which is impossible to estimate, e.g., the temperature of the work piece changes. Thus, exact information of welding parameter variables on the microstructure and the deposit wear resistance are difficult to estimate (Harris *et al*., 1983; Kapus, 1980; Murugan *et al.*, 1994).

The study plan for factorial analysis contains (Murugan *et al*., 1994):

1. identifying the important process variables,
2. identifying upper and lower limits of the studied variables,
3. developing the matrix,
4. conducting the experiments as per the design matrix,
5. recording the responses,
6. developing the mathematical models,
7. estimating the coefficients of the polynomials,
8. checking the adequacy of the models developed,

9. testing the significance of the regression coefficients and getting final mathematical models,
10. presenting the main effects and the significant interactions,
11. analysis of the results.

In Table 2 the effects of the welding parameters on the dilution, the hardness, the width, and the height of the deposit are presented. The effect of each of the six welding parameters was estimated at several levels of the other factors by a factorial analysis computer program. In the factorial matrix the welding parameters were plasma arc current, plasma gas, transport gas, oscillation frequency, welding speed, and working distance. One possible welding parameter to study by the factorial analysis experiment, which was not included in this test, is powder feed rate. 16 test combinations were carried out.

The studied deposit material was Stellite 6. The powder fraction range was 63-180 μm. Nominal composition of Stellite 6 was Cr 28,0 %, C 1,0 %, W 4,0 %, Si 1,0 %, and bal. Co. The base material was low alloyed steel (C 0,2 %, Mn 1,6 %, Si 0,3 %, and bal. Fe). The input factors were current 100-130 A, plasma gas Ar flow rate 1-3 l/min, carrier gas Ar flow rate 2-4 l/min, oscillation frequency 82-90 osc./min, welding speed 5-7 cm/min, torch distance 6-14 mm, and powder feed rate 1 kg/h. Shielding gas was Ar + 5 % $H_2$ (10 l/min). Preheating was not used (Herrström *et al.*, 1993).

The results indicate that the most significant parameters affecting the dilution and the hardness of the deposit are plasma arc current and plasma gas flow rate. The effects of welding speed and oscillation frequency on the dilution depend on the other parameters used such as powder feed, plasma arc current, oscillation mode, etc. These parameters in the first place determine the thickness and the width of the bead, even though they have a minor effect on the dilution according to the estimation. The increasing working distance has an increasing effect on the dilution. The effect of the transport gas on the dilution was unclear (Herrström *et al.*, 1993).

Table 2 Estimated direct and interaction effects of the welding parameters on the deposit properties estimated from the mathematical models (Herrström *et al*., 1993)

| | Dilution % | Hardness HV30 | Width mm | Height mm |
|---|---|---|---|---|
| Average | 16.24 | 377.5 | 15.24 | 2.89 |
| A:Plasma gas | 8.04 | -33.75* | 0.18 | -1.02* |
| B:Current | 11.36 | -76.75* | 3.12* | -0.32* |
| C:Osc.freq | 1.46 | -5.25 | 0.02 | -0.02 |
| D:Weld speed | 0.46 | -7.75 | -3.7* | -0.52 |
| E:Distance | 2.49 | -7.25 | 0.58 | -0.02 |
| F:Transport gas | 0.64 | 45.75* | 0.2 | 0.22 |
| AB+CE | 3.51 | -9 | -0.32 | 0.12 |
| AC+BE | 0.61 | -4.5 | -0.18 | 0.02 |
| AD+EF | 1.06 | 7* | -1.05 | 0.18 |
| AE+BC+DF | -3.16 | 12.5 | -0.68 | 0.08 |
| AF+DE | -4.14 | 26.5 | 0.6 | 0.12 |
| BD+CF | 0.84 | -10 | -0.7 | 0.02 |
| BF+CD | 2.29 | 1.5 | 0.05 | -0.12 |

* Significant effect at 95 % level.

## 2.5 Effects of main welding parameters on dilution

### 2.5.1 Plasma gas flow rate and plasma arc current

The dilution leads to an increase of alloying elements, mainly iron, from the base material to the deposit, which can cause a reduction in hardness, wear, or corrosion resistance (Hunt, 1988; Chattopadhyay, 1997). The diluted elements are partly concentrated in the deposit nearby the fusion line in the depth of 0,2-0,5 mm. It is assumed that evaporation of the alloying elements is negligible. Detrimental phase transformations can be controlled by adjusting the PTA welding method.

For a given consumable feed rate, welding speed, and other welding parameters, an increase in plasma arc current leads to an increase in the penetration and hence to an increase of the dilution of the deposit. The influence of plasma arc current in relation to the dilution is quite linear. In Figure 21 welding tests were welded with plasma gas flow rates 1 and 4 l/min. The differences in the dilutions of the beads are remarkable. The interaction between plasma gas flow rate and plasma arc current is obvious. When increasing plasma gas flow rate the increasing plasma arc current increases the dilution more rapidly. Thus, the effect of plasma gas flow rate on the dilution is similar when compared to the effect of plasma arc current. At a higher plasma gas flow rate more directional plasma arc column is obtained (Wilden *et al.*, 2006). It is also obvious that increasing powder feed rate decreases the dilution of the deposit, because more energy is needed to melt the powder. Pilot arc was 100 A, shielding gas Ar + 5 % $H_2$ 10 l/min, carrier gas Ar + 5 % $H_2$ 3,5 l/min, oscillation width 40 mm, oscillation speed 108 cm/min, welding speed 7,8 cm/min, working distance 20 mm, and powder range 60-200 µm. The base material was carbon steel St 37. The size of the work piece was

300×300×30 mm. The studied powder alloys were FeCr- and NiCr-alloys (Herrström *et al*., 1993; Hunt, 1988; Marantz *et al*, 1980; Mitelea *et al*., 1997).

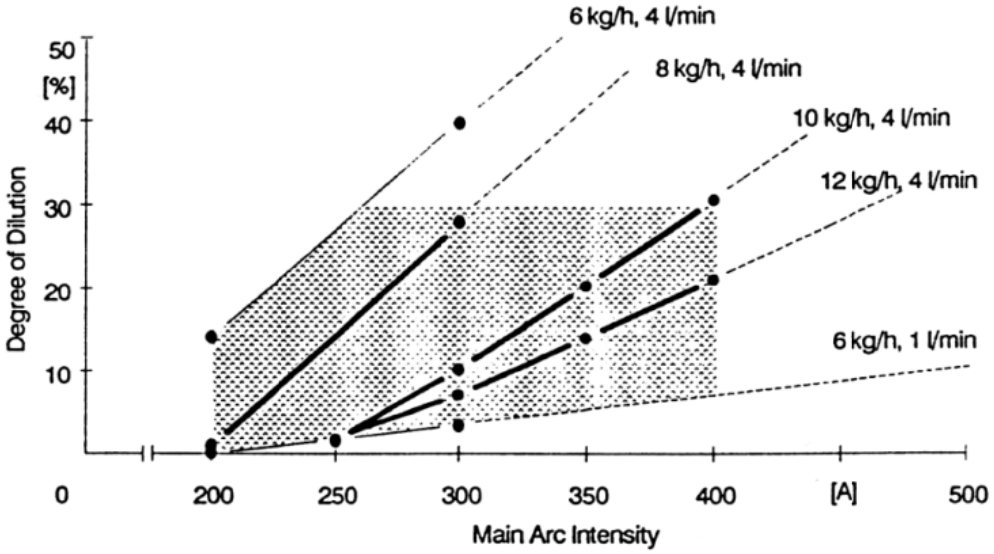


Figure 21 Effect of plasma arc current, plasma gas flow rate, and powder feed rate on the dilution of the deposit (Hallén *et al*., 1992a)

The diameter of the plasma nozzle affects plasma gas flow rate. When changing the plasma nozzle, which has a different diameter, plasma gas flow rate changes. With large flow rates of plasma or carrier gas the turbulent stream can leave pores and oxides into the deposit (Hallén *et al*., 1992b; Huang *et al*., 1998). The plasma arc has with large flow rates a pressing effect on the molten pool and, therefore, the deposit may be thinner in the centerline of the beads, Figure 22. Because of the negative effects of high plasma gas flow rate, plasma gas flow rate is usually between 2-6 l/min.

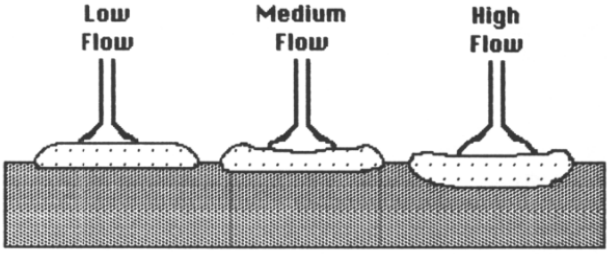


Figure 22 Effect of plasma gas flow rate on the shape of the deposit cross-section and the dilution of the deposit (Shubert, 1992)

According to many studies plasma arc current has the biggest effect on the dilution of the deposit. The size of the molten pool and the thickness of the weld bead have effects on the process control. The problem in the dilution control occurs, if the molten pool moves between the plasma arc and the base material. Thus, the plasma arc ability to form penetration may disappear. However, plasma arc current has a significant effect on the dilution. The simplest way to control the dilution is to adjust plasma arc current

(Marantz *et al*., 1980). Even penetration and continuing constant dilution can be achieved by suspending the plasma torch at an angle to the direction of welding (Röthig *et al*., 1997).

### 2.5.2 Working distance

One benefit of the PTA welding method is the consistent plasma arc column with wide range of working distances. Working distance ranges between 8 and 20 mm depending on the application. The distance can be even lower, if plasma arc current is low and the thickness of the deposit is small. At higher melting rates working distance is automatically higher, because the welded deposit is correspondingly thicker, as well. The torch is then exposed less to the fume and spatters (Babi, 1993; Hettiger, 1992; Wahl *et al.*, 1993).

Working distance has a similar, but less significant effect on the dilution as compared to plasma arc current. The difference increases with larger plasma arc current and higher deposition rate, Figure 23. When working distance was 15 mm, the dilutions of the deposits were higher when compared to the deposits welded with working distance 20 mm (Hallén *et al*., 1992a).

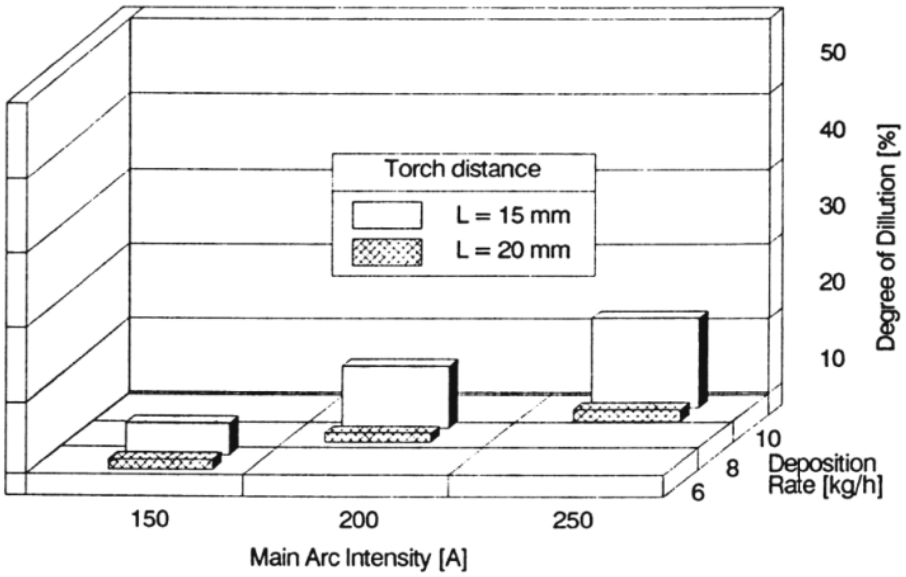


Figure 23 Effect of working distance on the dilution of the deposit (Hallén *et al*., 1992a)

### 2.5.3 Powder feed rate

Thickness of the deposit affects the size of the parameter window. The larger molten pool buffers the plasma arc and thereby reduces the dilution (Marantz *et al*., 1980). That is why plasma arc current, plasma gas flow rate following the shape of the plasma arc, and the size of the molten pool are closely related to each other. When welding a thin

deposit, the amount of mixed metal from the base material to the deposit is smaller than in welding a thick deposit on the same dilution. In the thinner deposits the growing plasma arc current increases the dilution faster than in the thicker deposits, Figures 24a, b. The powder alloys in Figures 24a, b are related to Stellite 1, the chemical compositions of which are Co 48 %, Cr 30 %, W 12 % with and without a small addition of boron. Boron reduces melting point of the alloy, improves wetting and, thus, thinner deposits at lower deposition rates were achieved.

In Figures 24a, b maximum thicknesses of the deposits were 6,0 and 4,5 mm, which are typical values for the PTA welding method. Even though the range of the bead thickness is from 1 to 6 mm, the range depends strongly about the chemical composition of the alloy. Mobility of the molten pool is the main reason, which restricts the penetration.

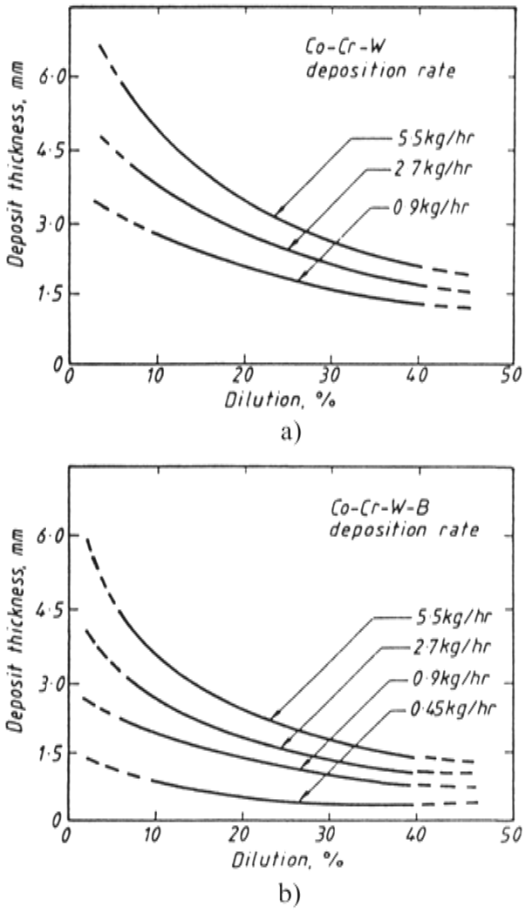


Figure 24 Effects of deposit thickness and powder feed rate on dilution, when welding with alloys: a) Stellite 1 and b) Stellite 1 with a small amount of boron (Marantz *et al*., 1980)

### 2.5.4 Powder fraction

The powder particle size has an effect on the surfacing behavior. Basically, the dilution increases, when the particle size fraction increases, because the consumable efficiency is larger for the fine fractions at the same plasma arc current (Babiak *et al*., 1986). With the coarse powder fractions the plasma arc melts more the base material than with the fine powder fractions, if welding parameters are not changed, because the consumable efficiency is larger for fine powder fractions.

In Figure 25 is presented the effect of the particle size range on the dilution of the deposit on a FeCr-alloy. The powder particle size of 53-180 µm caused the least penetration. The dilution was 14 %, which was about 50 % better result when compared to the dilution of the other powder particle size fractions. The PTA welding method is sensitive to small alterations, which can explain partly the result, e.g., between the fractions 53-180 and 53-150 µm. The reasons for the differences remain unclear (Hallén *et al.*, 1992b).

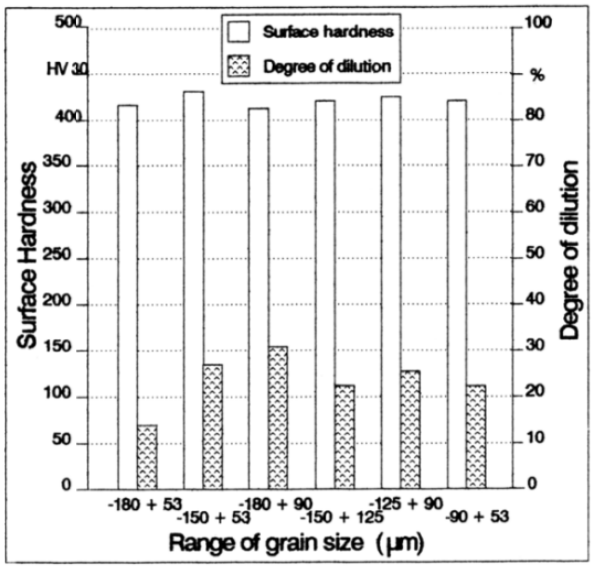


Figure 25 Effect of powder fraction on hardness and dilution of the deposit on a FeCr-alloy (Hallén *et al.*, 1992b)

### 2.5.5 Shielding and carrier gas flow rates

Increasing shielding gas flow rate decreases the dilution, because the gas flow refrigerates the molten pool and the base material. An increase in shielding gas flow rate has also been shown to have an increasing cooling effect on the plasma arc (Hunt, 1988; Sharples, 1985). Shielding gas flow rates are typically between 8 and 15 l/min. Over 15 mm working distances the shielding efficiency decreases (Babi, 1993; Deuis *et al.*, 1998). Shielding gas flow rate is always constant during the welding process and, thus, it has no noticeable effects on the dilution of the deposit.

Carrier gas flow rate does not have a noteworthy effect on the dilution. Carrier gas may refrigerate the plasma arc a little, which can decrease the dilution. The range of variation of carrier gas flow rate is so small that it does not have a remarkable effect on the dilution. A flow rate from 5 to 10 l/min is needed for the deposition rates from 8 to 14 kg/h with gas pressure 5 bar (Bouaifi *et al*., 1999; Hallén *et al*., 1992b; Herrström *et al*., 1993).

Carrier gas flow rate depends on the deposition rate. When carrier gas flow rate exceeds a certain limit value, carrier gas can suffer from turbulent flow and the air may enter into the plasma arc and porosity can form in the deposit. In Figures 26a, b poor powder feeding and undercutting were the results of too low and high flow rates of carrier gas. The suitable flow rate is between 3 and 5 l/min depending on the shape of the powder consumable. The welding parameters were powder feed rate <1 kg/h, plasma arc current 96 A, pilot arc current 35 A, and welding speed 56 cm/min. The studied base materials were austenitic steel, martensitic steel, and nickel-based alloys. The studied consumables were cobalt-based powders equivalent to Stellite 6, 12, F, and Colmonoy 6 alloys.

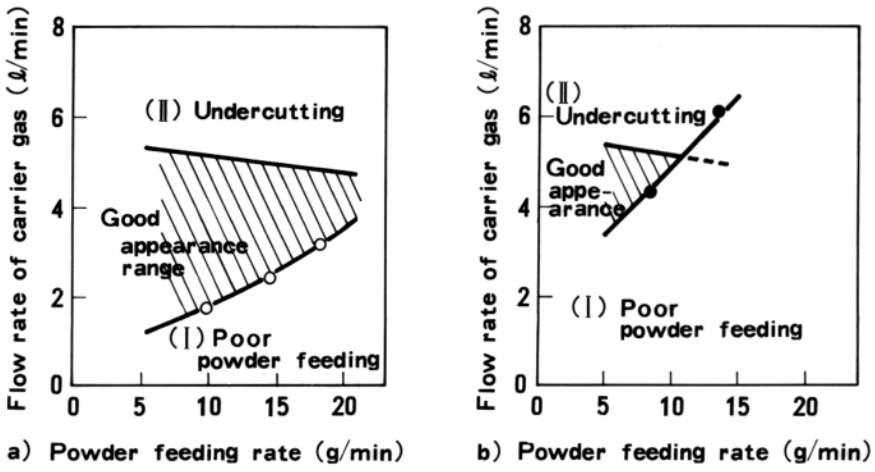


Figure 26 Comparison between the characteristics of the deposits welded by using: a) spherically and b) irregularly shaped cobalt-based powders equivalent to Stellite 6, 12, F, and Colmonoy 6 alloys (Takeuchi *et al*., 1985)

### 2.5.6 Preheating

It is very common to use a high preheating temperature in surfacing a component to ensure the crack-free deposit. The coefficients of thermal expansion have remarkable effects on the welding process, because the interface of the deposit and the base material is very sensitive to microcracking if gradient-layer deposit or butter-layer is not used. The work piece expands when it is heated and shrinks back as much when it cools down. The shrinkage level has to be about the same in both the deposit and the base material to avoid cracking in hard deposits. The main reason to use preheating is to prevent cracking of the deposit (Gregory, 1991).

Preheating temperatures of 250-300 °C are used to help the surfacing process of valve heads with cobalt-based powders (Klimpel *et al*., 2005). Preheating temperature of the work piece can be even 900 °C (Mathew *et al*., 1980). Temperature gradient in the component in front of the arc at the start and in the end of surfacing a weld bead can be 600-800 ºC (Nefedov *et al*., 1994). When heat input to the base material was controlled with decreasing plasma arc current, the temperature of the work piece decreased from 850 ºC (constant power) to 650 ºC (decreasing plasma arc current). The bead width increased about 1/3, when the power of the plasma arc was not adjusted (Nefedov *et al*., 1995). Cooling rate is lower with higher preheating temperatures. For the deposits welded by the GTA welding method the welding parameters were arc efficiency 0,7, arc current 200 A, and arc voltage 10 V; cooling rate without preheating was approximately 71 °C/s and for 250 °C preheating 20 °C/s (Kou, 1987).

The preheating temperature has a remarkable effect on the dilution of the deposit. For instance, using plasma arc current 100 A and powder feed rate 1,6 kg/h, the dilution of the deposit increases about 11 %, while the preheating temperature increases from RT to 200 °C (Hunt, 1988; Sharples, 1985). The effect of preheating temperature on the dilution depends on the welding parameters, i.e., plasma arc current, plasma gas flow rate, heat input per unit length, deposition rate, bead dimensions, and oscillation parameters. The difference is higher in the thinner deposits and the smaller components.

Gatto *et al*. (2004) welded by the PTA welding method a bead on a groove in a small disc-shaped sample, the size of which was Ø 150 x 35 mm. The temperature of the work piece increased from RT to 230-240 °C depending on the welding parameters. Thus, the temperature of small components increases rapidly, even though preheating is not used.

# 3 Degradation of materials

Degradation of the welded deposits depends on many factors. Wear of the materials depends firstly on the wear mechanisms. All of the wear mechanisms can take part to the wear of the deposit. Chemical composition of the deposit has an effect on the microstructure of the deposit. Material properties like hardness, carbon content, alloy content, hard phases, microstructure, and fracture resistance have an effect on the abrasive wear (Budinski, 1988; Zum Gahr, 1987). The microstructure has many factors, like the volume fraction of carbides, the size of carbides, the MFP, and the matrix phases, which have effects on the degradation of the deposit (Buchely *et al*., 2005; Zum Gahr, 1987). The abrasive, its hardness and size distribution are hard to estimate. The effects of the welding operator, the welding process, and the finishing process on the properties of the deposit are remarkable. Finally, the whole environment where the component surface is planned to survive, is seldom known. Thus, it is challenging to optimize the properties of a component.

The tribological performances of the coatings and their chemical, microstructural and mechanical features change, when plasma arc current, powder mass flow rate, and welding speed are modified, for instance. At different powder consumable feed rates current intensity influences both from the mechanical and the microstructural point of view (Sintoni *et al.*, 1992).

## 3.1 Wear mechanisms

Between two contacting surfaces exists always two or more wear mechanisms. One wear mechanism normally dominates. The role of each wear mechanism can be small or large depending mainly on the load type, the materials, and the environment. Basic material parameters, which have effects on the wear by all wear mechanisms are composition, grain size, modulus, thermal conductivity, degree of work hardening, and hardness (Bayer, 1997). The wear interactions between the two surfaces are focused on a relatively thin surface section. Wear mechanisms describe the interactions between energy, friction, contact surfaces and, thus, wear. Processes without friction are usually also without wear phenomena and increasing friction does not always mean measurable wear loss (Zum Gahr, 1995).

Interacting material surfaces have many tribological parameters. In any wear situation four tribocomponents can be identified, i.e., first and second triboelement, interfacial element, and environmental medium (Czichos, 1997). Typical interfacial element can be dust, lubricant, or wear debris. Environmental parameters are mainly air or corrosive atmospheres. Operational parameters, i.e., motion, load, velocity, temperature, and duration, characterize the functional conditions of the tribosystem. Interaction parameters between the tribocomponents characterize the contact mode between the tribocomponents. Tribological processes are also called as wear mechanisms. Depending on the source classification of the wear mechanisms varies. One of the classifications of wear mechanisms is adhesion, abrasion, surface fatigue, and tribochemical reactions (Blau, 1989; Holmberg *et al.*, 1994). Other wear modes, which can be included to basic wear mechanisms are at least cavitation, corrosive, delamination, erosion, fretting, and impact wear.

In Figures 27a-d are presented the basic wear mechanisms. In Figure 27a is presented adhesion, where asperities of two surfaces are in contact and the surfaces may adhere strongly and asperity junctions, i.e., cold-welded junctions, can be formed. Typically surface of the softer material is removed. In Figure 27b is presented plastic deformation both in asperity wear and in abrasive wear. Abrasive wear causes removal of material because of the scratching effect of the abrasive particle or asperity of the material surface. In Figure 27c is presented surface fatigue wear. Fatigue crack growth results from surface load and unload. The stress levels are such that the substrate can manage to survive once, but after repeated cycles a crack can be initiated. Surface fatigue leads to a formation of cracks in the contact surfaces and as a result to debris formation. In Figure 27d is presented chemical wear, which is initiated by environment atmosphere and contact mechanisms. The result can be the formation of small or bigger wear debris. The formation of chemical reaction products as a result of chemical interaction between the contact surfaces can also be possible (Blau, 1989; Holmberg *et al.*, 1994).

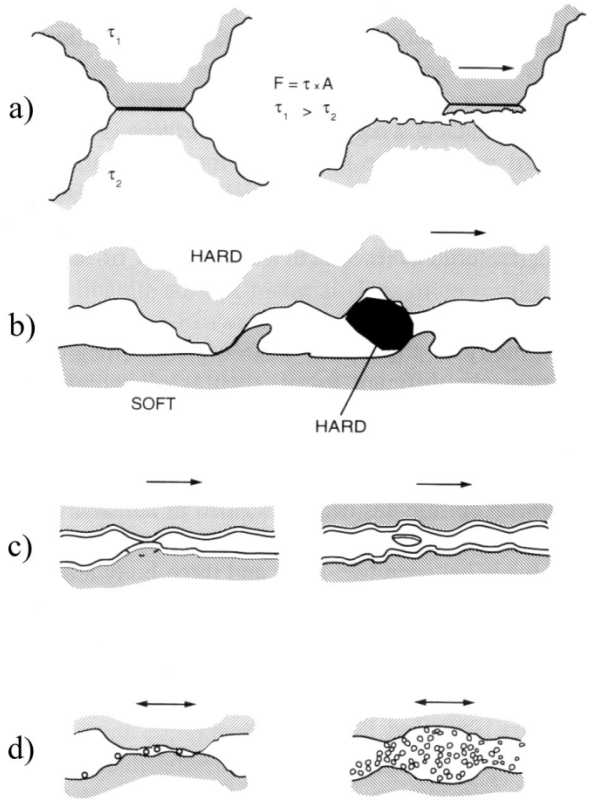


Figure 27 Basic wear mechanisms: a) adhesion, b) abrasion, c) surface fatigue, and d) tribochemical reactions (Blau, 1989; Holmberg *et al.*, 1994)

## 3.2 Abrasive wear

Abrasive wear is the main wear mechanism when a hard contact area of the tribocomponent or an abrasive between surfaces plastically deforms or cuts the surface. The abrasive particle has sharp angular shape which is capable of producing cutting or shearing force on the material surface. Abrasive wear can be two-body, i.e., one surface against the other surface or three-body, i.e., abrasives as a third-body between the surfaces, Figures 28a, b. In three-body abrasion the abrasive may roll between the surfaces and microchip formation, i.e., scratching is low. Wear loss is one to two times smaller in three-body abrasion than in two-body abrasion (Zum Gahr, 1987).

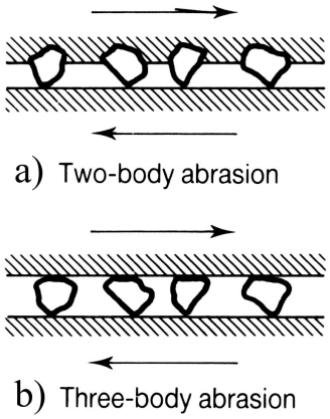


Figure 28 Two abrasive wear types: a) two-body and b) three-body abrasive wear (Hutchings, 1992)

Abrasive wear is a complicated wear mechanism, because of many affecting parameters like microstructure, mechanical properties, abrasive, loading condition, surface finish, temperature, and environmental atmosphere, Figure 29.

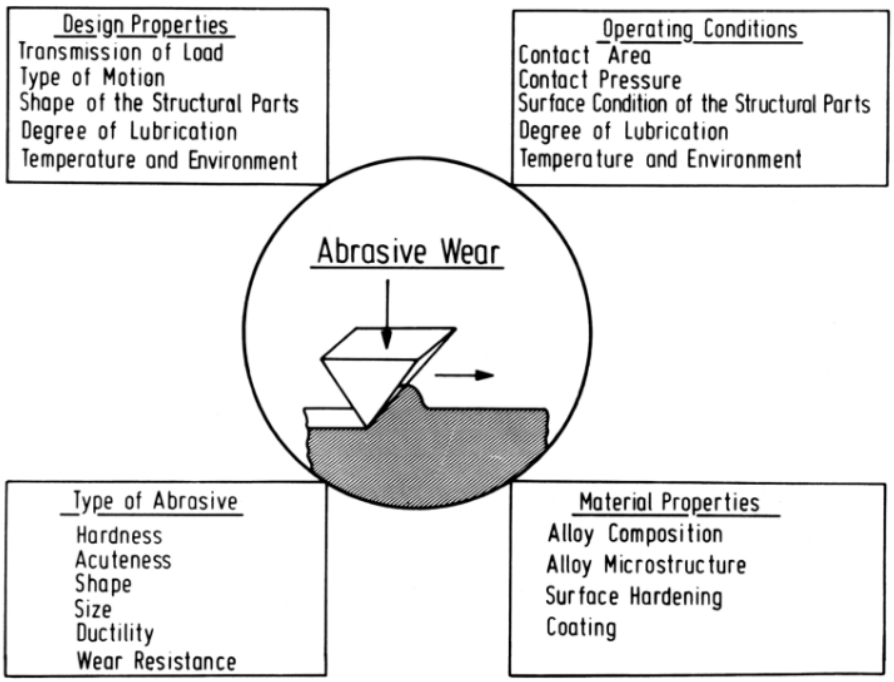


Figure 29 Main factors determining abrasive wear (Zum Gahr, 1987)

Abrasive wear has many categories. Abrasive wear can be categorized as low stress, high stress, gouging, and polishing abrasive wear (Budinski, 1988). Criterion for low stress abrasion is that the abrasive particle has to flow through the contact area without crushing phenomena of the abrasive particle (Bhansali, 1980). Normal force is then low enough without the ability to crush the abrasives. Usually scratches are obtained in the wear scars and the subsurface deformation is minimal. Low stress abrasion can be called

as scratching abrasion and high stress abrasion as grinding abrasion. However, wide range of abrasive contact stresses present in high stress abrasion and at least part of those stresses are in high stress range (Avery, 1981; Bhansali, 1980; Budinski, 1988).

High stress abrasion is obtained if the wearing parts have normal force high enough to crush the abrasives (Bhansali, 1980). Crushing strength of quartzite rock is 206 MPa or 21 kg/mm$^2$ (Avery, 1981). High stress abrasion is characterized by scratching, plastic deformation, and pitting of the indented abrasives. Plastic deformation is typically obtained with ductile materials. Deep scratches in the direction of motion are typically obtained from the wear surface. Enhancing compressive strength of the surface is an effective way to resist degradation. It is a benefit, if the surface hardness is higher than the abrasive hardness, since then crushed abrasive or at least its angular edges become more round. An example about high stress abrasion is milling of minerals (Avery, 1981; Bhansali, 1980; Budinski, 1988).

Gouging is a form of high stress abrasion where big-sized grooves and gouges are formed on the wear surface. Gouging can be a result of, e.g., low stress abrasion, high stress abrasion, or sliding wear and impact wear. The mechanism is plastic deformation and chip formation. Fatigue wear and fracture of materials may also be the result of repetitive action of, e.g., crushing of rocks. Hammermill hammers is one of the applications where gouging is obtained (Avery, 1981; Bhansali, 1980; Budinski, 1988).

Polishing wear is wear without scratching, fracture, or plastic deformation. Material is removed from the surface which causes changes in the material dimensions. Polishing causes micro-chip removal and, thus, it is a reason to categorize it to the abrasive wear mechanisms. Micro-chipping is occurring if the abrasive size is above 3 μm. With small abrasive particles and low normal forces molecular or atomic scale material removal may also occur. Steel handrail is a typical application under repeated polishing wear (Budinski, 1988; Zum Gahr, 1995).

In Figures 30a-c are presented the behavior of the deposits under the abrasive wear load. In Figure 30a is presented material loss of soft and ductile material by microploughing and microcutting. Microfatigue can also occur, when material is under repeating microploughing. In Figure 30b is presented material loss of relatively hard and brittle material as compared to Figure 30a. The material loss is happening due to microcutting and microcracking. In Figure 30c is presented spalling of the deposit. Spalling can occur depending on the properties of the deposit and the deposit-base material interface. Above critical loads, spalling of the deposit becomes more important type of wear. As a result of Figures 30a-c it can be seen that a combination of the deposit hardness and toughness must be found to optimize the abrasive wear resistance of the deposit (Zum Gahr, 1995).

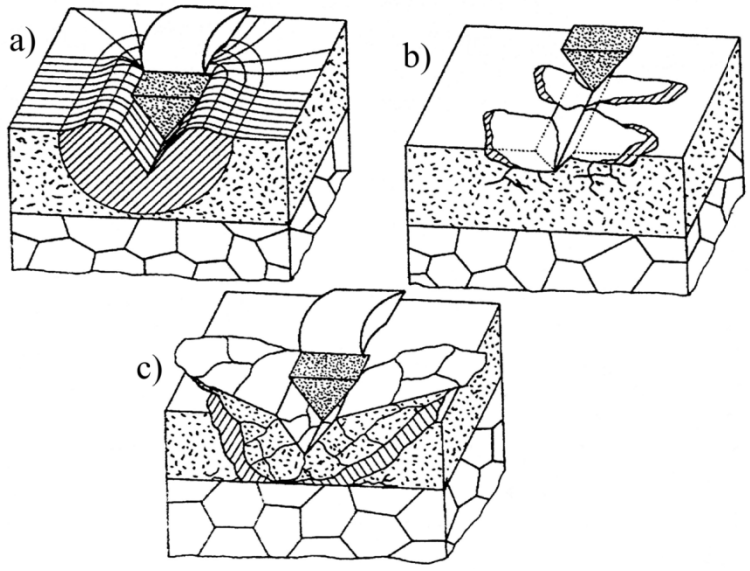


Figure 30 Behavior of the deposits under abrasive wear: a) microploughing and microcutting, b) microcutting and microcracking, and c) microcutting or spalling (Zum Gahr, 1995)

Between the wear mechanisms and the microstructure is a remarkable relationship. Different kinds of reinforcing phases can be used in the deposits to resist abrasive wear. During low stress abrasion increasing carbide content increases hardness and wear resistance of the Stellite 6 deposit (Shin *et al.*, 2003). The properties of the reinforcing phases vary in hardness, Young's modulus, size, shape, distribution, orientation, and bonding to the matrix (Zum Gahr, 1995). Sometimes several different kinds of hard phases, which have different properties, are used in the same deposit. The hard phases may settle into their own distances from the FZ, because of their different densities.

The abrasive wear resistance mainly increases when the volume fraction of the carbide phase and the size of the carbides increase. Under different loading, abrasive size, and wear type this may not always be true. The wear type may alter, e.g., between micro-ploughing, microcutting, and brittle fracture. Also microfatigue may occur. Transition from ductile to brittle wear depends on fracture toughness and stress fields nearby the contact point (Zum Gahr, 1987).

In Figures 31a-f are presented the effects of the hard and the soft abrasives on the abrasive wear of the deposits. In Figures 31a-c the hard abrasive is able to abrade-off both the matrix alloy and the reinforcement phase. The small reinforcement particles are digged-out and the larger ones are cracked or cut-out. Small separated reinforcement particles can act as an abrasive and, thus, further increase the wear loss of the deposit. In Figures 31d-e soft abrasive is able to abrade-off only small reinforcement particles and larger reinforcement particles, which are not well-bonded. When the volume fraction of the reinforcement phase and the carbide size increases and, thus, the MFP decreases, the soft particles are not able to abrade-off the reinforcement particles, but the matrix between the reinforcement particles cannot avoid indentation of the soft abrasive, Figure 31f. The abrasive wear resistance of the matrix alloy is not remarkably enhanced, when

the volume fraction of the reinforcing carbides is lower than 10 vol.-% (Bouaifi *et al.*, 1997; Yellup *et al.*, 1996; Zum Gahr, 1997).

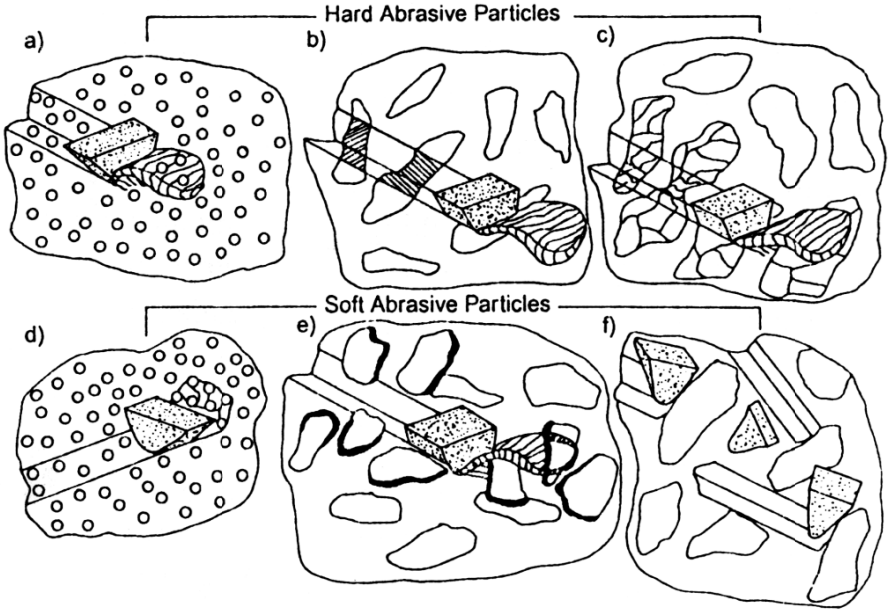


Figure 31 Schematically presented effects (a-f) of the sliding of hard (a-c) and soft abrasives (d-f) on the abrasive wear of the deposits (Zum Gahr, 1997)

By modeling it was found that after 30-35 vol.-% carbide volume fraction the lowest wear loss was obtained (Hu *et al.*, 2005). This limit changes, when the interfacial bond strength between the carbides and the matrix alters, e.g., when the carbide particles are replaced with other carbides. As usual, the deposit contains more than one reinforcing compound. The reinforcement can be any of the original, primarily, or secondarily precipitated carbides.

Usually pure abrasive wear resistance is increased when the volume fraction of carbides increases. 12V tool steel MMCs (Ala-Kleme *et al.*, 2007), the matrix of which contained 20 vol.-% VC carbides reinforced with 20 or 30 vol.-% WC carbides, were manufactured by the hot isostatic pressing process, HIP. The material with 30 vol.-% WC carbides had better abrasive wear resistance in the rubber wheel abrasion test, RWAT. The material with 20 vol.-% WC carbides had better wear resistance in the small-scale Nordberg laboratory compression stone cone crusher test, B90. The wear mechanisms in the RWAT abrasion test were microploughing, microcracking, and obviously microcutting. The wear mechanisms in the compressive stone cone crusher test were cutting and ploughing for the matrix or plastic deformation. The reinforcements were worn by microcracking. Pure compression/indentation was also obtained. Thus, the maximum amount of the reinforcement is strongly dependent on the wear mechanism.

The interfacial bond strength is difficult to estimate and accurate value is not available, which makes it difficult to use modeling for estimating wear (Hu *et al.*, 2005). The interaction between the matrix and the reinforcement during the wear can be digging-

out, cutting, cracking, or spalling. Wetting between the carbide and the matrix alloy is important for avoiding carbide detachment and becoming an abrasive (Nishida *et al.*, 1999).

In Figure 32 is presented schematically a cross-section of a groove, $A_g$, with ridges, $A_{r1}$ and $A_{r2}$. Wear loss of the plastically deformed material is typically overestimated because of plastic deformation. Equations for wear loss are easier to design for the brittle materials. Thus, wear loss of the material capable to plastic deformation is normally many orders of magnitude less than in the material wearing with brittle fracture (Challen *et al.*, 1979).

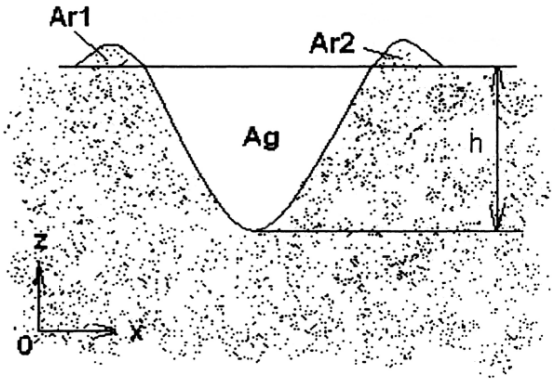


Figure 32 A cross-section of a scratch presenting abrasive efficiency (Fang *et al.*, 2001; Zum Gahr, 1987)

The abrasive efficiency is also called as the ratio of microcutting to microploughing. After critical load is exceeded in the wear process change from microploughing-microcutting to predominantly microcutting-microcracking occurs (Zum Gahr, 1988). This depends on operating parameters, microstructural elements, and the properties of the wearing material. The abrasive efficiency, $f_{ab}$, caused by an abrasive, which is presented in Figure 32, can be estimated by equation 26 (Zum Gahr, 1987):

$$f_{ab} = \frac{A_g - ( A_{r1} + A_{r2} )}{A_g}, \quad (26)$$

where $A_g$ is volume of a scratch groove and $A_{r1}$, $A_{r2}$ are ridges, which are formed during deformation by indented particle or asperity. $f_{ab} = 1$ describes the state of ideal material removal without ridge formation and $f_{ab} = 0$ means the state of ideal microploughing without material removal.

The fracture processes play an important role in abrasive wear of brittle materials. It is fundamental to know if either plastic deformation or fracture mechanism controls the rate of material removal. Still both plastic deformation and fracture mechanisms cause material removal during abrasive wear of brittle materials (Moore *et al.*, 1980). Dominating mechanism depends on wear environment and material properties (Zum Gahr, 1987).

## 3.3 Modeling abrasive wear

Modeling provides means for linking the different effects together following the better ability for understanding the effects controlling the abrasive wear under certain conditions. Designing tests and determining the correct variables are the main benefits, which can be achieved with the modeling. General sliding wear has many factors, more than 100 parameters and constants, which have an effect on the wear resistance. Average number of variables is 4,8 in empirical equations, 5,8 in simple mechanics-based models, and 8,9 in equations built from the material point of view. On average 1,5 wear coefficients are needed per equation (Meng *et al.*, 1995). For this reason it is extremely challenging to model abrasive wear. Three-body abrasive wear is already too complicated for modeling, because time cycles of rolling and trapping of abrasive are not possible to estimate exactly (Torrence, 2005).

Hardness is the material property for resisting indentation. The abrasive hardness has an effect on the wear resistance of the wear part. The relative wear depends on the correlation between the base material or the wearing material hardness ($H_{bm}$) and the abrasive hardness ($H_a$). If $H_a < K_2 \times H_{bm}$ ($K_2$ = 0,7-1,1), no wear occurs; $H_a > K_1 \times H_{bm}$ ($K_1$ = 1,3-1,7), wear does not depend on $H_a$ and the wear mechanism may change. In Figure 33 is presented the effect of abrasive and material hardness ratio on the wear losses of single- and multiphase materials. The wear loss of multiphase material can be greater than single-phase material at high wear rate, if reinforcing phase can be detached and it works as an abrasive (Zum Gahr, 1997). Multiphase material is more resistant to abrasive wear with abrasive and material hardness ratio around 1,2, than single-phase material.

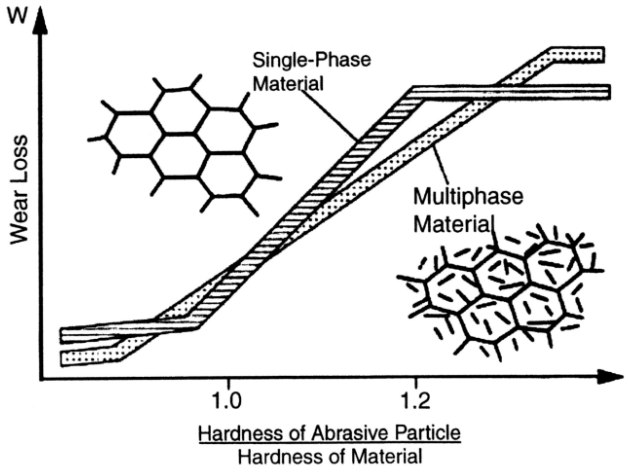


Figure 33 Effect of abrasive and material hardness on the wear losses of single- and multiphase materials (Zum Gahr, 1987; Zum Gahr, 1997)

For full abrasive cutting the abrasive hardness has to be greater than 1,2 × the base material hardness. Equation 27 estimates the relationship between attack angle of the abrasive and hardness of the base material and the abrasive (Torrence, 2005):

$$H_a \geq H_{bm} \frac{1 + \pi/2}{1 + \pi/2 - \propto_a}, \quad (27)$$

where $\propto_a$ is mean attack angle. Attack angle 30º results $H_a \geq 1{,}26\ H_{bm}$. Attack angle may vary in three-body abrasive wear, because abrasives can reorientate during rolling between contact surfaces (Zum Gahr, 1987).

The wear volume caused by conical indenter can be estimated by equation 28 (Rabinowicz, 1965):

$$V = \frac{\overline{\tan\theta}\, l}{\pi} \times \frac{P}{H_{bm}} \quad (28)$$

where V is wear volume, $\overline{\tan\theta}$ is a weighted average of the tan θ values of all the individual abrasives, P is normal load, and l is sliding distance.

The effect of the carbide size distribution on the abrasive wear resistance is not largely studied. The mono-sized carbide fraction is not an optimal microstructure for the wear resistant alloys, because no constant wear exists at real environments. Larger carbides are believed to hold the wearing load and the smaller carbides shield the matrix against the wearing load with the low MFP. By modeling it was found that with 19 % large, 8 % medium, and 8 % small scale particle contents the optimum wear resistance can be obtained (Hu *et al*., 2005).

As well as the carbide size distribution, the abrasive size distribution has an effect on the abrasive wear resistance. Mixed abrasive particle size distribution increases abrasive wear when compared to the mono-sized abrasives (Budinski, 1988).

The MFP ($\lambda_{MFP}$), can be estimated if the volume fraction of carbides, the volume fraction of matrix, and the number of carbides per unit length is known (Nishida *et al*., 1993). The MFP is related to average diameter of the abrasives, $d_a$. It is more accurate to measure the MFP from the microstructure. At the ratio $\lambda_{MFP}/d_a > 1$, the abrasive particles can wear-off the matrix, because the sizes of the abrasives are smaller than the MFP. At the ratio $\lambda_{MFP}/d_a < 1$, the abrasive particles cannot wear-off the matrix, because the MFP is smaller than the sizes of the abrasive particles leading to situation where the counterparts for the abrasives are the carbides. Therefore, the ratio $\lambda_{MFP}/d_a$ should be <1, when high abrasive wear resistance is needed. In Figures 34a, b is presented a schematic presentation of the abrasive wear mechanism of the composite materials.

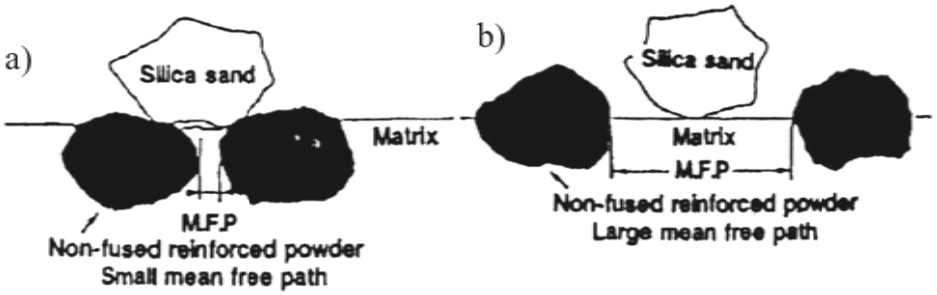


Figure 34 Schematic presentation of the abrasive wear mechanism of the deposit reinforced with carbides in relation with MFP and average size of the abrasive particles: a) shorter mean free path than abrasive size and b) longer mean free path than abrasive size (Nishida *et al*., 1993)

In Figure 35 is presented the effect of the matrix mean free path in relation with the average size of the silica sand on the abrasive wear resistance of the MMC alloys. The abrasive wear of the PTA welded Stellite 6 (C 1,3 %, Cr 30,2 %, W 4,5 %, Si 1,3 %, Mn 0,7 %, Fe 0,1 %, Ni 0,1 %, Mo 0,1 %, Co bal.) reinforced with TiC (75-106 µm) and $Cr_3C_2$ (75-180 µm) carbides increases rapidly, when the mean free path increases above the average size of the silica sand ($\lambda_{MFP}/d_a > 1$) (Araki *et al*., 1994; Nishida *et al*., 1993).

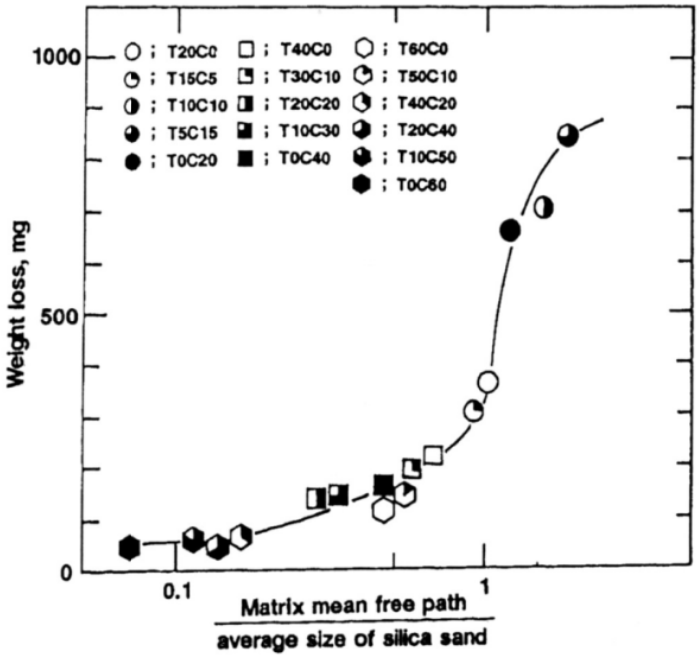


Figure 35 Effect of matrix MFP in relation with average size of the silica sand on abrasive wear of the Stellite 6 deposit reinforced with TiC and $Cr_3C_2$ carbides (Nishida *et al*., 1993)

The ratio, $h_r$, between the average penetration depth of the abrasives, h, and the average diameter of the reinforcing carbides, d, determines the abrasive wear resistance as well

as the MFP. Equation 29 estimates the abrasive penetration depth into the relatively soft material. When the material and the load stress are constant the penetration depth is depending on the ratio of the average abrasive particle size, $d_a$, and the average reinforcement size, d. Equation 29 still does not take into account the effect of the MFP. The average penetration depths are typically about 10-15 % of the mean abrasive particle diameters. Relative penetration depth is (Wang *et al*., 1991):

$$h_r = \left(\frac{2}{\pi K'}\right)^{1/2} \left(\frac{\sigma}{H_{bm}}\right)^{1/4} \left(\frac{d_a}{d}\right), \quad (29)$$

where σ is stress in the contact area and K' is geometrical constant.

The same ratio between the penetration depth of the abrasive and the reinforcement size determines the abrasive wear resistance as well as the MFP. The effect can be explained efficiently with soft matrix. In Figures 36 and 37a, b are presented relative wear resistance vs. relative abrasive penetration depth and schematic presentation of the interactions between the abrasive particles and the reinforcement particles at various h/d relationships. The lowest relative wear resistance is obtained, when the relative penetration depth estimated with equation 29 equals to 1. At lower penetration depths the relative abrasion resistance is relatively high. It has to be noticed that the deposit was Al 7091 (Cu 1,59 %, Mg 2,28 %, Zn 6,11 %, Co 0,4 %, Fe 0,07 %, and Al bal.) reinforced with 20 vol.-% SiC. The range of the SiC particles was 2-10 μm and mean was 5 μm. It is necessary to notice that the angle of abrasive or asperity and leading cross-section have effects on indentation and cutting of the surface of the base material. Sahin (2005) discussed results made by the Taguchi method for soft materials like aluminium composites that abrasive grain size is one of the major parameter for the soft composites. It may have even higher effect on the abrasive wear when compared to the applied load, reinforcement size, and sliding distance.

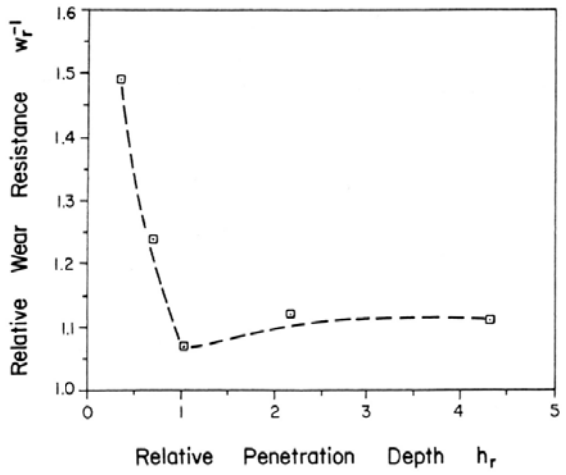


Figure 36 Relative wear resistance vs. relative abrasive penetration depth, $h_r$ (Wang *et al*., 1991)

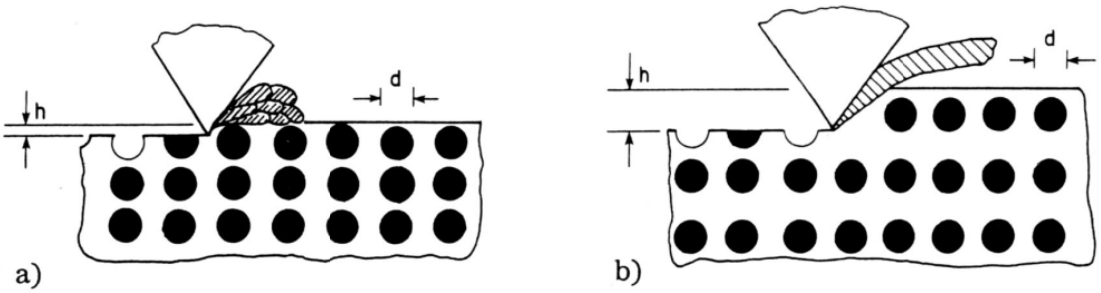


Figure 37 Schematic presentation of the interactions between the abrasive particle and the reinforcement particles: a) h < d and b) h > d (Wang *et al*., 1991)

In Figures 38a, b is presented the abrasive wear behavior of two phases. The steady state wear is obtained, when the distances of $x_1$ and $x_2$ from the original top surface remain constant. The applied load per surface areas of the phases is not equal, but the steady state abrasive wear is obtained (Garrison, 1982). Surface roughness has an effect on the abrasive wear, i.e., smoother surface may have a lower wear rate.

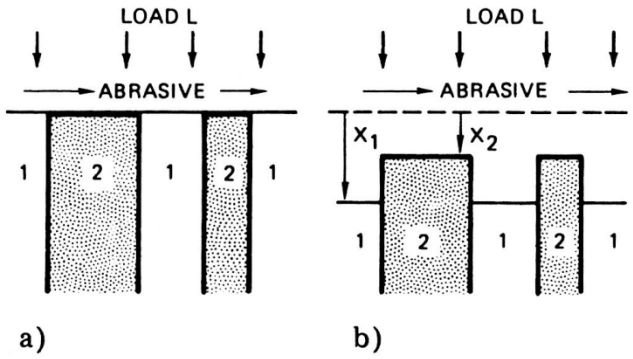


Figure 38 a) Initial stage and b) steady state of abrasive wear (Garrison, 1982)

The abrasive efficiency can be estimated by equation 30 (Zum Gahr, 1988):

$$f_{ab} = 1 - \left(\frac{\varphi_{lim}}{\varphi_s}\right)^{2/\beta}, \quad (30)$$

where $\varphi_{lim}$ is capability of deformation of the wearing material during abrasive wear, $\varphi_s$ is effective deformation of the wearing surface, and $\beta$ is a factor describing the decay of deformation with increasing depth below the wearing surface. $\beta$ can be estimated from equation 31 and $\varphi_s$ from equation 32 (Zum Gahr, 1987):

$$\beta = \left(\frac{H_{def}}{H_{bm}}\right)^{1/3}, \quad (31)$$

$$\varphi_s = 2 \ln \left\{\frac{P^{1/3} E^{2/3} \left(1+10\,\mu^2\right)^{1/2} \tan \vartheta}{6{,}16\, H_{def}\, {R_p}^{2/3}}\right\}, \quad (32)$$

where $H_{def}$ is hardness measured on the wear debris, E is elastic modulus, μ is coefficient of friction, 2ϑ is angle of abrasive tip, and $R_p$ is tip radius of an abrasive.

Hardness is not always in relationship with the wear resistance (Baeslack *et al.*, 1996). Normal load increases the abrasive wear of the Stellite 6 deposit more efficiently when compared to sliding velocity and track radius (Shanmugam *et al.*, 2004). The relationship between wear volume, hardness, normal load, and sliding distance in various tribological processes is estimated by equation 33. It is applied for many wear processes, especially for adhesive wear. The term hardness should have a correction multiplier from 1,5 to 3 (Budinski, 1988; Tucker, 1997). The Archard law is (Archard, 1953):

$$V = \frac{K\, l\, P}{H_{bm}}, \tag{33}$$

where K is a wear coefficient. K is a constant related to the probability per unit encounter of production of a wear particle. Constant K is related to the sharpness, geometry of the asperity or particle causing the wear (Bayer, 1997). Magnitude of constant K can vary in a large scale.

In equation 34, the abrasive efficiency, $f_{ab}$, is related to Archard wear coefficient K (Kato, 1997):

$$K = f_{ab} \frac{A_g\, H_{bm}}{P\, l}, \tag{34}$$

where volume of a scratch groove, $A_g$, is (Kato, 1997; Zum Gahr, 1987):

$$A_g = \frac{P\, l}{H_{bm}} \left\{ \frac{1}{5} \left( 1 + 10\, \mu^2 \right)^{1/2} + \frac{H_{bm}\, R_p^2}{P\, l \tan \vartheta} \left( \frac{\pi \tan \vartheta}{2} - 1 \right) \right\}. \tag{35}$$

According to the Khruschov's rule the wear resistance of a structurally heterogeneous material is equal to the sum of losses of the volumetric shares of the separate phases multiplied by the relative wear resistances. The Khruschov's rule cannot give exact estimations. For instance, the abrasive wear resistance of tungsten carbide with cobalt bond is 2,5 times lower than the rule estimates. The rule is designed for metal-metal composites, not for metal-ceramic composites. The Khruschov's rule for the multiphase system is (Garrison, 1982; Khruschov, 1974):

$$W = \sum_i v_i \mathcal{E}_i, \tag{36}$$

where W is wear resistance, $v_i$ is the volume fraction of *i*th phase, and $\mathcal{E}_i$ is wear resistance of *i*th phase.

Chen *et al*. (1990) have presented enhanced version of equation 36, which is presented in equation 37. Equation 37 has a modification factor for the second phase. Equation 37 is modified to interpret the wear data of the high-chromium white cast iron samples in which the microstructure, i.e., carbide volume fraction, carbide morphology, and matrix

structure, were varied. Abrasive wear resistance of a composite material, $V_{vf}$, is (Chen *et al*., 1990):

$$V_{vf} = V_m + ( k V_{sp} - V_m ) vf , \quad (37)$$

where vf is volume fraction of the second phase, $V_m$ is abrasive wear resistance of the matrix phase, $V_{sp}$ is abrasive wear resistance of the second phase, and k is modification factor in relation with interphase interaction. Both coarser carbide morphology and martensitic matrix have increasing effect on k values.

The abrasive efficiency increases with brittle materials, because microcracking can occur around scratches. The wear rate may be doubled. Abrasive wear rate of brittle materials or ceramics can be estimated by equation 38 (Moore *et al.*, 1980; Zum Gahr, 1997):

$$V_r = \Phi_1 \frac{\sqrt{d_a}\,\sigma^{5/4}}{K_C^{3/4}\sqrt{H_{bm}}} , \quad (38)$$

where $\Phi_1$ is constant and $K_c$ is fracture toughness of the wearing material.

In Figure 39 is presented overall wear resistance and fracture toughness for ceramics and metals (Zum Gahr, 1997). Diesburg *et al.* (1992) found similar kind of relationship between wear resistance and fracture toughness of austenitic and martensitic steels as presented in Figure 39.

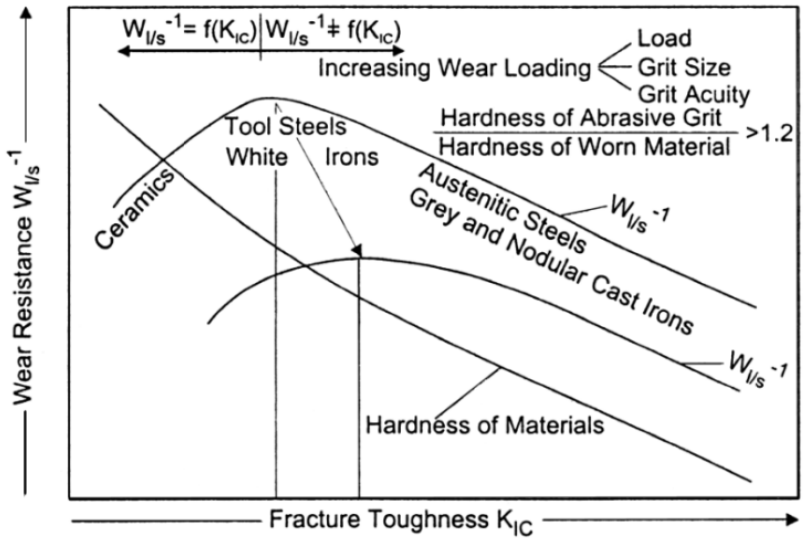


Figure 39 Wear resistance and fracture toughness for ceramics and metals (Zum Gahr, 1987)

## 3.4 Strengthening mechanisms

In crystals atoms are packed together in a regularly repeating pattern. Crystals are not perfect. The defects in them determine the crystal strength. The dislocation is a defect which allows material to deform plastically. Dislocation motion produces plastic strain, i.e., crystal yields. The possibilities of increase the resistance against dislocation motion are solid solution hardening, precipitate and dispersion hardening, and work-hardening. Also combination of previously mentioned ones is possible (Ashby *et al.*, 1980).

A crystal yields when the force (per unit length), τb, exceeds the resistance opposing the motion of a dislocation, f. $\tau$ is a shear stress. Most crystals have a certain intrinsic strength, which is the bond between the atoms. The bond has to brake and reform when the dislocation moves. Covalent bond has a large intrinsic lattice resistance per unit length of dislocation. Because of covalent bond, e.g., diamonds and carbides have their excellent hardness and strength. Strength of pure metals is low because of low lattice resistance. The dislocation yield strength, $\tau_y$, is (Ashby *et al.*, 1980):

$$\tau_y = \frac{f}{b}, \tag{39}$$

where f is resistance opposing the motion of a dislocation (a force per unit length) and b is unit of slip, the Burgers vector.

Hardening of metal is possible by making it impure. Impurities go into solution in a solid metal. Large atoms like chromium and nickel produce barriers to dislocation motion. The atoms replace the original metal atoms and form a random substitutional solution. The size of the atoms is different and after squeezing into the structure stresses generate. These stresses “roughen” the slip plane making dislocations harder to move. The smaller the spacing of the dissolved atoms the rougher is the slip plane. Thus, the resistance opposing the motion of a dislocation, f, and the dislocation yield strength, $\tau_y$, increases (Ashby *et al.*, 1980).

When the solute concentration in an alloy exceeds the limit of solubility of the matrix phase, nucleation and growth of second-phase particles begins if suitable thermal conditions are present. Second phase may precipitate as small particles, when it is dissolved in a metal or ceramic at a high temperature and the alloy is cooled to RT. At temperature close to solvus temperature only little driving force for the precipitation process exists even though diffusion kinetics is rapid. An optimal temperature for rapid precipitation is obtained at an intermediate temperature because of an ideal combination of particle nucleation and growth rates. It is also important to notice that dislocation looping is controlled by the spacing between particles, but not by the nature of the particle itself. Most steels are strengthened by the precipitates of the carbides obtained by this way. Small particles can be added into metals or ceramics by adding particles with powdered consumable, e.g., by the HIP process or the PTA welding method. Both ways increase the amount of small carbides in a path of dislocation, thus, preventing dislocation motion and plastic flow of materials. The greatest hardening is achieved with strong closely shaped precipitates or dispersoids, i.e., with the high volume

fraction and the small MFP of precipitates or dispersoids (Ashby *et al.*, 1980; Hertzberg, 1996).

Most crystals have several slip systems. The f.c.c. structure, which has four slip planes, slips on {111} planes. Plastic deformation by cold working produces dislocations. Dislocations move through crystals when crystals yield. Number of dislocations increases by cold working and interactions between dislocations reduce dislocation mobility. Dislocations interact, obstruct each other, and accumulate in the material. Stress-strain curve rises steeply after yield. Additional deformation is more difficult and larger stresses have to be applied to achieve more deformation. This is called as work-hardening, strain hardening, or cold working (Ashby *et al.*, 1980; Hertzberg, 1996).

In Figure 40 is presented the effect of hardness on abrasive wear resistance. Also solid solution hardening, precipitate and dispersion hardening, and work-hardening have effects on the abrasive wear resistance.

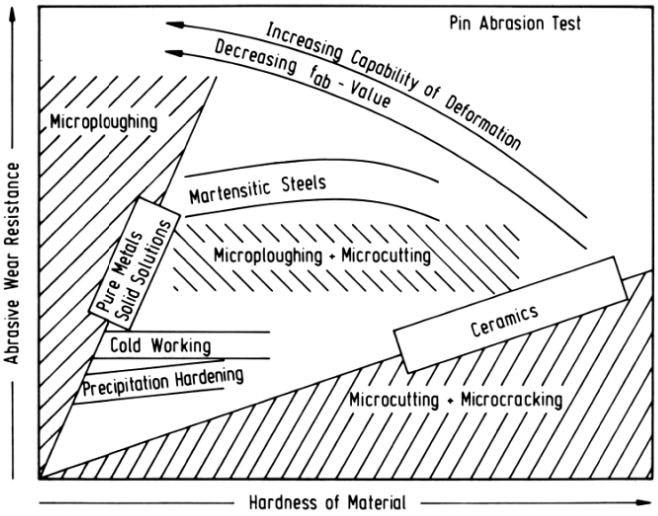


Figure 40 Schematic presentation of the abrasive wear resistances of the materials as a function of hardness (Zum Gahr, 1987)

In Figure 41 is presented the effect of hardness of various materials on the abrasive wear resistance. The highest abrasive wear resistance is obtained with martensite and retained austenite. Austenite phase can undergo transformation from austenite to martensite during abrasive wear. Phase transformation may induce positive volume transformation and the result can be positive compression stresses which are beneficial especially for the welded deposits (Zum Gahr, 1987).

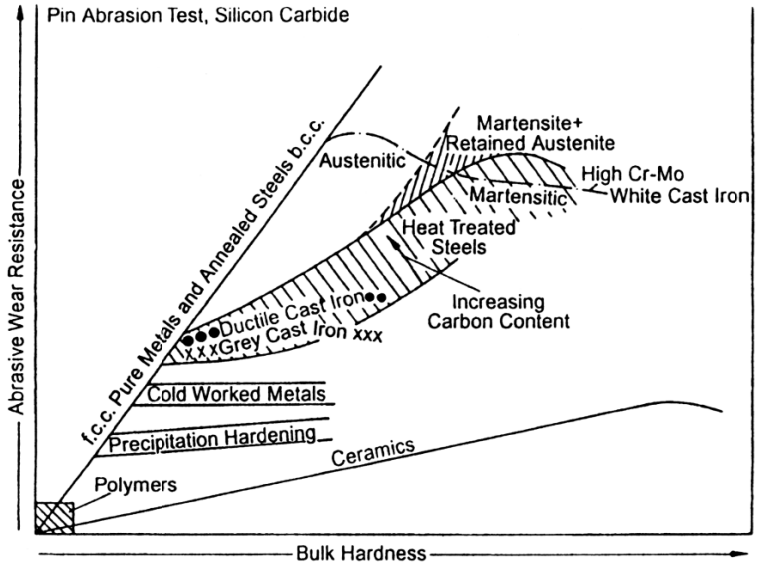


Figure 41 Abrasive wear resistances of the materials in pin abrasion test as a function of hardness (Zum Gahr, 1987)

The formation of martensite and retained austenite in the matrix of iron-based deposit has an effect on the abrasive wear resistance. Temperature changes during the use may change the microstructure, i.e., by lowering retained austenite content and leading to significant volume changes due to the increasing amount of martensite. With equation 40, martensite start temperature, $M_s$, can be estimated. Vanadium content is not included. The equation is valid only within the stated composition limits. Retained austenite contents of the martensitic stainless steel deposits welded by the PTA welding method can be estimated with equations 41 and 42 (Andrews, 1965; Wu *et al*., 2000):

$$M_s\ (^oC) = 273 - 12{,}1 \times Cr\ (\%) - 17{,}7 \times Ni\ (\%) - 7{,}5 \times Mo\ (\%) - 423 \times N\ (\%), \quad (40)$$

$$\gamma\ (\%) = 36{,}412 - M_s\ (^oC) \times 0{,}126, \quad (41)$$

$$\gamma\ (\%) = 2{,}014 + 1{,}525 \times Cr\ (\%) + 2{,}23 \times Ni\ (\%) + 0{,}945 \times Mo\ (\%) + 53{,}298 \times N\ (\%). \quad (42)$$

The matrix of the metastable austenitic FeMn-deposit can contain γ-austenite, Ɛ-martensite, and α'-martensite. Plastic deformation under mechanical load leads to the martensitic phase conversion from γ-austenite to Ɛ-martensite and finally to α'-martensite (Röthig *et al.*, 1997).

Wear resistance of tool steels depends on the matrix hardness, composition, precipitated carbides, the size of carbides, the MFP, and the volume fraction of carbides. In Figure 42 is presented the relative hardness of mixed carbides and martensite. MC and $M_2C$ carbides have high hardness when compared to hardness of cementite, $Fe_3C$, and martensite.

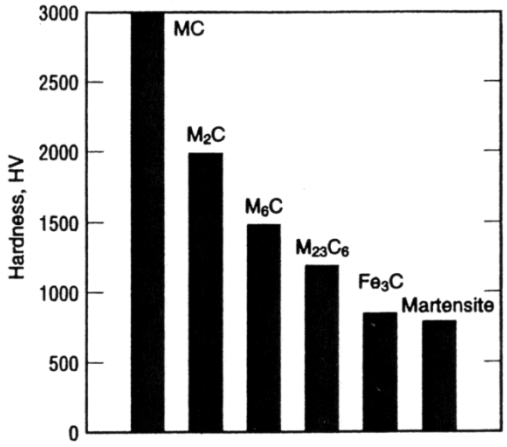


Figure 42 Relative hardness of various carbides, cementite, and martensite (Brandis *et al.*, 1980)

Draugelates *et al*. (1996) found that the microstructure of the deposit SG2 (10MnMo4-5) reinforced with 30 % VC carbides welded by the PTA welding method had VC carbides, the sizes of which were 5-10 µm. Wang *et al*. (2006) measured that the mean size of VC carbides of the LB welded deposit M4 (C 1,45 %, V 3,9 %, Cr 4,5 %, Mo 4,5 %, W 5,8 %, S 0,12 %, and Fe bal.) was 0,6 µm. Tsubouchi *et al*. (1997) reported that original 100 µm NbC carbides partly melted during the PTA welding tests and the size of the precipitated primary carbides was about 1 µm. Thus, as well as abrasive wear, local adhesion can be also prevented by high number of small-sized carbides. The size of the precipitated carbides depends on the alloy as well as welding parameters. Larger carbide volume fraction, coarser carbide morphology, and martensitic matrix are beneficial in improving the abrasive resistance (Chen *et al.*, 1990).

## 3.5 Rubber wheel abrasion test

In Figure 43 the rubber wheel abrasion test, RWAT, apparatus is presented. The apparatus conforms to standard ASTM G 65-94. The RWAT apparatus is suitable for testing low stress three-body abrasive wear. Abrasive size above 100 µm results in relatively constant abrasive wear for various materials (Fang *et al*., 2001; Wang *et al*., 1991). Normal force in the RWAT can be varied between 20-200 N. The rotating speed is normally 200 rpm, total 6000 revolutions.

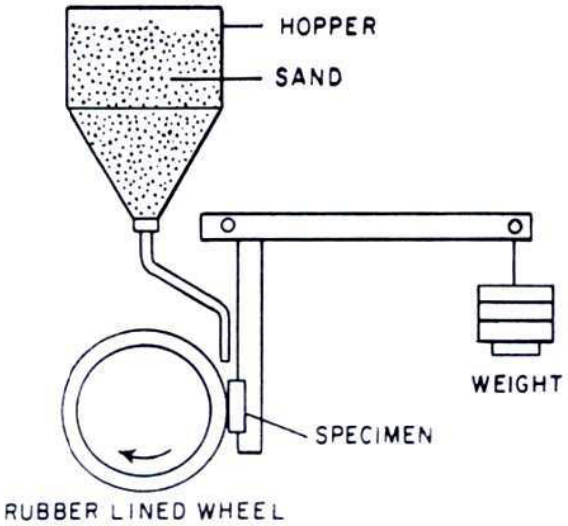


Figure 43 Rubber wheel abrasive wear test apparatus according to standard ASTM G 65-94

The rubber wheel has a major role in the accuracy of the results. A selection of the materials can be used in the rubber wheel. The material, hardness, and surface roughness of the rubber wheel have effects on the wear result. Temperature rise may soften the rubber wheel. Surface roughness of the rubber wheel may enhance the ability of the abrasive to hold on the surface, which are bigger and more angular than particles on average, thus rolling of the abrasive is prevented (Stevenson *et al*., 1996). The other remarkable variables are wheel size, velocity, temperature rise, angularity, abrasive feed rate, humidity, and area of wear scar (Avery, 1981).

The number of abrasive particles in the contact zone can be estimated by equation 43 (Stevenson *et al*., 1996):

$$N_p = \frac{m_{net}\, x_{cl}}{s\, m_p}, \tag{43}$$

where $m_{net}$ is abrasive net mass flow rate past the specimen, $x_{cl}$ is contact length between the rubber wheel and the specimen, s is relative sliding speed, and $m_p$ is mass of an abrasive particle.

Packing fraction, $m_{pf}$, describes the density of the abrasive-layer. Packing fraction of abrasive particles on the track can be estimated by equation 44 (Stevenson *et al*., 1996):

$$m_{pf} = \frac{m_{net}}{s\, d_a\, b_r\, \rho_a}, \tag{44}$$

where $b_r$ is width of the rubber wheel and $\rho_a$ is density of an abrasive particle.

# 4 Objectives of the dissertation

The main research areas in the development of the PTA welding method are the dilution of the deposits, the mechanical tests, the wear and corrosion tests, and the welding parameters which have effects on the dimensions of the weld beads. One of the biggest features of the process is the low dilution and, thus, the properties of the deposit are achieved by one-layer deposit. It is known that plasma arc current has a remarkable effect on the dilution, when the other welding parameters are constant.

The welding parameters depend on the alloy. It is necessary to know the interactions between the welding parameters and the microstructure. When the PTA welding method is used for surfacing 12V tool steel onto the base material, the characteristic phenomenon of the welding process is the large molten pool for obtaining thick deposit by welding only one layer and, thus, problems in the dilution control. Therefore, the microstructure depends on the selected welding parameters.

Firstly, the PTA welding tests were directed to evaluate the effects of the main welding parameters on the dilution control of the 12V tool steel deposit. The welding tests have been welded in seven parameter windows. To find out the effects of the plasma arc with selected parameters on the microstructure, the welding tests were made by varying plasma arc current step by step, while the other welding parameters were kept constant.

Secondly, two welding procedures were tested: the plasma arc in the edge and on the molten pool. The microstructures of the 12V tool steel deposits surfaced with various welding parameters were analyzed after the surfacing process. Ar, Ar + 3 % $H_2$, and Ar + 5 % $H_2$ were used as carrier gas to find out the effect of carrier gas on the dilution control and the microstructure. The volume fractions of VCs, the sizes of VCs, the MFPs, and the retained austenite contents of the deposits were measured. The effect of the location of the plasma arc in relation with the molten pool on the microstructure was analyzed. The wear test was ASTM G 65-94 dry quartz sand rubber wheel abrasion test. The microstructures of the deposits, the welding parameters, and the wear test results were compared to find out the factors affecting most the abrasive wear resistance of the 12V tool steel deposit.

# 5 Experimental

## 5.1 Materials

The powder consumable of this study was 12V-1 tool steel. The fraction was sieved from the powder used for manufacturing the 12V-1 HIP material. The PTA welded deposits were tested in as-welded condition. 15V-1 tool steel was a reference material for the PTA welding parameter tests and the materials manufactured by the HIP method, i.e., 10V, 12V-1, 12V-2, and 15V-2 tool steels were reference materials for the microstructure studies and the wear tests. The materials manufactured by the HIP process were austenized at 1040-1150 ºC, dwell time was 0,5-1 h and finally the materials were double tempered 2 hours at 540-650 ºC (normally 540-570 ºC) for decreasing the retained austenite content. The chemical compositions of the 12V-1 tool steel powder and the reference materials are presented in Table 3. P and S were <0,03 wt.-% for the 12V-1 tool steel powder.

The PTA welded deposits were surfaced onto a carbon steel St 52. The nominal powder fraction of the 12V tool steel powder was 53-150 µm. In this study the vanadium carbide structure was not analyzed. The mass ratio of vanadium to carbon is 1:0,235 for VC (Xu *et al.*, 2007). The melting point of VC is 2648 ºC, density 5,4 g/cm$^3$, and hardness 2900-2940 HV0,2 (Bouaifi *et al.*, 1993; Gebert *et al.*, 2001).

Table 3 Chemical compositions of the 12V-1 and the 15V-1 tool steel powders and the reference materials manufactured by the HIP process [wt.-%]

| | C | Cr | V | Mo | Si | Mn | Fe |
|---|---|---|---|---|---|---|---|
| 10V | 2,4-2,5 | 4,7-5,8 | 9,2-10,3 | 1,1-1,5 | 0,7-1,1 | 0,3-0,6 | Bal. |
| 12V-1 | 2,9 | 5,25 | 11,5 | 1,3 | <1,0 | <1,0 | Bal. |
| 12V-2 | 2,8 | 5,2 | 11,4 | 1,3 | 0,9 | 0,6 | Bal. |
| 15V-1 | 3,4 | 5,0 | 14,5-15,0 | 1,3 | - | - | Bal. |
| 15V-2 | 3,4 | 5,0 | 14,5 | 1,3 | - | - | Bal. |

## 5.2 Welding equipment

The welding tests were welded by the mechanized and the robotized welding units. The mechanized PTA welding unit equipments are presented in Table 4 and the robotized PTA welding unit equipments are presented in Table 5. In Figures 44a-c is presented the mechanized PTA welding unit and the robotized welding unit is presented in Figures 45a-b. The plasma torch was manufactured by Plasma Modules. Normally the plasma torch utilizes only plasma and carrier gas. The prototype external shielding gas torch was manufactured and installed to the plasma torch. The external shielding gas torch is presented in Figure 44c. A sintered bronze-plate was used to ensure laminar flow of

shielding gas. The powder feed was focused at 9 mm distance from the powder nozzle. Constant mass flow rate for plasma gas was arranged by a control unit.

Table 4 The equipments of the mechanized PTA welding unit

| | |
|---|---|
| Plasma torch | Plasma Modules 200 A |
| Powder feed supply | Plasma Modules TCP 101 |
| Pilot power source and process gas control unit | Esab PW 300 B |
| Plasma arc power source | Esab LUA 400 |
| External gas shield | Prototype |
| Conveyor | Esab Railtrack FW 1000 |
| Oscillation mode | Rectangular wave mode |

Table 5 The equipments of the robotized PTA welding unit

| | |
|---|---|
| Robot | Reis Robot SRV6 6 kg |
| Rotating table | RDK05 500 kg |
| PTA unit | Plasma Modules Ion PPAW |
| Plasma torch | Plasma Modules 200 A |
| Plasma gas control unit | Plasma Modules prototype |
| External gas shield | Prototype |
| Power source | Cebora Sound DC 2640 TIG Inverter max. 260 A Cebora Digibox TIG DC3 |
| Oscillation mode | Sine wave mode |

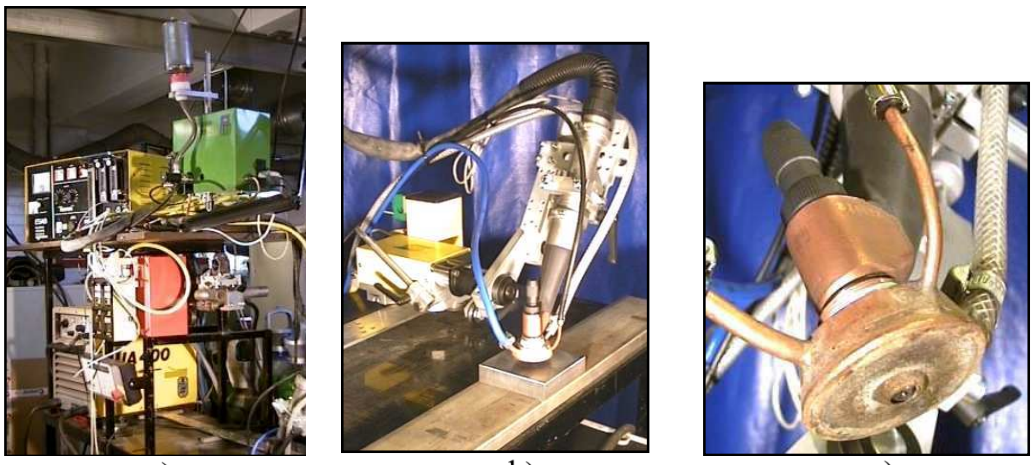

a) b) c)

Figure 44 The mechanized PTA welding unit: a) an overview, b) the conveyor, the plasma torch, and the work piece, and c) the plasma torch, the prototype external gas shielding torch, and the pipes for cooling liquid and shielding gas

a) b)

Figure 45 The robotized PTA welding unit: a) an overview and b) the robot, the rotating table, and an automatic torch change system for the GTA, the MIG/MAG, and the PTA welding torches

## 5.3 Welding experiments

### 5.3.1 Welding parameters

The PTA welding tests were first directed to evaluate the effects of the welding parameters, mainly the effects of plasma arc current, on the dilution control of the 12V-1 tool steel deposit. To find out the effects of plasma arc current with selected parameters on the dilution, welding tests were made by varying plasma arc current step by step, while the other welding parameters were kept constant. The effects of the dilution were determined by the rubber wheel abrasion tests.

The effect of the location of the plasma arc in relation with the molten pool on the microstructure and the abrasive wear resistance was analyzed. The effects of overlapping on the microstructures between the first and the second or the third overlapping weld beads were analyzed. Small variations in welding speed were analyzed. Two welding procedures were tested, i.e., the location of the plasma arc in the edge and on the molten pool. Ar, Ar + 3 % $H_2$, and Ar + 5 % $H_2$ gas were used as carrier gas to find out the effects of hydrogen on the dilution control and the microstructure. The effects of the sine and the rectangular wave oscillation modes on the microstructure were analyzed. The effects of plasma gas flow rate and working distance were analyzed.

The welding tests were welded in seven parameter windows, Tables 6-11. In Tables 6 and 9 are presented constant welding parameters and in Tables 7, 8, and 10 are presented welding parameters which were varied in the tests. In Table 11 are presented welding parameters for the welding test welded with straight passes, i.e., without oscillation movement.

Table 6 Constant welding parameters for the welding tests welded by the mechanized welding unit

| | |
|---|---|
| Shielding gas | Ar 12 l/min |
| Carrier gas | Ar 5 l/min |
| Oscillation wave mode | Rectangular |
| Oscillation width | 25 mm |
| Electrode | ∅ 2,4 mm,<br>1 mm inside the plasma nozzle |
| Pilot arc current | 5 A |
| Work piece /<br>torch alignment | Horizontal /<br>perpendicular to the work piece |

Table 7 Variable welding parameters for the welding tests welded by the mechanized welding unit

| | Parameters A | Parameters B | Parameters C |
|---|---|---|---|
| Plasma gas | Ar 4, 6 l/min | Ar 2 l/min | Ar 2 l/min |
| Powder feed rate | 3,7 kg/h | 2,7 kg/h | 5,0 kg/h |
| Plasma arc current | 120-140 A | 110-140 A | 175 A |
| Plasma nozzle | ∅ 3,0 mm | ∅ 2,7 mm | ∅ 2,7 mm |
| Preheating | RT, 200 °C, 300 °C | RT, 450 °C | RT |
| Overlapping | 24 mm | 24 mm | - |
| Transversal speed | 15 mm/s | 15, 25 mm/s | 15 mm/s |
| Movement in the end of wave | 2,2 mm | 2,1 mm | 2,1 mm |
| Working distance | 8-12 mm | 9 mm | 9 mm |
| Number of beads | 2 | 3 | 1 |
| Location of the plasma arc | On the edge of the molten pool | On the edge of the molten pool | On top of the molten pool |
| Size of the work piece | 200x100x25 mm | 100x100x25 mm | 200x100x25 mm |

Table 8 Welding tests with welding parameters A

| Test [No.] | Working distance [mm] | Plasma gas flow rate [l/min] | Plasma arc current [A] | Preheating temperature [°C] |
|---|---|---|---|---|
| 1 | 8 | 4 | 130 | 200 |
| 2 | 8 | 6 | 140 | 300 |
| 3 | 10 | 4 | 140 | RT |
| 4 | 10 | 6 | 120 | 200 |
| 5 | 12 | 4 | 120 | 300 |
| 6 | 12 | 6 | 130 | RT |

Table 9 Constant welding parameters for the welding tests welded by the robotized welding unit

| | |
|---|---|
| Plasma gas | Ar 2 l/min |
| Oscillation wave mode | Sine |
| Electrode | ∅ 2,4 mm, 1 mm inside the plasma nozzle |
| Plasma nozzle | ∅ 2,7 mm |
| Pilot arc current | 5 A |
| Oscillation width | 6,5 mm |
| Frequency | 1,2 osc./s |
| Working distance | 9 mm |
| Overlapping | 5 mm |
| Size of the work piece | 100x100x25 mm |
| Number of beads | 5 |
| Work piece / torch alignment | Horizontal / perpendicular to the work piece |

Table 10 Variable welding parameters for the welding tests welded by the robotized welding unit

| | Parameters D | Parameters E | Parameters F |
|---|---|---|---|
| Plasma arc current | 73-95, 52-65 A | 45-70 A | 40-65 A |
| Powder feed rate | 0,3-1,5 kg/h | 0,7 kg/h | 0,7 kg/h |
| Preheating | RT, 300 °C | RT | RT |
| Welding speed | 1,35-1,49 mm/s | 1,35 mm/s | 1,35 mm/s |
| Carrier gas | Ar<br>5 l/min | Ar + 3 % $H_2$<br>5 l/min | Ar + 5 % $H_2$<br>5 l/min |
| Shielding gas | Ar 12 l/min | - | - |
| Location of the plasma arc | On the edge / on top of the molten pool | On the edge of the molten pool | On top of the molten pool |

Table 11 Welding parameters G for the welding tests welded with straight passes without oscillation

| | |
|---|---|
| Plasma gas | Ar 2 l/min |
| Plasma arc current | 62 A |
| Pilot arc current | 5 A |
| Powder feed rate | 0,4 kg/h |
| Preheating | RT |
| Welding speed | 2,3 mm/s |
| Overlapping | 2,6 mm |
| Carrier gas | Ar 5 l/min |
| Shielding gas | Ar 12 l/min |
| Electrode | ∅ 2,4 mm, 1 mm inside the plasma nozzle |
| Plasma nozzle | ∅ 2,7 mm |
| Working distance | 9 mm |
| Size of the work piece | 100x100x25 mm |
| Work piece / torch alignment | Horizontal / perpendicular to the work piece |

## 5.4 Experimental methods

### 5.4.1 Powder consumable

The fractions of the new powder and the oversprayed powder were analyzed. The oversprayed powder was collected after the welding tests welded with welding parameters D, plasma arc current 80 A. The powders were analyzed by Beckman Coulter LS Particle Analyzer. The optical method was Fraunhofer.rfd LS 320 Small Volume Module. Run length was 60 s. The fluid was 2-propanol. The measured powder was cut to the fraction 40-200 μm. The surface and a cross-section of a powder particle were investigated by SEM.

### 5.4.2 Temperature of work piece

The temperature of the work piece was measured during the welding test. Welding parameters D were used for the welding test with powder feed rate 0,3 kg/h. The size of the work piece was 200x100x25 mm. In both ends of the work piece was one thermocouple for the temperature measurement. The temperature of the work piece was RT in the beginning of the test.

### 5.4.3 Microstructure

The sections for the metallographic samples were cut mainly from the end of the weld beads in comparison with welding direction. The dimensions of the weld beads were detected from the cross-sections. The samples were prepared by grinding with SiC water abrasive paper (80, 180, 360, 800, 1200, and 2500 grit). The samples were polished with 6 and 1 μm diamond pastes. Etchant for the microstructural investigation contained 120 ml ethanol, 100 ml HCl, 8 g $FeCl_3$, and 7 g $CuCl_2$.

The microstructures were studied by optical microscope and scanning electron microscope with backscattering detector. The volume fractions of VCs, the sizes of VCs, and the MFPs of the tool steel materials were determined from scanning electron microscopy pictures by Imagetool image analysis program. Microstructural changes in a weld bead cross-section welded with welding parameters B were measured from pictures taken by optical microscope. The shape ratios of VCs were measured automatically by ImageJ image analysis program. The shape ratio was estimated from 0 to 1 by measuring randomly each carbide width and height from the SEM picture and comparing the results. The sizes of VCs and the MFPs were measured randomly (100 measurements) from pictures taken from the core of the deposits. The carbide surface fraction corresponds to the carbide volume fraction according to the principle based on the Delesse's principle (Delesse, 1847). The principle is based on the idea that a two-dimensional random area of an object is an estimate of its volume fraction. Standard deviations of the volume fractions of VCs were estimated from the SEM pictures (94x70 μm), the pictures of which were divided into 9 equally sized pictures.

The amount of magnetic martensite phase was measured by Ferritescope MP3C. The apparatus was calibrated with δ-ferrite standard samples. Retained austenite to martensite ratio was measured by the X-ray diffraction method. The results measured from the PTA welded deposits and the materials manufactured by the HIP process by Ferritescope were converted to the martensite contents with correlation factors 1,7 and 1,1, respectively. The correlation factor 1,7 was the same as was measured by Talonen *et al*. (2004) for austenitic steels. The X-ray diffraction apparatus was Stresstech X3000. Test parameters were $CrK_{\alpha}$ radiation, ψ-oscillation ±30º, ferrite 3 times 20 s. and austenite 3 times 60 s.

### 5.4.4 Rubber wheel abrasion test

The abrasive wear resistances of the materials were tested by the dry sand rubber wheel abrasion test. The RWAT apparatus conforms to standard ASTM G 65-94. Procedure A was used to test the materials. The sizes of the samples were 30x60x27 mm. The deposits were on the side, the area of which was 30x60 mm. All samples were ground before testing to 1200 grit. Before the tests and after the tests weights of the samples were measured. After that the weight loss was converted to the volume loss. Density, 7,4 g/cm$^3$, was used in every deposit, even though the dilution from the base material has a small effect on density. The deposits welded by the PTA method were tested in the RWAT once because small variations in the microstructure have remarkable effects on the abrasive wear resistance.

The diameter and the width of the rubber wheel (NR/SBR, 60±5 ShA) were 236 mm and 12,7 mm, respectively. Total sliding distance per sample was 4437 m. Normal force was 126 N. Rotating speed was 200 rpm. Rotating speed 105 rpm was used to test the effect of sliding speed on the wear rate. Abrasive flow rate was approximately 250 g/min for rotating speed 200 rpm and 746 g/min for rotating speed 105 rpm.

Nilsiä quartz sand NFQ 0,1-0,6 was used as an abrasive sand. The sand is not in accordance with the standard. The chemical composition of the sand was $SiO_2$ 99,4 %, $Al_2O_3$ 0,27 %, $K_2O$ 0,06 %, and $Fe_2O_3$ 0,03 %. Specific gravity was 2,65 g/cm$^3$, density 1,4 t/m$^3$, hardness 7 Mohs, pH 5,5, and $D_{50}$ 0,29 mm. The abrasive particle size distribution is presented in Table 12.

Table 12 Distribution of sieve net passing abrasive particles

| Sieve [mm] | Passing [%] |
|---|---|
| 1 | 100 |
| 0,71 | 99,8 |
| 0,5 | 90,6 |
| 0,355 | 67,5 |
| 0,25 | 38,1 |
| 0,18 | 15,8 |
| 0,125 | 5,1 |

Surface roughness of one deposit was measured during the RWAT. The sample was welded with welding parameters B, 130 A, PH. The sample was polished before the test. Surface roughness was measured by Stylus Profilometer.

After the RWAT tests, the worn surfaces of three deposits welded by the PTA method were investigated by SEM. The samples were welded with welding parameters A, C, and D. The wear track of the 12V-1 tool steel reference material manufactured by the HIP process was also studied. The effects of low and high stress levels on the wear tracks were analyzed.

# 6 Results

## 6.1 12V tool steel powder

### 6.1.1 Microstructure

The powder particles were spherically shaped, Figure 46a. Only very minor internal porosity was observed. The mean size of the original carbides detected from a powder particle cross-section was 0,18 µm, Figure 46b. The size of the largest original carbide detected was 0,56 µm. The distribution of the original carbides in a powder particle was relatively homogeneous.

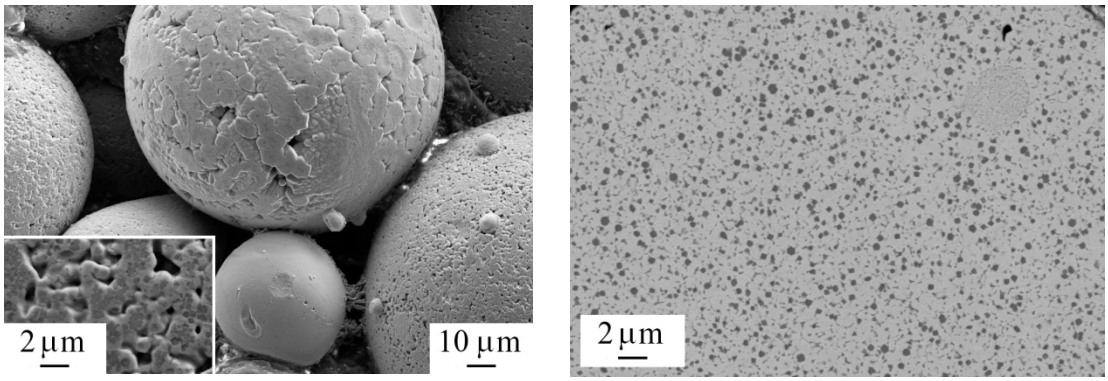


Figure 46 12V-1 tool steel powder particles: a) spherically shaped powder particles and surface of a powder particle and b) microstructure of a powder particle

### 6.1.2 Powder fraction

The powder fractions of the new and the oversprayed powders were analyzed. The oversprayed powder was collected after the welding test with welding parameters D.

The consumable efficiency was 55-65 % for welding parameters D. The consumable efficiency was >95 % in the welding tests welded with welding parameters C.

The results for the new powder were: mean 96,39 µm s.d. 27,94 µm, median 90,75 µm, $d_{10}$ 64,17 µm, $d_{25}$ 73,78 µm, $d_{50}$ 90,75 µm, $d_{75}$ 116,2 µm, $d_{90}$ 138,3 µm, D(3,2) 88,94 µm, mode 80,07 µm, skewness 0,608 right skewed, and kurtosis −0,468 platykurtic.

The results for the oversprayed powder were: mean 103,9 µm s.d. 27,43 µm, median 101,7 µm, $d_{10}$ 69,16 µm, $d_{25}$ 81,95 µm, $d_{50}$ 101,7 µm, $d_{75}$ 123,9 µm, $d_{90}$ 142,8 µm, D(3,2) 96,68 µm, mode 116,3 µm, skewness 0,323 right skewed, and kurtosis −0,642 platykurtic.

In Figures 47 and 48 are presented the differential and the cumulative volumes of the new and the oversprayed powders. The powder fraction was bigger in the oversprayed powder because the plasma arc had bigger ability to melt the powder particles, the fraction of which was 50-100 µm.

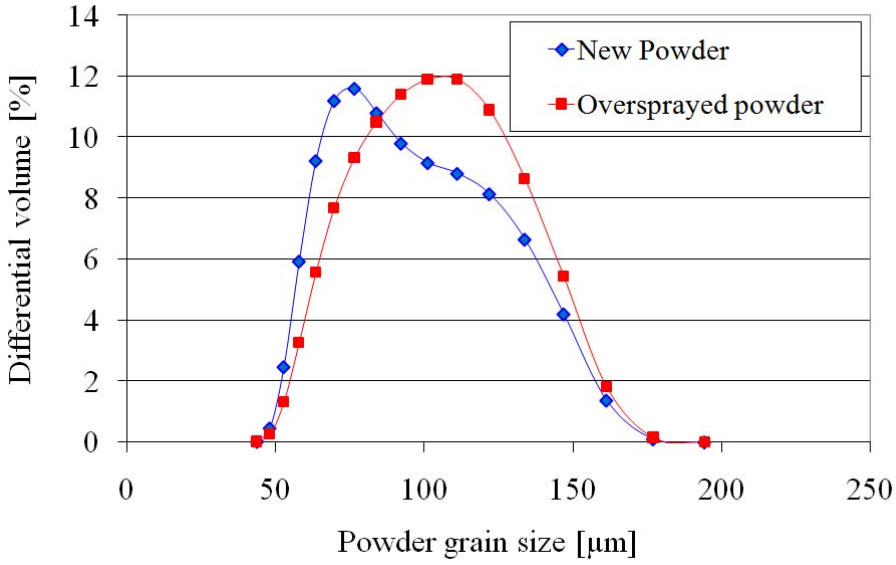


Figure 47 Differential volumes of the new and the oversprayed 12V-1 tool steel powders

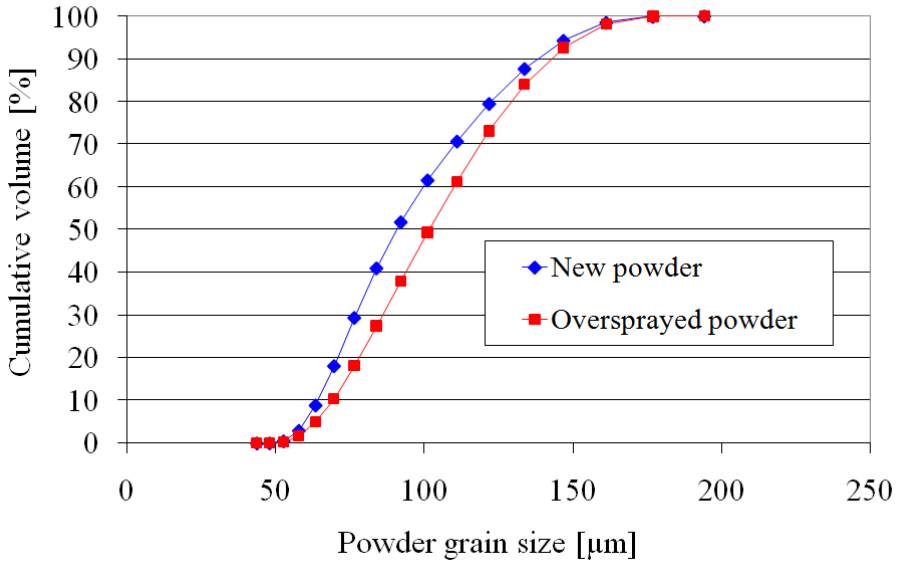


Figure 48 Cumulative volumes of the new and the oversprayed 12V-1 tool steel powders

## 6.2 Temperature of work piece during the welding process

The temperature of the work piece increased during the welding process from RT to 250 °C. Welding parameters D was used for the welding test. Plasma arc current was reduced during the welding process. In Figure 49 are presented temperatures of the work piece measured from two points locating in the both ends of the work piece. Plasma arc currents and dimensions of the deposit cross-section are presented in Table 13. The biggest difference in the temperature of the work piece was measured after the first weld bead was welded. Temperature rose from RT to 110 °C. After the twelfth weld bead was welded, temperature rose was from 245 to 250 °C, i.e. 5 °C.

Plasma arc current was first 74 A and finally it was 58 A. The biggest alteration was between the first and the second weld beads, from 74 to 64 A. The trend of lowering plasma arc current during the surfacing process, when the dilution had to stay constant, was similar as in the welding tests made by Nefedov *et al*. (1995). The mean dilution of the weld beads was 11,1 %. Because of the distortion it was difficult to measure the exact dilution. The fusion line was not straight. Therefore, the dilutions of the weld beads were slightly overestimated.

The maximum and the minimum thicknesses of the weld beads were 1,6 and 1,0 mm, respectively. The maximum penetration was 0,5 mm. In the overlapping areas lack of penetration was obtained. The highest bead was the first bead. Thickness of the deposit mainly decreased when the welding process proceeded.

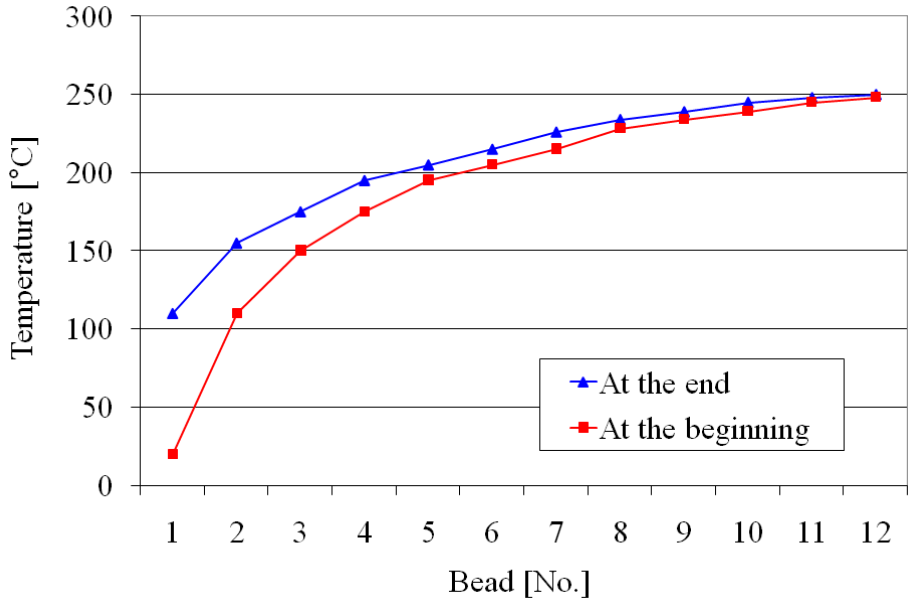


Figure 49 Temperatures of the work piece during the welding test welded with welding parameters D

Table 13 Temperatures of the work piece, plasma arc currents, and dimensions of the deposit cross-section welded with welding parameters D

| Bead number | 1 | 2 | 3 | 4 | 5 | 6 | 7 | 8 | 9 | 10 | 11 | 12 | Mean | S.d. |
|---|---|---|---|---|---|---|---|---|---|---|---|---|---|---|
| Temp. at the beginning [°C] | 20 | 110 | 150 | 175 | 195 | 205 | 215 | 228 | 234 | 239 | 245 | 248 | 188,7 | 64,6 |
| Temp. at the end [°C] | 110 | 155 | 175 | 195 | 205 | 215 | 226 | 234 | 239 | 245 | 248 | 250 | 208,1 | 41,3 |
| Plasma arc current [A] | 74 | 64 | 64 | 60 | 60 | 60 | 60 | 58 | 58 | 58 | 58 | 58 | 61,0 | 4,4 |
| Dilution [%] | 14,0 | 13,8 | 11,5 | 9,5 | 9,7 | 9,5 | 12,0 | 14,1 | 9,5 | 9,7 | 8,4 | 10,9 | 11,1 | 1,9 |
| Thickness max. [mm] | 1,6 | 1,4 | 1,3 | 1,4 | 1,4 | 1,3 | 1,4 | 1,3 | 1,4 | 1,4 | 1,4 | 1,3 | 1,4 | 0,1 |
| Thickness min. [mm] | 1,3 | 1,1 | 1,2 | 1,2 | 1,2 | 1,1 | 1,2 | 1,0 | 1,2 | 1,2 | 1,1 | 1,2 | 1,2 | 0,1 |
| Penetration max. [mm] | 0,5 | 0,5 | 0,3 | 0,3 | 0,3 | 0,3 | 0,3 | 0,4 | 0,3 | 0,3 | 0,2 | 0,2 | 0,32 | 0,08 |
| Penetration min. [mm] | 0 | 0 | 0 | 0 | 0 | 0 | 0 | 0 | 0 | 0 | 0 | 0 | 0 | 0,0 |
| Bead width [mm] | 6,7 | 5 | 5 | 5 | 5 | 5 | 5 | 5 | 5 | 5 | 5 | 6,7 | 5,3 | 0,6 |

## 6.3 Dilution

### 6.3.1 Welding parameters A

In the welding tests welded with welding parameters A, plasma arc current, plasma gas flow rate, working distance, and preheating temperature were varied. In Figure 50 is presented a cross-section of a deposit welded with welding parameters A, test 4. In Table 14 are presented dilutions and thicknesses of the weld beads.

The dilutions of the deposits 1 and 6 increased slightly during the welding tests when comparing the dilutions of the weld beads 1 and 2. The dilutions of the other deposits

decreased during the welding tests. In every deposit the bead thickness was higher in the second bead, because powder feed rate was constant and the overlapping distance was smaller than the widths of the weld beads.

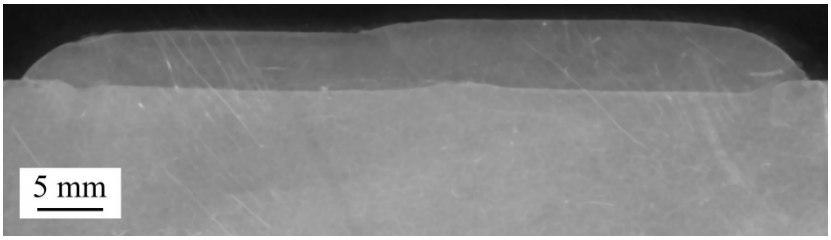


Figure 50 Cross-section of a deposit welded with welding parameters A, test 4

Table 14 Dilutions and thicknesses of the weld beads welded with welding parameters A

| Welding Test [No.] | Dilution Bead 1 / 2 [%] | Dilution Beads 1 and 2 [%] | Thickness Bead 1 / 2 [mm] |
|---|---|---|---|
| 1 | 18,7 / 19,0 | 18,9 | 3,3 / 3,8 |
| 2 | 26,3 / 12,7 | 19,2 | 3,8 / 4,3 |
| 3 | 17,8 / 15,6 | 16,3 | 3,9 / 4,3 |
| 4 | 16,3 / 11,8 | 13,9 | 3,6 / 4,4 |
| 5 | 11,9 / 7,2 | 9,5 | 4,0 / 4,3 |
| 6 | 5,9 / 6,0 | 6,0 | 4,1 / 4,7 |

### 6.3.2 Welding parameters B

The work pieces were preheated to 570 ºC. During the surfacing process temperatures of the work pieces decreased to 370-450 ºC. Because of the mechanized welding unit, the displacement of the plasma torch took time.

The dilution increased on average 7 % when plasma arc current increased 10 A. The same dilution was obtained without preheating with 28 A higher plasma arc current. In Figures 51 and 52 are presented a cross-sectional and a welding directional sample. In Table 15 are presented dilutions and thicknesses of the weld beads. The dilution increased non-linearly. In the deposits welded with plasma arc currents 130 and 140 A the dilutions of the first beads were higher than that of the dilutions in the third beads.

The thickness of the deposit was on average 2,9 mm. The thicknesses of the second and the third weld beads were higher when compared to the thicknesses of the first weld beads. It is also obvious that the size of the molten pool was the largest in the third bead as can be seen from Figure 51. Thus, the molten pool may restrict the penetration of the plasma arc, especially, when the size of the molten pool increases due to dilution from the base material.

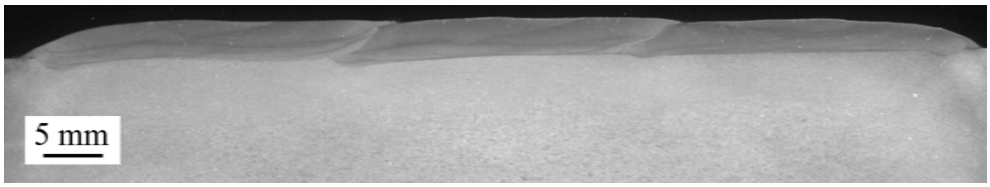


Figure 51 Cross-section of a sample welded with welding parameters B, plasma arc current 120 A

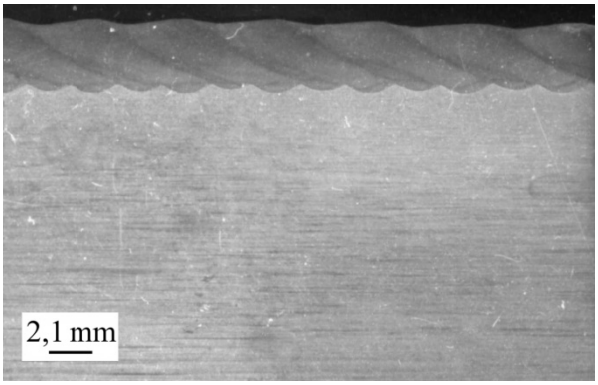


Figure 52 A sample cut in the welding direction from Figure 51, the second bead

Table 15 Dilutions and thicknesses of the weld beads welded with welding parameters B

| Plasma arc current [A] | Dilution Bead 1 / 3 [%] | Dilution Beads 1-3 [%] | Thickness Bead 1 / 3 [mm] |
|---|---|---|---|
| 110 A | 5,1 / 5,1 | 5,1 | 2,6 / 2,8 |
| 120 A | 7,9 / 12,9 | 11,3 | 2,9 / 3,0 |
| 130 A | 22,0 / 10,6 | 15,5 | 2,9 / 2,9 |
| 140 A | 26,5 / 24,5 | 25,3 | 2,7 / 3,1 |

### 6.3.3 Welding parameters C

The dilution of the deposit welded with welding parameters C was small, because the location of the plasma arc was on the molten pool. The thickness of the weld bead was 5,5 mm. Thus, even though plasma arc current was 175 A, the plasma arc was not able to form enough penetration.

In Table 16 is presented dimensions of the deposit welded with welding parameters C. In Figure 53 is presented a cross-section of a deposit welded with welding parameters C. In Figure 54 is presented welding defects in the fusion line. Lack of fusion was obtained occasionally in the fusion lines of the deposits welded with welding parameters C.

The size of the molten pool was relatively small. Thus, the molten pool was not flowing to the sides of the weld bead. Some oxides were formed on the surface of the deposit.

Table 16 Dimensions of the weld bead welded with welding parameters C

| Dilution [%] | Penetration max. [mm] | Penetration min. [mm] | Thickness [mm] |
|---|---|---|---|
| 0,5 | 0,2 | 0,0 | 5,5 |

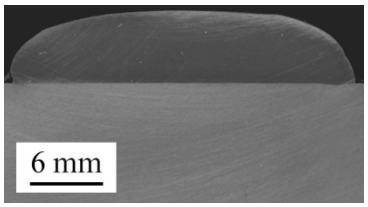


Figure 53 Cross-section of a sample welded with welding parameters C

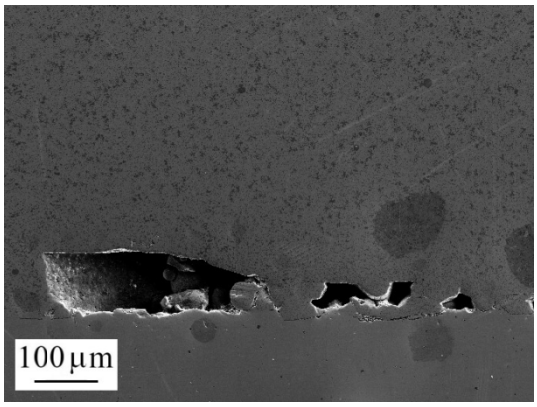


Figure 54 Welding defects in the fusion line of a deposit welded with welding parameters C

### 6.3.4 Welding parameters D-G

In Figures 55-57 are presented cross-sections of the deposits welded with welding parameters D, F, and G. In Figure 58 are presented dilutions of the deposits welded with welding parameters D-G as a function of plasma arc current. Ar-$H_2$ gas mixtures (97/3) and (95/5) were used as carrier gas for the welding tests welded with welding parameters E and F, respectively. The other welding parameters were kept constant except plasma arc current. The location of the plasma arc was set to the edge of the molten pool for the deposits welded with Ar as plasma, carrier, and shielding gas (welding parameters D). The dilution was then optimal. Thereby adjusted welding speed, 1,35 mm/s, was used also for the welding tests welded with welding parameters E and F.

The dilution increased approximately 2,5 and 6,5-8,0 % per 10 A increase in plasma arc current in the deposits welded with welding parameters F and D-E, respectively. The

dilution was easy to control when Ar + 5 % $H_2$ was used as carrier gas. Some welding defects were found occasionally from the fusion lines, when argon + 5 % hydrogen gas mixture was used as carrier gas, Figure 56.

Thicknesses of the deposits were between 2,2-2,9 mm, because of varying consumable efficiency. Small amount of hydrogen has an effect on the melting efficiency. Plasma arc current was reduced for argon-hydrogen gas mixtures. Thus, the consumable efficiency was lower when compared to the deposits welded with Ar as process gas.

The weld bead welded with welding parameters D, 65 A, PH, 5,0 mm had 0,5 % dilution. Heat input was low. The location of the plasma arc was slightly on the molten pool. Thus, penetration was not formed. Lack of fusion was obtained from the fusion line.

One deposit was welded with welding parameters G as a reference for the microstructure studies, Figure 57. The dilution and the thickness of the deposit were 5,0 % and 1,2 mm, respectively.

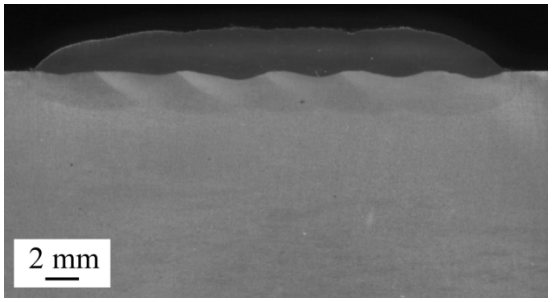


Figure 55 Cross-section of the deposit welded with welding parameters D

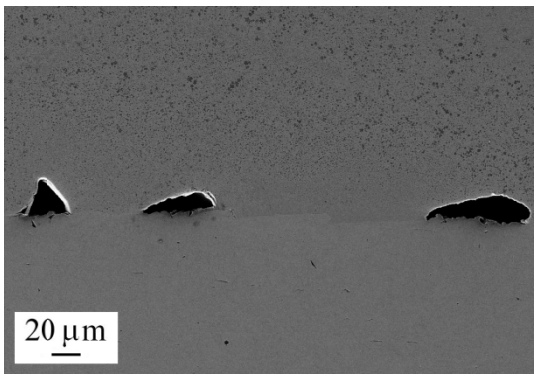


Figure 56 Welding defects in the fusion line of the deposit welded with welding parameters F, plasma arc current 38 A

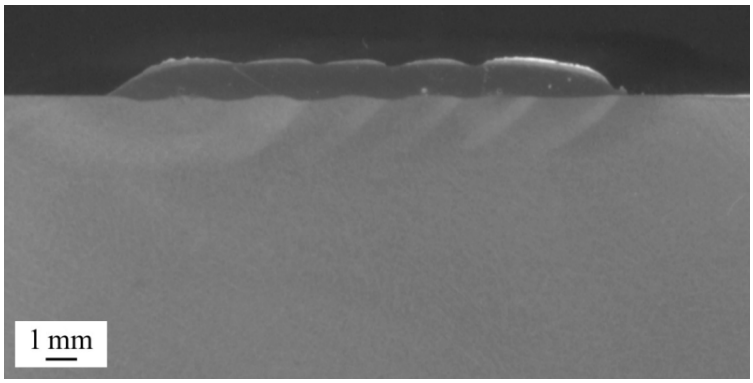


Figure 57 Cross-section of the deposit welded with welding parameters G

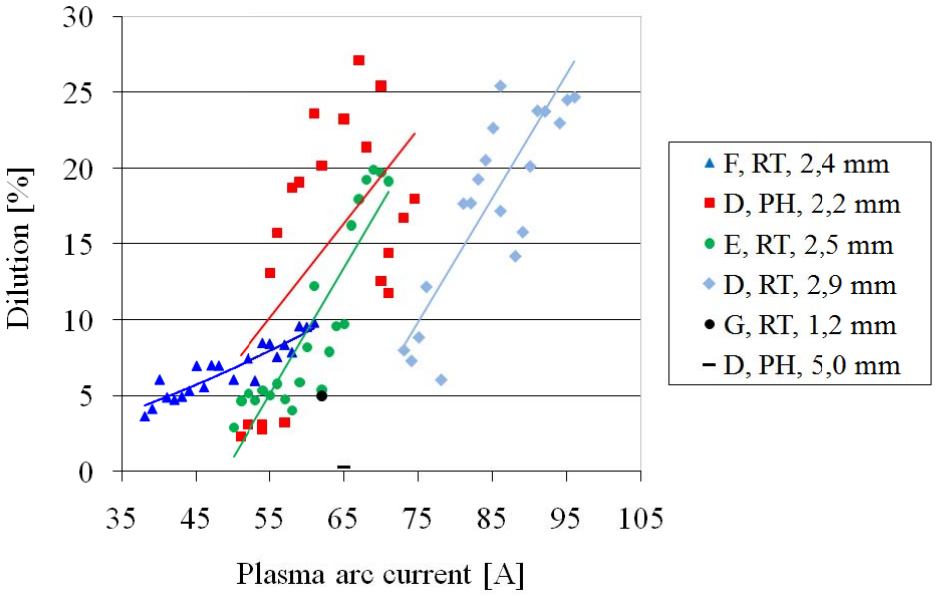


Figure 58 Dilutions of the 12V-1 tool steel deposits welded with welding parameters D-G as a function of plasma arc current

### 6.3.5 Hardness

The effect of the dilution on hardness is presented in Figure 59. Hardness of the 12V-1 tool steel deposit decreases when the dilution of the deposit increases. Because of high amount of welding parameters it is not possible to estimate an accurate relationship between the dilution and the hardness. Hardness of the 12V-1 tool steel deposit depends on the volume fraction of VCs, the size of VCs, the MFPs, and the matrix phases. The microstructure depends on the welding parameters.

A major part of the dilutions of the deposits were between 5 and 10 %. Hardness of the 12V-1 tool steel deposit decreases approximately –15 HV10, when the dilution of the deposit increases 8 %. Depending on the welding parameters, hardness of the 5 %

diluted deposit may vary between 780 and 880 HV10. Thus, hardness of the 12V-1 tool steel deposit is not an accurate estimate about the properties of the deposit.

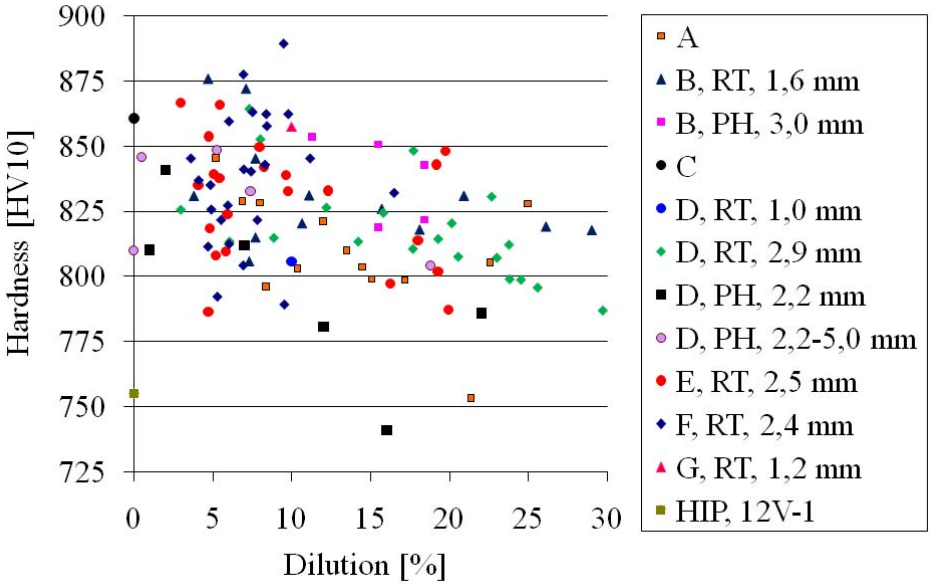


Figure 59 Effect of dilution on hardness of the 12V-1 tool steel materials manufactured by the PTA and the HIP processes

## 6.4 Hardness distribution

In Figures 60, 61, and 62 are presented hardness profiles of the deposits welded with welding parameters A-C and D-G. Hardness of the deposits was basically in the same level from the fusion lines to the top surfaces of the deposits. Hardness varies depending on whether the indenter hits on the carbide cluster or not. Also the microstructure has an effect on the results. The biggest variation was in the PTA welded 15V-1 two-layer deposit, the microstructure of which contains larger areas of VC clusters and also large areas of retained austenite.

The hardness distribution varies depending on from which bead it was measured. From Figure 62 it can be seen that hardness of the beads varies in a way which cannot be estimated. The weld beads 1, 2, 5, and 12 were measured and every bead had different kind of hardness distribution. The last twelfth bead had the biggest hardness 810 HV1 on average and the first bead had the lowest hardness 760 HV1 on average. Although the deposit was welded with the robotized welding unit and only plasma arc current was varied the microstructure shows small variations. The temperature of the work piece increased from RT to 250 °C, when the welding process proceeded from the first bead to the twelfth bead. Thus, small variations in the carbide content, the carbide morphology, the volume fraction of VCs, the size of VCs, the MFP, and in the ratio of austenite and martensite occur.

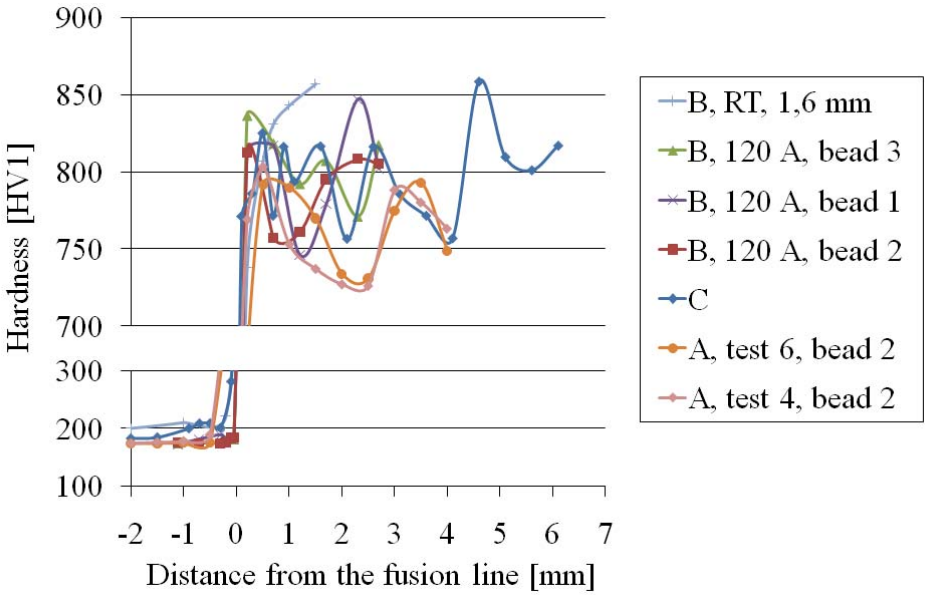


Figure 60 Hardness profiles of the 12V-1 tool steel deposits welded with welding parameters A-C

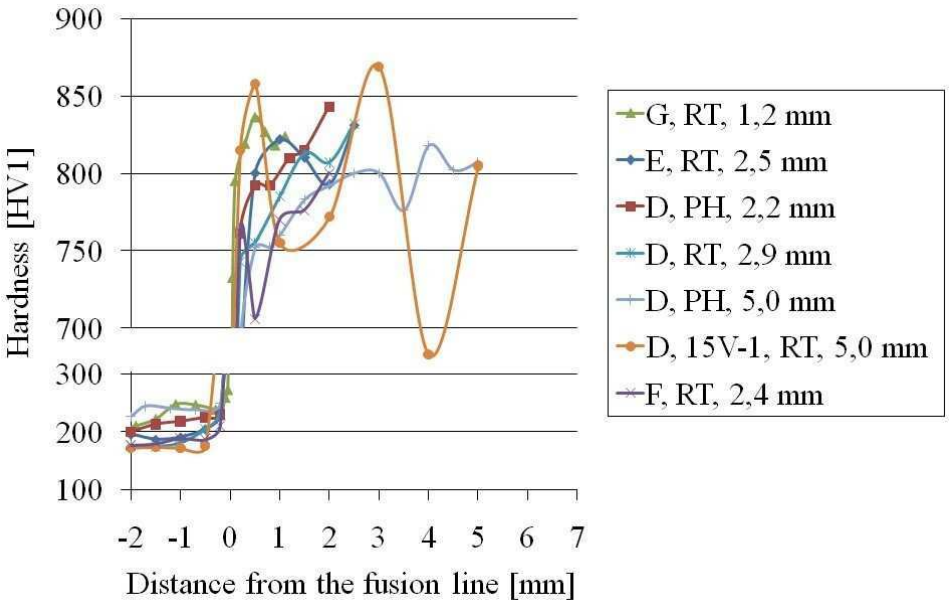


Figure 61 Hardness profiles of the tool steel deposits welded with welding parameters D-G

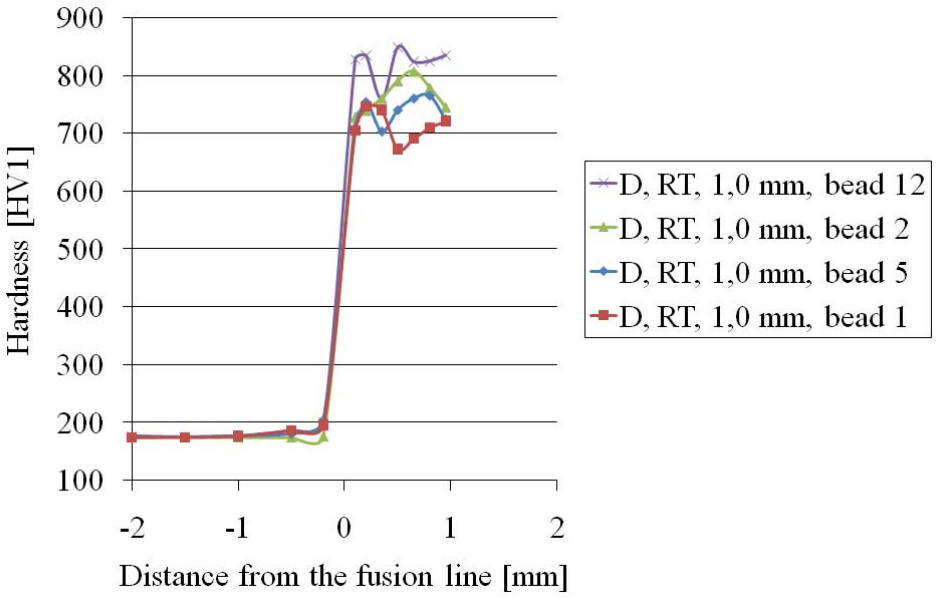


Figure 62 Hardness profiles of the weld beads 1, 2, 5, and 12 of the 1,0 mm thick 12V-1 tool steel deposit welded with welding parameters D

## 6.5 Optical metallography

### 6.5.1 Microstructure

In Figures 63a-l are presented the microstructures of the deposits welded with welding parameters A-G. In Figures 64a-d are presented the microstructures of the tool steel materials manufactured by the HIP process. Some pores can be seen in the microstructures of the materials manufactured by the HIP process.

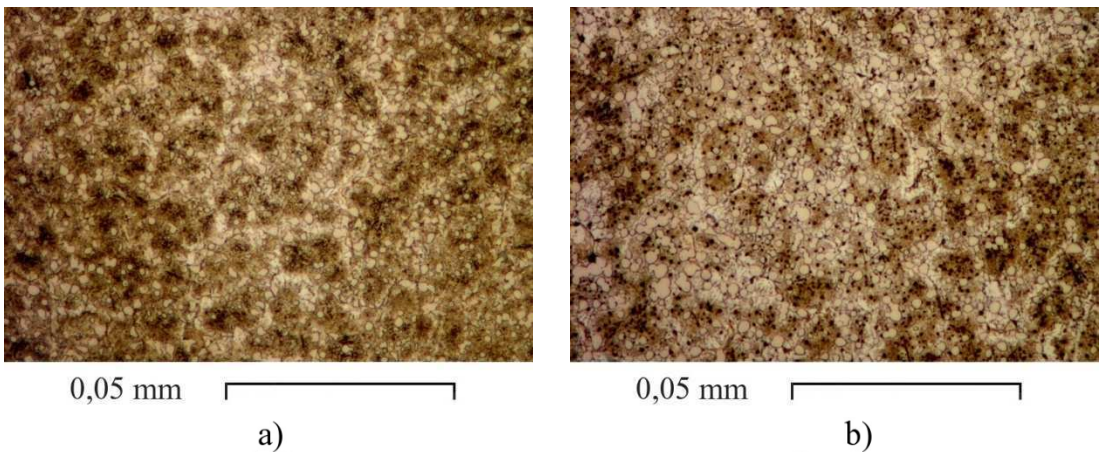

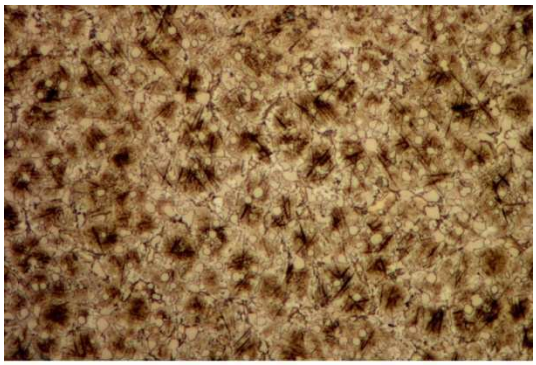

0,05 mm

c)

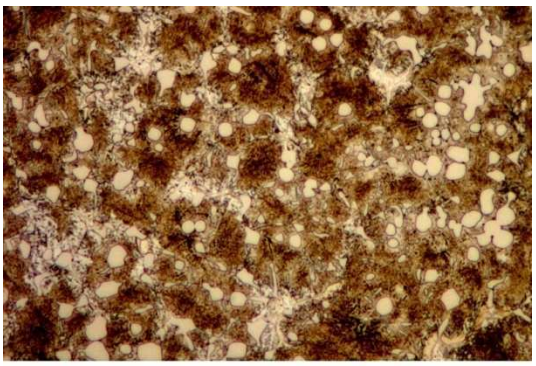

0,05 mm

d)

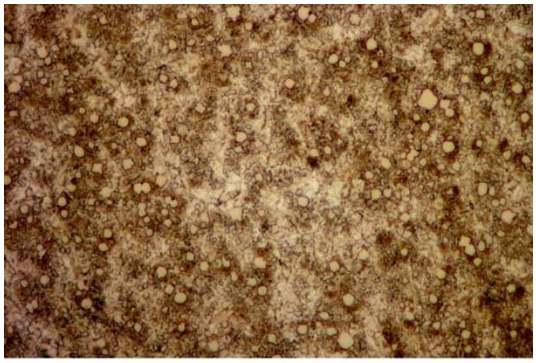

0,05 mm

e)

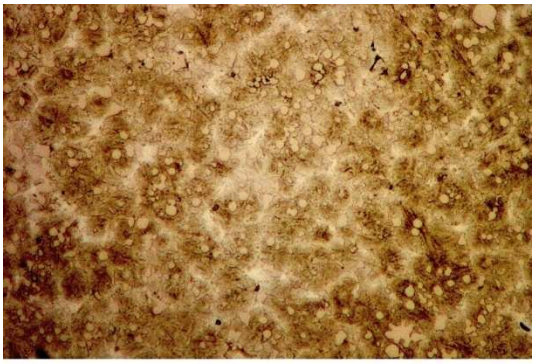

0,05 mm

f)

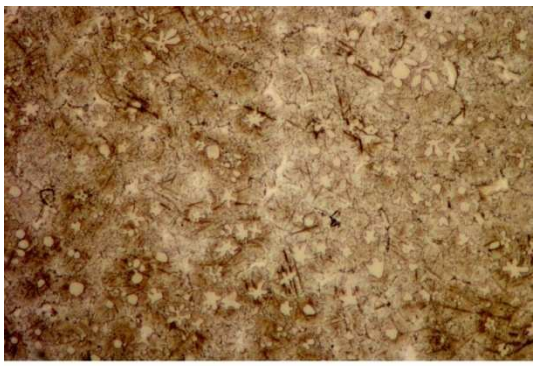

0,05 mm

g)

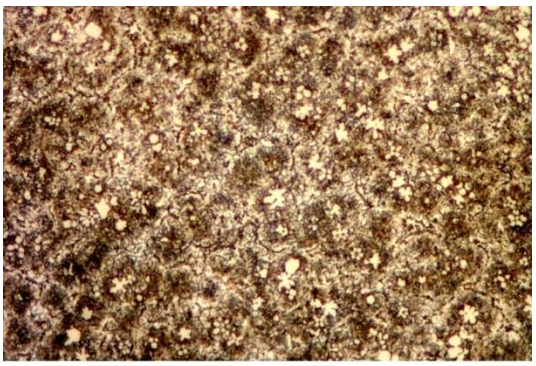

0,05 mm

h)

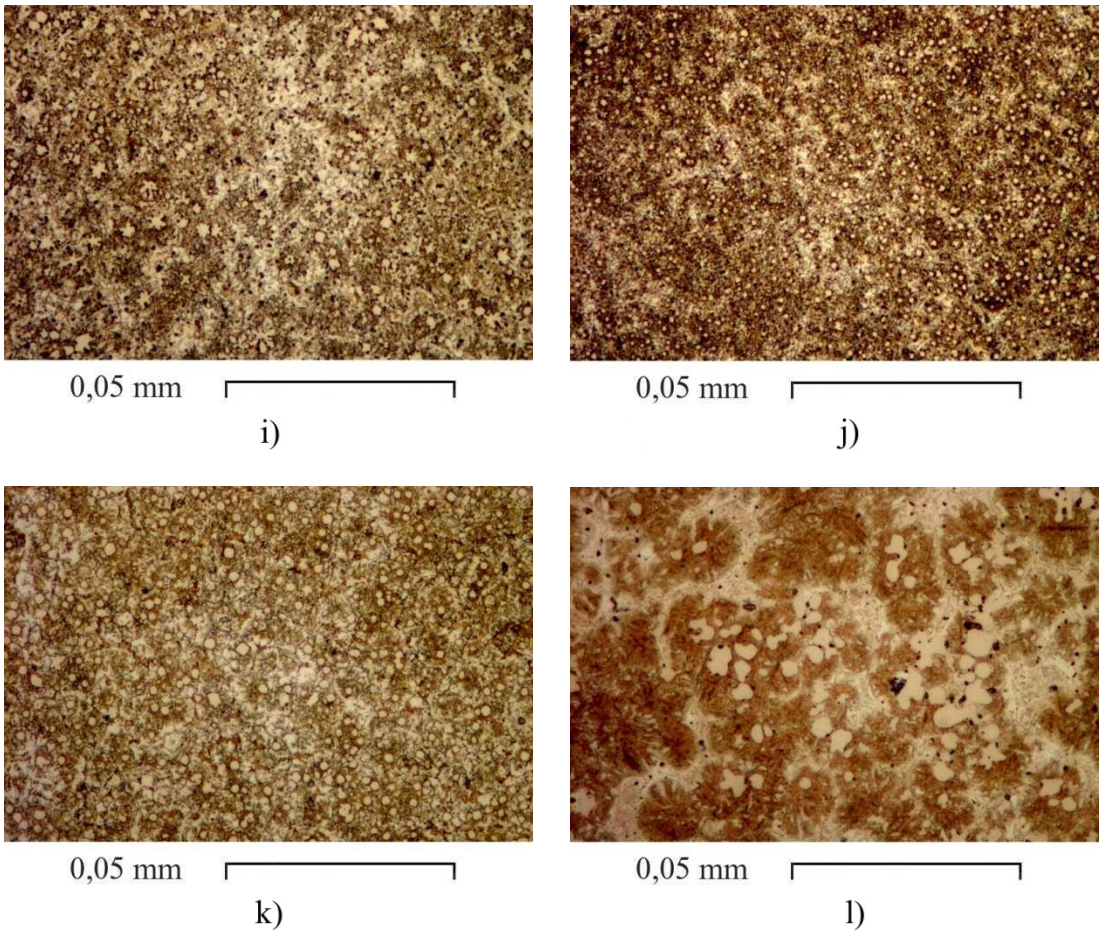


Figure 63 Microstructures of the tool steel deposits welded with welding parameters A-G: a) A, test 4, bead 2, b) A, test 6, bead 2, c) B, 120 A, bead 1, d) C, e) D, RT, 2,9 mm, f) D, PH, 5,0 mm, g) D, PH, 2,2 mm, h) E, RT, 2,5 mm, i) F, RT, 2,4 mm, j) D, RT, 1,0 mm, k) G, RT, 1,2 mm, and l) D, 15V-1, RT, 2,9 mm

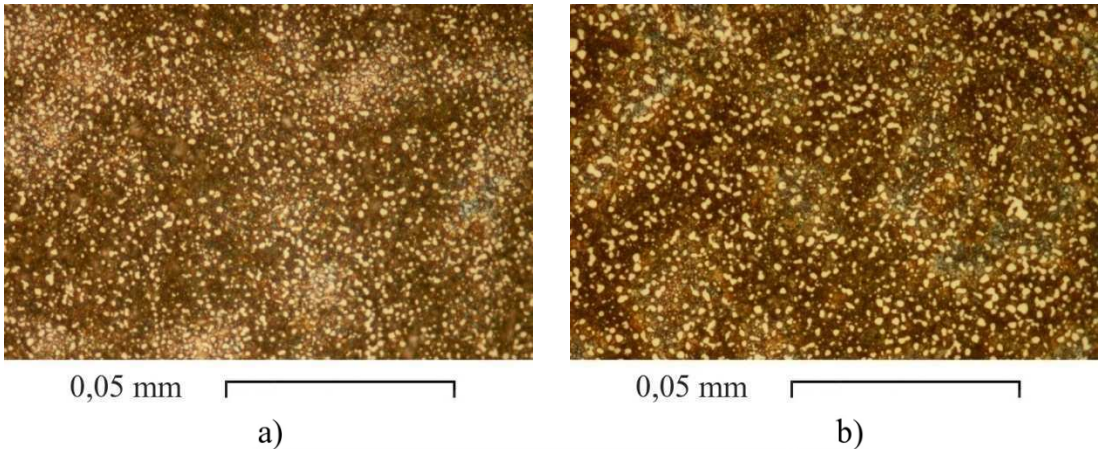

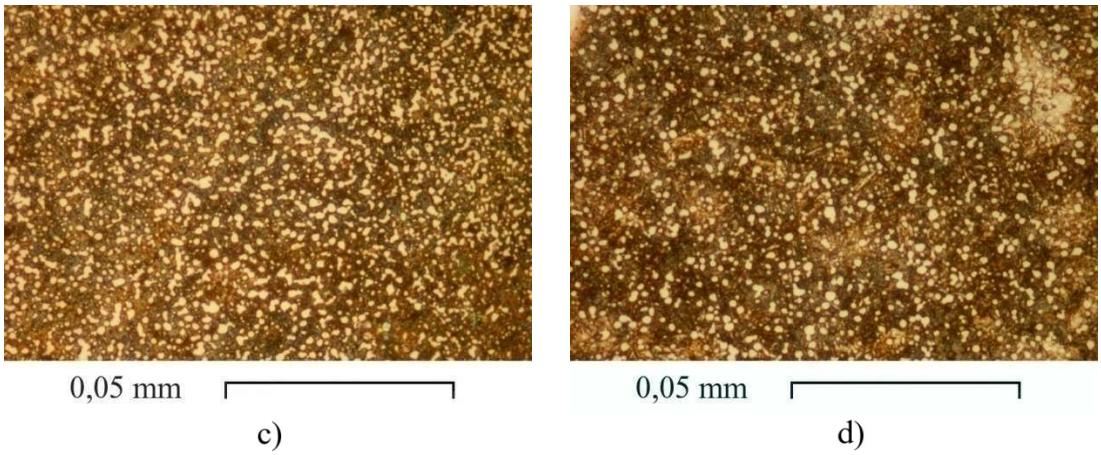


Figure 64 Microstructures of the tool steel materials manufactured by the HIP process: a) 12V-1, b) 12V-2, c) 15V-2, and d) 10V

### 6.5.2 Microstructural changes in weld bead cross-section

In a cross-section of a 12V-1 tool steel deposit welded with welding parameters B, the measurements were conducted from the fusion line to the top surface of the deposit. The dilution was 16 %. The thickness of the weld bead was 3,3 mm. The volume fraction, the mean size, and the MFP of VCs from the fusion line to the top surface are presented in Figures 65-67.

The volume fraction of VCs was different nearby the fusion line, in the core, and at the top surface. Nearby the fusion line the volume fraction of VCs was approximately 3 vol.-% lower when compared to the core of the bead. The volume fraction and the mean size of VCs increase, when the distance from the fusion line increases. The volume fraction of VCs and the MFP were constant in the core of the deposit. The effect of the dilution was the highest at 0,5 mm distance from the fusion line. The minimum and the maximum penetrations were 0,2 and 1,3 mm, respectively. Therefore, low volume fraction and small-sized carbides can be found from the area, which has been originally the base material.

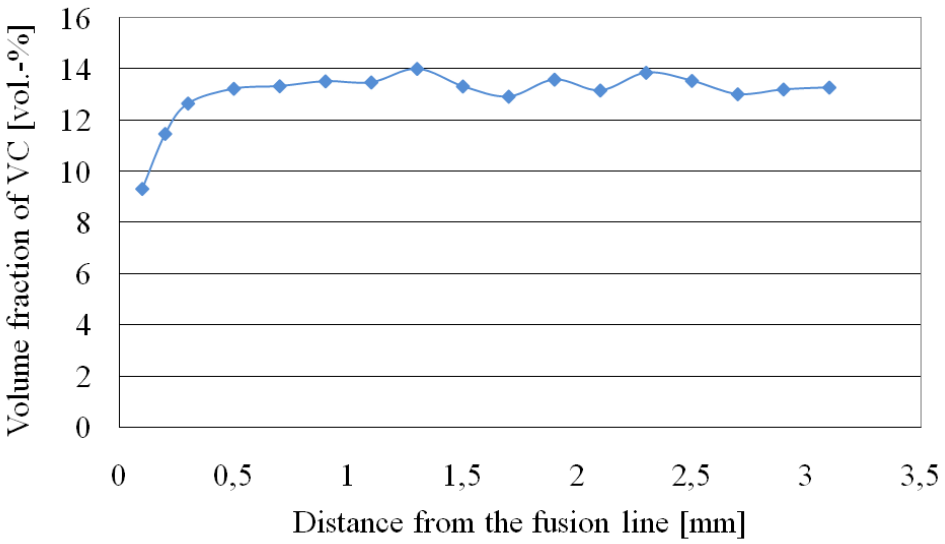


Figure 65 Volume fraction of VCs as a function of distance from the fusion line

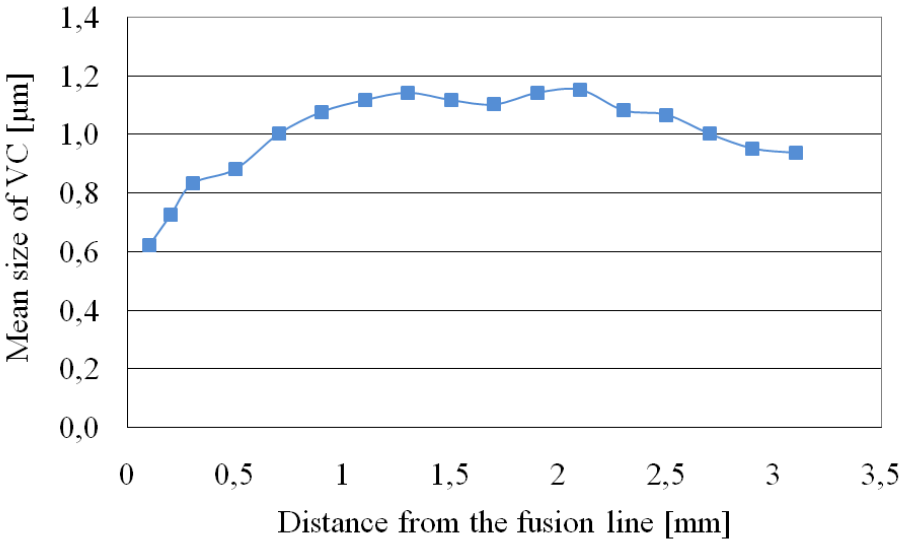


Figure 66 Mean size of VCs as a function of distance from the fusion line

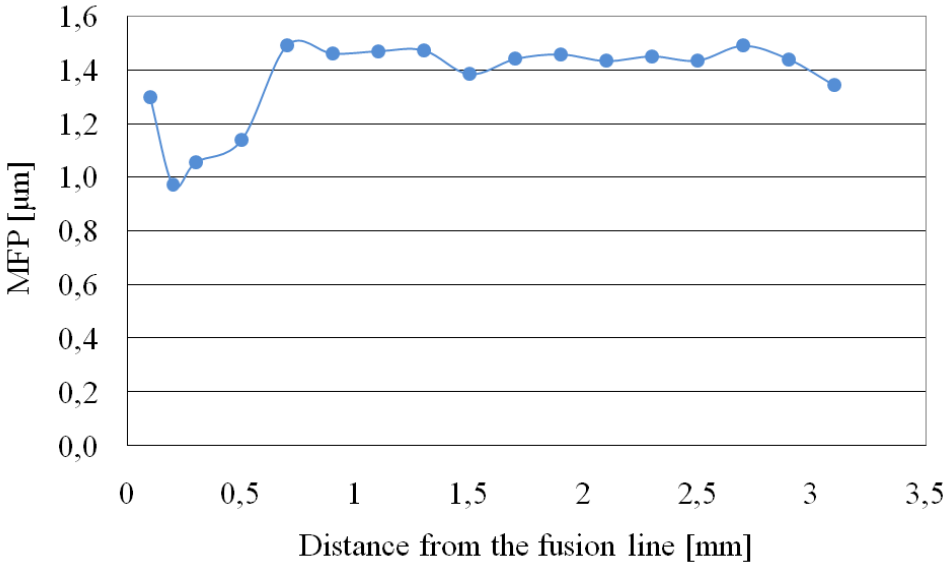


Figure 67 MFP as a function of distance from the fusion line

## 6.6 Scanning electron microscopy

### 6.6.1 Welding parameters A-C

In Figures 68a-g are presented the microstructures of the 12V-1 tool steel deposits welded with welding parameters A-C. In Table 17 are presented the volume fractions, the mean sizes, and the MFPs of VCs. In Figures 69 and 70 are presented the cumulative volumes of the sizes and the MFPs of VCs measured from Figures 68a-g. The sizes of VCs were below 5-10 µm for similar kinds of tool steel alloys according to Teupke (2002).

In Figures 68a, b and 68c, d are presented the microstructures of the deposits welded with welding parameters A. The microstructures are relatively homogeneous and most of the VCs are round-shaped. The microstructures contain 20-40 % of carbides, the sizes of which are less than 1 µm, Figure 69.

In Figure 68e is presented the microstructure of the deposit welded with welding parameters B, 120 A. Transversal welding speed was 15 mm/s. When the microstructure presented in Figure 68e is compared to the microstructures presented in Figures 68a-d, the VCs are more needle-shaped. The microstructure of the deposit welded with welding parameters B, 120 A contains 70 % of carbides, the sizes of which are less than 1 µm, Figure 69.

In Figure 68f is presented the microstructure of the deposit welded with welding parameters B, transversal welding speed 25 mm/s. The microstructure contains only 3

% of carbides, the sizes of which are above 1,5 µm. In the deposit B, 120 A, 15 mm/s the microstructure contains 20 % of carbides, the sizes of which are above 1,5 µm.

In Figure 68g is presented the microstructure of the deposit welded with welding parameters C. The microstructure contains larger round-shaped carbides and smaller needle-shaped carbides. The microstructure is not homogeneous. The volume fraction of VCs is relatively high, 17,5 vol.-%. The plasma arc was on the molten pool.

Table 17 Volume fractions, mean sizes, and MFPs of VCs of the deposits welded with welding parameters A-C

| Material | Volume fraction [vol.-%] | Mean size / s.d. [µm] | MFP / s.d. [µm] |
|---|---|---|---|
| A, test 4, bead 2 | 15,5 | 1,2 / 0,5 | 1,4 / 0,8 |
| A, test 6, bead 2 | 15,7 | 1,4 / 0,5 | 1,5 / 1,0 |
| B, 120 A, bead 1 | 13,4 | 1,0 / 0,5 | 1,4 / 0,8 |
| B, RT, 1,6 mm | 12,2 | 0,8 / 0,3 | 1,4 / 0,9 |
| C | 17,5 | 1,8 / 1,0 | 2,2 / 1,3 |

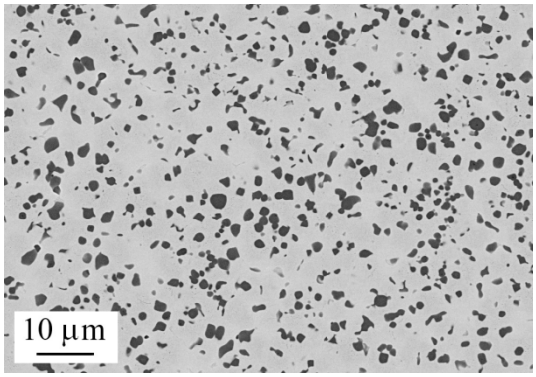


a)

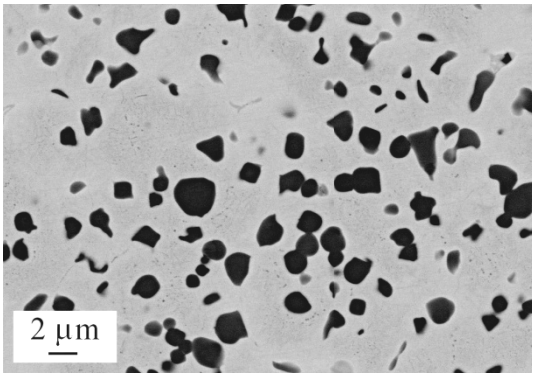


b)

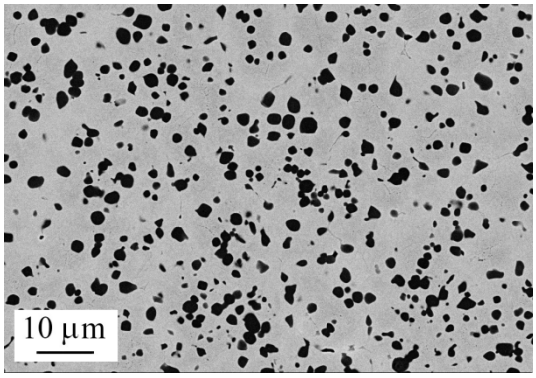


c)

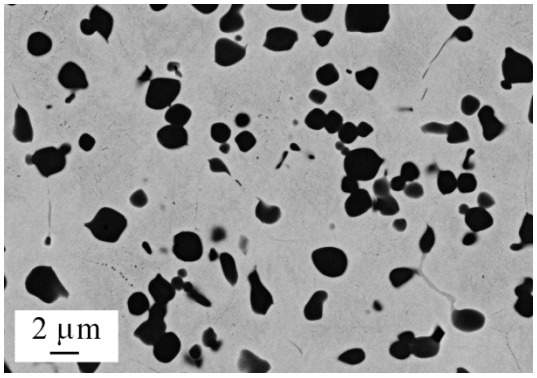


d)

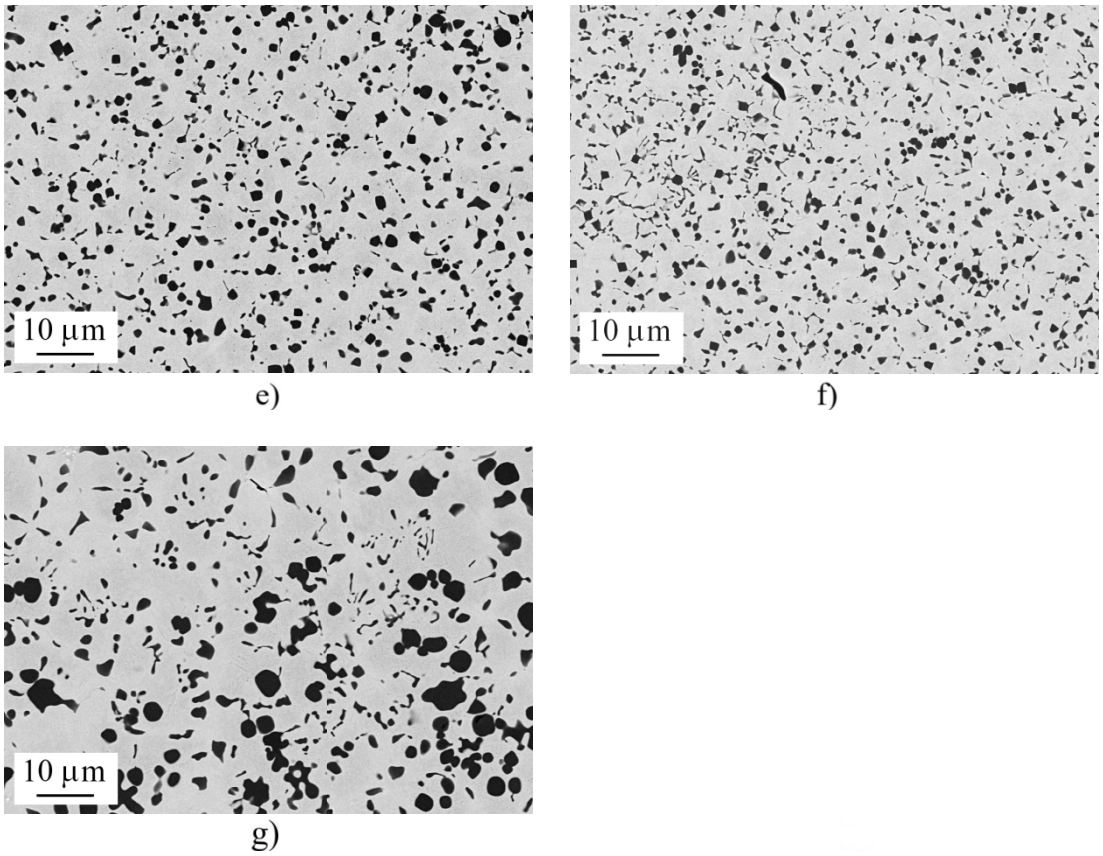


Figure 68 Microstructures of the tool steel deposits welded with welding parameters A-C: a, b) A, test 4, bead 2, c, d) A, test 6, bead 2, e) B, 120 A, bead 1, f) B, RT, 1,6 mm, and g) C

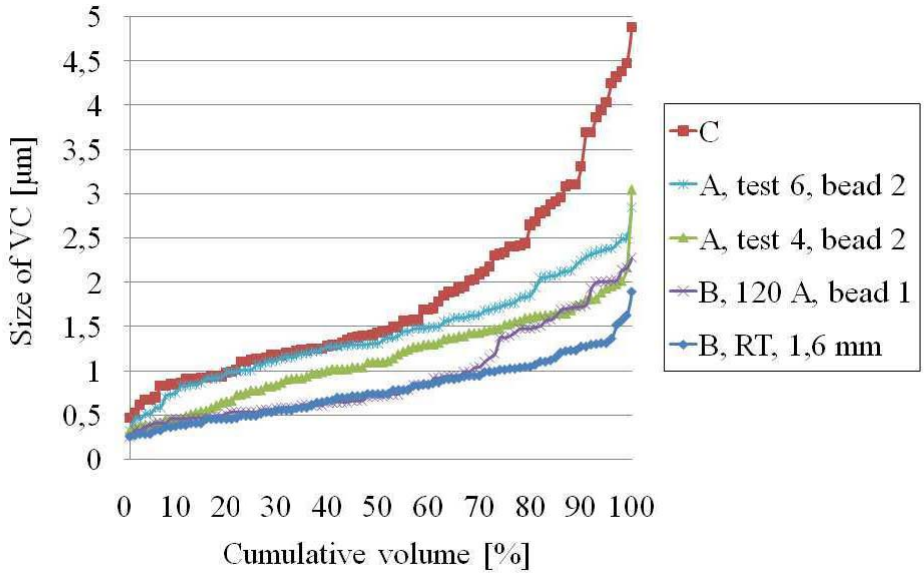


Figure 69 Cumulative volumes of VC sizes of the deposits welded with welding parameters A-C

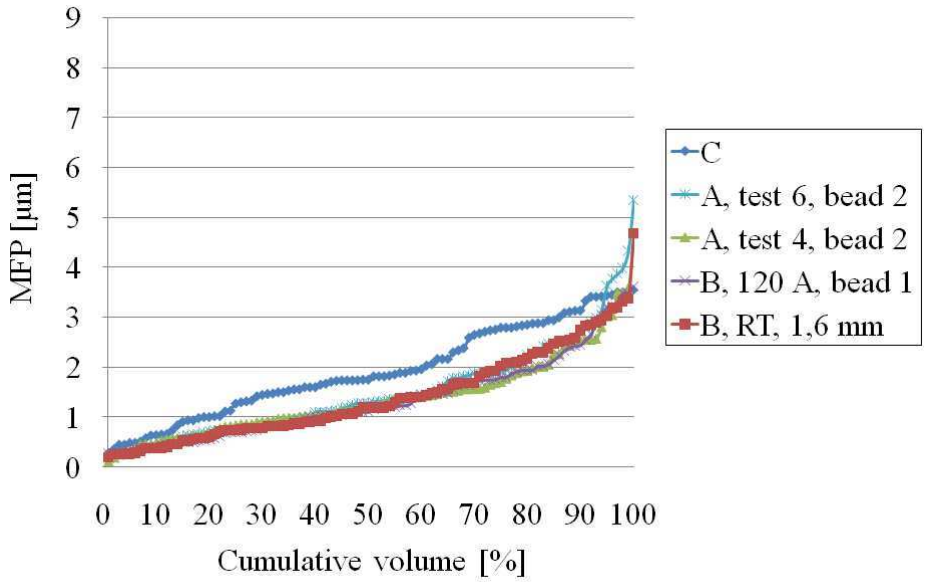


Figure 70 Cumulative volumes of MFPs of the deposits welded with welding parameters A-C

### 6.6.2 Welding parameters D-F

In Figures 71a-i are presented the microstructures of the 12V-1 tool steel deposits welded with welding parameters D-F and the 15V-1 tool steel deposit welded with welding parameters D. In Table 18 are presented the volume fractions, the mean sizes, and the MFPs of VCs. In Figures 72 and 73 are presented the cumulative volumes of the sizes and the MFPs of VCs measured from Figures 71a, d, e, g-i.

The microstructures are close to equal in the deposits, the microstructures of which are presented in Figures 71 a, d, e, g. The deposits were welded with welding parameters D-F. The volume fractions, the mean sizes, and the MFPs of VCs are quite the same in these deposits. The microstructures are not homogeneous. Both large, 1,5-2,5 µm, as well as small, 0,2-0,5 µm, sized carbides present. 3-5 % amount of hydrogen in the carrier gas had a decreasing effect on the mean size of VCs and the MFP and an increasing effect on the volume fraction of VCs.

In the deposits welded with welding parameters D with increasing welding speed the volume fraction of VCs decreased. The mean size of VCs and the MFP increased with increasing welding speed. The VCs were more round-shaped, when the plasma arc distance from the molten pool increased.

The location of the plasma arc was slightly on top of the molten pool and plasma arc current was 65 A for the 5,0 mm thick deposit welded with welding parameters D. The location of the plasma arc was in the edge of the molten pool and plasma arc current was 75 A for the 2,9 mm thick deposit. The biggest difference was the mean size of

VCs, which was increased from 0,5 to 1,3 μm, when the location of the plasma arc was moved slightly on the molten pool by increasing powder feed rate.

The deposits, which were welded with welding parameters D, PH, had reduced plasma arc current. The melting efficiency decreased also, thus, thicknesses of the deposits were lower. The microstructures are basically similar as in the deposits welded without preheating.

15V-1 tool steel was a reference material. The 15V-1 tool steel deposit was welded with welding parameters D. In Figure 71i is presented the microstructure of the 15V-1 deposit. In Table 18 is presented the volume fraction, the mean size, and the MFP of VCs of the 15V-1 tool steel deposit (second weld bead layer). The microstructure contains 2,5-3,8 μm sized large carbides and clusters, as well as small, 0,2-0,5 μm sized carbides. In the deposit D, RT, 5,0 mm the mean size of VCs was bigger than in the deposit D, 15V-1, RT, 2,9 mm, Table 18 and Figure 72.

Table 18 Volume fractions, mean sizes, and MFPs of VCs of the tool steel deposits welded with welding parameters D-F

| Material | Volume fraction [vol.-%] | Mean size / s.d. [μm] | MFP / s.d. [μm] |
|---|---|---|---|
| D, RT, 2,9 mm, 1,35 mm/s | 14,6 | 0,5 / 0,3 | 0,8 / 0,5 |
| D, RT, 2,8 mm, 1,42 mm/s | 13,0 | 0,8 / 0,6 | 1,1 / 0,7 |
| D, RT, 2,7 mm, 1,49 mm/s | 12,5 | 0,9 / 0,5 | 1,5 / 1,0 |
| D, PH, 2,2 mm | 14,3 | 0,5 / 0,4 | 0,7 / 0,4 |
| E, RT, 2,5 mm | 15,0 | 0,5 / 0,4 | 0,6 / 0,3 |
| F, RT, 2,4 mm | 16,0 | 0,5 / 0,3 | 0,7 / 0,5 |
| D, RT, 5,0 mm | 16,9 | 1,3 / 0,7 | 1,7 / 1,3 |
| D, 15V-1, RT, 2,9 mm | 20,3 | 1,0 / 0,9 | 1,1 / 0,8 |

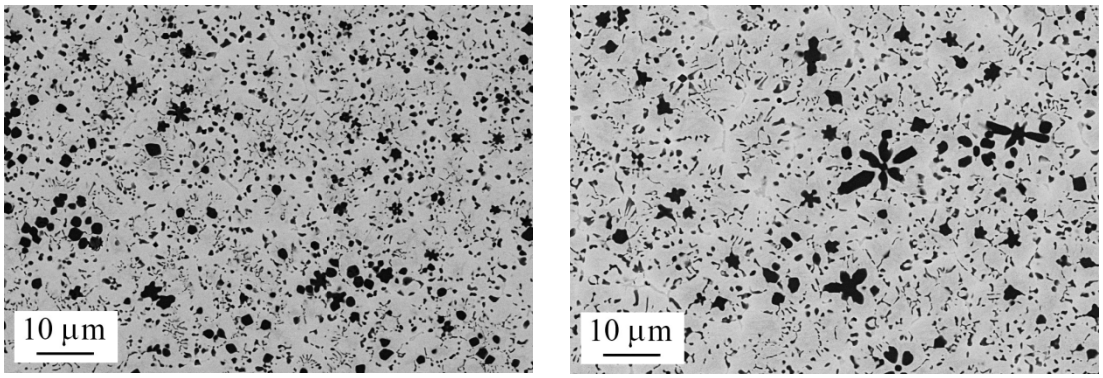


a) b)

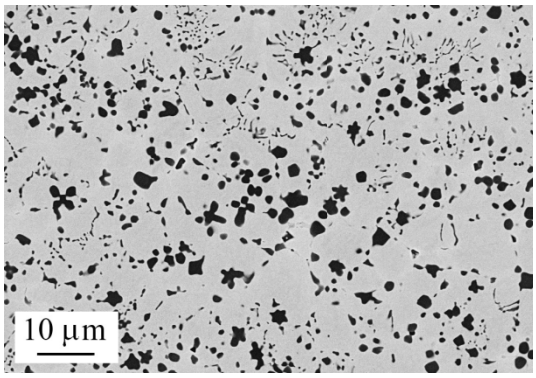


c)

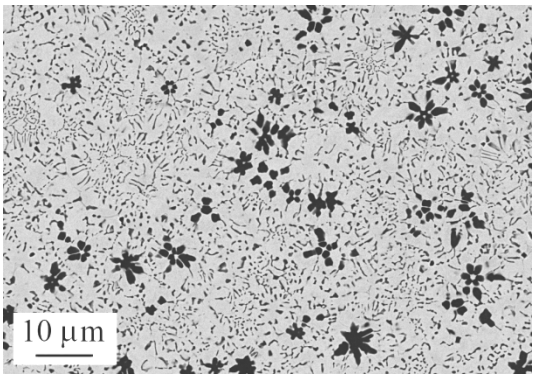


d)

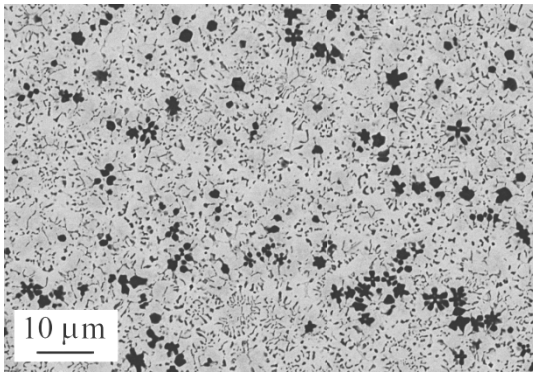


e)

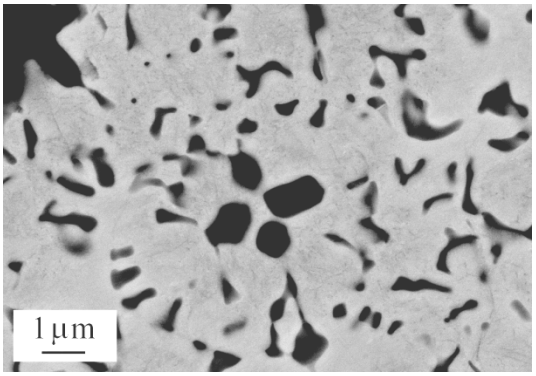


f)

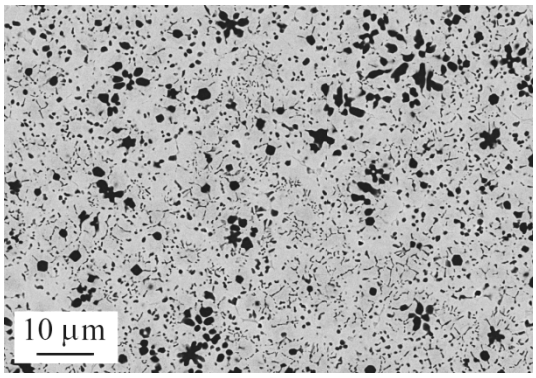


g)

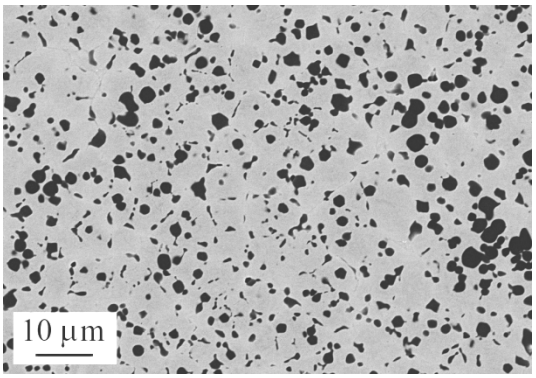


h)

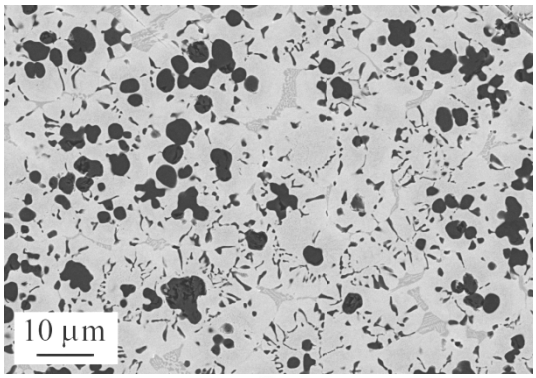


i)

Figure 71 Microstructures of the tool steel deposits welded with welding parameters D-F: a) D, RT, 2,9 mm, 1,35 mm/s, b) D, RT, 2,8 mm, 1,42 mm/s, c) D, RT, 2,7 mm, 1,49 mm/s, d) D, PH, 2,2 mm, e, f) E, RT, 2,5 mm, g) F, RT, 2,4 mm, h) D, PH, 5,0 mm, and i) D, 15V-1, RT, 2,9 mm

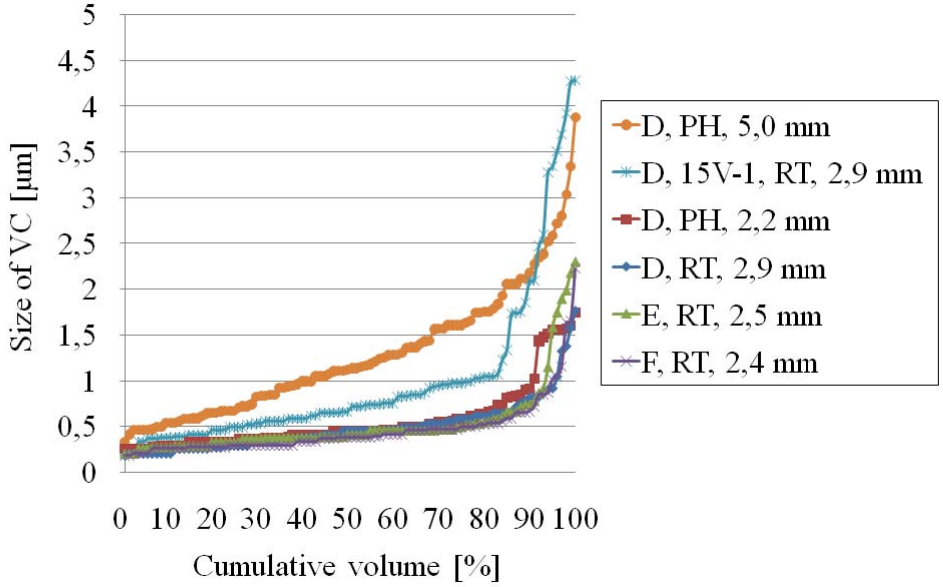


Figure 72 Cumulative volumes of VC sizes of the deposits welded with welding parameters D-F

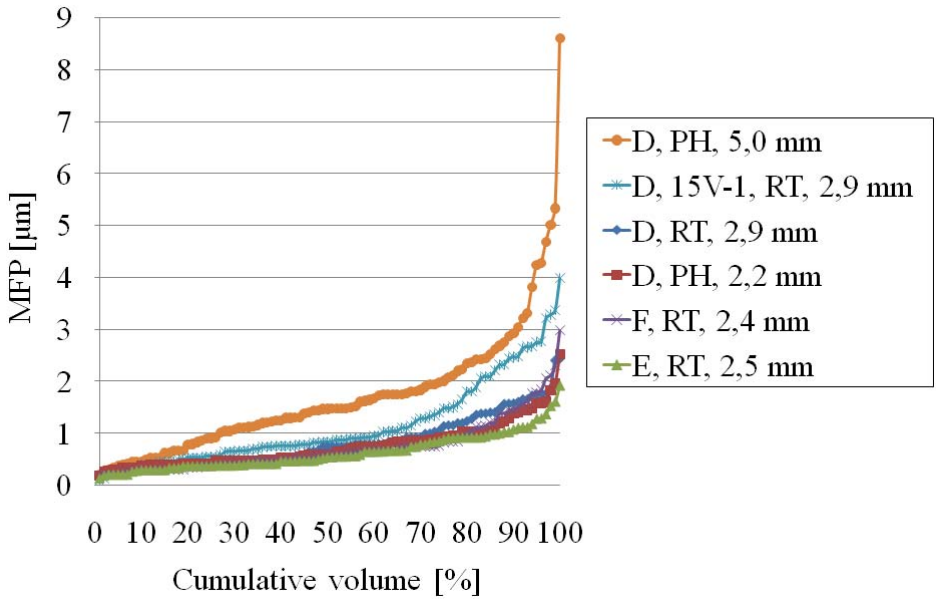


Figure 73 Cumulative volumes of MFPs of the deposits welded with welding parameters D-F

### 6.6.3 Welding parameters G

One deposit was welded with straight weld beads without oscillation. In Figures 74a, b is presented the microstructure of the deposit. In Table 19 is presented the volume fraction, the mean size, and the MFP of VCs. The volume fraction, the mean size, and the MFP of VCs are similar as in the microstructures of the deposits welded with welding parameters D-F. The microstructure is not homogeneous. The microstructure contains both large, 2,5 µm sized round-shaped, as well as small, 0,2-0,5 µm, sized needle-shaped carbides, Figures 74a, b and 75.

Table 19 Volume fraction, mean size, and MFP of VCs of the deposit welded with welding parameters G

| Material | Volume fraction [vol.-%] | Mean size / s.d. [µm] | MFP / s.d. [µm] |
|---|---|---|---|
| G, RT, 1,2 mm | 14,5 | 0,7 / 0,6 | 0,8 / 0,6 |

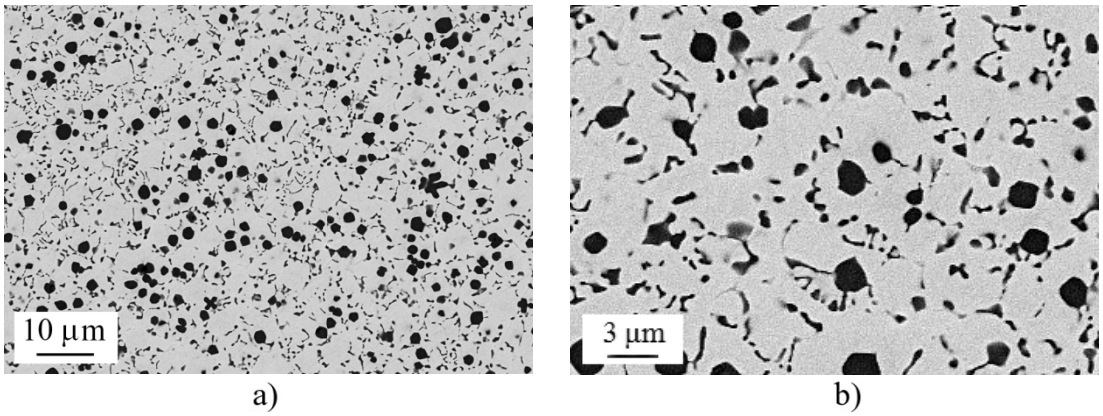


Figure 74 a, b) Microstructure of the deposit welded with welding parameters G

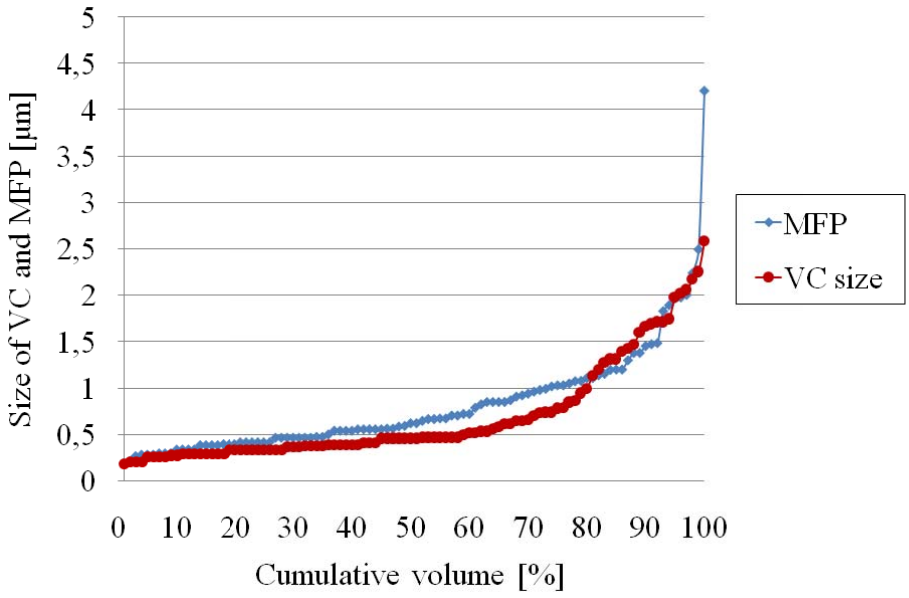


Figure 75 Cumulative volumes of VC sizes and MFPs of the deposit welded with welding parameters G

### 6.6.4 Materials manufactured by the HIP process

In Figures 76a-d are presented the microstructures of the HIP materials. In Table 20 are presented the volume fractions, the mean sizes, and the MFPs of VCs. In Figures 77 and 78 are presented the cumulative volumes of the sizes and the MFPs of VCs measured from Figures 76a-d.

The distribution of VCs is relatively homogeneous in every material. The volume fractions of VCs of the 12V-1 and the 12V-2 tool steels are close to 18 vol.-%. The 10V tool steel has slightly lower volume fraction of VCs. The mean sizes of the carbides are quite close to each other. The mean size of VCs is bigger in the 10V tool steel as in the other materials, Table 20 and Figure 76d.

Table 20 Volume fractions, mean sizes, and MFPs of VCs of the tool steel materials manufactured by the HIP method

| Material | Volume fraction [vol.-%] | Mean size / s.d. [μm] | MFP / s.d. [μm] |
|---|---|---|---|
| HIP, 12V-1 | 18,0 | 0,8 / 0,2 | 1,0 / 0,5 |
| HIP, 12V-2 | 18,3 | 0,9 / 0,3 | 1,0 / 0,6 |
| HIP, 15V-2 | 20,6 | 0,9 / 0,3 | 0,8 / 0,4 |
| HIP, 10V | 14,7 | 1,1 / 0,4 | 1,3 / 0,8 |

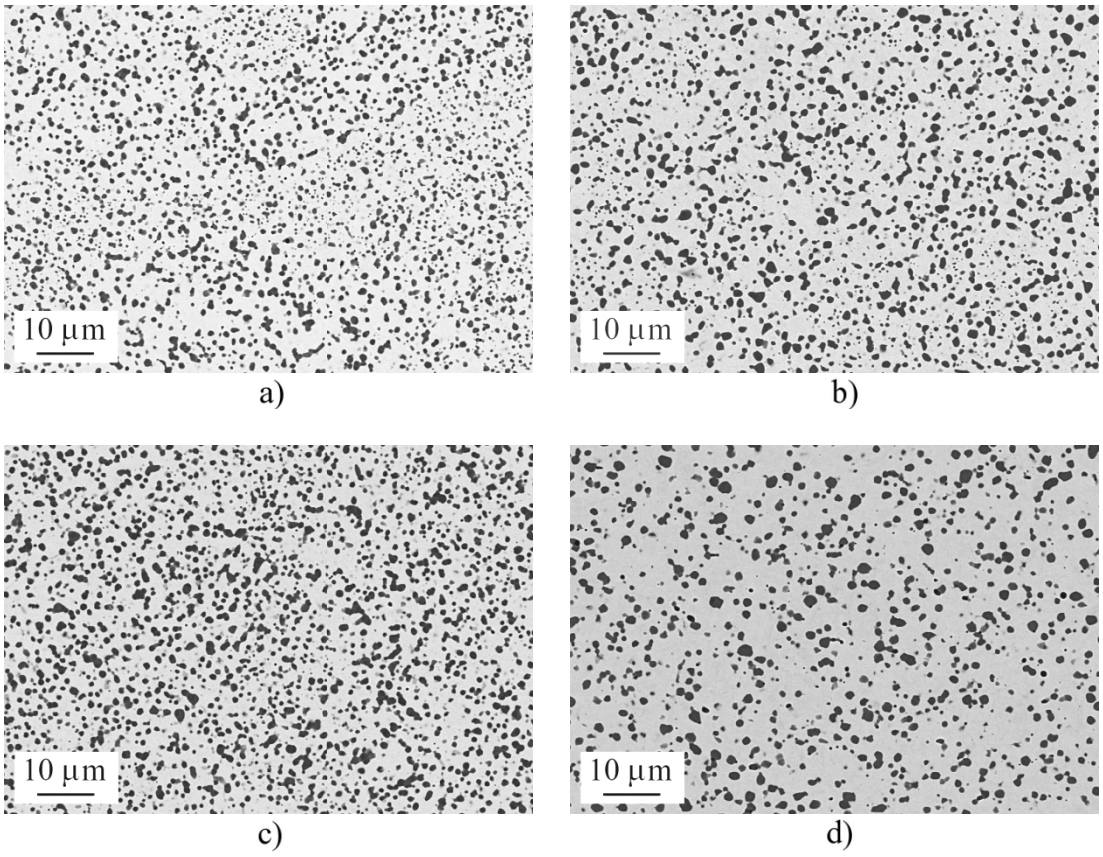


Figure 76 Microstructures of the HIP materials: a) 12V-1, b) 12V-2, c) 15V-2, and d) 10V tool steel

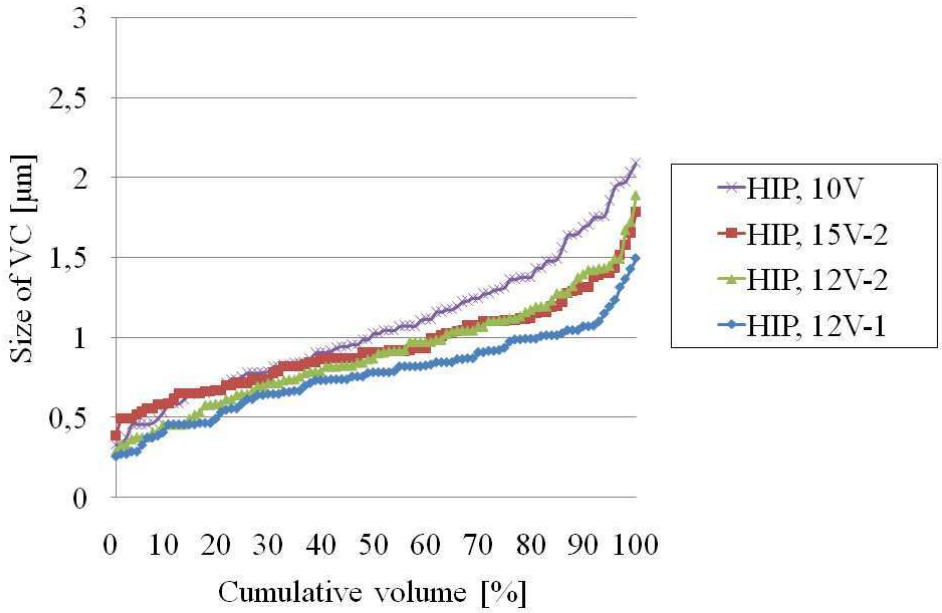


Figure 77 Cumulative volumes of VC sizes of the tool steel materials manufactured by the HIP method

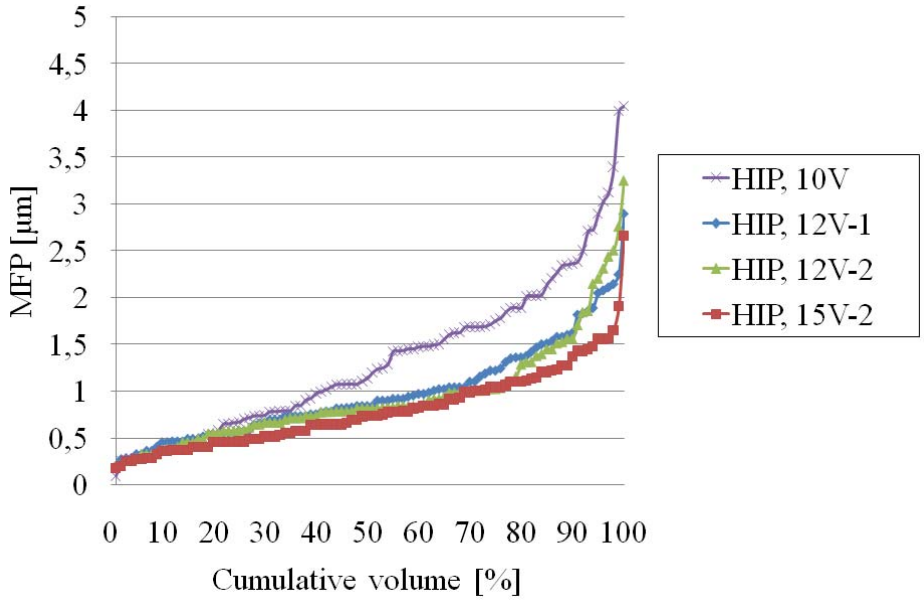


Figure 78 Cumulative volumes of MFPs of the tool steel materials manufactured by the HIP method

### 6.6.5 Microstructure of overlapping beads

In Figures 79a-c are presented the microstructures of the weld beads welded with welding parameters B by overlapping. Plasma arc current was 120 A. The dilution of the whole deposit was 11,3 %. In Table 21 are presented the volume fractions, the mean sizes, and the MFPs of VCs. In Figures 80 and 81 are presented the cumulative volumes of the sizes and the MFPs of VCs measured from Figures 79a-c.

The microstructures of the first and the third beads are close to each other. The microstructure of the first bead has more round-shaped carbides as the microstructures of the second and the third beads have. The microstructure of the second bead contains smaller and more needle-shaped VCs as the microstructures of the first and the third beads have. The displacement of the plasma torch was made manually. Small variations in the overlapping displacement may occur, but the effects on the microstructure are not possible to analyze from small amount of samples.

Table 21 Volume fractions, mean sizes, and MFPs of VCs of the weld beads welded with welding parameters B, 120 A

| Material | Volume fraction [vol.-%] | Mean size / s.d. [μm] | MFP / s.d. [μm] |
|---|---|---|---|
| B, 120 A, bead 1 | 13,4 | 1,1 / 0,5 | 1,4 / 0,8 |
| B, 120 A, bead 2 | 14,4 | 0,8 / 0,5 | 1,1 / 0,7 |
| B, 120 A, bead 3 | 14,4 | 1,2 / 0,7 | 1,8 / 1,2 |

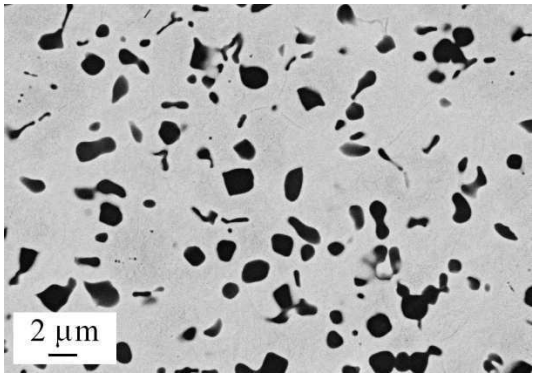


a)

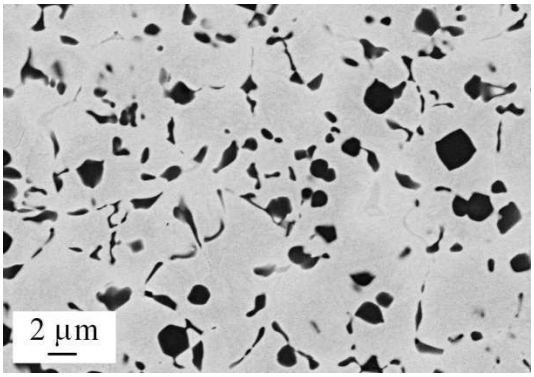


b)

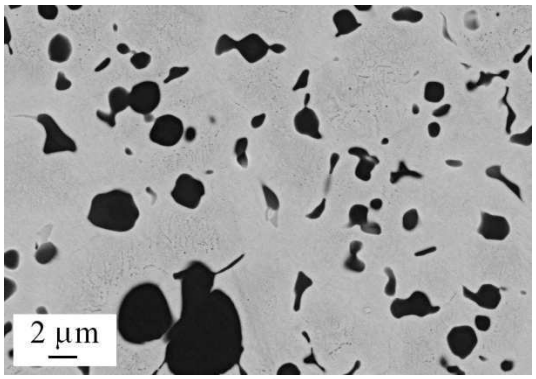


c)

Figure 79 Microstructures of the 12V-1 tool steel weld beads welded with welding parameters B, 120 A: a) first bead, b) second overlapping weld bead, and c) third overlapping weld bead

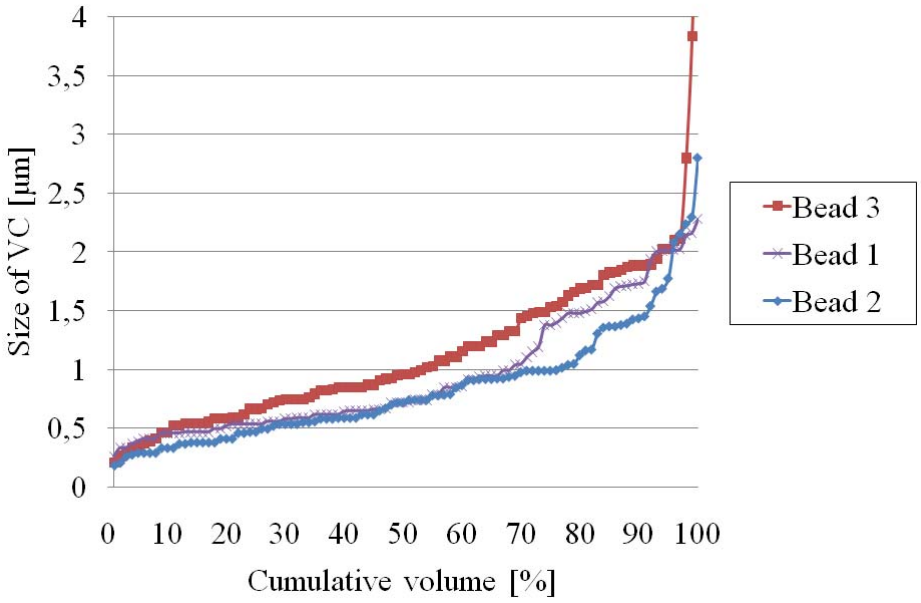


Figure 80 Cumulative volumes of VC sizes of the weld beads welded with welding parameters B, 120 A by overlapping

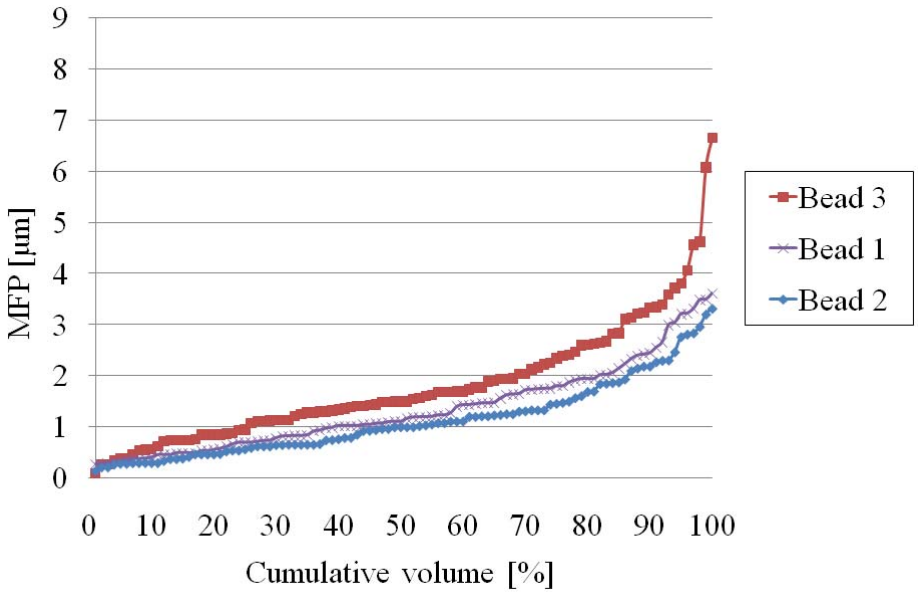


Figure 81 Cumulative volumes of MFPs of the weld beads welded with welding parameters B, 120 A by overlapping

In Figures 82a-h are presented the microstructures of the weld beads welded with welding parameters D by overlapping. Powder feed rate was 0,3 kg/h. In Table 22 are presented the volume fractions, the mean sizes, and the MFPs of VCs. In Figures 83 and 84 are presented the cumulative volumes of the sizes and the MFPs of VCs measured from Figures 82a, c, e, g. The deposit is the same as was presented in Table 13.

The biggest difference in the carbide morphology is between the microstructures of the first and the second beads. In the first bead the carbides are mainly round-shaped. The microstructures of the weld beads 2, 5, and 12 contain also needle-shaped VCs. The volume fraction of VCs increased when the surfacing process continued. The MFPs of the weld beads 1 and 2 are different. The second bead contains a lot of small carbides. The weld beads 1, 5 and 2, 12 have similar kinds of cumulative volume carbide size distributions, Figure 83.

Table 22 Volume fractions, mean sizes, and MFPs of VCs of the deposit welded with welding parameters D and powder feed rate 0,3 kg/h

| Material | Volume fraction [vol.-%] | Mean size / s.d. [µm] | MFP / s.d. [µm] |
|---|---|---|---|
| D, RT, 1,0 mm, bead 1 | 12,6 | 0,6 / 0,2 | 1,2 / 0,9 |
| D, RT, 1,0 mm, bead 2 | 13,6 | 0,5 / 0,3 | 0,6 / 0,4 |
| D, RT, 1,0 mm, bead 5 | 14,8 | 0,7 / 0,3 | 0,9 / 0,6 |
| D, RT, 1,0 mm, bead 12 | 14,1 | 0,5 / 0,3 | 1,0 / 0,6 |

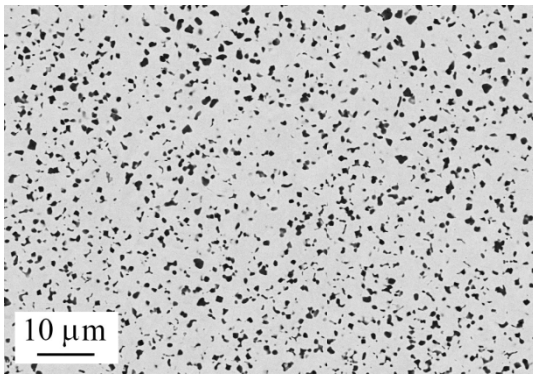


a)

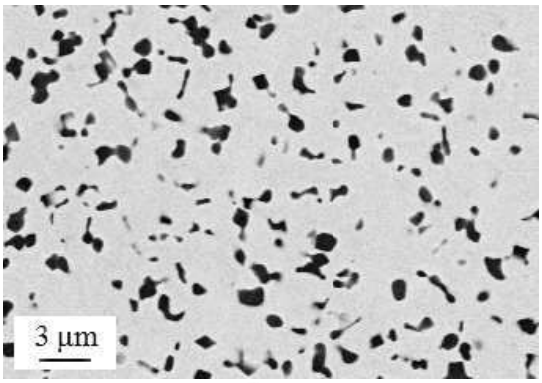


b)

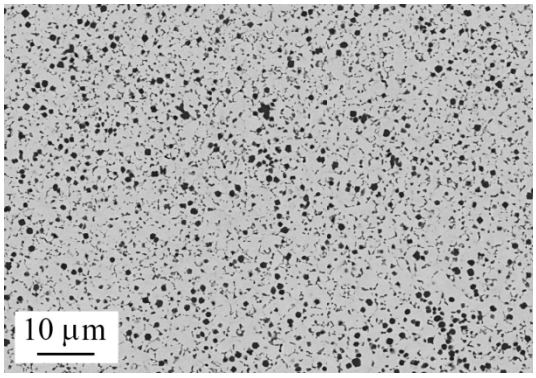


c)

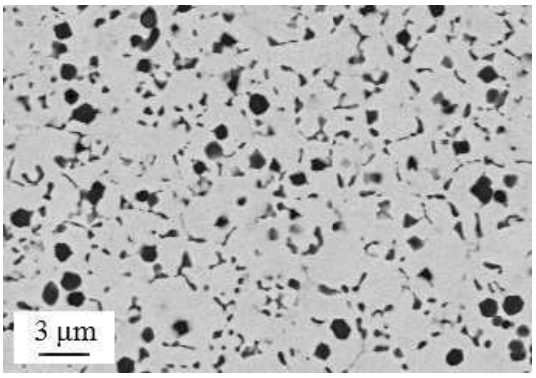


d)

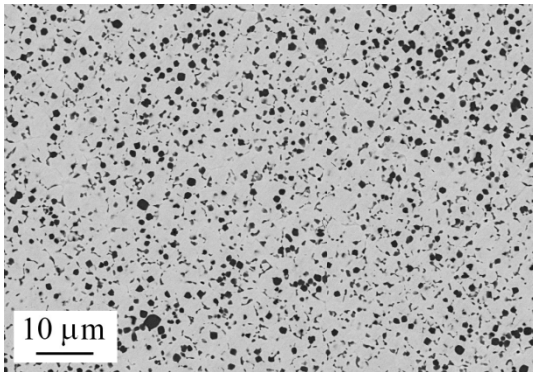


e)

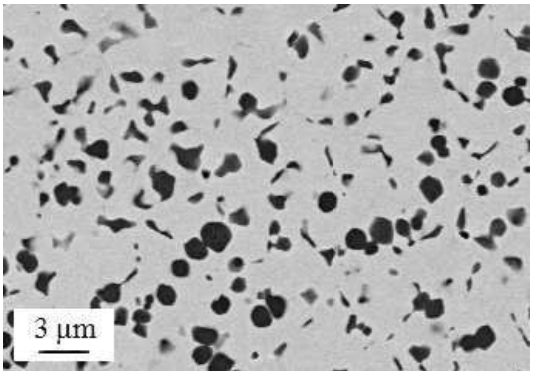


f)

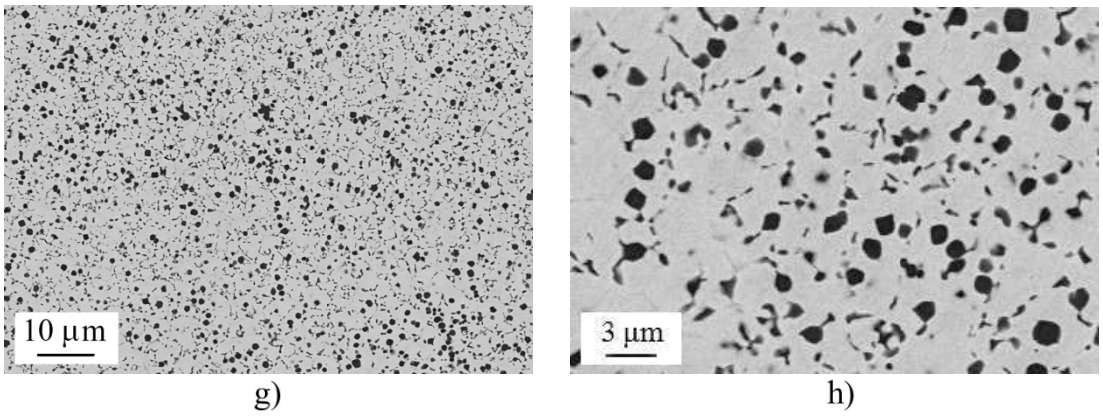


Figure 82 Microstructures of the weld beads welded with welding parameters D and powder feed rate 0,3 kg/h: a, b) first bead, c, d) second bead, e, f) fifth bead, and g, h) last twelfth bead

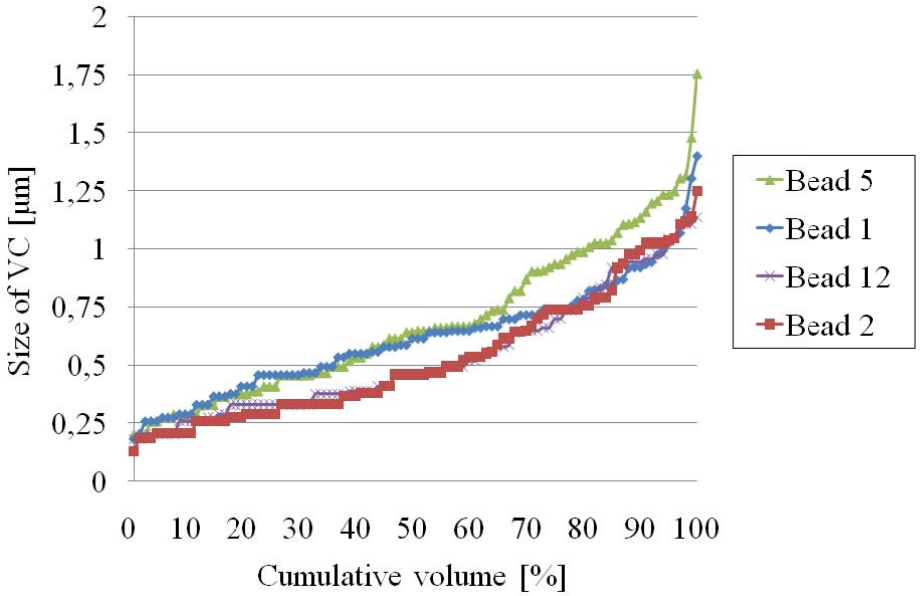


Figure 83 Cumulative volumes of VC sizes of the weld beads 1, 2, 5, and 12 welded with welding parameters D and powder feed rate 0,3 kg/h

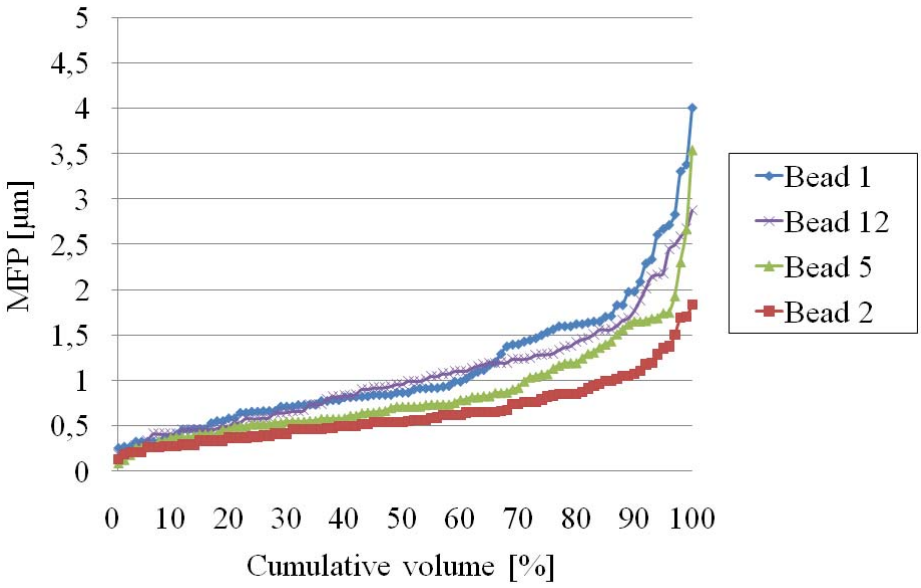


Figure 84 Cumulative volumes of MFPs of the weld beads 1, 2, 5, and 12 welded with welding parameters D and powder feed rate 0,3 kg/h

### 6.6.6 Microstructural changes in weld bead in welding direction

In Figures 85a-c are presented the microstructures taken from the second weld bead welded with welding parameters B, 120 A by overlapping. The sample was cut along the centerline and in the welding direction. In Table 23 are presented the volume fractions, the mean sizes, and the MFPs of VCs measured from three locations. In Figure 85a is presented the microstructure of the weld bead approximately 15 mm from the plasma arc ignition point. In Figure 85b is presented the microstructure after 30 mm welding from the plasma arc ignition point. In Figure 85c is presented the microstructure after 50 mm welding from the plasma arc ignition point and about 25 mm from the end of the weld bead. In Figures 86 and 87 are presented the cumulative volumes of the sizes and the MFPs of VCs measured from Figures 85a-c.

The volume fraction of VCs increased from 7,5 to 13,0-14,0 vol.-% during welding a weld bead. The mean size of the carbides increased from 0,6 to 1,2-1,3 µm. The MFP remained constant. Therefore, the biggest differences in the microstructure can be obtained after ignition of the plasma arc.

Table 23 Volume fractions, mean sizes, and MFPs of VCs of the second weld bead welded with welding parameters B, 120 A

| Location | Volume fraction [vol.-%] | Mean size [μm] / s.d. | MFP [μm] / s.d. |
|---|---|---|---|
| Bead beginning | 7,5 | 0,6 / 0,3 | 1,5 / 1,2 |
| After 30 mm | 13,0 | 1,3 / 0,6 | 1,6 / 1,2 |
| After 50 mm | 14,2 | 1,2 / 0,6 | 1,6 / 1,2 |

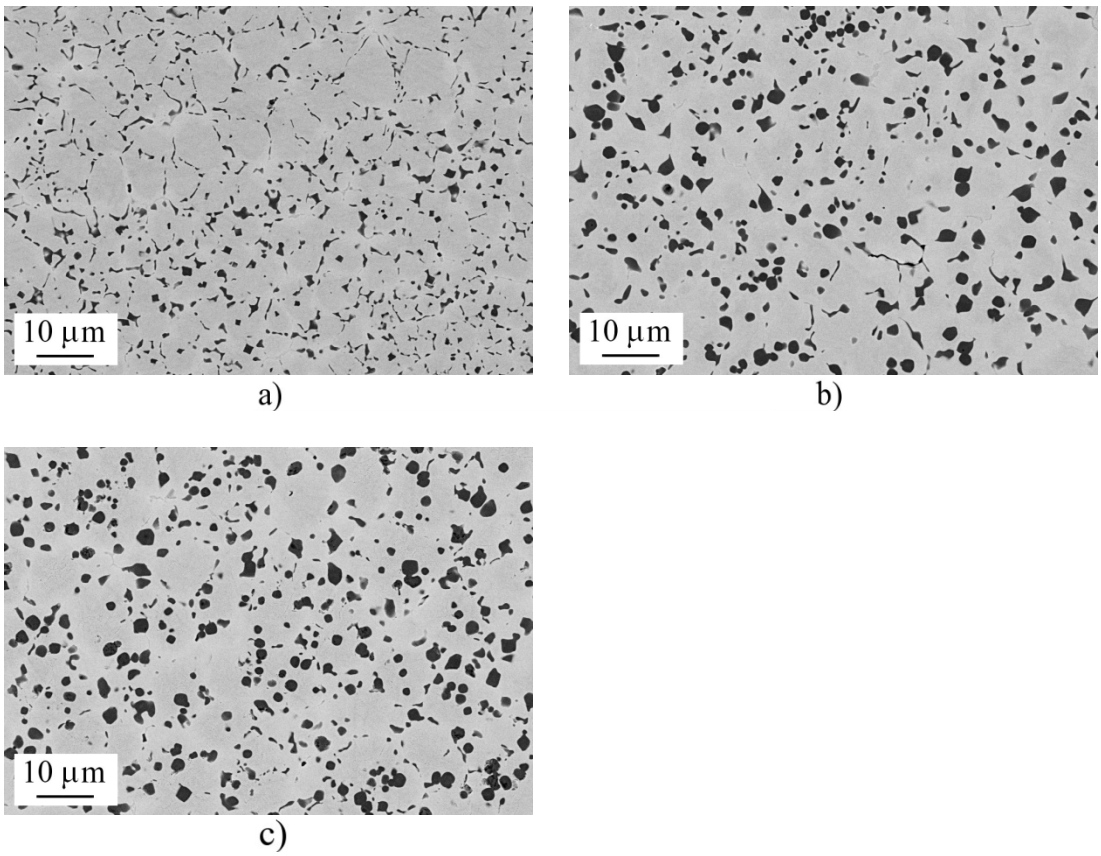


Figure 85 Microstructures of the second weld bead welded with welding parameters B, 120 A: a) at the beginning of the bead, b) after 30 mm welding, and c) after 50 mm welding and 25 mm from the end of the bead

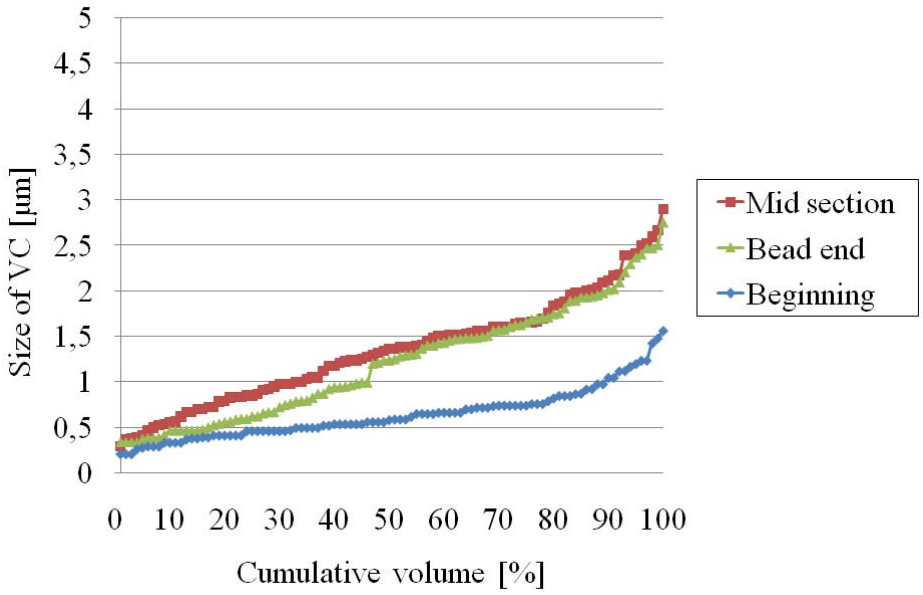


Figure 86 Cumulative volumes of VC sizes of the second weld bead welded with welding parameters B, 120 A from the bead beginning to the bead end

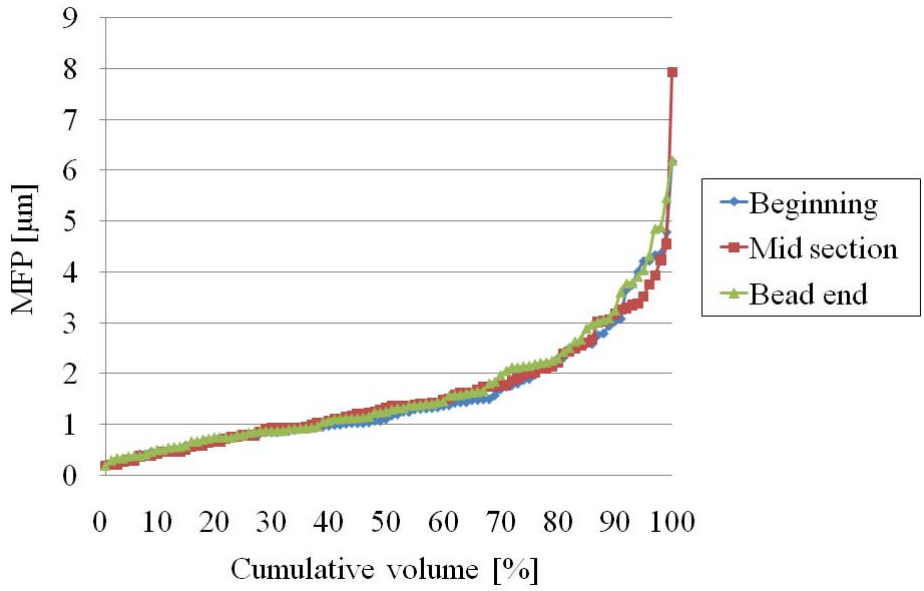


Figure 87 Cumulative volumes of MFPs of the second weld bead welded with welding parameters B, 120 A from the bead beginning to the bead end

## 6.7 Abrasive wear resistance

### 6.7.1 Surface roughness

Surface roughness of the deposit welded with welding parameters B, 130 A, PH was measured during the RWAT. Surface roughness of the deposit ($R_a$) was initially 0,06±0,06 μm. The volume fraction, the mean size, and the MFP of VCs were 13,8 vol.-%, 1,1±0,4 μm, and 1,5±0,6 μm, respectively. The dilution was 16 %.

Surface roughness of the 12V-1 tool steel deposit increased from the initial state to 0,90±0,08 μm during first one hundred rounds of the rubber wheel. Surface roughness 1,60±0,30 μm was obtained after 6000 revolutions, Table 24.

Table 24 Surface roughness of the deposit B, 130 A, PH during the RWAT

| Wheel revolutions [rev] | $R_a$ / s.d. [μm] |
|---|---|
| 0 | 0,06 / 0,06 |
| 2 | 0,13 / 0,01 |
| 10 | 0,30 / 0,06 |
| 20 | 0,43 / 0,09 |
| 30 | 0,51 / 0,08 |
| 40 | 0,67 / 0,06 |
| 50 | 0,63 / 0,15 |
| 60 | 0,78 / 0,05 |
| 70 | 0,87 / 0,11 |
| 80 | 0,83 / 0,07 |
| 90 | 0,86 / 0,06 |
| 100 | 0,90 / 0,08 |
| 150 | 0,97 / 0,07 |
| 200 | 1,10 / 0,04 |
| 250 | 0,96 / 0,02 |
| 300 | 1,05 / 0,11 |
| 350 | 1,06 / 0,07 |
| 400 | 1,06 / 0,12 |
| 450 | 1,10 / 0,09 |
| 500 | 1,11 / 0,04 |
| 600 | 1,22 / 0,17 |
| 700 | 1,22 / 0,16 |
| 800 | 1,14 / 0,13 |
| 900 | 1,19 / 0,13 |
| 1000 | 1,23 / 0,18 |
| 1500 | 1,05 / 0,15 |
| 3000 | 1,64 / 0,23 |
| 4500 | 1,53 / 0,36 |
| 6000 | 1,60 / 0,30 |

### 6.7.2 Applied load

In Figure 88 is presented the effect of applied normal force on the abrasive wear resistance of the deposit welded with welding parameters A. The deposit was welded with welding parameters A, test 2, bead 1. The rubber wheel abrasion tests were made with the same sample, i.e., the sample was ground after each test and was tested again.

The normal force was increased step by step from 126 to 174 N. The volume loss of the tested deposit increased linearly with the increasing normal force from 126 to 150 N. This is in accordance with the Archard's law presented in equation 33 (Archard, 1953). With higher normal forces from 150 to 174 N the volume loss decreased. Thus, low stress abrasive wear test can be arranged below normal force 150 N and high stress abrasive wear test above it. Normal force 126 N was used to characterize the abrasive wear resistance of the studied materials.

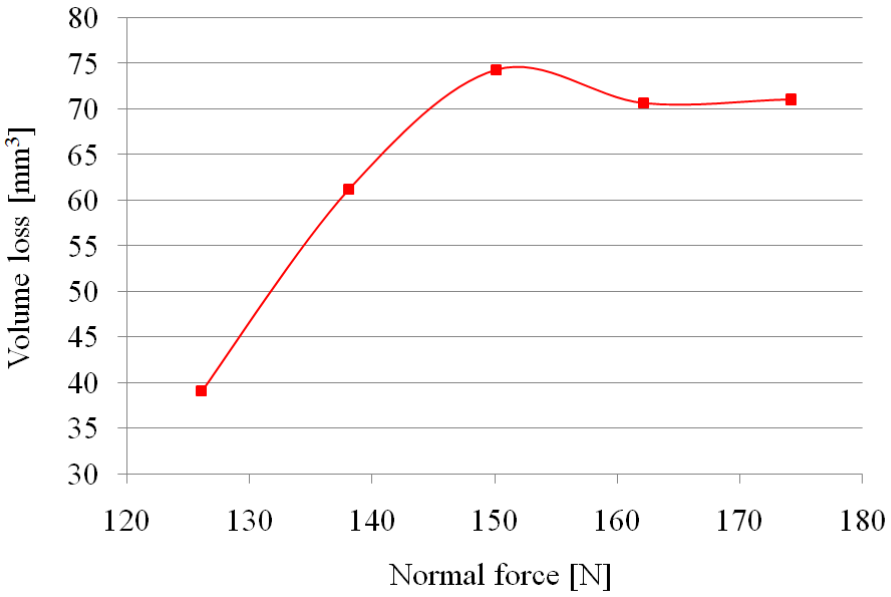


Figure 88 Effect of normal force in the RWAT on volume loss of the deposit welded with welding parameters A, test 2, bead 1

### 6.7.3 Dilution

The abrasive wear resistances of the weld beads welded with welding parameters A, B, and C are compared in Figure 89 and Tables 25-27. In Figure 89 and Table 26 are presented also the effect of rubber wheel rotating speeds 105 and 200 rpm on the abrasive wear resistances of the weld beads welded with welding parameters B.

In the RWAT the volume losses of the weld beads welded with welding parameters A were higher in the first beads of the deposits 4 and 6. The abrasive wear resistances of

the first beads of the deposits 1, 2, 3, and 5 were higher when compared to the abrasive wear resistances of the second beads.

The effect of the dilution on the abrasive wear resistance is not clear. In Table 25 the dilutions of the deposits 2, 3, 4, and 5, decreased when the welding process proceeded. The volume losses were in the deposits 1, 2, 3, and 5 slightly higher in the second weld beads. In the deposit 4 both the volume loss and the dilution were higher in the first bead. Also in the deposits 1 and 6 the interaction between the dilution and the abrasive wear resistance remain unclear.

In the deposits welded with welding parameters B the volume loss was higher with lower sliding speed. The difference was approximately two times. The more diluted deposits had lowering abrasive wear resistance in the RWAT, when the rotating speed was 105 rpm. The abrasive wear resistance of the more diluted deposits remained almost at the same level, when the rotating speed was 200 rpm.

The abrasive wear resistances of the deposits welded with welding parameters B were mainly lower in the third beads, Table 26. In the deposits welded with plasma arc currents 130 and 140 A the dilutions were lower in the third beads, even though the volume losses were mainly higher. The dilution had no clear relationship with the abrasive wear resistance.

The location of the plasma arc was on the molten pool, when the weld bead was welded with welding parameters C. The dilution was low, Table 27. Welding defects like small pores or lack of fusion were obtained. The abrasive wear resistance was approximately two times lower when compared to the deposits welded with welding parameters A, test 4 and A, test 6.

Table 25 Dilutions and volume losses of the deposits welded with welding parameters A

| Welding Test [No.] | Dilution Bead 1 / 2 [%] | Volume loss Bead 1 / 2 [$mm^3$] |
|---|---|---|
| 1 | 18,7 / 19,0 | 37,4 / 44,1 |
| 2 | 26,3 / 12,7 | 39,1 / 47,4 |
| 3 | 17,8 / 15,6 | 30,1 / 35,8 |
| 4 | 16,3 / 11,8 | 29,2 / 20,4 |
| 5 | 11,9 / 7,2 | 27,6 / 31,8 |
| 6 | 5,9 / 6,0 | 26,1 / 23,9 |

Table 26 Dilutions and volume losses of the deposits welded with welding parameters B

| Plasma arc current [A] | Dilution Bead 1 / 3 [%] | Volume loss Bead 1 / 3 105 rpm [$mm^3$] | Volume loss Bead 1 / 3 200 rpm [$mm^3$] |
|---|---|---|---|
| 110 A | 5,1 / 5,1 | 54,7 / 61,1 | 34,1 / 36,5 |
| 120 A | 7,9 / 12,9 | 65,5 / 51,9 | 33,8 / 31,6 |
| 130 A | 22,0 / 10,6 | 66,9 / 61,8 | 38,4 / 42,0 |
| 140 A | 26,5 / 24,5 | 79,1 / 92,8 | 36,1 / 43,9 |

Table 27 Dilution and volume loss of the deposit welded with welding parameters C

| Plasma arc current [A] | Dilution [%] | Volume loss [$mm^3$] |
|---|---|---|
| 175 A | 0,5 | 50,0 |

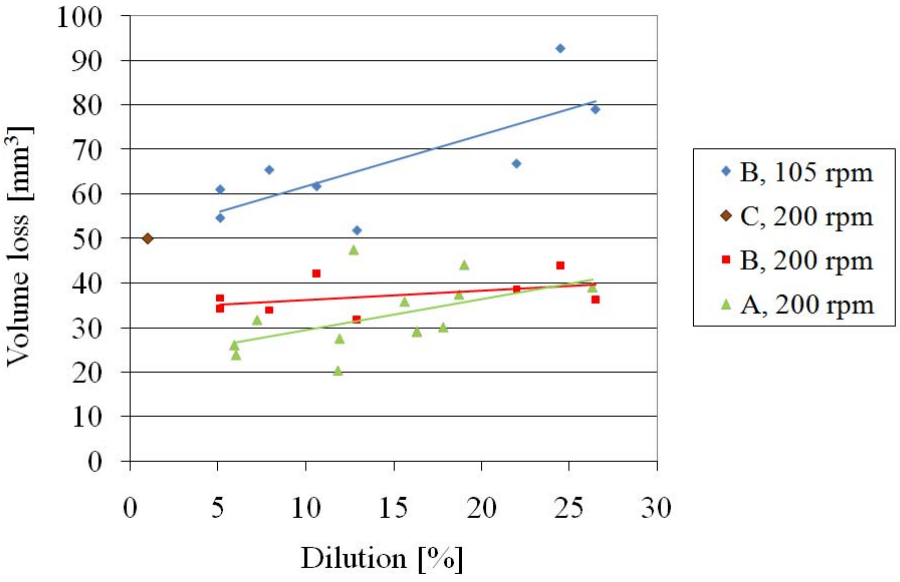


Figure 89 Volume losses of the deposits welded with welding parameters A-C plotted as a function of dilutions of the weld beads

The volume losses of the deposits welded with welding parameters D-G was plotted as a function of dilution, Figure 90. The best abrasive wear resistance was obtained with the 5,0 mm thick weld bead welded with welding parameters D. The location of the plasma arc was then slightly on the molten pool. The abrasive wear resistance was at the same level as in the 12V-1 tool steel material manufactured by the HIP process.

The deposits welded with welding parameters D, PH, 2,2 mm had relatively low abrasion wear resistance. The location of the plasma arc was in the edge of the molten pool. The abrasive wear resistance of the deposits welded with welding parameters D decreased rapidly when the dilution increased.

The abrasive wear resistances of the deposits welded with Ar-$H_2$ gas mixtures, i.e., welding parameters E-F, were equal. The abrasive wear resistance was lower than in the deposits welded with welding parameters D with optimized dilution. Because of the problems in the dilution control, when welding with welding parameters D, the abrasive wear resistance may be better maintained with welding parameters E and F.

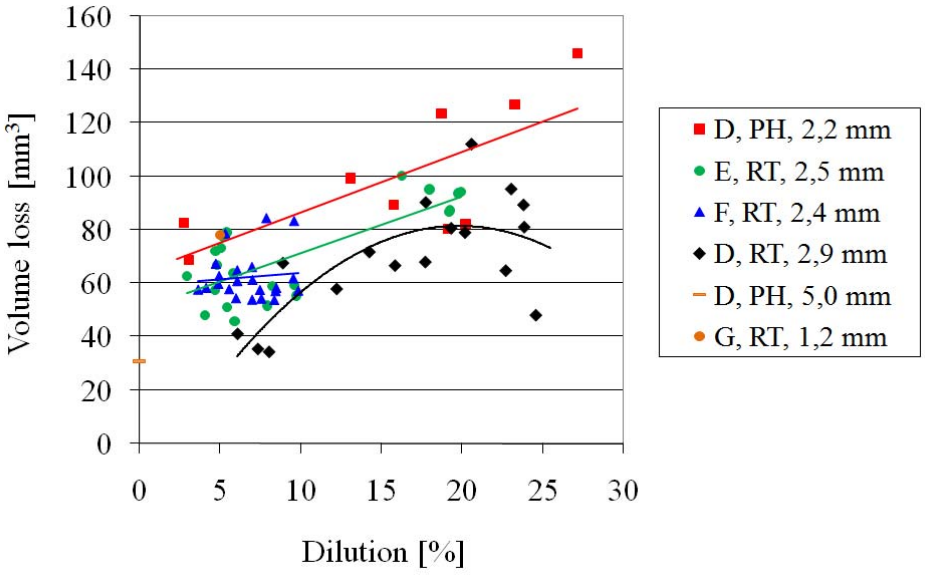


Figure 90 Volume losses of the deposits welded with welding parameters D-G plotted as a function of dilutions of the deposits

### 6.7.4 Hardness

Hardness of the deposit is one parameter, which estimates abrasive wear resistance of the deposit. No straight relationship between abrasive wear resistance and hardness was obtained. It is difficult to estimate the abrasive wear resistance of the 12V-1 tool steel deposit as a function of hardness, even though the deposits welded with the same welding parameters are compared. Hardness of the 12V-1 tool steel deposits varied between 803 and 861 HV10 depending on the welding parameters, Table 28 and Figure 91. Average hardness of the deposits welded with welding parameters A-G and the tool steel materials manufactured by the HIP process are presented in Table 28.

Table 28 Hardnesses and volume losses of the deposits welded with welding parameters A-G and the tool steel materials manufactured by the HIP process

| Material | Hardness / s.d. [HV10] | Volume loss / s.d. [$mm^3$] |
|---|---|---|
| A, test 4, bead 2 | 803 / 29 | 20,4 / - |
| A, test 6, bead 2 | 828 / 32 | 23,9 / - |
| B, 120 A, bead 1 | 854 / 14 | 33,8 / - |
| C | 861 / 22 | 50,0 / - |
| D, RT, 2,9 mm | 815 / 22 | 35,3 / - |
| D, PH, 2,2 mm | 841 / 21 | 68,9 / - |
| D, PH, 5,0 mm | 810 / 27 | 30,8 / - |
| D, 15V-1, RT, 2,9 mm | 803 / 29 | 41,9 / - |
| E, RT, 2,5 mm | 808 / 23 | 57,3 / - |
| F, RT, 2,4 mm | 845 / 20 | 57,7 / - |
| G, RT, 1,2 mm | 857 / 18 | 78,0 / - |
| HIP, 12V-1 | 755 / 4 | 29,9 / 3,8 |
| HIP, 12V-2 | 803 / 3 | 28,3 / 0,8 |
| HIP, 15V-2 | 796 / 7 | 21,9 / 0,9 |
| HIP, 10V | 734 / 5 | 30,0 / 2,6 |

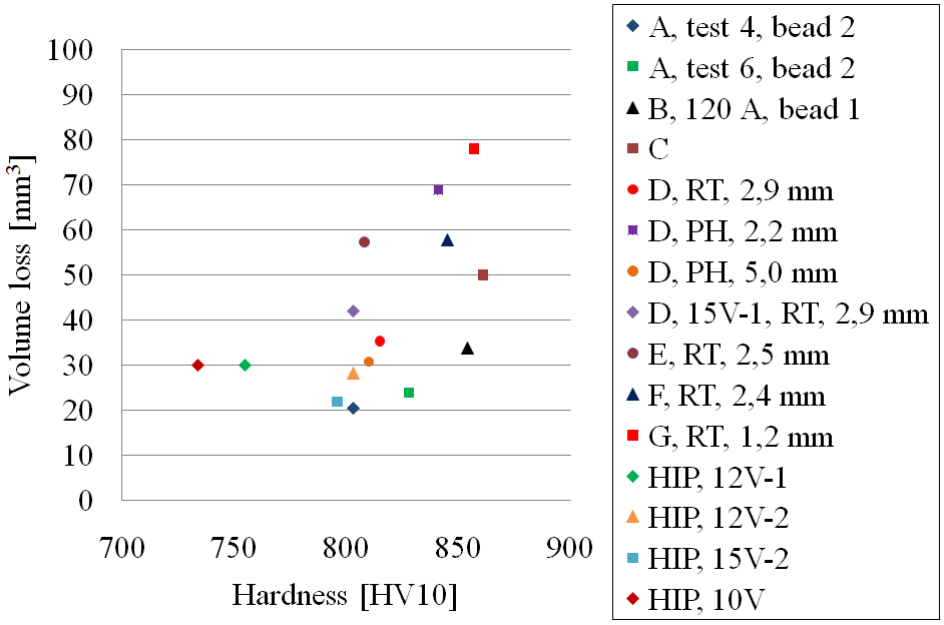


Figure 91 Volume losses of the tool steel deposits welded with welding parameters A-G and the tool steel materials manufactured by the HIP process as a function of hardness

### 6.7.5 Mean size of vanadium carbides

In Figure 92 and Table 29 are presented the effect of the mean size of VCs on the abrasive wear resistance of the tool steel deposits welded with welding parameters A-G and the tool steel materials manufactured by the HIP method. The abrasive wear resistance mainly increases, when the mean size of VC carbides increases. The maximum mean size of VC carbides of the deposits welded with parameters D was 1,3 μm. The maximum abrasive wear resistance was obtained with welding parameters A, when the mean size of VCs was from 1,2 to 1,4 μm. The tool steel materials manufactured by the HIP process had the mean size of VCs from 0,8 to 1,1 μm. The abrasive wear resistances of the HIP materials were better than that of the abrasive wear resistances of the deposits which had the mean size of VCs in the same range.

Table 29 Mean sizes of VCs and volume losses of the tool steel deposits welded with welding parameters A-G and the tool steel materials manufactured by the HIP process

| Material | Mean size / s.d. [μm] | Volume loss / s.d [$mm^3$] |
|---|---|---|
| A, test 4, bead 2 | 1,2 / 0,5 | 20,4 / - |
| A, test 6, bead 2 | 1,4 / 0,5 | 23,9 / - |
| B, 120 A, bead 1 | 1,0 / 0,5 | 33,8 / - |
| C | 1,8 / 1,0 | 50,0 / - |
| D, RT, 2,9 mm | 0,5 / 0,3 | 35,3 / - |
| D, PH, 2,2 mm | 0,5 / 0,4 | 68,9 / - |
| D, PH, 5,0 mm | 1,3 / 0,7 | 30,8 / - |
| D, 15V-1, RT, 2,9 mm | 1,0 / 0,9 | 41,9 / - |
| E, RT, 2,5 mm | 0,5 / 0,4 | 57,3 / - |
| F, RT, 2,4 mm | 0,5 / 0,3 | 57,7 / - |
| G, RT, 1,2 mm | 0,7 / 0,6 | 78,0 / - |
| HIP, 12V-1 | 0,8 / 0,2 | 29,9 / 3,8 |
| HIP, 12V-2 | 0,9 / 0,3 | 28,3 / 0,8 |
| HIP, 15V-2 | 0,9 / 0,3 | 21,9 / 0,9 |
| HIP, 10V | 1,1 / 0,4 | 30,0 / 2,6 |

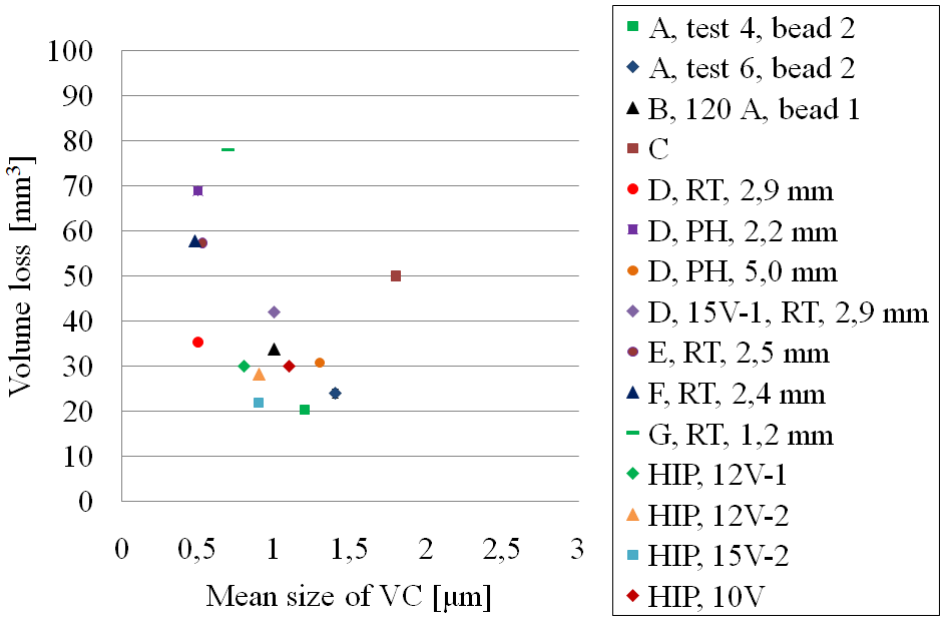


Figure 92 Volume losses of the tool steel deposits welded with welding parameters A-G and the tool steel materials manufactured by the HIP process plotted as a function of mean size of VC

### 6.7.6 Carbide morphology

In Table 30 and Figure 93 are presented width to height ratios of VCs of the PTA welded deposits and the materials manufactured by the HIP process. The PTA welded deposit welded with welding parameters A, test 6, bead 2 had the shape ratio of 0,83. The shape ratios of the PTA welded deposits varied between 0,66-0,83. The 15V-1 tool steel deposit had the lowest shape ratio, 0,66. The most round-shaped carbides were obtained with the tool steel materials HIP 12V-1 and HIP 12V-2, 0,86 and 0,85, respectively. The tool steel materials HIP 15V-2 and HIP 10V had the shape ratios of 0,83. The best abrasive wear resistance was obtained with the samples having the best shape ratio.

The carbides shape ratios of the weld beads 1, 2, 5, and 12 of the 1,0 mm thick deposit welded with welding parameters D were 0,78, 0,78, 0,73, and 0,75, respectively. The carbides shape ratios of the weld beads 1-3 welded with welding parameters B were 0,75, 0,71, and 0,74, respectively. Thus, the carbides shape ratios seem to decrease due to overlapping in the deposits welded with welding parameters B and D.

The carbides shape ratios of the weld beads 1 and 5 welded with welding parameters E and F were 0,74, 0,77 and 0,77, 0,80, respectively. Thus, the carbides shape ratios of the deposits welded with welding parameters E and F seem to increase during the surfacing procedure.

Table 30 VCs shape ratios and volume losses of the tool steel deposits welded with welding parameters A-G and the tool steel materials manufactured by the HIP process

| Material | Carbides shape ratio / s.d. / median | Volume loss / s.d. [$mm^3$] |
|---|---|---|
| A, test 4, bead 2 | 0,75 / 0,20 / 0,79 | 20,4 / - |
| A, test 6, bead 2 | 0,83 / 0,18 / 0,88 | 23,9 / - |
| B, 120 A, bead 1 | 0,75 / 0,22 / 0,80 | 33,8 / - |
| B, 120 A, bead 2 | 0,71 / 0,24 / 0,72 | - |
| B, 120 A, bead 3 | 0,74 / 0,22 / 0,78 | 31,6 / - |
| C | 0,68 / 0,22 / 0,71 | 50,0 / - |
| D, RT, 2,9 mm | 0,74 / 0,24 / 0,79 | 35,3 / - |
| D, RT, 2,9 mm, bead 1 | 0,77 / 0,23 / 0,83 | - |
| D, RT, 2,9 mm, bead 5 | 0,71 / 0,24 / 0,74 | - |
| D, RT, 1,42 mm/s, 2,8 mm | 0,69 / 0,25 / 0,73 | - |
| D, RT, 1,49 mm/s, 2,7 mm | 0,76 / 0,22 / 0,82 | - |
| D, PH, 2,2 mm | 0,70 / 0,26 / 0,75 | 68,9 / - |
| D, PH, 5,0 mm | 0,74 / 0,21 / 0,80 | 30,8 / - |
| D, 15V-1, RT, 2,9 mm | 0,66 / 0,26 / 0,70 | 41,9 / - |
| D, RT, 1,0 mm, bead 1 | 0,78 / 0,20 / 0,82 | - |
| D, RT, 1,0 mm, bead 2 | 0,78 / 0,22 / 0,85 | - |
| D, RT, 1,0 mm, bead 5 | 0,73 / 0,23 / 0,80 | - |
| D, RT, 1,0 mm, bead 12 | 0,75 / 0,22 / 0,81 | - |
| E, RT, 2,5 mm | 0,75 / 0,24 / 0,81 | 57,3 / - |
| E, RT, 2,5 mm, bead 1 | 0,74 / 0,25 / 0,80 | - |
| E, RT, 2,5 mm, bead 5 | 0,77 / 0,23 / 0,83 | - |
| F, RT, 2,4 mm | 0,78 / 0,23 / 0,86 | 57,7 / - |
| F, RT, 2,4 mm, bead 1 | 0,77 / 0,23 / 0,85 | - |
| F, RT, 2,4 mm, bead 5 | 0,80 / 0,22 / 0,87 | - |
| G, RT, 1,2 mm | 0,70 / 0,25 / 0,74 | 78,0 / - |
| HIP, 12V-1 | 0,86 / 0,17 / 0,92 | 29,9 / 3,8 |
| HIP, 12V-2 | 0,85 / 0,17 / 0,91 | 28,3 / 0,8 |
| HIP, 15V-2 | 0,83 / 0,18 / 0,90 | 21,9 / 0,9 |
| HIP, 10V | 0,83 / 0,17 / 0,88 | 30,0 / 2,6 |

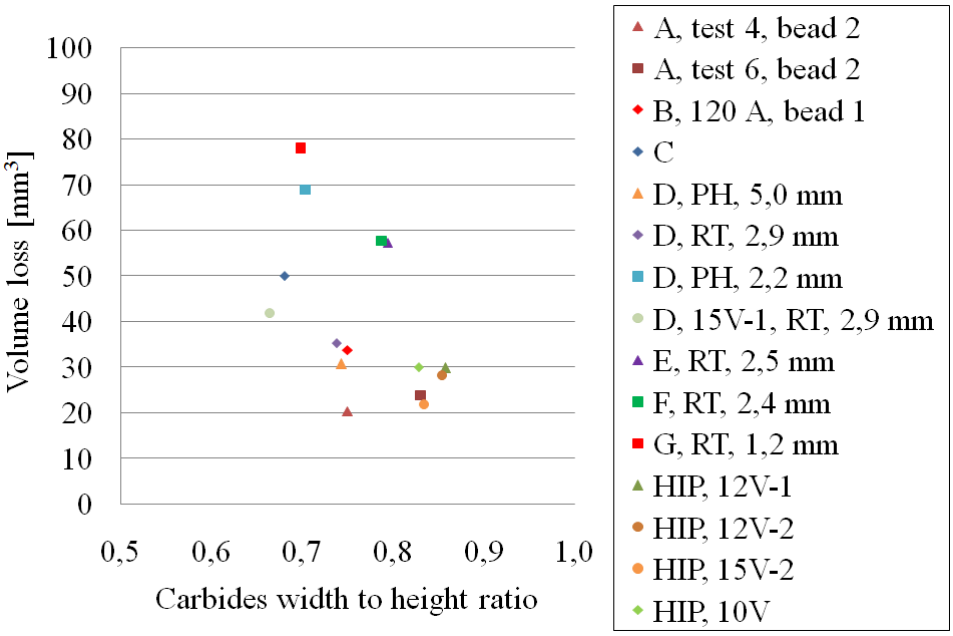


Figure 93 Volume losses of the tool steel deposits welded with welding parameters A-G and the tool steel materials manufactured by the HIP method as a function of carbides width to height ratio

### 6.7.7 Mean free path

The MFPs of the 12V-1 tool steel deposits were between 0,6-2,2 µm, Table 31 and Figure 94. The lower limit of the abrasive was about 100 µm. Thus, the whole abrasive is not able to degrade the matrix material between the VCs. The best abrasive wear resistance was obtained, when the MFP was 1,5 µm. The sample was welded with welding parameters A. The MFPs of the tool steel materials manufactured by the HIP process were between 0,8-1,3 µm.

Table 31 MFPs and volume losses of the tool steel deposits welded with welding parameters A-G and the tool steel materials manufactured by the HIP process

| Material | MFP / s.d. [µm] | Volume loss / s.d. [$mm^3$] |
|---|---|---|
| A, test 4, bead 2 | 1,4 / 0,8 | 20,4 / - |
| A, test 6, bead 2 | 1,5 / 1,0 | 23,9 / - |
| B, 120 A, bead 1 | 1,4 / 0,8 | 33,8 / - |
| C | 2,2 / 1,3 | 50,0 / - |
| D, RT, 2,9 mm | 0,8 / 0,5 | 35,3 / - |
| D, PH, 2,2 mm | 0,7 / 0,4 | 68,9 / - |
| D, PH, 5,0 mm | 1,7 / 1,3 | 30,8 / - |
| D, 15V-1, RT, 2,9 mm | 1,1 / 0,8 | 41,9 / - |
| E, RT, 2,5 mm | 0,6 / 0,3 | 57,3 / - |
| F, RT, 2,4 mm | 0,7 / 0,5 | 57,7 / - |
| G, RT, 1,2 mm | 0,8 / 0,6 | 78,0 / - |
| HIP, 12V-1 | 1,0 / 0,5 | 29,9 / 3,8 |
| HIP, 12V-2 | 1,0 / 0,6 | 28,3 / 0,8 |
| HIP, 15V-2 | 0,8 / 0,4 | 21,9 / 0,9 |
| HIP, 10V | 1,3 / 0,8 | 30,0 / 2,6 |

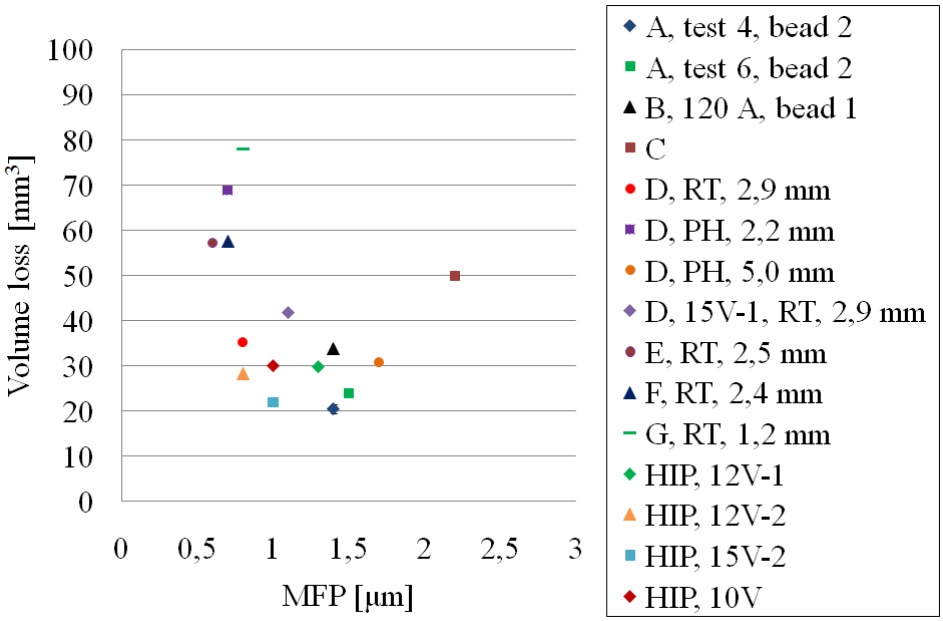


Figure 94 Volume losses of the tool steel deposits welded with welding parameters A-G and the tool steel materials manufactured by the HIP process plotted as a function of MFP

### 6.7.8 Volume fraction of vanadium carbides

In Figure 95 is presented the effect of the volume fraction of VCs on the abrasive wear resistance. The highest volume fraction of VCs of the 12V-1 tool steel material was obtained with the 12V-1 tool steel material manufactured by the HIP process, 18,0 vol.-%. The volume fraction of VCs of the HIP material containing 11,5 % vanadium has been earlier measured to be 18,2 (Kivikytö-Reponen, 2006) and 20,0 vol.-% (Ala-Kleme *et al*., 2007).

The best abrasive wear resistance was in the deposits welded with welding parameters A. The volume fraction was then between 15,5-15,7 vol.-%. In the 12V-1 tool steel deposit welded by the PTA method the volume fraction of VCs was between 12,2 and 17,5 vol.-%, Tables 17 and 32. Thus, the welding parameters have a remarkable effect on the microstructure and the abrasive wear resistance.

Table 32 Volume fractions of VCs and volume losses of the tool steel deposits welded with welding parameters A-G and the tool steel materials manufactured by the HIP process

| Material | Volume fraction / s.d. [vol.-%] | Volume loss / s.d. [$mm^3$] |
|---|---|---|
| A, test 4, bead 2 | 15,5 / 2,1 | 20,4 / - |
| A, test 6, bead 2 | 15,7 / 2,8 | 23,9 / - |
| B, 120 A, bead 1 | 13,4 / 1,7 | 33,8 / - |
| C | 17,5 / 5,5 | 50,0 / - |
| D, RT, 2,9 mm | 14,6 / 2,0 | 35,3 / - |
| D, PH, 2,2 mm | 14,3 / 1,7 | 68,9 / - |
| D, PH, 5,0 mm | 16,9 / 1,7 | 30,8 / - |
| D, 15V-1, RT, 2,9 mm | 20,3 / 3,7 | 41,9 / - |
| E, RT, 2,5 mm | 15,0 / 2,3 | 57,3 / - |
| F, RT, 2,4 mm | 16,0 / 2,4 | 57,7 / - |
| G, RT, 1,2 mm | 14,5 / 1,6 | 78,0 / - |
| HIP, 12V-1 | 18,0 / 0,8 | 29,9 / 3,8 |
| HIP, 12V-2 | 18,3 / 1,3 | 28,3 / 0,8 |
| HIP, 15V-2 | 20,6 / 0,7 | 21,9 / 0,9 |
| HIP, 10V | 14,7 / 1,2 | 30,0 / 2,6 |

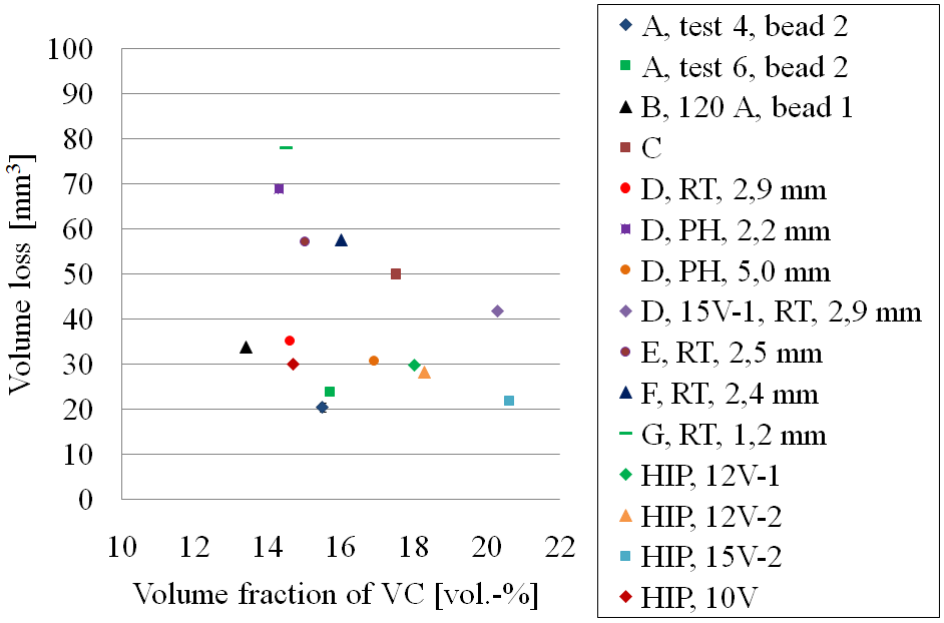


Figure 95 Volume losses of the tool steel deposits welded with welding parameters A-G and the tool steel materials manufactured by the HIP process plotted as a function of volume fraction of VC

### 6.7.9 Martensite and retained austenite contents

In Table 33 is presented martensite and retained austenite contents. In Figure 96 the volume loss of the tool steel materials is plotted as a function of martensite and retained austenite contents. Martensite contents were between 59,0-63,7 and 47,2-61,9 % in the deposits welded with welding parameters A-C and D-G, respectively. The materials manufactured by the HIP process had low retained austenite and high martensite contents. The HIP samples were double tempered at temperature 540-570 ºC. Hold time was 2 h. After heat treatment retained austenite content is low.

In the PTA welded deposits retained austenite contents were between 22,9 and 32,5 %. Retained austenite contents were slightly higher in the deposits welded with welding parameters E-G, between 28,3-31,3 %. Retained austenite contents were between 22,9-25,3 % in the deposits welded with welding parameters A-C. The deposit 15V-1 tool steel had 9,0 % higher retained austenite content when compared to the 12V-1 tool steel deposit welded with the same welding parameters D.

Teupke (2002) measured retained austenite contents for variety of PTA welded tool steel alloys. Similar composition as 12V-1 tool steel was not present. According to the X-ray measurements retained austenite content for the PTA welded 12V-1 tool steel deposit should be between 22-30 vol.-%. Bourithis *et al.* (2005) measured retained austenite contents of the PTA welded deposits according to ASTM E975-95 standard, and obtained 25±5 vol.-%. The alloy contained C 1,9 %, Ti 5,2 %, Cr 4,3 %, Mo 1,5 %, Mn 0,8 %, and Si 0,2 %. The proportion of TiC in the layer was 23±4 vol.-%. Wang *et al.* (2006) measured that LB welded deposits CPM 9V, CPM 10V, CPM 15V, and M4

had relative volumetric ratios of retained austenite to martensite of 8,5, 1,3, 1,5, and 0,26 in as-welded condition and 0,2, 0,1, 0,0, and 0,0 after heat treatment at 600 °C, respectively. Xu *et al*. (2007) measured retained austenite contents based on ferromagnetism for an alloy C 2,98 %, V 9,8 %, Cr 4,25 %, Mo 2,95 %, Si 0,65 %, Mn 0,83 %, S 0,05 %, and P 0,06 % manufactured by casting. After quenching/tempering at temperatures 900/550, 900/600, 950/550, 950/600 ºC retained austenite contents were 6,8, 2,0, 6,0, and 4,3 vol.-%, respectively.

Table 33 Martensite and retained austenite contents of the tool steel deposits welded with welding parameters A-G and the tool steel materials manufactured by the HIP process

| Material | Martensite / s.d [%] | Retained austenite [%] |
|---|---|---|
| A, test 4, bead 2 | 60,9 / 1,4 | 23,6 |
| A, test 6, bead 2 | 59,0 / 0,4 | 25,3 |
| B, 120 A, bead 1 | 63,7 / 1,0 | 22,9 |
| C | 59,1 / 1,1 | 23,4 |
| D, RT, 2,9 mm | 61,9 / 4,5 | 23,5 |
| D, PH, 2,2 mm | 57,9 / 1,9 | 27,8 |
| D, PH, 5,0 mm | 54,4 / 5,1 | 28,7 |
| D, 15V-1, RT, 2,9 mm | 47,2 / 3,0 | 32,5 |
| E, RT, 2,5 mm | 53,7 / 2,3 | 31,3 |
| F, RT, 2,4 mm | 54,7 / 4,7 | 29,3 |
| G, RT, 1,2 mm | 57,2 / 4,0 | 28,3 |
| HIP, 12V-1 | 78,3 / 2,2 | 3,7 |
| HIP, 12V-2 | 74,9 / 5,7 | 6,8 |
| HIP, 15V-2 | 75,5 / 1,2 | 3,9 |
| HIP, 10V | 80,2 / 1,8 | 5,1 |

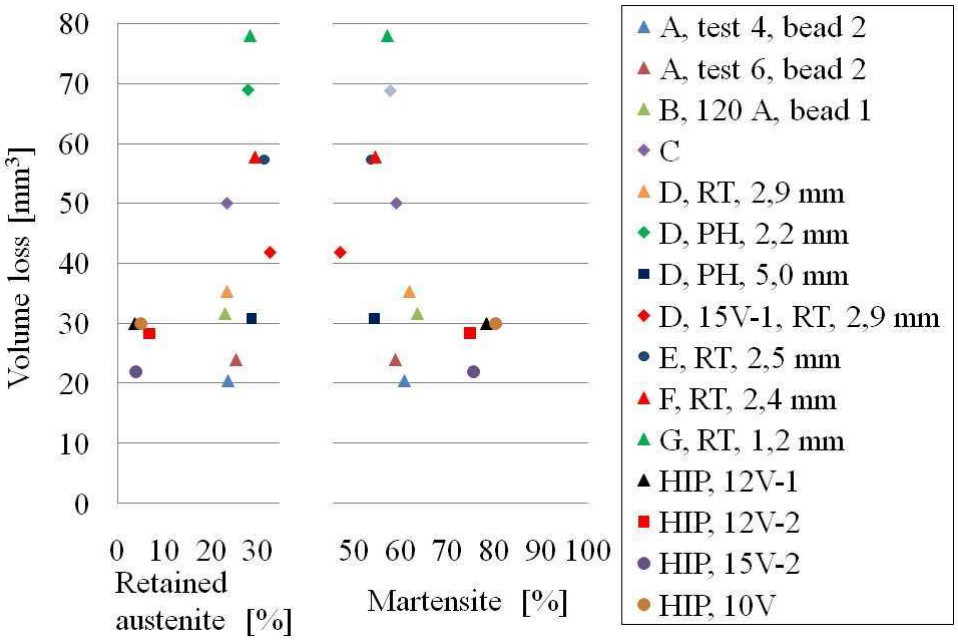


Figure 96 Volume losses of the tool steel deposits welded with welding parameters A-G and the tool steel materials manufactured by the HIP process as a function of retained austenite and martensite contents

## 6.8 Wear tracks

### 6.8.1 Low stress abrasive wear

The wear tracks of the samples welded with welding parameters A, C, and D are presented in Figures 97a-f. In Figures 98a, b is presented the wear track of the tool steel 12V-1 reference sample manufactured by the HIP process. Microcracking of VCs can be seen in every wear track.

The deposit welded with welding parameters A, test 4, bead 2, had the best abrasive wear resistance in the RWAT. In Figures 97a, b can be seen the round-shaped, relatively homogeneously precipitated VC carbides. The volume fraction of VCs in the wear track was approximately 25-30 vol.-%. The matrix metal has worn away and the carbides are slightly above the matrix surface as was presented in Figure 38b. The volume fraction of VCs has increased when compared to the microstructure, Figures 68a, b. Due to abrasive wear the carbides in different depths can be seen, thus, the volume fraction of VCs increases. Some of the VCs were crushed during the RWAT.

The abrasive wear resistance of the deposits welded with welding parameters C and D was quite the same. In Figures 97c, d and 97e, f can be seen bigger and smaller carbides as well as areas where carbides are not present. Thus, these microstructures are not as homogeneous as the microstructures presented in Figures 68a, b and 68c, d. Microcracking of VCs can be seen. The volume fractions of VCs in the wear tracks

were 20-23 vol.-%. Thus, in the wear tracks the volume fractions of VCs were higher as were estimated from the microstructures because of abrasive wear.

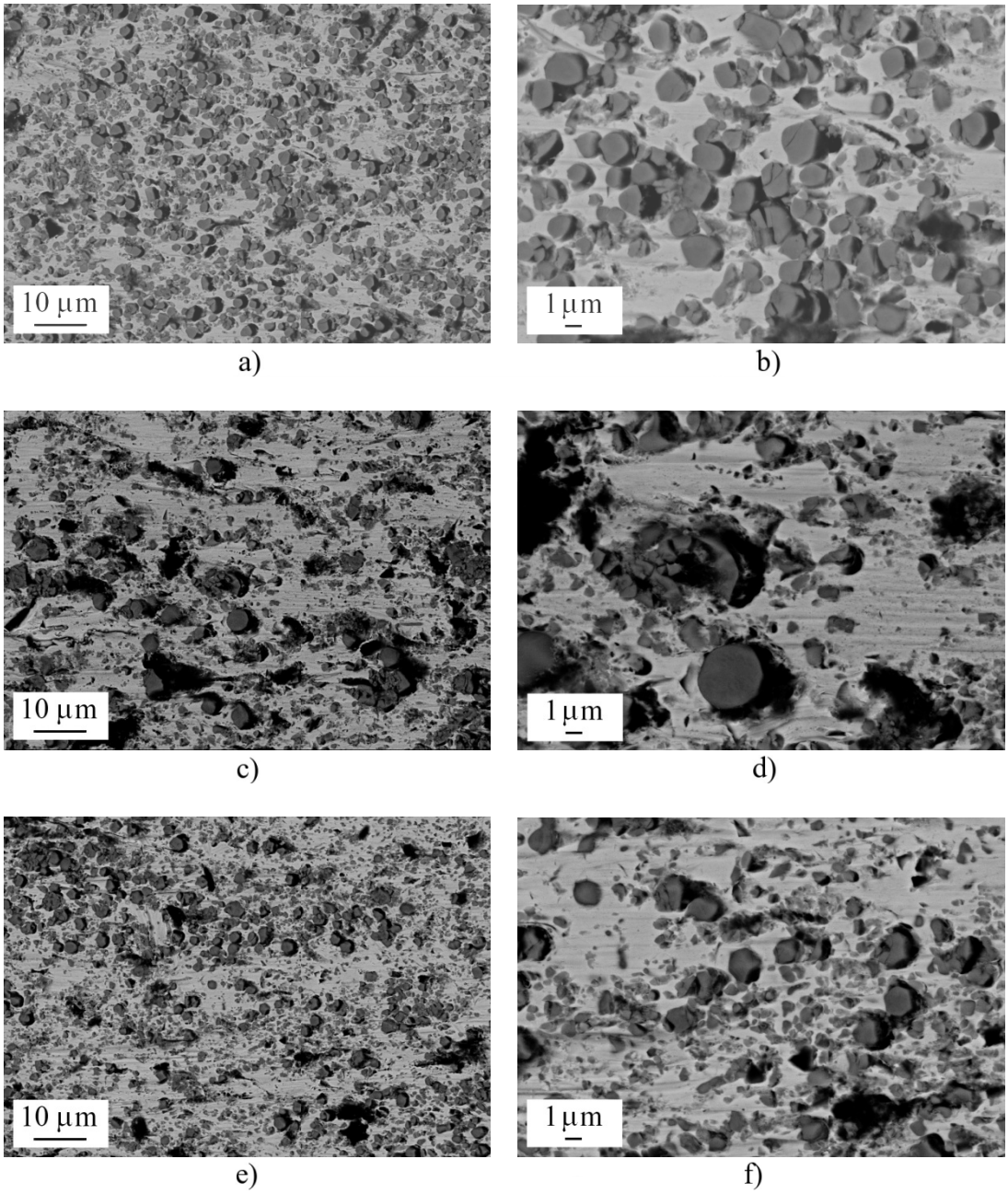


Figure 97 Wear tracks of the samples welded with welding parameters: a, b) A, test 4, bead 2, c, d) C, and e, f) D, RT, 2,9 mm, 73 A

In the reference material, i.e., the 12V-1 tool steel material manufactured by the HIP process, the wear track was similar as the wear track of the deposit welded with welding parameters A, Figures 98a, b. VCs were relatively homogeneously distributed. Cracking of VCs was minor. The volume fraction of VCs in the wear track was approximately 23 vol.-%, which is approximately 5 vol.-% higher amount as was estimated from the microstructure.

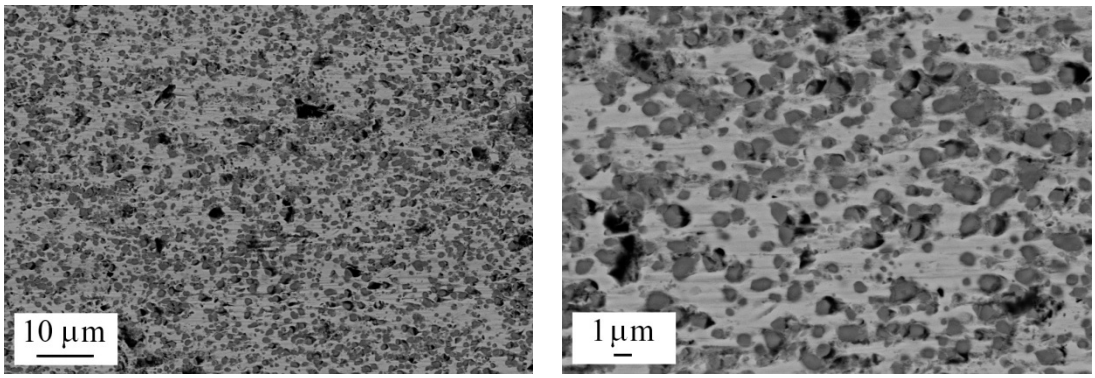


Figure 98 a, b) Wear track of the 12V-1 tool steel material manufactured by the HIP process

### 6.8.2 High stress abrasive wear

In Figures 99a, b is presented the wear track of the deposit welded with welding parameters A, test 2, bead 1. Normal load 174 N was used for testing high stress abrasive wear. Microcutting and microploughing can be seen in the areas where the MFP is high. Rolling of the abrasives was at least partly prevented. In Figure 99b can be seen three wear scars ending to a 3,2 µm sized carbide edge. Thus, normal load has been high enough to crush abrasives. Also a lot of crushed VCs were observed on the wear track.

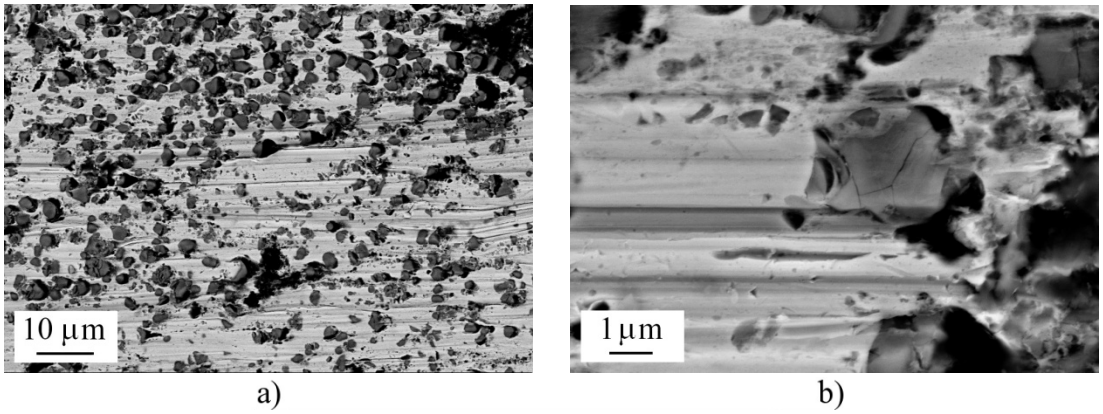


Figure 99 Wear track of the 12V-1 tool steel deposit welded with welding parameters A, test 2, bead 1, and abraded with load 174 N in the RWAT: a) an overview and b) three wear scars ending to the edge of the crushed 3,2 µm sized vanadium carbide

# 7 Discussion

## 7.1 PTA equipment

In this study the deposits were surfaced by the mechanized and the robotized PTA welding units. The number of welding parameters is high in the PTA process. In mass production the surfacing process has to be very stable. The effect of each welding parameter and their interactions has to be known.

The wear resistant welded deposits are normally 1-6 mm thick. The weldability of the 12V-1 tool steel powder was good. Surfaces of the deposits were relatively even. Thickness range 2-4 mm for the 12V-1 tool steel deposits is easy to weld by the PTA method. Thickness range 4,5-6,0 mm for the 12V-1 tool steel deposit is challenging. Problems in the dilution control and, thus, welding defects may occur in the fusion line because of the large size of the molten pool.

Basically the dilution was easier to control, when the robotized PTA unit was used, because reproducibility of the process was much better. Overlapping movement was made manually with the mechanized unit, which is time consuming process. Programming of the robot takes time. Both the mechanized and the robotized welding units were suitable for the PTA process.

## 7.2 Dilution

### 7.2.1 Temperature of work piece

Preheating was used with welding parameters A, B, and D. The work pieces were preheated by the acetylene torch. The preheated work pieces were surfaced by 2-5 overlapping weld beads. One reason for inaccuracy in the dilutions of the deposits was the change in the temperature of the work piece during the welding process. Because of the mechanized welding unit, the plasma torch was displaced manually between the weld beads during the PTA welding process. This procedure took from 2 to 4 min. During this waiting time the temperature of the work piece decreased. With welding parameters D the deposits were welded by the robotized welding unit. Thus, the welding process was continuous and no decreasing temperature of the work piece was obtained.

The preheating temperatures for welding parameters A were 200 or 300 °C. Two overlapping weld beads were welded and no remarkable decreasing temperature was detected. At temperatures 200-300 °C the temperature of the work piece may decrease 20-50 °C while displacing the plasma torch. The effect of the temperature change of the work piece on the dilution was 1 % / 30 °C in the 4 mm thick deposits (Hunt, 1988; Sharples, 1985).

The temperature change was the biggest for the deposits welded with welding parameters B, because of high preheating temperature, 450 °C. The work piece was preheated to 570 °C, but the temperature decreased to 450 °C while welding the first bead. The temperatures of the work pieces welded with welding parameters B were on average 370-450 °C after the third bead was welded. The effect of the temperature change of the work piece on the dilution was 1 % / 30 °C in the 4 mm thick deposits and 2 % / 30 °C in the 2 mm thick deposits (Hunt, 1988; Sharples, 1985). In according to theory, the dilutions of the second and third weld beads welded with welding parameters B can be decreased approximately 2 % per each bead due to temperature changes of the work pieces.

### 7.2.2 Plasma arc current

The dilution of the deposit is the easiest to adjust by plasma arc current. In Table 13 was presented used plasma arc currents and the dilutions of the welded beads. The temperature of the work piece increased from RT to 250 ºC, while plasma arc current was reduced from 74 to 58 A. The dilution control is challenging, because the welding operator has to adjust plasma arc current during the welding process. Without any auxiliary equipment like optical emission spectrometer, the adjustment can be made only by experience of the welding operator.

Preheating for the 12V-1 tool steel powder is not necessary to avoid cracking of the deposit. It is possible to preheat the deposit to 250-300 °C temperature, which is typical temperature of the work piece during the PTA welding process. Typical operating temperature for the middle-sized application is on average 288 ºC (Kapus, 1980). Thus, need to adjust plasma arc current during the welding process is minor, if suitable preheating temperature is used. Therefore, preheating makes it easier to control the dilution. The PTA process is then stable, powder fraction can be more precisely tailored for used heat input and the consumable efficiency can be optimized. Then, the PTA process is economical.

### 7.2.3 Powder feed rate

In Table 13 was presented thicknesses of the weld beads. Because plasma arc current had to be reduced for getting the optimal dilution, the reduced heat input was not enough to melt the larger particle fractions. Therefore, thicknesses of the weld beads were reduced when plasma arc current was decreased. The decreasing size of the molten pool changes the location of the plasma arc in relation with the molten pool. This effect has an effect on the dilution, because the plasma arc heats then more the base material.

The powder fraction was the same in all welding tests, even though welding parameters changed a little. By increasing powder feed rate the decreasing consumable efficiency can be controlled. If powder feed rate is varied also plasma arc current has to be adjusted for melting the increased amount of powder. However, in the mass production the powder fraction is optimized with plasma arc current and heat input to maximize the consumable efficiency.

In the welding tests A, B, D, E, and F with overlapping weld beads the thickness of the deposits increased bead by bead. After the 2-5th weld bead was welded depending on the welding parameters, the thickness of the deposits achieved their maximum thickness. Because the overlapping distances were shorter than the widths of the beads, the thicknesses of the beads increased. This effect has an effect on the dilution, because the plasma arc heats then more the molten pool. To get even surface powder feed rate has to be decreased after the first weld bead is welded. Heat input has to be balanced to the changed powder feed rate.

### 7.2.4 Location of plasma arc

The plasma arc column was directed to the edge of the molten pool, when the deposits were welded with welding parameters A, B, D, and E. The location of the plasma arc was detected visually. The dilutions of the deposits were then optimal. When heat input and the dilution increased, the molten pool increased, too. Therefore, the plasma arc heated more the molten pool and its size increased further. This caused penetration problems, because the plasma arc moved more on the molten pool. The molten pool restricts the plasma arc ability to form penetration.

In welding tests with welding parameters C and F the location of the plasma arc was on the molten pool. Even though plasma arc current was increased, the dilution remained at low level. Welding defects were occasionally found from the fusion lines. In case of pure abrasive wear resistance some welding defects in the fusion line have no effects on the detachment of the deposit. The dilution control is easier when the location of the plasma arc is on the molten pool than in the edge of the molten pool.

### 7.2.5 Argon-hydrogen gas mixtures

Hydrogen increases mobility and the size of the molten pool and, thus, the molten pool restricts the formation of the penetration. Because hydrogen also increases the wettability of the molten pool, welding defects were seldom detected. The molten pool was between the plasma arc and the work piece when Ar + 5 % $H_2$ gas mixture was used.

Because of enhanced wettability due to hydrogen, the dilution control was the easiest with welding parameters F, then with E, and worst with D. With welding parameters D the controllability of the dilution still decreased, when the temperature of the work piece was increased.

## 7.3 Microstructure

The microstructures of the PTA welded deposits are not completely homogeneous, thus, the point from where the picture has been taken, can have an effect on the results. The analyzing method also may have an effect on the accuracy of the results.

### 7.3.1 Volume fraction of vanadium carbides

The volume fractions of VCs in the 12V-1 tool steel deposits varied between 12,2-17,5 vol.-% depending on the welding parameters. The measurements were made from the core of the deposits. The volume fraction varies as a function of distance from the fusion line. Nearby the fusion line the volume fraction of VCs was 3 vol.-% lower when compared to the core and top of the deposit welded with welding parameters B. The dilution from the base material is the main explanation. Preheating was high with welding parameters B. Thus, the base material had no remarkable effect on cooling time nearby the fusion line.

The deposits welded with 25 mm oscillation width had slightly higher volume fraction of VCs as the deposits welded with 6,5 mm oscillation width, when the location of the plasma arc was in the edge of the molten pool. By relocating the plasma arc more on the molten pool, the volume fraction of VCs increased. The volume fractions of VCs of the deposits C, 175 A and D, RT, 5,0 mm were 17,5 and 16,9 vol.-%, respectively. The volume fraction of VCs of the 12V-1 tool steel material manufactured by the HIP process was approximately 18,0 vol.-%. The volume fractions of VCs of the deposits welded by the PTA process are lower than in the tool steel materials manufactured by the HIP process. The location of the plasma arc on the molten pool is useful when high volume fraction of VCs is necessary. The highest volume fraction of VCs was obtained with welding parameters C. The size of the molten pool and the bead thickness were the biggest.

The volume fractions of VCs of the deposits having V 10-12 % and V 15-18 % were 17-20 vol.-% and 26-31 vol.-%, respectively, when welding tests were welded by the PTA welding method, while the other chemical components were Cr 4-6 %, Mo 1-2 %, Si 1 %, and Mn 1 % (Gebert *et al*., 2001). The deposit welded with welding parameters C had similar volume fraction of VC.

### 7.3.2 Size and morphology of vanadium carbides

The mean size of VCs depends on the welding parameters. The mean size of VCs was the highest in the deposit welded with welding parameters C. The location of the plasma arc was then on the molten pool. Even though the mean size of the VCs was high, the shapes of the VCs were partly round-shaped and partly needle-shaped in the deposit welded with welding parameters C. The most round-shaped VCs was obtained with welding parameters A, test 6, bead 2, having the shape ratio of 0,83. The carbides shape ratio of the weld bead welded with welding parameters A, test 4, bead 2, 0,75, does not correlate with the shapes of the carbides presented in Figures 97a, b. The PTA welded deposits are not as homogeneous as the materials manufactured by the HIP process. In the materials manufactured by the HIP process the shape ratios were 0,83-0,86. In the other welding parameter windows the shapes of the VCs were more needle-shaped. In the microstructure of the deposit D, RT, 5,0 mm some round-shaped VCs were obtained, even though the location of the plasma arc was slightly on the molten pool. Low heat input may explain the result. In the deposits welded with welding parameters E-F, the sizes of VCs were relatively small. The shapes of VCs of the deposits welded

with welding parameters E and F were more needle-shaped in the first beads when compared to the shapes of VCs of the fifth beads.

Convection of the molten pool by the plasma arc has an effect on the deposit microstructure. Convection of the molten pool caused stirring effect, thus, the VCs were formed as long, narrow needle-shaped carbides. The strength of the factors affecting the weld pool convection, i.e., electromagnetic or Lorentz force, buoyancy or gravity force, surface tension or Marangoni force, and impinging, friction or aerodynamic drag force of the arc plasma, cannot be analysed from the SEM pictures.

### 7.3.3 MFP

The MFP was the highest in the deposit welded with welding parameters C. Also the mean size of VCs was the highest. In the deposits welded with welding parameters A, tests 4 and 6 the MFPs and the mean sizes of VCs were almost the same. Stirring by the plasma arc may produce smaller and needle-shaped VCs as well as smaller MFP. The MFP was the lowest in the deposits welded with welding parameters D-F, RT.

### 7.3.4 Cumulative volumes of vanadium carbide sizes and MFPs

The cumulative volumes of the VC sizes and the MFPs of the deposits were analyzed. In the deposits welded with welding parameters A, B, C, D-F, and G, 20-40, 70, 20, 40-96, and 80 % of VCs were smaller than 1 μm, respectively. In the materials manufactured by the HIP process, 48-81 % of VCs were smaller than 1 μm. The sizes of VCs can be controlled by adjusting the welding parameters. For instance, in the parameter window D the amount of the sub-micron-sized VCs can be in the range of 40-96 %, mainly depending on the location of the plasma arc.

The MFP is not constant in the 12V-1 tool steel deposits. In the deposit welded with welding parameters C it has remarkably higher value when compared to the other deposits. 80 % of the measured distances between the carbides were higher than 1 μm. 15 % of the distances were higher than 3 μm. The MFP was 0,8-1,3 μm for the materials manufactured by the HIP process. Thus, the MFPs were bigger in the deposits welded with welding parameters A-C.

### 7.3.5 Retained austenite

Retained austenite contents were between 22,9 and 32,5 % depending on the welding parameters. The volume fraction of VCs has an effect on the retained austenite content. Retained austenite content is one of the explanations to the volume loss in the RWAT. In Figure 96 the volume loss increases rapidly when the retained austenite content increases. However, the volume loss of the PTA welded 12V-1 tool steel deposit depends on the volume fraction of VCs, the size of the VCs, the MFP, the carbides morphology, and the matrix phases.

Retained austenite content can be decreased by double tempering. The best abrasive wear resistance was obtained after double tempering at 560 ºC. Bouaifi *et al*. (1993) had the highest hardness for the 5 % diluted 240 Cr5MoV10 deposit at the same temperature. Hardness of the 240 Cr5MoV10 deposit was in as-welded condition 59-61 HRC and after double tempering 63,8-65 HRC. After double tempering at 560 ºC the volume loss of a 10 % diluted deposit welded with welding parameters E decreased from 61,4 to 43,7 $mm^3$.

### 7.3.6 Microstructural changes in weld bead

The PTA method is used sometimes for surfacing small-sized components or small-sized areas. Changes in the microstructure were detected in a bead welded with welding parameters B. In Table 17 and Figure 68e are presented the volume fraction, the mean size, and the MFP of VCs of the deposit welded with welding parameters B. The original VCs melt completely and precipitate during cooling time. In the beginning of the bead, after the plasma arc is ignited, the size of the molten pool is small and cooling time is short. VCs do not have enough time to grow. As can be seen from Table 23 and Figures 85a-c the volume fraction of VCs increases from the plasma arc ignition point to the end of the bead. The shape ratio increased from 0,67±0,25, 0,71±0,20 to 0,76±0,21. The changes in the microstructure were small after 25 mm welding distance. However, it has to be noticed that the best abrasive wear resistance can be achieved at the end of the weld bead.

### 7.3.7 Oscillation mode and welding speed

The deposits welded with welding parameters D-F were welded with sine wave oscillation mode. The carbides were mainly needle-shaped and relatively small-sized. The welding speed was 1,35 mm/s. The welding speed was increased from 1,35 to 1,42 and 1,49 mm/s to detect its effect on the microstructure. In Table 18 and Figures 71a-c are presented the volume fraction, the mean size, and the MFP of VCs of the deposits welded with welding parameters D by varying welding speed. The increasing welding speed enhanced the shapes of VCs, i.e., with welding speed 1,49 mm/s the carbides were more round-shaped. The volume fraction decreased rapidly, thus, heat input was too low to maintain the volume fraction of VCs. The increasing welding speed had no remarkable beneficial effects on the microstructure. With sine wave oscillation mode the plasma arc has to be too far away from the molten pool to get round-shaped carbides. In the edge of the sine wave the plasma arc has not movement in the welding direction. Thus, the plasma arc moves over the molten pool and stirs it, which has a detrimental effect on the shapes of the carbides.

In the deposits welded with welding parameters B the linear movement in the end of the oscillation wave was 2,1 mm. The microstructure contained especially with higher dilutions more needle-shaped carbides. It was obvious that the plasma arc was moved slightly on the molten pool, because of the increased dilution, following the increased size of the molten pool, and the location of the plasma arc was then more on the molten pool.

The welding tests with welding parameters A were made by increasing the linear movement in the end of the oscillation wave from 2,1 to 2,2 mm. Mainly round-shaped VCs were obtained. The volume fraction of VCs remained at 15,5-15,7 vol.-%, which is 2,3-2,5 vol.-% lower value as in the 12V-1 tool steel material manufactured by the HIP process. The rectangular wave oscillation mode was the most useful oscillation wave mode, because it had minor stirring effect on the molten pool after dwell time was adjusted. Also the location of the plasma arc was easy to maintain during the welding tests.

Thickness and width of the weld bead, deposition rate, oscillation mode, welding speed, heat input, and location of the plasma arc determine mainly the size of the molten pool in the PTA process. When the volume of the molten pool increases, the volume fraction and the size of the carbides increase. The PTA process is just in the right range of variation, so that the sizes of the carbides can be determined within specified limits by changing the oscillation parameters and the deposition rate.

### 7.3.8 Overlapping

The effects of overlapping on the microstructure were detected from the deposits welded with welding parameters B and D. In the first weld bead, especially in the deposit welded with welding parameters D, VCs were more round-shaped. In the deposits welded with both welding parameters the next weld beads contained more needle-shaped VCs. The differences were small and may vary in the deposit cross-section. Two- or three-dimensional heat flow may have effect on the microstructure when surfacing larger areas including edges of the component. However, the carbides shape ratios of the weld deposits welded with welding parameters E and F increased during the surfacing process.

## 7.4 Abrasive wear resistance

### 7.4.1 Microstructure

The abrasive wear resistance of the 12V-1 tool steel deposit depends on the volume fraction of VCs, the mean size of VCs, the shapes of the carbides, the MFP, and the matrix phases. These factors can be lightly adjusted by the welding parameters. Also the wear environment, mainly the sizes of the abrasives, its asperities, attack angle, and normal load have effects on the abrasive wear resistance.

The abrasive wear resistance increased when the mean size of VC carbides increased from 0,5 to 1,2-1,4 μm. Above 1,4 μm mean size of VC carbides, no increase in the abrasive wear resistance was obtained. The MFP was the highest in the deposit welded with welding parameters C. Thus, it is possible that the MFP above 2 μm reduces dramatically the abrasive wear resistance because at the ratio $\lambda_{MPF}/d_a > 1$ the abrasive particles can wear-off the matrix. The abrasive range was from 100 to 600 μm. Thus,

only asperities of the abrasives can abrade the matrix material between VCs. In the wear tracks presented in Figures 97a-f can be seen that between the carbides are lots of wear scars, the widths of which are between 0,1-0,5 μm. The abraded material may be cut-off carbides, crushed carbides, crushed abrasives, or asperities of the quartz sand particles.

The shape of VCs had remarkable effect on the abrasive wear resistance. In the deposits welded with welding parameters A the most round-shaped VCs were detected from the microstructures and especially from the wear tracks. The abrasive wear resistances of the deposits welded with welding parameters A were 1,5-3,0 times higher than in the deposits welded in the other parameter windows. The deposits welded with welding parameters A had low retained austenite contents. Thus, higher amount of martensite had greater ability to support the round-shaped carbides.

### 7.4.2 Dilution

The effect of the increasing dilution of the 12V-1 tool steel deposit on the abrasive wear resistance was not possible to analyze exactly. The dilution means that the alloying elements from the thin layer of the base material are diluted to the deposit. In the PTA method, 5-10 % dilution is easy to maintain during the welding process. Thus, its effect on the microstructure and the wear resistance remain constant during the welding process. In Table 13 was presented the dilution of the weld beads, which remained quite constant during the welding process.

The increasing dilution changes the location of the plasma arc in relation with the molten pool. When the dilution increases, increases the size of the molten pool and if the location of the plasma arc is not changed during the welding process, the microstructure changes because of stirring effect of the plasma arc and convection of the molten pool. This phenomena has to be noticed when the abrasive wear resistance and the dilution are compared to each other.

If only dilution is taken into account the volume loss in the deposits welded with welding parameters A and B increased from 4 to 25 $mm^3$ per 20 % increase in the dilution. In the deposits welded with welding parameters D the increased dilution from 7 to 15 % increased the volume loss 30 $mm^3$. In the deposits welded with welding parameters E the increased dilution from 5 to 15 % increased the volume loss 22 $mm^3$. In the deposits welded with welding parameters F the increased dilution from 4 to 9 % increased the volume loss 3 $mm^3$.

### 7.4.3 Plasma arc location

The dilution is not the only phenomenon explaining the wear resistance of the deposit. If the 6 and 0,5 %, 7 and 7 % diluted samples welded with welding parameters A and C, D and F are compared, the volume loss increased from 23,9 to 50 $mm^3$ and from 40 to 62 $mm^3$, respectively. Thus, even though the dilution remained constant the volume loss increased remarkably, depending on the welding parameters. The areas of the bead

cross-section in the deposits welded with welding parameters A, C and D, F were quite the same. Thus, it has no remarkable effect on the abrasive wear resistance.

The best abrasive wear resistance was obtained, when the plasma arc was in the edge of the molten pool. The location of the plasma arc was adjusted by linear movement in the edge of the oscillation wave, when rectangular wave mode was used. The best deposits welded with welding parameters A differ from the other welding parameters in addition with increased plasma gas flow rate and increased working distance. In the deposits welded with welding parameters B-G plasma gas flow rate was 2 l/min. It has not enough constricting effect on the plasma arc, i.e., the plasma arc column is still quite wide. With plasma gas flow rates 4 and 6 l/min the abrasive wear resistance was enhanced. By increasing further working distance from 8-9 to 10-12 mm, the abrasive wear resistance was optimized. The plasma arc is then more columnar. Higher working distance reduces the velocity of the plasma gas. The changes needed in surfacing parameters are often very fine.

In the deposits welded with welding parameters B the abrasive wear resistance was mainly better in the first beads. It is obvious that the microstructure changes due to overlapping, because the location of the plasma arc changes due to increased volume of the weld beads. When the second and the third weld bead were welded, the molten pool moved to the welding direction, and the location of the plasma arc changed. The changed location of the plasma arc restricts formation of penetration. Abrasive flow rate was higher with 105 rpm. Higher abrasive flow rate increases the volume loss. Also it has to be noticed, that the samples were first abraded with 105 rpm and after that test the samples were ground and tested again with 200 rpm. Variations in the RWAT may explain part of the results. Standard deviations 0,8-3,8 $mm^3$ were obtained for the materials manufactured by the HIP process. Standard deviations in hardness tests were larger in the deposits welded by the PTA process than in the materials manufactured by the HIP process. The effect of the dilution was not possible to analyze clearly.

Effect of plasma arc location on the abrasive wear resistance of the deposits welded with welding parameters D-F, RT, is not possible to analyze. The abrasive wear resistances of the weld beads welded with welding parameters D-F, RT, were not possible to analyse because of the smaller bead widths than the rubber wheel size. The microstructures of the deposits welded with welding parameters D, E, and F contained mainly small-sized and needle-shaped carbides. The microstructures and the abrasive wear resistances of the deposits D-F were quite the same. In the deposits welded with welding parameters E and F the carbides shape ratios seem to increase when the welding procedure continues. The size of the molten pool and cooling time are maybe both enough for VCs to grow up more round-shaped.

The deposit welded with welding parameters D, PH, 5,0 mm had the same abrasive wear resistance than that of the 12V-1 tool steel material manufactured by the HIP process. The abrasive wear resistance of the small-sized deposit may be enhanced by welding the plasma arc more on the molten pool. Then plasma gas flow rate, plasma arc current, and oscillating parameters have to be adjusted so that the stirring effect of the plasma arc remains low. The dilution is then close to zero, but usually only small pores

are detected from the fusion line, the defects of which do not have any effects on the detachment of the deposit.

### 7.4.4 Preheating

In parameter windows A-B and D, preheating had no measurable effect on the abrasive wear resistance. Excellent abrasive wear resistance is obtained with high amount of martensite. Preheating may have an effect on the amount of martensite. However, the effect of preheating was not possible to analyze from the welding tests. The austenite phase can undergo transformation from austenite to martensite during abrasive wear.

### 7.4.5 Wear tracks

The hard wear resistant carbides are needed to resist abrasive wear in the 12V-1 tool steel deposits. Because of the wear type, hard wear resistant matrix is also needed so that the benefits of the wear resistant carbides can be fully exploited. The surfaces of the 12V-1 tool steel wear test samples were even in visual inspection after the rubber wheel abrasion tests. Surface roughness measurements revealed that $R_a$ was 1,60 μm in the end of the test. Therefore, no deep grooves were formed.

In the 12V-1 tool steel deposits the abrasive wear resistance depends mainly on the volume fraction of VCs, the mean size of VCs, the carbides shape ratio, the MFP, and the matrix phases. The wear track of the deposit welded with welding parameters A contained after the RWAT relative homogeneously precipitated round-shaped carbides. The volume fraction of VCs in the wear surface was bigger than was estimated from the microstructure. The carbides were slightly above the wear surface, therefore, the volume fraction of VCs was increased. Thus, the round-shaped carbides have shielded the wearing surface very well.

In the wear tracks of the deposits welded with welding parameters C and D, the biggest carbides were left on the worn surface. A lot of crushed carbides can be seen. In the wear tracks can be seen areas, where the MFP was high. It is obvious that the smallest carbides have cut-off, while the biggest carbides are still present on the wear surface. The biggest carbides were crushing piece by piece. Some crushed and adhered carbides can be seen in the wear tracks.

In the wear track of the 12V-1 tool steel material manufactured by the HIP process can be seen 0,1-0,5 μm sized wear grooves. The distribution of VCs was homogeneous. Some crushed carbides can be seen. As a conclusion the material wears quite evenly without any dramatic carbide cut-off or grooving.

### 7.4.6 Welding parameters G

The deposit welded with welding parameters G was welded without oscillation, i.e., by straight passes. The microstructure contained VCs, the mean size of which was 0,7 μm.

The abrasive wear resistance was remarkably low, 78,0 $mm^3$. The abrasive wear resistances were 20,4-68,9 $mm^3$ in the deposits welded with welding parameters A-F by oscillating the plasma arc. Some pores were detected from the microstructure. These defects may decrease the abrasive wear resistance.

### 7.4.7 Reference material 15V-1 tool steel

The reference material 15V-1 tool steel for the microstructure and the abrasive wear tests was welded with welding parameters D without preheating. Layer thickness was 2,9 mm. The 15V-1 tool steel powder was more alloyed when compared to the 12V-1 tool steel powder. The volume loss of the 15V-1 tool steel deposit was 41,9 $mm^3$, while it was 37-112 $mm^3$ for the 12V-1 tool steel deposits welded with the same parameters. The volume fraction of VCs was 20,3 vol.-% for the 15V-1 tool steel deposit. It was 6 vol.-% higher volume fraction when compared to the 12V-1 tool steel deposits welded with the same welding parameters. Also the mean size of VCs was higher, 1,0 μm. The retained austenite content was the highest, 32,5 %, and the carbides shape ratio was the lowest.

Even though the 15V-1 tool steel powder was more alloyed, when comparing the 15V-1 tool steel deposit to the 12V-1 tool steel deposit welded with welding parameters A, the 15V-1 deposit had lower test result in the rubber wheel abrasion test. Therefore, it is obvious that by selecting more alloyed material, the wear resistance is not automatically better. The welding parameters have to be optimized for every alloy.

### 7.4.8 Modeling abrasive wear of weld deposits

Modeling of abrasive wear of the PTA welded deposits is very complicated. The welding parameters have all together effects on the dilution and the microstructure of the deposits. The microstructure alteration is related to the distance from the base material fusion line to the top of the deposit. Also small variations in the dilution and the microstructure may be present in the first and the following weld beads.

37 variables for the PTA welding method are identified effecting on the welding process (Kapus, 1980). General sliding wear has more than 100 different variables and constants effecting on the wear resistance (Meng *et al*., 1995). In equations 43 and 44 for the RWAT can been seen 7 variables. The other remarkable variables are wheel size, temperature rise, angularity, humidity, and area of wear scar (Avery, 1981). Stress level has an effect on the abrasive wear resistance in the RWAT. From the wear tracks abraded with low and high stress levels can be seen that rolling of the abrasives may prevent with high stress load, Figures 97-99. It can be said that abrasion is the main wear mechanism in the RWAT, but also other wear mechanisms can occur in small scale. In the field test the amount of process parameters effecting on the degradation of the deposits can be seldom known exactly. Interactions between different kinds of parameters have effects on the wear resistance. Welding operator and welding engineer as well as the welding unit have their own effects on the deposit quality (Kapus, 1980).

The differences in the microstructures of the 12V-1 tool steel deposits were low, but the effect of these differences on the wear resistance with used abrasive was high. It was also stated that the same welding parameters do not automatically fit for every alloys, even though the difference between alloy compositions is low. The abrasive wear models do not take into account the carbides shape ratio, the MFP, the size of carbides, the retained austenite content, and the volume fraction of carbides. These parameters change during the welding process, which makes it more difficult to estimate abrasive wear resistance by modeling.

### 7.4.9 Optimized welding parameters

The best abrasive wear resistance was obtained with welding parameters A, test 4, bead 2 and A, test 6, bead 2, 20,4 and 23,9 $mm^3$, respectively. In both deposits the abrasive wear resistance of the first bead was lower when compared to the abrasive wear resistance of the second bead. In the abrasive wear test the standard deviation of the relatively homogeneous 12V-1 tool steel material manufactured by the HIP process was 3,8 $mm^3$. The materials manufactured by the HIP process had the most homogeneous microstructure. Thus, the abrasive wear test results of A, test 4, bead 2 and A, test 6, bead 2 are almost in the range of standard deviation.

For optimizing the abrasive wear resistance of the first and the following beads the welding parameters have to be slightly varied. Powder feed rate can be decreased and plasma gas flow rate can be increased. The dilution of the deposit can be adjusted by plasma arc current.

The deposits welded with welding parameters A, tests 4 and A, test 6 had better abrasive wear resistance in the RWAT when compared to the 12V-1 tool steel material manufactured by the HIP process. More alloyed 15V-2 tool steel HIP material had the same abrasive wear resistance as the weld beads of the 12V-1 tool steel deposits A, test 4, bead 2 and A, test 6, bead 2 welded by the PTA method.

# 8 Conclusions

1. The main phenomenon of the 12V-1 tool steel deposit is its molten pool good mobility. The molten pool is prone to move between the plasma arc and the base material. Thus, dilution control is challenging and small variation in the plasma arc location in relation with the molten pool has large effect on the microstructure and the abrasive wear resistance.

2. The microstructure of the materials manufactured by the HIP process was the most homogeneous. Standard deviations of the volume fractions of VCs, the mean sizes of VCs, and the carbides shape ratios were lower than in the deposits welded by the PTA process. The most homogeneous deposits were welded with welding parameters A.

3. The shape ratio has an effect on the abrasive wear resistance of the 12V-1 tool steel deposit. The materials manufactured by the HIP process had the most round-shaped VCs, the shape ratio was between 0,83-0,86. The PTA welded deposits had the shape ratio between 0,66-0,83. Stirring of the molten pool by the plasma arc column seems to reduce the shape ratio in the deposits welded with welding parameters B and D. The shape ratio seems to increase in the deposits welded with welding parameters E and F during the surfacing procedure.

4. The best abrasive wear resistance of the PTA welded deposits was obtained with the mean size of VCs from 1,2 to 1,4 μm. The mean size of the carbides of the materials manufactured by the HIP process was between 0,8-1,1 μm.

5. The volume fraction of VCs of the PTA welded deposits was 0,5-5,5 vol.-% lower when compared to the 12V-1 tool steel material manufactured by the HIP process. The highest volume fraction was obtained in a sample welded with welding parameters C. The bead thickness was 5,5 mm and the location of the plasma arc was then on the molten pool.

6. The effect of the MFP on the abrasive wear resistance with the used abrasive size was not clearly detected. In the deposits where standard deviation of the MFP was high, it can be seen areas in the wear tracks where grooving was the dominating wear mode. Thus, even though the nominal abrasive fraction was remarkably larger than the MFP, asperities of the abrasives, crushed carbides, crushed abrasives, or detached abrasives were degrading the wearing surfaces.

7. The volume fraction of VCs increased in the wear track when compared to the microstructure. The round-shaped carbides were prone to stay in the wearing surface. The matrix wears off between the carbides and, thus, the volume fraction of the carbides increases in the wearing surface.

8. The VC size and the MFP distributions of the PTA welded deposits vary in ranges of 0,2-5,0 and 0,2-5,0 μm depending on the welding parameters,

respectively. The materials manufactured by the HIP process had ranges of 0,2-2,2 and 0,2-4,0 μm, respectively.

9. The retained austenite content was the lowest in the samples welded with welding parameters A-C. Low amount of retained austenite and high amount of martensite enhance the ability of carbides to resist abrasive wear.

10. The effect of the dilution on the abrasive wear resistance was not possible to measure exactly. The effects of the dilution of the deposits were mainly nearby the fusion line, i.e., approximately 0,5 mm from the fusion line. The volume fraction and the mean size of VCs were smaller nearby the fusion line. The location of the plasma arc in relation with the molten pool had stronger effect on the abrasive wear resistance than that of the dilution.

11. A lot of crushed carbides were detected from the wear surfaces of the deposits welded with welding parameters C and D. In the wear surfaces of the deposit welded with welding parameters A and the 12V-1 tool steel material manufactured by the HIP process, only some of the carbides were crushed during the RWAT. Round-shaped carbides resist microcracking.

12. The high stress abrasive wear test can be arranged by the rubber wheel abrasive test apparatus for tool steel alloys. With normal load 174 N the wear surface contained a lot of small grooves, especially on the areas where the MFP was large. A lot of crushed VCs can be detected. The 3,2 μm sized VC carbide was capable to crush the abrasive. Rolling of the abrasives was at least partly prevented.

13. Hardness of the 12V-1 tool steel deposit cannot be used for estimating the abrasive wear resistance of the 12V-1 tool steel deposit. Hardness depends on the volume fraction of VCs, the sizes of VCs, the MFP, the retained austenite content, and the dilution. The abrasive, the wear environment, and the microstructure together determine the wear rate. Small variations in the microstructure have remarkable effects on the abrasive wear resistance.

14. Surface roughness of the 12V-1 tool steel deposit was 1,6±0,3 μm in the end of the rubber wheel test. Surface roughness of 0,9±0,3 μm was obtained after 100 rounds of the rubber wheel. The measurements were made from the deposit, the mean size of VCs of which was 1,1 μm. Thus, when the VCs size distribution is taken into account, VCs shield the wear surface, and the penetration depth of the abrasives is smaller than the mean diameter of the abrasives.

15. The best abrasive wear resistance of both the deposits welded by the PTA method and the materials manufactured by the HIP process were detected from the deposits welded with rectangular wave mode, 4-6 l/min plasma gas flow rates, and 10-12 mm working distances. With 4-6 l/min plasma gas flow rate the plasma arc is more columnar when compared to plasma gas flow rate 2 l/min.

16. The PTA welding parameters have to be optimized for every tool steel alloy. The volume losses in the RWAT were from 20,4 to 146,0 $mm^3$ depending on the welding parameters. The 15V-1 tool steel deposit welded with welding parameters D had lower wear test result as the best 12V-1 tool steel deposit welded with welding parameters A, even though 15V-1 tool steel was more alloyed.

# References

Ait-Mekideche, A. 1989. Plasma-Pulver-Auftragschweissen verschleiβfester Pseudolegierungssysteme auf Cobalt-Chrom-Wolfram-Kohlenstoff-Basis. Doctoral Thesis, Rheinisch-Westfälischen Technischen Hochschule Aachen, Germany, 154 p.

Ala-Kleme, S., Kivikytö-Reponen, P., Liimatainen, J., Hellman, J. and Hannula, S.-P. 2007. Abrasive Wear Properties of Tool Steel Matrix Composites in Rubber Wheel Abrasion Test and Laboratory Cone Crusher Experiments. Wear, 263 (1-6), pp. 180-187.

Anderson, M., Chiovelli, S. and Llewellyn, R. 2003. The Use of Tungsten Carbide Materials for Oilsand Wear Applications. In: Moreau, C. and Marple, B.R. (Eds.). Thermal Spray 2003 – Advancing the Science and Applying the Technology, Proceedings, International Thermal Spray Conference (ITC 2003), Orlando, USA, 5-8 May 2003, pp. 509-518.

Andrews, K.W. 1965. Empirical Formulae for the Calculation of Some Transformation Temperatures. Journal of the Iron and Steel Institute, 203, July 1965, pp. 721-727.

Araki, T., Nishida, M., Hirose, A. and Fujita, H. 1994. Effects of Particle Size of Carbide Powder and Silica Sand on Abrasive Wear Resistance of an Overlay Composite Alloy. Welding International, 8 (1), pp. 23-29.

Archard, J.F. 1953. Contact and Rubbing of Flat Surfaces. Journal of Applied Physics, 24 (8), pp. 981-988.

Ashby, M.F. and Jones, D.R.H. 1980. Engineering Materials 1, An Introduction to Their Properties and Applications. International Series on Materials Science and Technology, Volume 34, Pergamon Press, 280 p.

ASTM G 65-94. Standard Test Method for Measuring Abrasion Using the Dry Sand / Rubber Wheel Apparatus. American Society for Testing and Materials, Philadelphia, USA, 12 p.

Avery, H.S. 1981. An Analysis of the Rubber Wheel Abrasion Test. In: Rhee, S.K., Ruff, A.W. and Ludema, K.C. (Eds.). Wear of Materials: International Conference on Wear of Materials, New York, USA, pp. 367-378.

Babi, M. 1991. A Study of Intermetallic Compounds in Plasma Transferred Arc Co-deposited Nickel-aluminum and Nickel-boron Carbide Blends. In: ISTFA/91; The 17th International Symposium for Testing & Failure Analysis, Los Angeles, USA, 11-15 November 1991, pp. 553-560.

Babi, M.A.K. 1993. An Innovative High Deposition Rate Plasma Transferred Arc Surfacing Technique. In: Berndt, C.C. and Bernecki, T.F. (Eds.). Thermal Spray

Coatings: Research, Design and Applications, Proceedings, 5th National Thermal Spray Conference, Anaheim, USA, 7-11 June 1993, pp. 133-138.

Babiak, Z. and Ambroziak, A. 1983. Analysis of the Factors Influencing the Hardness of Plasma Weld Surfaced Layers. Journal of Technical University of Silesia-Mechanica, 78, Gliwice, Poland.

Babiak, Z. and Dudziński, W. 1986. Tungsten Carbide Stability in Plasma Weld Surfacing. Surfacing Journal International, 1 (3), pp. 87-90.

Baeslack, W.A., Bucklow, I.A. and Abson, D.J. 1996. High Stress Abrasive Wear Testing of Chromium Boride/Stainless Steel and Tungsten-Vanadium-Carbide/Stainless Steel Hard-facing Materials. TWI Journal (UK), 5 (1), pp. 79-114.

Bayer, R.G. 1997. Wear Testing. In: Friction and Wear Testing, Source Book: Selected References from ASTM Standards and ASM Handbooks, ASM International, Materials Park, OH, USA, pp. 30-37.

Bhansali, K.J. 1980. Wear Coefficients of Hard-surfacing Materials. In: Peterson, M.B. and Winer, W.O. (Eds.). Wear Control Handbook, ASME, 1980, pp. 373-383.

Blau, P.J. 1989. Friction and Wear Transitions of Materials – Break-in, Run-in, Wear-in. Noyes Publications, Park Ridge, New Jersey, USA, 476 p.

Blunt, F.J. 2000. Magnetic Arc Oscillation for Weld Surfacing, Using Mechanized TIG, MIG and PTA Processes. In: Surfacing, Core Research from TWI, Abington, Cambridge, UK, Abington Publishing, pp. 80-124.

Bols, I. and Hunt, C.S. 1997. Shielding Gases – Product and Productivity. Welding Review International, 16 (1), pp. 157-159.

Bouaifi, B., Gebert, A. and Heinze., H. 1993. Plasma-Pulver-Auftragschweiβungen zum Verschleiβschutz abrasiv beanspruchter Bauteile mit Kantenbelastung. Schweissen & Schneiden, 45 (9), pp. 506-509 and E170-E172.

Bouaifi, B., Bartzsch, G., Gebert, A. and Heinze, H. 1997. Untersuchungen zum Plasma-Auftragschweiβen von verschleiβfesten Hartstoffschichten mit vanadiumcarbiden. Schweissen & Schneiden, 49 (4), pp. 213-219 and E54-E56.

Bouaifi, B. and Schultze, S. 1999. High-performance Plasma-powder-overlay Welding with CrNiMoN-alloyed Duplex Materials. Stainless Steel World, 11 (1), pp. 51-56.

Bourithis, L. and Papadimitriou, G. 2005. Three Body Abrasion Wear of Low Carbon Steel Modified Surfaces. Wear, 258 (11-12), pp. 1775-1786.

Box, G.E.P., Hunter, W.G. and Hunter, J.S. 1978. Statistics for Experiments, an Introduction to Design, Data Analysis, and Model Building. John Wiley & Sons, Inc., 657 p.

Brandis, H., Haberling, E. and Weigand, H.H. 1980. Metallurgical Aspects of Carbides in High-speed Steels. In: Wells, M.G.H. and Lherbier, L.W. (Eds.). Processing and Properties of High-speed Tool Steels, Las Vegas, USA, 26-28 February, TMS-AIME, pp. 1-18.

Buchely, M.F., Gutierrez, J.C., León, L.M. and Toro, A. 2005. The Effect of Microstructure on Abrasive Wear of Hardfacing Alloys. Wear, 259 (1), pp. 52-61.

Budinski, K.G. 1988. Surface Engineering for Wear Resistance. Prentice Hall, Englewood Cliffs, New Jersey, USA, 420 p.

Burgardt, P. and Heiple, C.R. 1986. Interaction between Impurities and Welding Variables in Determining GTA Weld Shape. Welding Journal, 65 (6), pp. 150-155.

Challen, J.M. and Oxley, P.L.B. 1979. An Explanation of the Different Regimes of Friction and Wear Using Asperity Deformation Models. Wear, 53 (2), pp. 229-243.

Chattopadhyay, R.N. 1998. The Effect of Dilution on Corrosion and Wear of Superalloy Weld Overlays. In: Khanna, A.S., Totlani, M.K. and Singh, S.K. (Eds.). Corrosion and its Control: Proceedings of International Conference on Corrosion, II, CORCON-97, Mumbai, India, 3-6 December 1997, pp. 1246-1250.

Chen, L.H., Chang, L.C. and Lui, T.S. 1990. The Abrasion Resistance of High-chromium White Cast Irons as a Linear Function of Carbide Volume Fraction. In: Proceedings of the Japan International Tribology Conference, Nagoya, Japan, 29 October-1 November 1990, pp. 227-231.

Chen, T.M., Lui, T.S. and Chen, L.H. 1993. Overlaying of Stellite 6 Superalloy on Austenitic Manganese Steel by PTA Method. In: Sudarshan, T.S. and Braza, J.F. (Eds.). Surface Modification Technologies VI, Chicaco, Illinois, USA, 2-5 November 1992, pp. 569-580.

Cochran, W.G. and Cox, G.M. 1950. Experimental Designs. John Wiley & Sons, Inc., New York, USA, 454 p.

Craig, E. 1988. The Plasma Arc Process – A Review. Welding Journal, 67 (2), pp. 19-25.

Czichos, H. 1997. Basic Tribological Parameters. In: Friction and Wear Testing, Source Book: Selected References from ASTM Standards and ASM Handbooks, ASM International, Materials Park, OH, USA, pp. 1-7.

David, S.A. and Vitek, J.M. 1989. Correlation between Solidification Parameters and Weld Microstructures. International Materials Reviews, 34 (5), pp. 213-245.

Delesse, M.A. 1847. Procédé Mécanique pour Déterminer la Composition des Roches. Comptes Rendus Hebdomadaires des Séances de l´Académie des Sciences. Académie des Sciences (France), Paris, 25, p. 544.

Deuis, R.L., Yellup, J.M. and Subramanian, C. 1997. Aluminium Composite Coatings Produced by Plasma Transferred Arc Surfacing Technique. Materials Science and Technology, 13 (6), pp. 511-522.

Deuis, R.L., Yellup, J.M. and Subramanian, C. 1998. Metal-matrix Composite Coatings by PTA Surfacing. Composites Science and Technology (UK), 58 (2), pp. 299-309.

Diesburg, D.E. and Borik, F. 1974. Optimizing Abrasion Resistance and Toughness in Steels and Irons for the Mining Industry. Symposium on Materials for the Mining Industry, Climax Molybdenum Co., Vail, USA, pp. 15-41.

Dilthey, U., Ellermeier, J., Gladkij, P. and Pavlenko, A.V. 1993. Combined Plasma-arc Powder Surfacing. Schweissen & Schneiden, 45 (5), pp. 241-244 and E75-E76.

Dilthey, U., Ellermeier, J. and Pavlenko, A.V. 1994. Computer-controlled Welding System for Combined Plasma Transferred Arc Surfacing. In: Welding, Joining, Coating and Surface Modification of Advanced Materials, Proceedings, Pre-assembly Symposium, 47th Annual Assembly of IIW, Dalian, China, 1-2 September 1994, pp. 391-396.

Dilthey, U., Pavlenko, A.V. and Ellermeier, J. 1996a. Automation of Plasma Transferred Arc Surfacing – Concepts for Operation and Control. DVS-Berichte, (175), TS96, Thermal Spraying Conference, Proceedings, Conference, Essen, Germany, 6-8 March 1996, pp. 433-437.

Dilthey, U., Pavlenko, A.V. and Ellermeier, J. 1996b. Influence of Different Alloying Elements on the Coating Quality in PTA Surfacing on Large Engine Valves with Co- and Ni-base Alloys. DVS-Berichte, (175), TS96, Thermal Spraying Conference, Proceedings, Conference, Essen, Germany, 6-8 March 1996, pp. 147-151.

Dilthey, U. and Kabatnik, L. 1998. Central Powder Feed in the Plasma Arc Powder Surfacing Process. Schweissen & Schneiden, 50 (12), pp. 766, 768-771 and E230-E232.

Donskoi, A.V. and Klubnikin, V.S. 1979. Electric Plasma Processes and Equipment in Engineering, Mashinostroenie, Leningrad, 170 p.

Draugelates, U., Bouaifi, B., Plegge, T., Franzoni, U., Sintoni, F. and Gimondo, P. 1993. Innenbeschichten von Rohren geringer Durchmesser durch Plasma-Pulver-Auftragschweiβen. DVS-Berichte, (152), TS93, Thermal Spraying Conference, Proceedings, Conference, Aachen, 3-5 March 1993, pp. 160-163.

Draugelates, U., Bouaifi, B., Gieβler, S. and Schreiber, F. 1996. Wear Protection against Complex Component Impact by PTA Surfacing with Hard Phase Reinforcements. DVS-Berichte, (175), TS96, Thermal Spraying Conference, Proceedings, Conference, Essen, Germany, 6-8 March 1996, pp. 143-147.

Dresvin, S.V. (Ed.), Donskoi, A.V., Goldfarb, V.M., and Klubnikin, V.S. 1972. Physics and Technology of Low-temperature Plasmas. Ames, IA, The Iowa State University Press, 1977, 471 p.

DuMola, R.J. and Kammer, P.A. 1988. A New Portable Plasma Transferred-arc System for on-site Wear Applications. In: Thermal Spray, Advances in Coatings Technology, Proceedings, National Thermal Spray Conference, Orlando, USA, 14-17 September 1987, pp. 131-136.

Dunkley, J.J. 1998. Atomization. In: ASM Handbook 1998, Volume 7, Powder Metal Technologies and Applications, ASM International, Materials Park, OH, USA, pp. 35-52.

DuPont, J.N. and Marder, A.R. 1996. Dilution in Single Pass Arc Welds. Metallurgical and Materials Transactions B, 27B (3), pp. 481-489.

DuPont, J.N. 1998. On Optimization of the Powder Plasma Arc Surfacing Process. Metallurgical and Materials Transactions B, 29B (4), pp. 932-934.

Dören, H. and Wernicke, K. 1985. Influence of the Welding Parameters in Plasma Arc Overlay Welding with Powder. DVS-Berichte, (100), Welding and Cutting, Proceedings, Conference, Essen, Germany, 11-13 September 1985, pp. 72-77.

Elizagàrate, C. and Penche, J. 1981. The Use of Plasma Surfacing in Industry. Revista de Soldadura, 11 (4), pp. 187-197.

Fang, L., Xing, J., Liu, W., Xue, Q., Wu, G. and Zhang, X. 2001. Computer Simulation of Two-body Abrasion Processes. Wear, 251 (2), pp. 1356-1360.

Feng, Z., White, R.A., Willis, E. and Solomon, H.D. 1999. Development of Compressive Residual Stresses in Underwater PTA Welds. Technical Information Series, GE Research & Development Center, August 1999, 8 p.

Fromowicz, J., Ait-Mekideche, A. and Lugscheider, E. 1993. Plasmabeschichten mit gepulstem Lichtbogen. DVS-Berichte, (152), TS93, Thermal Spraying Conference, Proceedings, Conference, Aachen, Germany, 3-5 March 1993, pp. 394-398.

Fuerschbach, P.W. and Knorovsky, G.A. 1991. A Study of Melting Efficiency in Plasma Arc and Gas Tungsten Arc Welding. Welding Journal, 70 (11), pp. 287-297.

Garrison, W.M. Jr., 1982. Khruschov's Rule and the Abrasive Wear Resistance of Multiphase Solids. Wear, 82 (2), pp. 213-220.

Gatto, A., Bassoli, E. and Fornari, M. 2004. Plasma Transferred Arc Deposition of Powdered High Performances Alloys: Process Parameters Optimisation as a Function of Alloy and Geometrical Configuration. Surface & Coatings Technology, 187 (2-3), pp. 265-271.

Gebert, A., Bouaifi, B. and Teupke, E. 2001. Neue vanadinkarbidhaltige Schweiβzusätze zum Schutz gegen Verschleiβ und Korrosion. DVS-Berichte, (216), pp. 365-370.

German, R.M. 2005. Powder Metallurgy and Particulate Materials Processing, the Processes, Materials, Products, Properties, and Applications. Metal Powder Industries Federation, Princeton, New Jersey, USA, 528 p.

Giedt, W.H., Tallerico, L.N. and Fuerschbach, P.W. 1989. GTA Welding Efficiency: Calorimetric and Temperature Field Measurements. Welding Journal, 68 (1), 1989, pp. 28-32.

Gladky, P. and Pavlenko, A. 1990. Development of Physical Concepts about the Plasma Transferred Arc Surfacing. In: Machida, S. (Ed.). Advanced Technology in Welding, Materials Processing and Evaluation, Proceedings, 5th International Symposium of the Japan Welding Society, Tokyo, Japan, 17-19 April 1990, pp. 399-404.

Goldak, J., Chakravarti, A. and Bibby, M. 1984. A New Finite Element Model for Welding Heat Sources. Metallurgical Transactions B, 15B (2), pp. 299-305.

Gregory, N. 1991. Cracking of Hardfacing Alloys – Prevent, Cure or Ignore? Bulletin 3, May/June 1991, TWI, pp. 52-54.

Hallén, H., Lugscheider, E. and Ait-Mekideche, A. 1992a. Plasma Transferred Arc Surfacing with High Deposition Rates. In: Bernecki, T.F. (Ed.). Thermal Spray Coatings: Properties, Processes and Applications, Proceedings, 4th National Thermal Spray Conference, Pittsburgh, USA, 4-10 May 1991, pp. 537-539.

Hallén, H., Mathesius, H., Ait-Mekideche, A., Hettiger, F., Morkramer, U. and Lugscheider, E. 1992b. New Applications for High Power PTA Surfacing in the Steel Industry. In: Berndt, C.C. (Ed.). Thermal Spray: International Advances in Coatings Technology, Proceedings, 13th International Conference, Orlando, USA, 28 May-5 June 1992, pp. 899-902.

Harris, P. and Smith, B.L. 1983. Factorial Techniques for Weld Quality Prediction. Metal Construction, 15 (11), pp. 661-666.

Heiple, C.R. and Roper, J.R. 1982. Mechanism for Minor Element Effect on GTA Fusion Zone Geometry. Welding Journal, 61 (5), pp. 97-102.

Herrström, C., Hallén, H., Ait-Mekideche, A. and Lugscheider, E. 1993. Factorial Analysis Applied to the PTA Process. DVS-Berichte, (152), TS93 Thermal Spraying Conference, Proceedings, Conference, Aachen, 3-5 March 1993, pp. 409-412.

Hertzberg, R.W. 1996. Deformation and Fracture Mechanics of Engineering Materials. John Wiley & Sons, Inc., New York, USA, 786 p.

Hettiger, F. 1992. Plasma Welding Known Since the 50s. PMI, 24 (1), pp. 14-18.

Holmberg, K. and Matthews, A. 1994. Coatings Tribology: Properties, Techniques and Applications in Surface Engineering. Dowson, D. (Ed.). Tribology Series, 28, Elsevier, Amsterdam, The Netherlands, 442 p.

Hu, J., Li, D.Y. and Llewellyn, R. 2005. Computational Investigation of Microstructural Effects on Abrasive Wear of Composite Materials. Wear, 259 (1), pp. 6-17.

Huang, X., Wang, R., Xu, L., Luo, H. and Yin, X. 1998. Applications of PTA Powder Welding in Petroleum Chemical Industry. In: Proceedings of the 15th International Thermal Spray Conference, Nice, France, 25-29 May 1998, pp. 1013-1017.

Hunt, C.S. 1988. Plasma Transferred Arc (PTA) Surfacing of Small and Medium Scale Components – a Review. Welding Institute Members Report 364/1988, pp. 3-46.

Hutchings, I.M. 1992. Tribology: Friction and Wear of Engineering Materials. Department of Materials Science and Metallurgy, University of Cambridge, Great Britain, 273 p.

Ishizaki, K., Okada, T. and Yokoya, S. 1994. Electromagnetic Force near the Anode Boundary and Double Convention in a TIG Arc Weldpool. Welding International, 8 (10), pp. 790-797.

Jones, H. 1981. Experimental Methods in Rapid Quenching from the Melt. In: Herman, H. (Ed.). Treatise on Materials Science and Technology, Volume 20, Ultrarapid Quenching of Liquid Alloys, Academic Press, New York, USA, pp. 1-72.

Kammer, P.A., Weinstein, M. and DuMola, R.J. 1992. Characteristics and Applications for Composite Wear-resistant Overlays. In: Bernecki, T.F. (Ed.). Thermal Spray Coatings: Properties, Processes and Applications, Proceedings of the 4th National Thermal Spray Conference, Pittsburgh, USA, 4-10 May 1991, pp. 513-518.

Kapus, B.G. 1980. Computer Control Takes the Variations Out of Hardfacing. Welding Design & Fabrication, 53 (6), pp. 84-88.

Kato, K. 1997. Wear Mechanisms. In: Hutchings, I.M. (Ed.). New Directions in Tribology, Conference, London, UK, 8-12 September 1997, pp. 39-56.

Khruschov, M.M. 1974. Principles of Abrasive Wear. Wear, 28 (1), pp. 69-88.

Kivikytö-Reponen, P. 2006. Correlation of Material Characteristics and Wear of Powder Metallurgical Metal Matrix Composites. Doctoral Thesis, Helsinki University of Technology, Espoo, Finland, 93 p.

Klimpel, A., Dobrzański, L.A., Lisiecki, A. and Janicki, D. 2006. The Study of the Technology of Laser and Plasma Surfacing of Engine Valves Face Made of X40CrSiMo10-2 Steel using Cobalt-based Powders. Journal of Materials Processing Technology, 175 (1-3), pp. 251-256.

Koivula, J., Ahola, K. and Ahola, T. 1992. Plasmahitsaus helpottuu. Hitsaustekniikka, (6), pp. 13-16.

Kou, S. and Wang, Y.H. 1986. Weld Pool Convection and Its Effect. Welding Journal, 65 (3), pp. 63-70.

Kou, S. 1987. Welding Metallurgy. John Wiley & Sons, Inc., New York, USA, 411 p.

L'Estrade, L., Hallén, H. and Ljunggren, R. 1988. Internal Porosity of Gas Atomized Powders. In: Modern Developments in Powder Metallurgy, 20, Conference, Orlando, USA, 5-10 June 1988, pp. 187-203.

Lugscheider, E. and Ait-Mekideche, A. 1990. Increasing the Life of Components by Plasma Arc Surfacing with Composite Carbide Metal and Hard Alloy Powders. Schweissen & Schneiden, 42 (2), pp. 76-82 and E26-E29.

Lugscheider, E., Morkramer, U. and Ait-Mekideche, A. 1992. Advances in PTA Surfacing. In: Bernecki, T.F. (Ed.). Thermal Spray Coatings: Properties, Processes and Applications, Proceedings of the 4th National Thermal Spray Conference, Pittsburgh, USA, 4-10 May 1991, pp. 529-535.

Lugscheider, E., Ait-Mekideche, A. and Melzer, A. 1994. Improving the Properties of Hard Alloys by Weld Surfacing with Carbide Composite Powders. Schweissen & Schneiden, 46 (3), pp. 109-114 and E34-E37.

Lugscheider, E., Dehelean, D., Molnar, R. and Morkramer, U. 1995. Improving Abrasive Wear Resistance of Functional Surfaces by Plasma Transferred Arc Surfacing Using Particle Reinforced Alloys. In: Achievements and Prospects in the Fields of Welding and Materials Testing, Proceedings of 25 Year Jubilee Conference, Timisoara, Romania, 2, 24-26 May 1995, pp. 23-32.

Marantz, D.R. and Richardson, S.J. 1980. Plasma Transferred Arc Hardfacing, an Improved Process for Surfacing. In: General Aspects of Thermal Spraying, Preprints, Paper 38, 9th International Thermal Spraying Conference, ITSC 1980, The Hague, Netherlands, 19-23 May 1980, pp. 207-210.

Marimuthu, K. and Murugan, N. 2003. Prediction and Optimization of Weld Bead Geometry of Plasma Transferred Arc Hardfaced Valve Seat Rings. Surface Engineering, 19 (2), pp. 143-149.

Mathew, M.D., Mannan, S.L. and Gupta, S.K. 1980. Influence of Preheat Temperature on Stellite Deposits. Welding Journal, 59 (7), pp. 213-216.

Meng, H.C. and Ludema, K.C. 1995. Wear Models and Predictive Equations: Their Form and Content. Wear, 181-183 (2), pp. 443-457.

Menzel, M. 2003. The Influence of Individual Components of an Industrial Gas Mixture on the Welding Process and the Properties of Welded Joints. Welding International, 17 (4), pp. 262-264.

Messler, R.W. Jr. 1999. Weld Pool Convection, Oscillation, and Evaporation. In: Principles of Welding, Processes, Physics, Chemistry, and Metallurgy, Chapter 10, John Wiley and Sons, Inc., New York, USA, pp. 291-312.

Meyer, J.J. 1976. Plasma Hot Wire Surfacing. Welding Journal, 55 (2), pp. 97-100.

Mitelea, I. and Molnar, R. 1997. The Influence of Some Technological Parameters on the PTA Welded Layers Dilution. In: 60 Years of Scientific Co-operation in Welding, Proceedings, Jubilee Conference, Timisoara, Romania, 19-21 November 1997, pp. 437-442.

Moore, M.A. and King, F.S. 1980. Abrasive Wear of Brittle Solids. Wear, 60 (1), pp. 123-140.

Murugan, N. and Parmar, R.S. 1994. Effects of MIG Process Parameters on the Geometry of the Bead in the Automatic Surfacing of Stainless Steel. Journal of Materials Processing Technology, 41 (4), pp. 381-398.

Nefedov, B.B. and Lyalyakin, V.P. 1994. Calculating the Conditions of Plasma-powder Hardfacing of Shafts. Welding International, 8 (3), pp. 223-225.

Nefedov, B.B, Lyalyakin, V.P. and Steshenko, V.A. 1995. Programming the Process of Plasma-powder Surfacing of Shafts. Welding International, 9 (12), pp. 989-991.

Nishida, M., Araki, T. and Fujita, H. 1993. Effect of TiC-$Cr_3C_2$ Particles Content on Abrasive Resistance of Co-base Overlay Weld Alloy. Transactions of the Japan Welding Society, 24 (2), pp. 107-112.

Nishida, M., Araki, T., Shigekawa, Y., Asano, I. and Hayashi, Y. 1999. Sliding Wear Characteristics of Cobalt-based Overlay Weld Metal with Dispersed Boride Particles. Welding International, 13 (2), pp. 123-132.

Oberländer, B.C. and Lugscheider, E. 1992. Comparison of Properties of Coatings Produced by Laser Cladding and Conventional Methods. Materials Science and Technology, 8 (8), pp. 657-665.

Oechsle, M. and Szieslo, U. 2000. Einfluss von Schutzgasen auf die Schichtqualität von Plasmapulverschweiβungen. DVS-Berichte, (209), Welding and Cutting 2000, Proceedings, Welding Conference, Nurnberg, Germany, 27-29 September 2000, pp. 326-333.

Pavelic, V., Tanbakuchi, R., Uyehara, O.A. and Myers, P.S. 1969. Experimental and Computed Temperature Histories in Gas Tungsten-arc Welding of Thin Plates. Welding Journal, 48 (7), pp. 295-305.

Pavlenko, A. 1996. Neue Kenntnissse über Physikalische Grundlagen des Plasma-Pulver-Auftragschweiβens als Basis für die Prozeβsteuerung. Doctoral Thesis, Rheinisch-Westfälischen Technischen Hochschule Aachen, Germany, 119 p.

Pfeiffer, E. and Wittmann, P. 1984. Metallurgy and Welding Parameters of Mechanized Plasma Overlay Welding Processes. DVS-Berichte, (90), Schweissen und Schneiden 1984, Proceedings, Conference, Frankfurt, Germany, 26-28 September 1984, pp. 36-39.

Rabinowicz, E. 1965. Friction and Wear of Materials. John Wiley and Sons, Inc., New York, USA, 244 p.

Radaj, D. 1992. Heat Effects of Welding. Springer-Verlag, Berlin, Heidelberg, Germany, 348 p.

Raghu, D. and Webber, R. 1996. PTA Proves Its Worth in High-Volume Hardfacing Jobs. Welding Journal, 75 (2), pp. 34-40.

Rasche, S. 1973. Grundsätzliche Untersuchungen zur Physik und Technologie des Plasma-Auftragschweiβens. Doctoral Thesis, Rheinisch-Westfälischen Technischen Hochschule Aachen, Germany, 179 p.

Rykalin, N.N. 1957. Berechnung der Wärmevorgänge beim Schweissen. VEB Verlag Technik, Berlin, Germany, 326 p.

Röthig, J., Kecke, H.J., Reiter, R. and Draugelates, U. 1997. Iron Carbide Coatings with Metastable Iron-manganese Matrix. Schweissen & Schneiden, 49 (4), pp. 220-222, 224 and E56-E58.

Sahin, Y. 2005. The Prediction of Wear Resistance Model for the Metal Matrix Composites. Wear, 258 (11-12), pp. 1717-1722.

Saltzman, G.A. and Aufderhaar, W.B. 1985. New Antiwear Coatings Applied by Plasma-transferred Arc Wearsurfacing. Journal of the American Society of Lubrication Engineers, 41 (4), 39th Annual Meeting, Chigaco, USA, 7-10 May 1984, pp. 233-241.

Saltzman, G.A. and Sahoo, P. 1992. Applications of Plasma Arc Weld Surfacing in Turbine Engines. In: Bernecki, T.F. (Ed.). Thermal Spray Coatings: Properties, Processes and Applications, Proceedings, 4th National Thermal Spray Conference, Pittsburgh, USA, 4-10 May 1991, pp. 541-548.

Sexton, G.D. and Walduck, R.P. 1994. Plasma Transferred Arc Weld Surfacing. In: Eurojoin 2, Proceedings, 2nd European Conference on Joining Technology, Florence, Italy, 16-18 May 1994, pp. 545-554.

Shanmugam, R. and Murugan, N. 2004. Optimization and Sensitivity Analysis of Wear Model of Stellite-6 Hardfacing by Gas Tungsten Arc Welding Process. Journal-MM, 85, The Institution of Engineers (India), pp. 65-70.

Sharples, R.V. 1985. The Plasma Transferred Arc (PTA) Weld Surfacing Process. Welding Institute Members Report, 283/1985.

Shin, J.-C., Doh, J.-M., Yoon, J.-K., Lee, D.-Y. and Kim, J.-S. 2003. Effect of Molybdenum on the Microstructure and Wear Resistance of Cobalt-base Stellite Hardfacing Alloys. Surface and Coatings Technology, 166 (2-3), pp. 117-126.

Shubert, G. 1992. Advances in Plasma Transferred Arc Process Equipment and How This Can Effect New Application Development. In: Bernecki, T.F. (Ed.). Thermal Spray Coatings: Properties, Processes and Applications, Proceedings, 4th National Thermal Spray Conference, Pittsburgh, USA, 4-10 May 1991, pp. 519-524.

Siagam, A.T., Brenner, G., Giese, P. and Wesling, V. 2008. Numerical and Experimental Study of Particle Motion in Plasma Arc Welding. FDMP, 4 (2), pp. 77-83.

Sintoni, F., Gimondo, P., Grifoni, B. and Taraschi, I. 1992. Tribological and Microstructural Characterization of Grade 60 NiCrBSi Welded Coatings Deposited by PTA Technology on a Steel Substrate. In: Berndt, C.C. (Ed.). Thermal Spray: International Advances in Coatings Technology, Proceedings, 13th International Conference, Orlando, USA, 28 May-5 June 1992, pp. 887-891.

Steklov, O.I., Alekseev, A.V., Aleksandrov, O.A., Smirnov, V.I. and Ovcharenko, L.V. 1989. A High-productivity Process of Plasma Arc Hot Wire Surfacing. Welding International, 3 (12), pp. 1058-1059.

Stevenson, A.N.J. and Hutchings, I.M. 1996. Development of the Dry Sand/Rubber Wheel Abrasion Test. Wear, 195 (1), pp. 232-240.

Stout, R.D. 1987. Weldability of Steels. 4th ed., Welding Research Council, New York, USA, 441 p.

Sun, Z. and Huang, Z.H. 1998. Micro-PTA Powder Cladding on a Hot Work Tool Steel. International Journal of Materials and Product Technology, 13 (3-6), pp. 146-154.

Talonen, J., Aspegren, P. and Hänninen, H. 2004. Comparison of Different Methods for Measuring Strain Induced α´-martensite Content in Austenitic Steels. Materials Science and Technology, 20 (12), pp. 1506-1512.

Takeuchi, Y. and Nagata, M. 1985. Application of Plasma Powder Welding to Engine Valves. SAE International, SAE Technical Papers, No. 850518, 7 p.

Teupke, S.E. 2002. Entwicklung vanadinkarbidhaltiger Schweiβzusätze auf Eisenbasis fűr den Schutz gegen komplexe Beanspruchungen. Doctoral Thesis, Technischen Universität Clausthal, Germany, 112 p.

Torrence, A.A. 2005. Modelling Abrasive Wear. Wear, 258 (1-4), pp. 281-293.

Tsubouchi, K., Akiyama, M. and Okuyama, T. 1997. Development and Optimization of Carbide-reinforced Tools and Application to Hot Rolling of Stainless Steel. Journal of Tribology, 119 (4), pp. 687-693.

Tucker, R.C. Jr. 1997. Wear Failures. In: Friction and Wear Testing, Source Book: Selected References from ASTM Standards and ASM Handbooks, ASM International, Materials Park, OH, USA, pp. 168-185.

Ushio, M. 1991. Mathematical Modelling of Flow in the Weld Pool, Part II. Welding International, 5 (8), pp. 593-597.

Wahl, W. and Krauskopf, F. 1993. Plasmapulverauftragschweiβen von Eisenwerkstoffen. Schweissen & Schneiden, 45 (2), pp. 84-85 and E27-E28.

Wang, A. and Rack, H.J. 1991. Abrasive Wear of Silicon Carbide Particulate- and Whisker-reinforced 7091 Aluminium Matrix Composites, Wear, 146 (2), pp. 337-348.

Wang, S.-H., Chen, J.-Y. and Xue, L. 2006. A Study of the Abrasive Wear Behaviour of Laser-clad Tool Steel Coatings. Surface & Coatings Technology, 200 (11), pp. 3446-3458.

Wilden, J., Bergmann, J.P. and Frank, H. 2006. Plasma Transferred Arc Welding – Modeling and Experimental Optimization. Journal of Thermal Spray Technology, 15 (4), pp. 779-784.

Wu, W., Hwu, L.Y., Lin, D.Y. and Lee, J.L. 2000. The Relationship between Alloying Elements and Retained Austenite in Martensitic Stainless Steel Welds. Scripta Materialia, 42 (11), pp. 1071-1076.

Xibao, W. and Hua, L. 1998. Metal Powder Thermal Behaviour during the Plasma Transferred-arc Surfacing Process. Surface and Coatings Technology, 106 (2-3), pp. 156-161.

Xibao, W., Jia, F.-S., Wang, X.-F. 2002. Evaluation of Powder's Thermal Behaviour in Plasma Transferred-arc Space (Part I). Transactions of the China Welding Institution, 23 (4), pp. 13-16.

Xibao, W. 2003. Comparisons of Particles Thermal Behaviour between Fe-base Alloy and Boron Carbide during Plasma Transferred-arc Powder Surfacing. China Welding, 12 (1), pp. 67-71.

Xu, L., Xing, J., Wei, S., Zhang, Y. and Long, R. 2007. Study on Relative Wear Resistance and Wear Stability of High-speed Steel with High Vanadium Content. Wear, 262 (3-4), pp. 253-261.

Yamamoto, A. and Hashimoto, Y. 1997. New Surface Treatment Technology with a Plasma Transferred Arc Welding Process. Kobelco Technology Review, (20), pp. 42-46.

Yellup, J.M. and Wigley, P. 1996. Variation in Properties of Chromium Carbide Surfaces Deposited at Extremities of Recommended Welding Parameters. Australian Welding Research, CRC (16), 20 p.

Yokoya, S., Okada, T. and Matsunawa, A. 1994. Penetration Shape in Carbon Steel Welds Produced by a Stationary TIG Arc. Welding International, 8 (10), pp. 781-789.

Zum Gahr, K.-H. 1987. Microstructure and Wear of Materials. Tribology Series, 10, Elsevier, Amsterdam, The Netherlands, 560 p.

Zum Gahr, K.-H. 1988. Modelling of Two-body Abrasive Wear. Wear, 124 (1), pp. 87-103.

Zum Gahr, K.-H. 1995. Development of Materials to Resist Unlubricated Sliding Wear. In: Sudarshan, T.S., Jeandin, M., and Stiglich, J.J. (Eds.). Surface Modification Technologies VIII: Proceedings of the 8th International Conference on Surface Modification Technologies Held in Nice, France, September 26-28, 1994, The Institute of Materials (Great Britain), pp. 3-16.

Zum Gahr, K.-H. 1997. Wear by Hard Particles. In: Hutchings, I.M. (Ed.). New Directions in Tribology, Conference, London, UK, 8-12 September 1997, pp. 483-494.

Ågren, J. 1990. Kinetics of Carbide Dissolution. Scandinavian Journal of Metallurgy, 19 (1), pp. 2-8.

ISBN 978-952-60-3109-5
ISBN 978-952-60-3110-1 (PDF)
ISSN 1795-2239
ISSN 1795-4584 (PDF)